The University Of Sheffield.

Tuned-Inerter-Based-Dampers with Linear Hysteretic Damping for Earthquake Protection of Building Structures

By:

Predaricka Deastra

Supervisors:

Prof. David J Wagg

Prof. Neil D Sims

A thesis submitted in partial fulfilment of the requirements for the degree of Doctor of Philosophy

March 2021

Abstract

The inerter is a two-terminal device that generates a resisting force proportional to the relative acceleration between its two terminals. To date, three main types of inerters have been introduced in the literature based on inertial mass (inertance) generation mechanisms: fluid inerters, rack-and-pinion inerters, and ball-screw inerters. In such mechanisms, significant levels of inertance can be generated while keeping the actual mass to a minimum.

This feature of inerters has attracted many researchers in the earthquake engineering community to explore their use for protecting building structures against earthquakes. For this purpose, inerters are often combined with a stiffness and a damping element in various configurations to form so-called tuned-inerter-based-dampers (TIBDs). There are three TIBDs mostly found in the literature: (1) tuned-viscous-mass-damper (TVMD); (2) tuned-inerter-damper (TID); (3) tuned-mass-damper-inerter (TMDI).

One common layout of the three TIBDs is they have at least two elements connected in parallel. In the TVMD, the two elements are viscous damper and inerter, while in the TID and TMDI, the two elements are spring and viscous damper. For the first time, the possibilities for the devices to exhibit hysteresis through the two elements in parallel are explored in this thesis. In particular, two linear hysteretic damping concepts are discussed: (1) complex damping; and (2) complex stiffness.

Furthermore, novel concepts of passive tuned inerter dampers with linear hysteretic damping, namely the tuned inerter hysteretic damper (TIhD) and the tuned mass hysteretic damper inerter (TMhDI) are introduced. Both concepts were developed based on the well established TID concept whereby the parallel connected viscous damping and spring elements are replaced by a complex stiffness model. The idea is to design a more realistic tuned inerter damper that captures the hysteretic behavior of the dampers. The aim is to develop a modified method to solve the equation of motion of structures with complex stiffness in the time domain.

Finally, a shake table experiment was performed for a three-storey structure equipped with a TMhDI device on its base storey, subjected to both harmonic and earthquake base inputs. The TMhDI uses gel dampers as its hysteretic damping element. The inerter element was realised by a flywheel inerter which was designed by using a frictionless linear guide mechanism. For comparison, a shake table experiment was also performed for the same three-structure equipped with a TMDI device on its base storey level. The viscous damping element was realised using eddy current dampers. It is shown that the analytical model of both TMhDI and TMDI are in good agreement with the experimental results. Furthermore, these experiments also confirm the distinction between both devices, particularly in the structure's second and third modes of vibrations, where the structure equipped with the TMhDI has a larger response.

Acknowledgments

I gratefully acknowledge Prof David J Wagg and Prof Neil D Sims for their continuous support and the fruitful discussions. This thesis would not have been possible without their guidance.

I acknowledge the funding from Indonesia Endowment Fund for Education (LPDP) for the full PhD scholarship. This research also made use of The Laboratory for Verification and Validation (LVV) which was funded by the EPSRC (grant numbers EP/R006768/1 and EP/N010884/1), the European Regional Development Fund (ERDF) and the University of Sheffield.

I also would like to thank Dr Robin S Mills, Mr Michael J Dutchman, and Mr Mathew Hall for their help on the experiments. Lastly, I want to dedicate my deepest gratitude to my family and friends.

List of Publications

During my PhD study, I have published and submitted some journal and conference articles as listed below:

Journal papers

1. Dario De Domenico, **Predaricka Deastra**, Giuseppe Ricciardi, Neil D. Sims, David J.Wagg. "Novel fluid inerter based tuned mass dampers for optimised structural control of base-isolated buildings" *Journal of the Franklin Institute,* vol. 356, no. 14, pp. 7626-7649, 2019.
   DOI: https://doi.org/10.1016/j.jfranklin.2018.11.012

2. **Predaricka Deastra**, David J. Wagg, Neil D. Sims, Mahesa Akbar. "Tuned inerter dampers with linear hysteretic damping" *Earthquake Engineering and Structural Dynamics*
   DOI: https://doi.org/10.1002/eqe.3287

Conference papers

1. **Deastra,P.**, Wagg, D. J., Sims, N.D. "The Application of Inerter-Based Damper Using A Fluid Inerter for Earthquake Response Reduction of MDOF Structures". *1st International Conference on Seismic Design of Structures and Foundations (SEISMICON 2017). London, UK, December 2017.*

2. **Deastra,P.**, Wagg, D. J., Sims, N.D. "The Realisation of An Inerter-Based System Using Fluid Inerter." *Dynamics of Civil Structures, Volume 2, Springer, Cham, 2019. 127-134.*

3. Tipuric,M., **Deastra,P.**, Wagg, D. J., Sims, N.D. "Semi-active Inerters Using Magnetorhelogical Fluid: A Feasibility Study." *Active and Passive Smart Structures and Integrated Systems XII (Conference proceeding). Colorado, USA, March 2018.*

4. **Deastra,P.**, Wagg, D. J., Sims, N.D. "The Effect of A Tuned-Inerter-Damper On The Seismic Response of Base-Isolated Structures." *16th European Conference on Earthquake Engineering (ECEE). Thessaloniki, Greece, June 2018.*

5. **Deastra,P.**, Wagg, D. J., Sims, N.D. "Modelling the hysteretic behaviour of a fluid inerter for use as a parallel-viscous-inerter-damper device." *7th World Conference on Structural Control and Monitoring (WCSCM). Qingdao, China, July 2018.*

6. **Deastra,P.**, Wagg, D. J., Sims, N.D. "Time domain analysis of structures with hysteretic vibration suppression systems." *Journal of Physics: Conference Series 1264 (2019) 012032.*

7. De Domenico, D., **Deastra, P.**, Ricciardi, G., Sims, N.D., Wagg, D.J. "Improved seismic base isolation combined with fluid inerter and tuned mass damper." *16th World Conference on Seismic Isolation, Energy Dissipation and Active Vibration Control of Structures (16WCSI), St. Pettersburg, Russia, July 2019.*

8. **Deastra,P.**, Wagg, D. J., Sims, N.D. "Optimum design of a tuned-inerter-hysteretic-damper (TIhD) for building structures subjected to earthquake base excitations." *Accepted to appear in proceedings of XI International Conference on Structural Dynamics (EURODYN 2020), Athens, Greece, June 2020.*

9. **Deastra,P.**, Wagg, D. J., Sims, N.D. "Shake table tests of a three-storey structure with an inerter-based-hysteretic-damper." *Accepted to appear in proceedings of 17th World Conference on Earthquake Engineering (17WCEE), Sendai, Japan, September 2020.*

10. **Deastra,P.**, Wagg, D. J., Sims, N.D. "Using a tuned-inerto-viscous-hysteretic-damper (TIVhD) for vibration suppression in multi-storey building structures." *Accepted to appear in proceedings of 2nd International Conference on Disaster Management (ICDM 2020), Padang, Indonesia, September 2020.*

Contents

List of Figures

List of Tables

Nomenclature

$\bar{\mu}$	viscosity of fluid
$\bar{X}$	amplitude of displacement excitation
$[\ddot{\ }]$	second derivative with respect to the time
$\ddot{q}_A$	acceleration at gyro-mass terminal A
$\ddot{q}_B$	acceleration at gyro-mass terminal B
ΔP	area inside a hysteresis loop of the complex damping model
ΔW	work done by the damper (area inside a hysteresis loop of the complex stiffness model)
$[\dot{\ }]$	first derivative with respect to time
η	loss factor
η_{opt}	optimum loss factor
λ	stiffness ratio, k/k_d
$\mathbf{\Phi}$	eigenvector matrix of $\mathbf{A}$
$\mathbf{A}$	eigenvalues matrix
$\mathbf{F}$	force vector
$\mathbf{G}$	damping coefficient matrix
$\mathbf{K}$	stiffness matrix
$\mathbf{L_F}$	coefficient vector of elements' load factor
$\mathbf{M}$	mass matrix
$\mathbf{q_{k_a}}$	matrix of analytic modal coordinate for stable parts
$\mathbf{q_{l_a}}$	matrix of analytic modal coordinate for unstable parts

$\mathbf{x}$	displacement vector
μ	mass ratio
ω	circular frequency (rad/s)
ω_n	natural circular frequency (rad/s)
ϕ	phase shift
ρ	density of fluid
ζ	viscous damping ratio
ζ_{opt}	optimum viscous damping ratio
A_1	area of piston
A_2	area of channel
b	inertance of fluid inerter
b_d	inertance
c	viscous damping coefficient
c_d	viscous damping coefficient of TVAs and TIBDs
C_i	capacitance
D_h	channel diameter
F	device force
F_{damper}	helical fluid inerter force
F_{fd}	friction force
F_{hys}	hysteretic damping force
f_{opt}	optimum frequency (Hz)
F_{vd}	viscous damping force
H	Hilbert transform
h	helix pitch
i_i	current
J	moment inertia of disks

j	$\sqrt{-1}$
k	stiffness
k_d	stiffness of TVAs and TIBDs
l	length of helical channel
L_i	inductance
L_t	length of tube
m	mass
m_d	secondary mass of TVAs and TIBDs
m_s	gyro-mass inertance $= J/r_s^2$
m_{hel}	mass of fluid inside helical channel
q	frequency ratio, ω/ω_n
R	Laplace transform of ground displacement $r(t)$
$r(t)$	ground displacement
r_3	helix radius
R_h	channel bend radius
R_i	resistance
r_s	disks radius
s	Laplace transform variable
s_h	parameter with a unit of stiffness
t	time
v	velocity
X	Laplace transform of displacement $x(t)$
x	displacement
z	reversed time
$[\,']$	derivative in the reversed time
ECD	Eddy Current Damper

PVID Parallel Viscous Inerter Damper

TIBD Tuned Inerter Based Damper

TID Tuned Inerter Damper

TIhD Tuned Inerter hysteretic Damper

TMDI Tuned Mass Damper Inerter

TMhDI Tuned Mass hysteretic Damper Inerter

TVMD Tuned Viscous Mass Damper

Chapter 1

Introduction

1.1 Background

Earthquakes have long been major problems for people living in the seismic prone areas. During the twentieth century, more than 1,200 destructive earthquakes occured and caused extensive damage worth more than $1 trillion worldwide [1]. Moreover, with regard to loss of life on average 10,000 people died each year between 1900 and 1999 due to earthquakes [2].

In Indonesia, the 2004 earthquake with a magnitude of 9.0 on the Richter scale followed by a tsunami caused 283,000 deaths in addition to damage costing $13.5 billion [3] and in 2005 an earthquake with a magnitude of 8.7 caused 1,520 deaths. In Indonesia between 2000 and 2006, there were five earthquakes with magnitudes higher than 7.0 which caused billions of dollars' worth of structural damage [3]. More recently, in December 2016 an earthquake with a magnitude of 6.5 on the Richter scale occured in Aceh, Indonesia, and killed nearly 100 people [4].

Worldwide, devastating earthquakes have caused extensive damage and killed many thousands of people. For example the Northridge earthquake (1994) in US caused damage $30 billion and killed 60 people, the Alaska earthquake (1964) in US caused damage $311 million and killed 115 people, the earthquake in Hyogo-ken Nanbu, Japan (1995) caused damage $150 billion and killed 6000 people [5].

Several reports have concluded that 75% of earthquake fatalities were caused by building collapse during the last century [5]. For example, 73% of deaths during the 1995 Kobe earthquake were caused by collapsed houses [5]. On the other hand, 63% of deaths during the 1989 Loma Prieta earthquake were caused by bridge failures [5]. This implies that protecting structures from severe damage during earthquakes is key to reducing the loss of life. Thus, in the earthquake engineering community, there is an earthquake-resistant design philosophy for structures that has since been accepted worldwide: the structures should resist (1) minor earthquakes without damage; (2) moderate earthquakes with minor structural damage; and (3) major earthquakes with-

out collapse.

In this regard, various types of seismic protection strategies have been proposed in the literature. The three most common are: (1) making the structure stiffer by adding bracings; (2) isolating the superstructure from its foundation; and (3) using vibration suppression devices. The first approach aims to increase the stiffness and the natural frequency of the structure such that the predominant frequency of the earthquakes is far below the fundamental frequency of the structure. On the other hand, the second approach reduces the natural frequency of the structure due to the lateral flexibility of the isolators. Lastly, the third approach reduces the structural response around resonance by using energy dissipation devices.

One of the most widely-used base isolators is rubber bearing. These consist of rubber and steel layers. The rubber contributes to the horizontal flexibility while the steel plates provide vertical load carrying capacity of the device [6]. The isolators are usually installed between the foundations and the superstructures of buildings, while for bridges they are usually between the piers and the deck. So far, the application of base isolators has been limited to particular facilities such as hospitals, power stations, and other critical buildings because of the high-cost of manufacture and installation [7, 8].

There are three types of vibration suppression system in building structures; active, semi-active, and passive control devices. Passive control devices are preferred and are the most widely used nowadays due to their simplicity in maintenance. Unlike passive devices, active devices require energy input, and it is quite challenging to ensure that they remain functional during earthquakes. However, they have the advantage of wider range of operation. Semi-active devices on the other hand, combine the principles of active and passive devices. Their parameters can be adjusted to fit the different types of earthquakes and require less power than that of active devices. Moreover, semi-active devices can also be designed to include a passive fail-safety. In this thesis, only passive control type of devices are considered, both active and semi-active devices are beyond the scope.

Numerous examples exist of buildings where passive vibration control devices are implemented. Taipei 101 is one of the most famous. It employs a Tuned Vibration Absorber (TVA) consisting of cable-suspended mass and viscous dampers which are tuned to a particular frequency [9]. The TVA is attached to the top of the building to limit its sway due to unwanted vibrations imposed by dynamic loads such as earthquakes and wind. TVAs were, however, shown to only be effective when their host structures are vibrating within a specific frequency range [10]. Their performance is also affected by the characteristics of the ground motion. Villaverde and Koyoama [10] found that the TVAs perform better when the ground motion has narrow band frequency and long duration. They also require a huge amount of mass to be added to the primary structure which affects the design of the structural members.

In the late 1990's, Okumura Atsushi [11] patented a concept of gyro-mass, consisting

of a spring in parallel with flywheels and a geared rod. The force generated by the device is proportional to the relative acceleration between its two nodes. With the concept of inertial force, this device can produce inertance several times larger than its actual mass. This important feature has attracted researchers, particularly in the earthquake engineering community.

The term "inerter" was coined by Smith in the early 2000s [12]. Since then, various works on the development of the inerter have been conducted. Three main types of inerters have been introduced in the literature, namely fluid inerters [13], rack-and-pinion inerters [12], and ball-screw inerters [14, 15]. Wider applications of the inerters were also explored, such as for civil [16–23], mechanical [24–27], and aerospace engineering [28–34].

The feasibility of inerters for use as earthquake protection devices in building structures has been widely investigated. For this purpose, inerters must be combined with other mechanical elements: springs and dampers. The inerter-spring-damper configurations are also known as tuned-inerter-based-dampers (TIBDs).

One of the earliest TIBDs described in the literature is the Tuned Viscous Mass Damper (TVMD) consisting of a parallel inerter-damper connected in series to an inerter. The device was firstly introduced in 2008 by Saito *et al.* [35]. The first application of the TVMD in a real structure was in a 14-storey office building in Tohoku, Japan [36] and to this date, the TVMD is the only variant of TIBDs that has been applied in a real structure.

One of the TIBD variants that has received considerable attention in the literature recently is the Tuned Inerter Damper (TID) proposed by Lazar *et al.* [37]. The TID is an inerter-based system consisting of a parallel-connected viscous damper and spring connected in series with an inerter. The layout of the TID is similar to the Tuned Mass Damper (TMD), a well-established tuned vibration absorber (TVA) device. The tuning of the TID is also adopted from the TMD proposed by Den Hartog in the 1940s [38]. Lazar *et al.* [37] pointed out that the TID is an excellent alternative of the TMD. For the same mass ratio (or inertance-to-mass ratio in case of TID), similar performance can be achieved to that of TMD because the inerter element of the TID can generate larger inertance with a smaller mass. Another benefit of the TID is that the optimum performance of the structures can be achieved by placing the TID at the base of the structure. It also works based on relative motion and is sufficient to reduce the response amplitude at the resonant frequencies of at all modes, not just the targeted one as in the case of the TMD.

In 2014 Marian and Giaralis [39] introduced a variant of the TIBD known as the Tuned Mass Damper Inerter (TMDI). The layout is similar to that of the TID with an additional secondary mass m_d element between the inerter and parallel spring-damper. This m_d can represent the physical mass of the inerter device when it is too significant to be neglected. Some examples of TMDI application for building structures can found

in [40, 41].

In recent years, research on TIBDs has mostly focused on three things: the behaviour of TIBD with various possible inerter-spring-damper configurations [42, 43]; the effect of nonlinearity on each element of the TIBD [44–47]; and the application of the TIBD [26, 37, 48–50]. However, only a few have made successful experimental verification [51–53]. The only TIBDs that have been successfully installed in a real structure are the Tuned Viscous Mass Damper (TVMD) [36] with a ball-screw mechanism to generate inertance. However, despite the other two variants of the TIBD (TID and TMDI) which have received considerable attention in the literature, neither has been implemented in any real structure.

This research will focus on bringing the concept of the three TIBDs (TID, TMDI and TVMD) into practical implementation through simulations and experiments. In particular, the devices will be developed for use as earthquake protection of building structures.

The concept of using linear hysteretic damping is motivated by the fact that, in practice, most damping in materials exhibit hysteresis rather than viscous behaviour, meaning the energy dissipated per cycle is independent of the excitation frequency [54]. The results from the helical fluid inerter experiments by Smith and Wagg [55] also show that the device exhibits hysteresis in its force-velocity relationship.

Considering the inerter-spring-damper configuration in the TID, TMDI and TVMD (shown in the following chapter in Figure 2.6), the hysteresis may occur in at least two ways: (1) for TID and TMDI, the parallel spring-damper may exhibit hysteresis in the force-displacement relationship; and (2) for TVMD, the parallel inerter-damper may exhibit hysteresis in the force-velocity relationship. Although these hysteretic behaviours may also exhibit nonlinearity, such as in the rubber bearing and metallic materials, this is all are beyond the scope of this thesis.

1.2 Research Objectives

This research focuses on the novel concept of the TIBDs with linear hysteretic damping. The research **Objectives** can be divided into three main parts:

[O1] To propose novel analytical models for TIBDs with linear hysteretic damping.

[O2] To propose a new design concept for the realisation of the TIBDs with linear hysteretic damping for application as an earthquake protection device in building structures.

[O3] To verify results from **O1** and **O2** by performing shake table experiments of a multi-storey structure equipped with a TIBD with linear hysteretic damping.

1.3 Thesis Outline

Following this introductory chapter, Chapter 2 presents a literature review, looking at several well-established passive control strategies. The scope of the discussion falls into six sections: (1) base isolation; (2) dampers; (3) tuned vibration absorber; (4) combined isolation and TVA; (5) inerters; and (6) combined isolation and TIBDs.

In Chapter 3, two linear models of hysteretic damping are presented: complex damping and complex stiffness. The two models assume a parallel-connected inerter-damper and parallel-connected stiffness-damper, respectively. Firstly, a helical fluid inerter is studied. The experimental results from the literature have shown that the helical fluid inerter has both inerter and damping parameters in parallel. Further investigation shows that its force versus velocity relationship exhibits hysteresis. A complex damping model is proposed to capture this hysteretic behaviour. Secondly, a complex stiffness model which is a spring and damper in parallel is discussed. The discussion includes a novel computational time-domain method implemented in Matlab.

In Chapter 4, an new design approach is proposed for the helical fluid inerter. The main objective of this chapter is to design the helical fluid inerter for use as a TIBD. The helical fluid inerter is connected in series to a spring to form a TVMD-like device. However, here both inertance and damping are coupled.

In Chapter 5, two novel concepts – the TIhD and the TMhDI – are proposed based on the concepts of the TID and the TMDI. The difference is that they use a complex stiffness model to capture the behaviour of the coupled spring-damper. The optimum design and placement of these two devices are discussed in detail, including time-domain analysis.

In Chapter 6, a new design of the TMhDI device is proposed. The hysteretic damping of the TMhDI is given by a gel damper, while the inertance is given by a flywheel inerter. The characterisation tests of both devices are presented in detail. For comparison, a new design of TMDI is also proposed. The viscous damping properties of the TMDI is realised by using Eddy Current Dampers (ECDs) which consist of permanent magnets. Both TMhDI and TMDI proposed in this Chapter will be used for shake table experiments presented in Chapter 7.

In Chapter 7, the results from the shake table experiments are presented. A three-storey structure equipped with a TMhDI device was subjected to both harmonic sinewave and seismic excitations. The comparison between the proposed analytical model and the results from the experiment is also discussed. For comparison, the structure is also tested when equipped with a TMDI proposed in Chapter 6.

Finally, Chapter 8 gives the overall conclusion of the thesis and future work.

Chapter 2

Literature Review

2.1 Introduction

The idea of reducing structural response to prevent severe damage during earthquakes has attracted researchers for many years, especially from those countries where earthquake hazards are important in the structural design processes such as Japan, Taiwan, the USA, and Indonesia. The structural response is important because it is directly correlated to the severity of damage in the structural and non-structural elements of the structures.

Numerous methodologies have been proposed. Mainly there are two methods of preventing damage in structures. Firstly, by strengthening the structural elements, especially the beam-column connections. Often non-structural elements such as walls are also important to be strengthened [56]. Secondly, by providing additional control devices on the structures such as energy dissipation, mass mechanism, and base isolation devices.

There are three types of control devices: passive; semi-active; and active. Combining two out of the three is known as a hybrid control system, each with advantages and disadvantages [57, 58]. This research focuses on inerters as passive control systems in building structures. The passive control system is preferred due to its simplicity of design and maintenance, meaning no power input or design of control system is required. It also provides a fail-safe in the case that power is lost in an earthquake.

In this Chapter 2, a review of several control devices/systems is given. The scope of the review falls into six sections: (1) Base Isolation; (2) Dampers; (3) Tuned Vibration Absorber; (4) Combined Isolation and Tuned Vibration Absorber; (5) Inerters; and (6) Combined Isolation and Tuned Inerter Based Dampers.

2.2 Base Isolation

There has been significant progress in seismic protection strategies for civil structures to modify the dynamic interaction between the structure and the ground motions and to control the structural response. There are three categories of response control systems: base isolation (BI), energy dissipation unit and the mass effect mechanism such as a TVA. The main difference between base isolation and the other control devices is that the superstructure is isolated from the foundations to limit the seismic energy transferred to the superstructure.

The development of modern seismic base isolation systems started in 1870 when Jules Touaillon was issued a US patent for the first seismic base isolation device for buildings [59]. As shown in Figure 2.1, the device consisted of an array of double concave surfaces with spherical balls in-between. The modern application of seismic isolation began in the late 1960s with the development of modern materials such as rubber. The first application of rubber bearing seismic isolation was in 1969 on a three-storey concrete structure [60]. Since this first application, the development of seismic base isolation systems has grown rapidly and their application has spread worldwide.

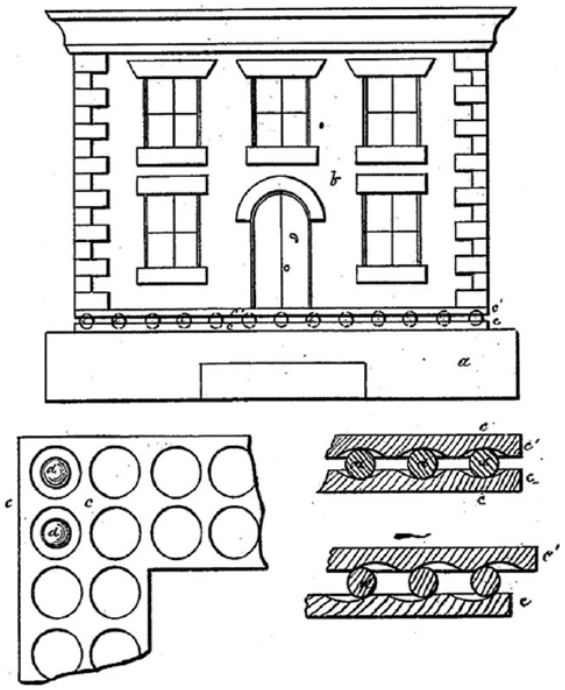

Figure 2.1: Jules Touaillon's 1870 seismic isolated structure [61]

Based on the mechanism, base isolation can be grouped into three categories: sliding bearings, friction bearings and rolling bearings. One of the variants of the sliding bearing is elastomeric bearings which is the most widely used base isolation [62]. Previously, there were two types of elastomeric bearings, high damping rubber bearings

and low damping rubber bearings, made up of a rubber material and thin steel plates. The rubber is needed to provide horizontal flexibility and the steel plates act as reinforcements to resist the vertical load from the buildings. In 1982, the elastomeric bearing was modified by adding a lead core to form a device called lead rubber bearings (LRB) [63]. For analysis, the elastomeric bearings are either modelled as a linear spring and damper in parallel or as a nonlinear model, for example see [64, 65]. The non-linearities of the isolation system can also be simplified as a linear model [66].

Friction bearings reduce the ground-to-superstructure transmissibility using a friction mechanism. One of the most famous examples of this type of isolator is the friction pendulum system (FPS) [67–69] consisting of a spherical sliding surface and a pendulum. The sliding surface is polished with chrome providing friction when it is in contact with the pendulum during earthquakes. The sliding surface is usually designed as concave with a curvature allowing the device to have restoring force which is proportional to the displacement and the gravitational loads from the superstructure carried by the pendulum. Further discussion on the friction isolators can be found in [70–77].

Rolling type isolators limit the seismic energy transmitted to the superstructures using a rolling mechanism. One of its variants is rocker bearing isolators which have been used in many old traditional buildings in Indonesia [56]. The concept is based on the rotational motion of the bearing placed on the foundations. This rotational motion protects the superstructure from undergoing large deformation imposed by the ground shaking. This concept has been extensively discussed in [78] as to how the rocker bearing can effectively reduce the transmitted forces into the structure and reduce the damage. Further discussion on other types of roller isolator can be found in [79–87].

Ideally, the superstructure remains unaffected by a seismic event if no seismic energy is transmitted from the ground. The isolators must be capable of undergoing the movement imposed by the earthquakes without losing their gravitational load carrying capacity, but the isolators may experience excessive displacement [88]. During long duration and long-period earthquakes, the superstructure also tends to have large displacement due to resonance. Therefore, often the use of isolators is combined with other control devices such as dampers and TVAs.

2.3 Dampers

Dampers dissipate energy via several mechanisms. In general, there are four types of damper used in civil engineering structures: (1) metallic dampers; (2) friction dampers; (3) viscoelastic dampers; and (4) viscous dampers. Metallic and friction dampers dissipate energy through the relative displacement between their two ends or terminals. The energy dissipated per cycle by this type of damper is usually frequency-independent. On the other hand, viscous dampers dissipate energy through the relative velocities between their two terminals. Unlike the metallic and friction dampers, viscous dampers

are frequency-dependent devices, meaning the energy dissipated per cycle depends on the frequency of the motion. Viscoelastic dampers however, dissipate energy through both relative displacements and relative velocity between their two ends.

The concept of using dampers for seismic protection was firstly introduced in the late 1960s in Japan [89] and later in New Zealand [90, 91]. Early studies introduced the concepts of using separate elements to enhance damping in a structure. These studies have led to the development of metallic dampers in which energy is dissipated by hysteretic yielding of materials. One of the first applications of metallic dampers was in the railroad bridge in the South Rangitikei viaduct in New Zealand in 1981 [92].

Similarly, the concept of using friction dampers as a seismic protection device was introduced in the early seventies [93]. In buildings, the first application of friction dampers was in the early 1980s at the Library of Concordia, University of Montreal [94].

Unlike both metallic and friction dampers that dissipate energy through relative displacements between their two ends, the fluid viscous dampers dissipate energy through the relative velocities between their two terminals. In 1995, fluid viscous dampers were used for the first time in a building in California [95]. Since then, the use of this type of damper has been rapidly increased because of their ability to significantly reduce storey response displacements, accelerations and shears in buildings [96].

Modelling damping in a structural system is important. Figure 2.2 shows a single degree of freedom structure with three different damping models that are commonly used in vibration analysis. The first model in Figure 2.2(a) represents a pure linear viscous damping, such as is typically assumed for a fluid damper. The damping force is given by $F_{vd} = c_d\dot{x}(t)$, where $\dot{x}(t)$ is the velocity of the mass m, and c_d is the viscous damping coefficient. The equation of motion is therefore

$$m\ddot{x}(t) + c\dot{x}(t) + kx(t) = 0 \tag{2.1}$$

Figure 2.2(b) represents an SDOF structure equipped with a friction damper with friction force F_{fd}. This force always opposes the motion, hence the equation of motion becomes

$$m\ddot{x}(t) + kx(t) + F_{fd}(t) = 0 \tag{2.2}$$

Figure 2.2(c) represents an SDOF structure equipped with a material damping. The force generated by the parallel elements $k - s_h$ is given by $F_{hys} = k(1 + j\eta)x(t)$. This $k(1 + j\eta)$ is also known as the complex stiffness model which is able to capture the frequency-independency of most material dampers, see [97, 98]. The equation of motion is therefore

$$m\ddot{x}(t) + k(1 + j\eta)x(t) = 0 \tag{2.3}$$

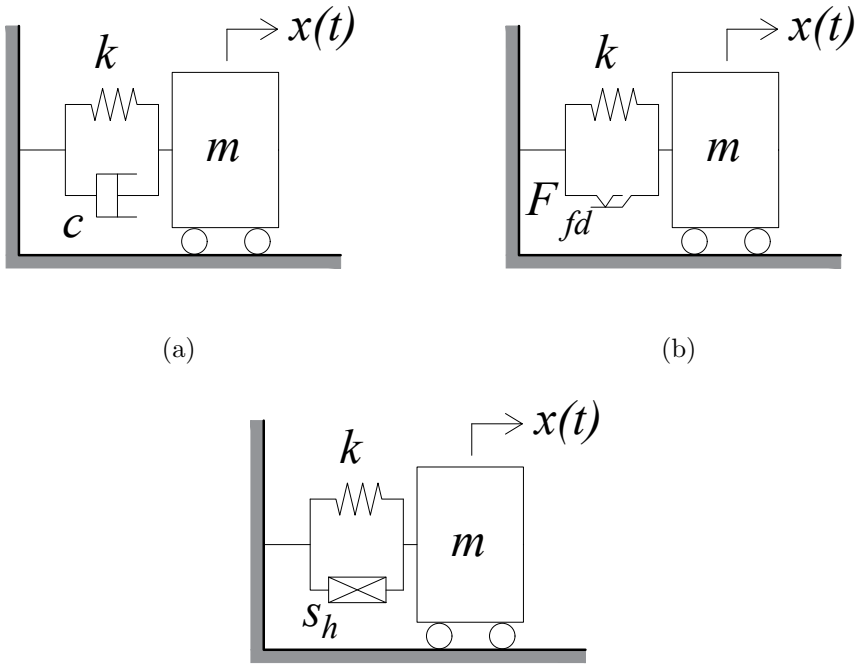

Figure 2.2: Schematic diagram of an SDOF structure with (a) viscous damper, and (b) friciton damper, (c) material damper

where η represents the loss factor of materials. Table 2.1 gives the loss factor values of some common materials. Further details of complex stiffness are discussed in Chapter 3.3.

Table 2.1: Loss factor of some materials [97]

Materials	Loss factor
Aluminium-pure	0.00002-0.002
Aluminium alloy-dural	0.0004-0.001
Steel	0.001-0.008
Lead	0.008-0.014
Cast iron	0.003-0.03
Manganese copper alloy	0.05-0.1
Rubber-natural	0.1-0.3
Rubber-hard	1
Glass	0.0006-0.002
Concrete	0.01-0.06

2.4 Tuned Vibration Absorbers (TVAs)

TVAs dissipate energy through an auxillary mass mechanism. They consist of mass, spring and dashpot. The devices are tuned to be in resonance with a targeted mode of the host structure on which they are installed. Two types of TVA will be briefly discussed in this section, namely the Tuned Mass Damper (TMD) and Tuned Liquid Damper (TLD).

2.4.1 Tuned Mass Damper

The Tuned Mass Damper (TMD) consists of a mass m_d attached to a spring k_d and viscous damper c_d in parallel. This is later called the traditional TMD to distinguish it from the non-traditional TMD whose three elements are in series [99]. The TMD is attached to a structure and tuned to a particular frequency such that the motion of the structure is out of phase with the TMD's resonance during vibrations. The building's oscillation is reduced due to the force of the TMD being transmitted to the structure in opposition to the structural motion.

The concept of the TMD was first introduced by Frahm [100]. The concept was to link a spring-mass system to a primary structure to suppress its oscillations due to harmonic excitation. This early concept was developed by Ormondroyd and Den Hartog (1928) by adding a viscous damper in parallel to the linear spring [101]. The optimum tuning of this system was first derived by Den Hartog in [38] and is known as 'fixed-points theory'. He discovered that the frequency response curves of an SDOF structure with attached TMD for various damping c_d pass through two fixed points at the lower frequency zone. The optimum tuning is then based on the iteration of the TMD stiffness k_d in such a way as these two fixed points have the same amplitude. Finally, the frequency response curve whose gradient is zero to the fixed points is selected as the optimum TMD damping c_d. The formulations of the optimum frequency and damping ratio are then given by [38]:

$$f_{opt} = \frac{1}{1+\mu} \quad \text{and} \quad \zeta_{opt} = \sqrt{\frac{3\mu}{8(1+\mu)}} \tag{2.4}$$

where μ is the ratio between the TMD and the main mass, which is m_d/m.

The ideas and concepts of the TMD have attracted many researchers who are later proposing several formulations for optimum frequency and damping ratio of the TMD: Warburton [102]

$$f_{opt} = \frac{\sqrt{1-(\mu/2)}}{1+\mu} \quad \text{and} \quad \zeta_{opt} = \sqrt{\frac{\mu(1-\mu/4)}{4(1+\mu)(1-\mu/2)}} \tag{2.5}$$

Nicola *et al.* [103]

$$f_{opt} = \frac{1}{1+\mu}\sqrt{1-\frac{\mu}{2}} \quad \text{and} \quad \zeta_{opt} = \sqrt{\frac{3\mu}{8(1+\mu)(1-\mu/2)}} \tag{2.6}$$

Sadek *et al.* [104]

$$f_{opt} = \frac{1}{1+\mu}\left[1-\zeta\sqrt{\frac{\mu}{1+\mu}}\right] \quad \text{and} \quad \zeta_{opt} = \frac{\zeta}{1+\mu} + \sqrt{\frac{\mu}{1+\mu}} \tag{2.7}$$

Most of the optimisation of the TMD parameters is accomplished through either conventional mathematical methods or numerical techniques, for example see [99]. The fixed-points theory cannot give a global optimum solution of the TMD, because the main structural damping is neglected. Leung and Zhang [105] formulated an optimum solution for the parameters of the TMD using a novel technique called "particle swarm optimisation (PSO)". It offers an optimum solution for the TMD when attached to a viscously damped SDOF system, which is given by:

$$f_{opt} = \frac{\sqrt{1-(\mu/2)}}{1+\mu} + (-4.9453 + 20.2319\sqrt{\mu})\sqrt{\mu\zeta} + (-4.8287 + 25\sqrt{\mu})\sqrt{\mu\zeta^2} \tag{2.8}$$

$$\zeta_{opt} = \sqrt{\frac{\mu(1-\mu/4)}{4(1+\mu)(1-\mu/2)}} - 5.3024\zeta^2\mu \tag{2.9}$$

The most famous example of TMD applications in buildings is the one attached to the Taipei 101. It has a huge mass of 726 tonnes hanging on the top of the structure [9]. Taipei 101, at 508m tall, is one of among the tallest buildings in the world equipped with TMD (complete list available in [106]).

2.4.1.1 Hysteretic TMD

Hysteretic TMD (HTMD) was firstly introduced by Nicola *et al.* [103]. Instead of having spring and viscous damper in parallel, the proposed TMD is designed with hysteretic damping realised by wire rope attached to the TMD mass. Basically, an equivalent viscous damping method can be used to convert the hysteretic damping of the TMD into a viscous damping. However, Wong [107] showed that using this approach will not give the same result for its frequency response function after the optimisation process. Therefore, he proposed a new optimum tuning formula for the damping ratio of the hysteretic TMD as follows:

$$\eta_{opt} = \sqrt{\frac{3\mu}{2} + \frac{\mu^2}{2(2+\mu)}} \tag{2.10}$$

where η_{opt} is the optimum loss factor of a hysteretic damping of the HTMD. Figure 2.3(a) and 2.3(b) illustrate the layout of the structure with TMD and HTMD, respectively.

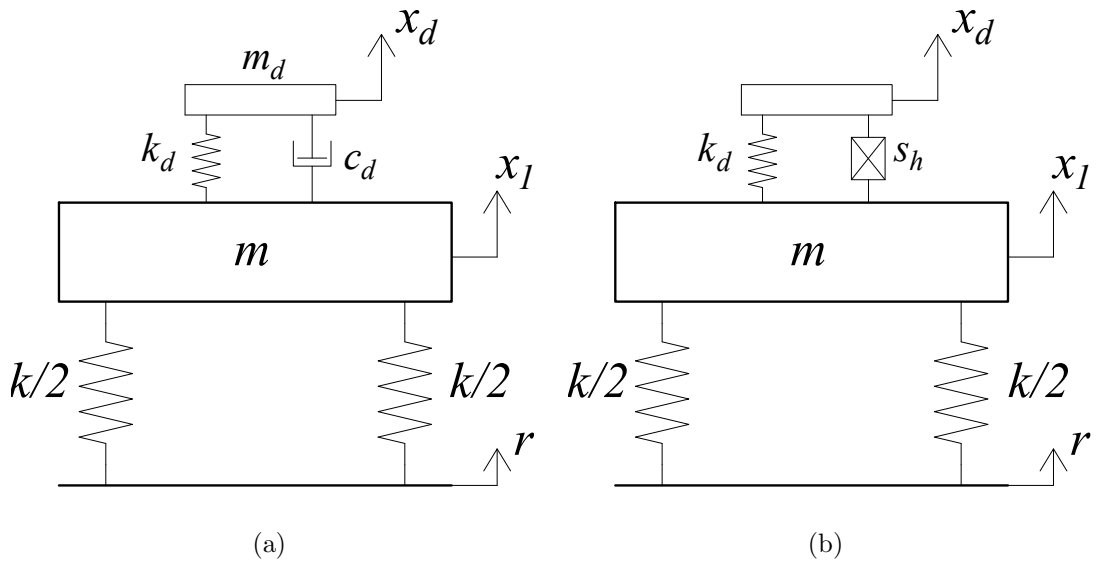

(a) (b)

Figure 2.3: Schematic diagram of an SDOF structure with (a) traditional TMD, and (b) hysteretic TMD

2.4.1.2 Non-traditional TMD

Non-traditional TMD is considered to be a more efficient form of a TMD. It has been extensively discussed by Xiang and Nishitani in [99]. The device consists of three elements as in the case of traditional TMD: mass m_d, viscous damper c_d, and spring k_d. However, instead of a parallel connection between the spring and damper elements, the non-traditional TMD has the three elements in series: spring-mass-damper or damper-mass-spring.

Xiang and Nishitami [99] give examples of non-traditional TMD application in base-isolated (BI) structures. As is well known, resonance is the biggest challenge for base-isolated structures when subjected to long-period and long-duration earthquake ground motions. A combined strategy of TMD-BI has been proven to be effective in solving this problem. Examples of this strategy can be found in [108] and [109]. However, due to the large stroke of the TMD, much space is required. The non-traditional TMD was proposed in [99] to overcome this problem. They have proven that the non-traditional TMD could be a better solution.

To sum up, the application of TMDs for minimisation of the structural response has been well established for many years. However, there are two downsides associated with them: (i) a large stroke that requires space, and (ii) large masses are required to provide a larger mass ratio. For tall buildings, the TMD's mass required might be very large. Despite the promising performance of the non-traditional TMD, the issues with the mass and stroke are still challenging.

2.4.2 Tuned Liquid Damper

Unlike the TMDs, the mass element of a Tuned Liquid Damper (TLD) is liquid. One example of TLD is the Tuned Liquid Column Damper (TLCD) consisting of a U-shaped tube filled with liquid with an orifice at the middle of the horizontal portion. The TLCD was firstly introduced by Sakai *et al.* in 1989 [110]. Similar to the TMD, the motion of the fluid mass is tuned to the targeted frequency as such that the motion of the fluid inside the columns is in opposition to the direction of the main mass of the structure. One example of experimental analysis of the TLD to reduce vibration of structures imposed by earthquakes can be found in [111].

In 2011, Saif *et al.* [112] developed a new type of TLD, the Tuned Liquid Ball Damper (TLBD). The TLBD simply is a TLCD with the presence of a rolling steel ball to replace the fixed orifice in the TLCD. The TLBD was shown to be capable of providing more reduction on the response of the main structure under earthquake excitations [113].

In practice, the realisation of this type of TVA is difficult because not every structure has a place on the top to put the TLD, especially when the required size of the TLD is tremendous. As in the case of the TMD, the required fluid mass to control the vibrations is often extremely high. As a result, the design of structural members (e.g. columns, beams, foundations) will be significantly affected.

2.5 Combined Base Isolation and Tuned Vibration Absorber

Base isolated structures often experience large displacements at the base due to resonance. The maximum lateral forces that can be resisted are also limited because of its low lateral stiffness. These issues have attracted many researchers to propose new control strategies. One of the proposed methods is the combined base isolation and tuned mass damper.

Among the first to study the combined control strategy of BI-TMD were Palazzo et.al in [108] and [114]. Experimental works to verify this concept were published in [109]. Combined BI-TMD strategies have an advantage in long-period earthquakes. However, the TMD could experience a large stroke that requires some considerable space. To overcome this problem, the non-traditional TMD [99] is employed. Figure 2.4 illustrates some of the combined control strategies found in the literature. In particular, the combined BI-TID (Figure2.4(e)) will be discussed next in Chapter 2.7.

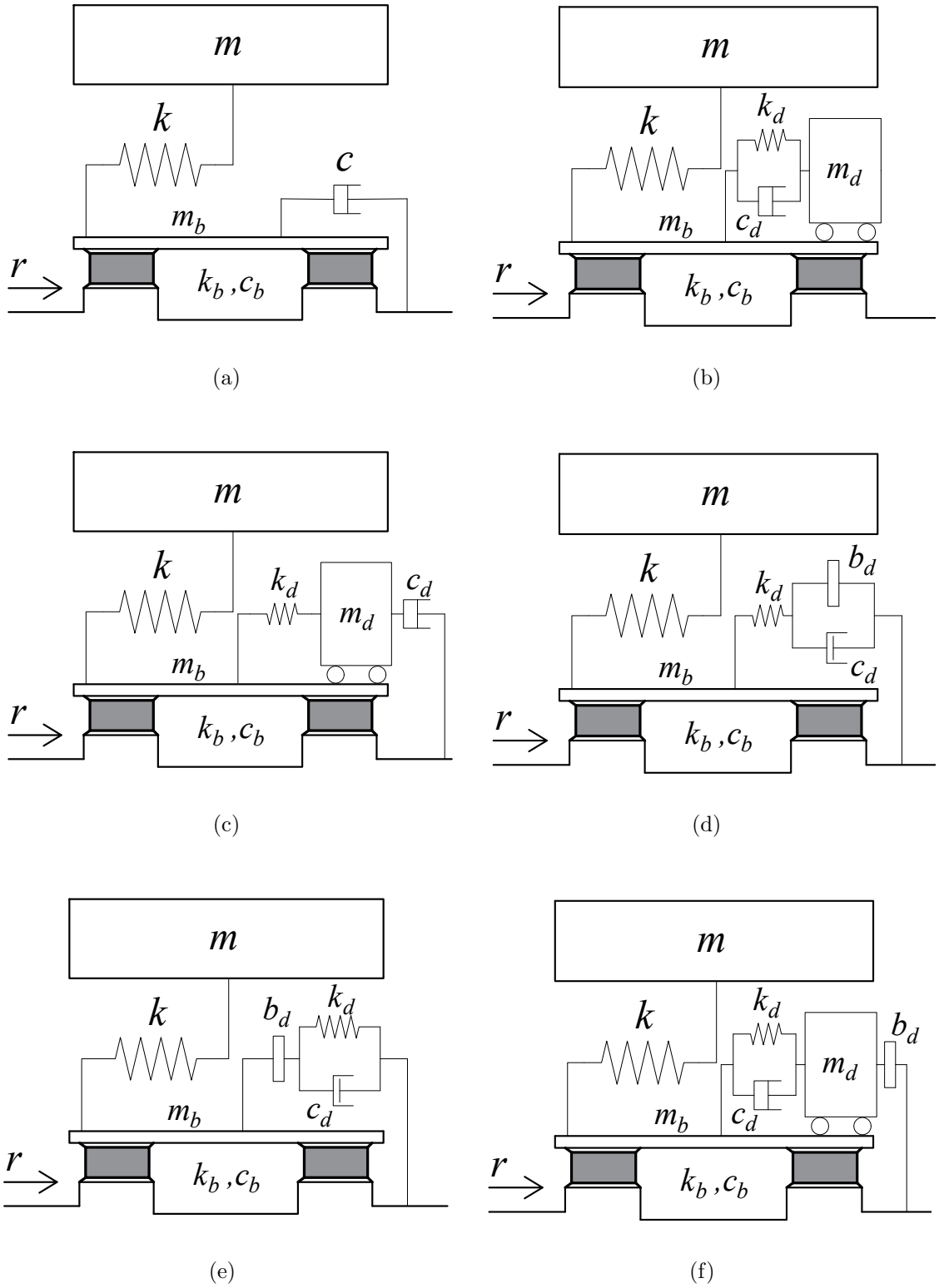

Figure 2.4: Base-isolated structure with (a) Damper (b) TMD [108, 114] (c) Non-traditional TMD [99] (d) TVMD [115] (e) TID [41] (f) TMDI [116]. Here m and k are the mass and stiffness of the primary structure, k_b and c_b are the stiffness and damping of the BI system, m_b is the mass of the storey attached to BI system, and r is the ground motion.

In civil structure applications, especially for high-rise buildings, the mass element of the TMD is often very large - that of Taipei 101 is 726 tonnes [9]. This could result in an inefficient design for the whole building and lead to large reaction forces acting on the foundations. As a result, additional reinforcements for the foundations are required.

2.6 Inerters

In 1997, Okumura Atsushi [11] patented a device so-called gyro-mass in parallel connection with a spring and a damper. This gyro-mass consisting of two disks acting as inertia elements, rotating on a geared rod in such a way that the force generated by the gyro-mass F is equivalent to the relative acceleration between its two nodes. This relation can be expressed as:

$$F = m_s(\ddot{x}_a - \ddot{x}_b) \tag{2.11}$$

where:

$$m_s = J/r_s^2 \tag{2.12}$$

Here, J is the moment inertia of the disks, and r_s is the distance from the centre of the disks to the point where the rod is attached. The term m_s is later also called inertance b_d which can be achieved by several mechanisms, such as fluid flow [55] and rotational motion of a flywheel [14]. Several types of gyro-mass devices have since been proposed. Smith [12] proposed a device called the inerter, consisting of a flywheel, rack, pinions, and gears. The force generated by the inerter can be expressed as:

$$F = b_d(\ddot{x}_a - \ddot{x}_b) \tag{2.13}$$

for a suitable constant of inertance b_d which is measured in kg. $\ddot{x}_a$ and $\ddot{x}_b$ stand for the acceleration at the terminals a and b respectively.

The inerter completes the force-current analogy between mechanical and electrical networks which was firstly introduced by Firestone [117]. In this analogy, equivalence between mechanical and electrical networks is made based on the three main elements in the vibration control systems: mass, spring and damper; spring and damper are equivalent to the inductor and resistor. However, capacitor and mass element equivalency in this analogy was not complete because the mass element must always be connected to the ground. The inerter was defined to fill this gap. With this new element, any type of electrical circuit can now be translated into the mechanical one. The force-current analogy between mechanical-electrical networks is given in Table 2.2, where v is velocity, L_i is inductance, R_i is resistance, and C_i is capacitance.

The inerter application was at first limited to mechanical devices, such as vehicles and trains. Nowadays, research in this area has wider objectives and the inerter systems are specifically studied for earthquake response reductions of civil structures.

Table 2.2: Force-current ($F - i_i$) analogy between mechanical-electrical networks

Mechanical networks	Electrical Networks
Spring $\frac{dF}{dt} = k(v_2 - v_1)$	Inductor $\frac{di_i}{dt} = \frac{1}{L_i}(v_2 - v_1)$
Damper $F = c(v_2 - v_1)$	Resistor $i_i = \frac{1}{R_i}(v_2 - v_1)$
Inerter $F = b_d \frac{d(v_2 - v_1)}{dt}$	Capacitor $i_i = C_i \frac{(v_2 - v_1)}{dt}$

Numerous works on the application of the inerters in buildings have been published. Wang *et al.* [118] investigated the performance of buildings employing inerters under two external excitations, earthquakes and traffic. In comparison with the TMD, a well established TVA in civil engineering application, the inerter has been shown by [37] to be able to replace the mass element of the TMD to form a new device called Tuned Inerter Damper (TID). Other papers that studied the performance of building employing inerters are [36, 116, 119–121].

2.6.1 Type of Inerters

Three main types of inerters have been proposed and discussed in the literature based on their mechanism of generating inertance: fluid inerters [13], rack-and-pinion inerters [12], and ball-screw inerters [14, 15]. Figure 2.5 illustrates schematics of these inerters.

The rack-and-pinion inerters were the first introduced and patented type of inerter. This was by Okumura Atsushi [11], who introduced a device called gyro-mass, consisting of geared rack and pinion and a rod in parallel with a spring. This concept was later developed by Smith [12] who introduced the term “inerter”.

The inertance of a mechanical geared inerter (rack-and-pinion inerters and ball-screw inerter) is achieved through the linear motion between its two terminals which is converted to rotational motion of its flywheel via gearing. One type of ball-screw inerter, the tuned viscous mass damper (TVMD), has been implemented in a real building in Japan [36]. Detail discussion of the TVMD will be presented in the next section.

The second type of inerter is the fluid inerter. The concept is based on the fluid motion inside the device moving the flywheel to generate inertial forces. Glover *et al.* [122] hold the first patent of fluid-type inerter which is called hydraulic inerter in 2009. Another realisation of fluid inerter was proposed by Wang [13] in 2011. In 2013, Swift *et al.* [123] introduced a new type of fluid inerter called the helical inerter, whose inertance is generated by the mass of the fluid itself moving inside the helical channel.

Smith and Wagg [55] conducted a set of experimental works on the helical inerter and studied the influence of helical pipe diameter to the inertance being generated. The optimisation of the helical inerter is studied by Shen *et al.* [124] where they studied the nonlinearities of the device compromising the friction and the viscosity of the fluid.

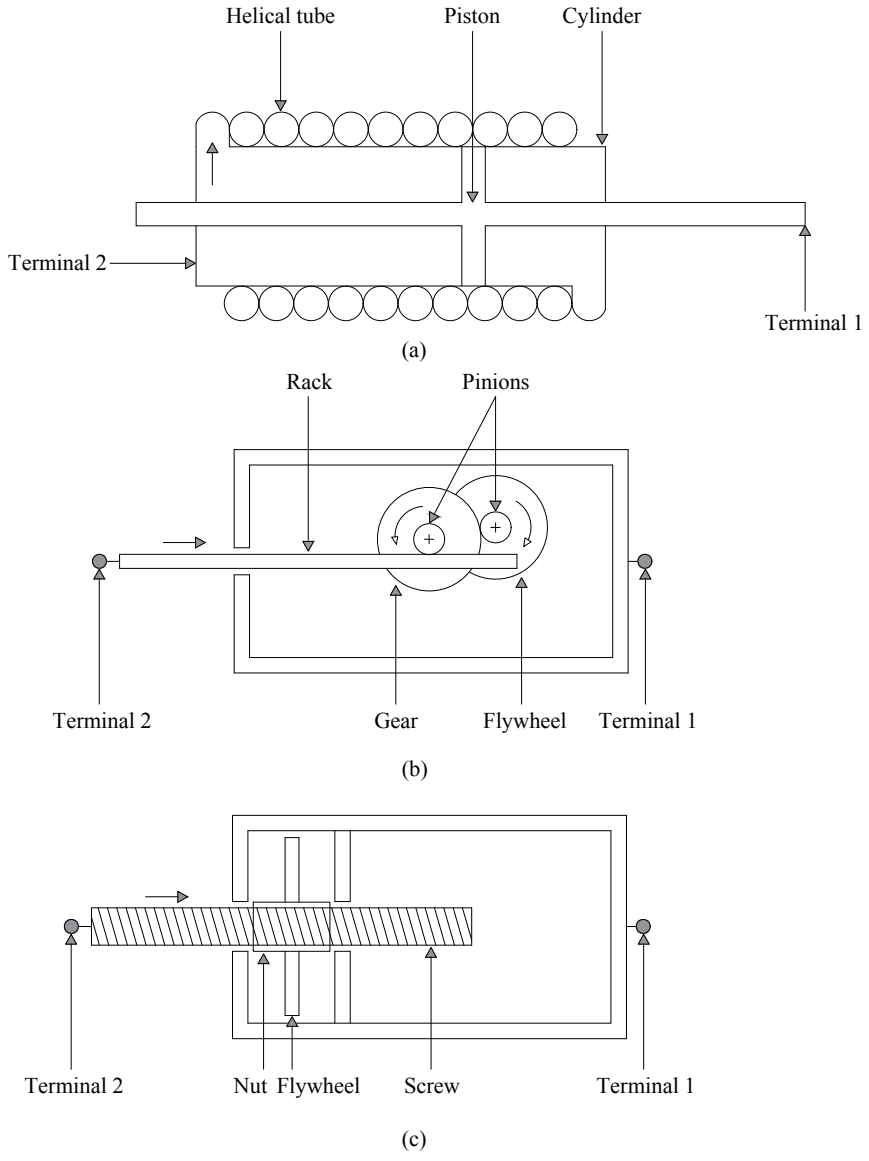

Figure 2.5: Schematics of three of types of the inerter (a) fluid inerter (b) rack and pinion inerter (c) ball-screw inerter.

In 2014, Nakamura *et al.* [51] introduced an electromagnetic inerter whose concept is based on a combined electromagnetic damper and inertial mass damper (IMD) to form a new device called electromagnetic inertial mass damper (EIMD). The IMD is a

damper using a ball screw mechanism to generate inertial forces [125, 126]. The EIMD consists of a ball screw mechanism, a flywheel, a gear and an electric generator. The ball screw mechanism converts the axial motion of its rod into rotational motion of the internal flywheel which also turns the generator. The inertial and electromagnetic damping force are produced by the flywheel and generator which also amplify the actual mass of the flywheel. The concept of electromagnetic inerter is also given in [127].

2.6.2 Tuned-Inerter-Based-Dampers (TIBDs)

The use of TMDs for seismic protection devices in building structures is often unrealistic because a huge amount of supplemental mass is required [36]. Employing inerters is one of the solutions. The use of inerters for vibration control devices requires other mechanical elements - spring and dampers.

Saito *et al.* [35] introduced the first variant of the TIBDs composed of arranging an inerter and viscous damping elements in parallel-connection to a spring element in series as depicted in Figure 2.6(c). This system is called a Tuned Viscous Mass Damper (TVMD). In this device, the mass amplification effect was achived by ball-screw mechanism converting the translational motion imposed by the structure into the rotational motion of a flywheel.

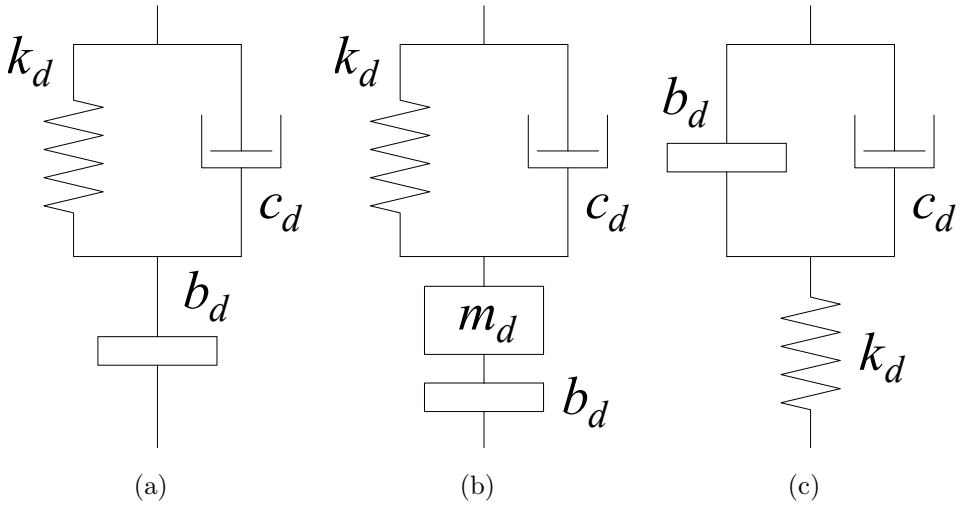

Figure 2.6: TIBDs layout variants: (a) TID (b) TMDI (c) TVMD

Ikago *et al.* [14] proposed the realisation of the TVMD by adding a flywheel to a rotational viscous damper (Figure 2.7(a)). A ball-screw mechanism was designed to convert the translational motion from the building structures to the rotational motion of the flywheel. In practice, a large inertance can be generated. This device is called a viscous mass damper (VMD) as depicted in Figure 2.7(b). This VMD is connected to the structure via a bracing system to form a TVMD 2.8. The first three applications of the TVMD in buildings are in Sendai Aoba-dori Building (Nippon Telegraph and

Telephone East Corporation), Akasaka Inter-city AIR, and Headquarter Building of Hulic Co., Ltd. Other studies on the TVMD can be found in [14, 125, 128–130].

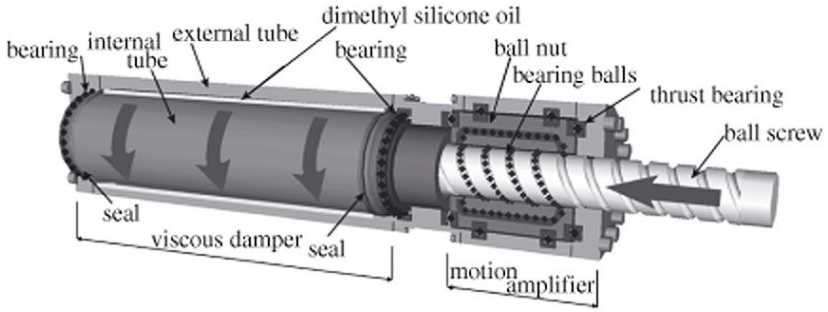

(a)

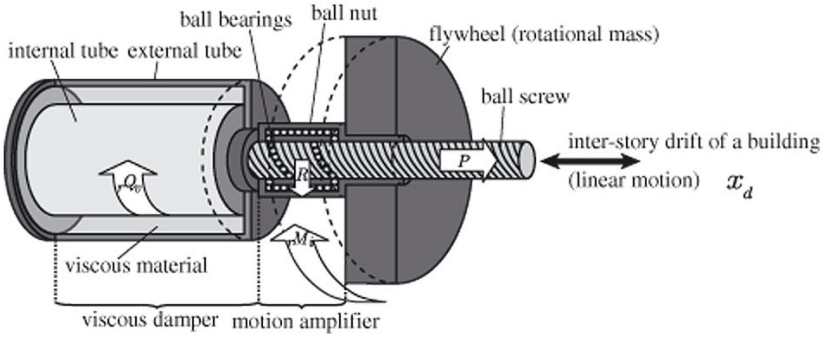

(b)

Figure 2.7: (a) Rotational viscous damper [14](b) Viscous mass damper (VMD) [14]. *Images reproduced with permission of the rights holder, John Wiley & Sons.*

Lazar *et al.* [37] introduced the Tuned Inerter Damper (TID) consisting of a parallel spring-viscous damper system connected in series to an inerter as illustrated in Figure 2.6(a). The optimum tuning of the device in SDOF structures follows the tuning rules of the TMD by Den Hartog [38] with the mass m_d replaced by an inerter b_d. Unlike the TMD, the TID achieves its best performance when placed at the base of the structure [37]. This is another important feature of the TID compared to the TMD. Furthermore, the application of the TID in MDOF structures shows that the TID is not only capable of reducing the structural response around the targeted resonant mode, but also around all other resonant modes [37].

In 2015, Brzeski *et al.* [131] introduced the concept of TMD with an inerter and experimentally tested it in [52]. The device is called the Tuned Mass Damper Inerter (TMDI) which is basically a TID with an additional mass m_d as shown in Figure 2.6(b). The idea of the TMDI is to enhance the TMD performance by adding an inerter connecting the mass m_d to the ground or to the structural storey mass. As a result, a large mass ratio can be easily achieved without significantly increasing the physical mass of the system. Studies on the optimal design of the TMDI are also discussed in [40] and [39].

Along similar lines, Hu *et al.* [42] studied several inerter-spring-damper configurations for passive vibration control systems and compared their optimum performance when employed on an SDOF structure. The optimum tuning of the devices adopted the fixed-point theory by Den Hartog [38] via algebraic solutions.

(a)

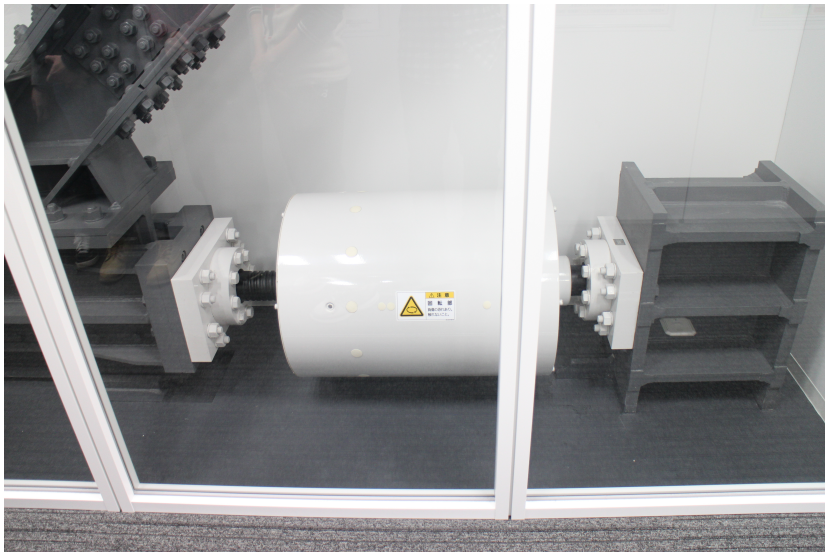

(b)

Figure 2.8: (a) TVMD bracing in Akasaka Inter-city AIR building, Tokyo, Japan (b) TVMD in a telecomunication building, Japan. *Images reproduced with permission of the rights holder, Professor Kohju Ikago.*

More recently, Pan *et al.* [132] studied a Parallel Viscous Inerter Damper (PVID) based on demand-based design. The PVID layout is the same as that of TVMD. They found that the fixed-points theory cannot be used to achieve a global optimal solution as it neglects the damping of the primary structure. The optimum solution for the

PVID in a damped SDOF structure is therefore determined by a numerical optimisation technique, using allowable parametric bounds [132]. They also showed that the response of structures under dynamic excitations, including seismic excitations, can be minimised by the PVID.

Several studies have been conducted to compare the performance of various configurations of the inerter-spring-damper systems [116, 121]. Most inerter applications in buildings are still in the conceptual stages. Except for the TVMD, none of the inerter concepts has been used in a real structure. This has been a challenge and motivation throughout these research activities to fill the gaps between the conceptual study and practical implementation.

2.7 Combined Base Isolation and TIBDs

This section presents preliminary results of this thesis which has also been published in [133]. As one of the first paper to investigate the effect of TID in BI structure, this study is important to be included in this literature review to show other benefit of inerters to solve problems associated with BI structure.

Using rubber bearings to isolate structures from their foundations has been an established method to protect the structures against unwanted vibrations including earthquakes. Typically, rubber bearings are placed underneath the structure's columns to isolate the upper structure from ground vibrations. In this study, a scenario where a TID is also installed in combination with the rubber bearings is investigated. The objective of this combined system is to give significantly improved isolation of the upper structure.

Seismically isolated structures using rubber bearings have been found to have limitations in some cases. For example, it has been shown that under certain conditions, rubber bearings can cause large displacements at the base of the structure. Hence, a large clearance space is required to provide enough room for the rubber bearing to deform. Additionally, it was also found that large displacements at the top of the structure can occur during a long period and long duration earthquake excitations [88]. This can occur when the location of the structure is far from the epicentre.

In this section, a TID is proposed specifically to overcome these problems. It is important to be included in this literature review to show the effectiveness of inerters for minimizing problems associated with BI structures. For this purpose, the TID is tuned to effectively work when the structure is subjected to long-period ground motion.

The layout of the combined BI-TID system is based on the fact that, unlike a tuned-mass-damper, the TID has been shown to work most effectively when it is installed in the base of the structure [37]. This makes it an obvious choice for being used in combination with rubber bearings, which are also installed at the base of the structure.

Several combined control strategies employing dampers and base isolation devices

have also been studied. Tsai [134] studied the effect of a TMD on the response of a five-storey BI building. In this study, the TMD was installed on the base floor. The same model was also studied by [108] which looked at the influence of TMD location on a BI structure [114]. The TMD performance was assessed by varying its location between top and base floors. An experimental study of the effectiveness of the TMD in BI structures was carried out in [109]. Xiang and Nishitani [99] studied a non-traditional TMD in combination with a BI system. Most recently, [135] studied the performance of the TMD in BI structure by considering the nonlinearities of the isolation system.

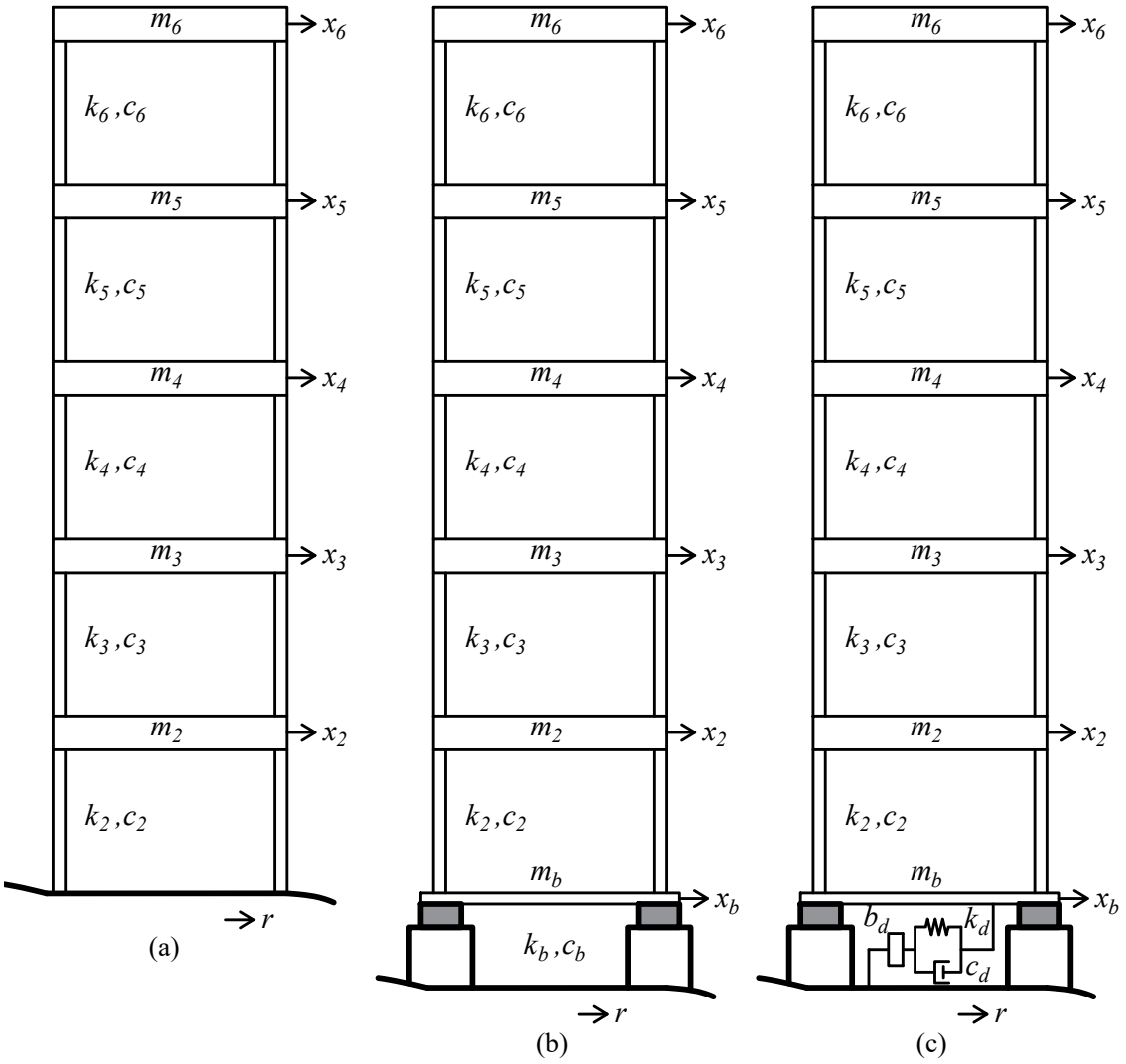

Figure 2.9: (a) Fixed-base structure (b) BI without TID (c) BI with a TID

Employing an inerter-based device on a BI structure was firstly discussed in [115]. Several layouts were studied in combination with rubber bearings modelled as linear spring-dashpot elements. The inertance is achieved by a rack-and-pinion type of inerter which is also called a gyro-mass damper. One of the models has the inerter element in parallel with a linear spring and in series with a linear viscous damping element. This

configuration of the TID layout was also studied in [37] and [42]. The application of inerter-based devices in multi-storey BI structures was studied in [116]. The authors considered the use of tuned-mass-damper-inerter (TMDI) to mitigate the response of multi-storey BI structures. Most recently, a combined TMDI and BI have also been studied in [41].

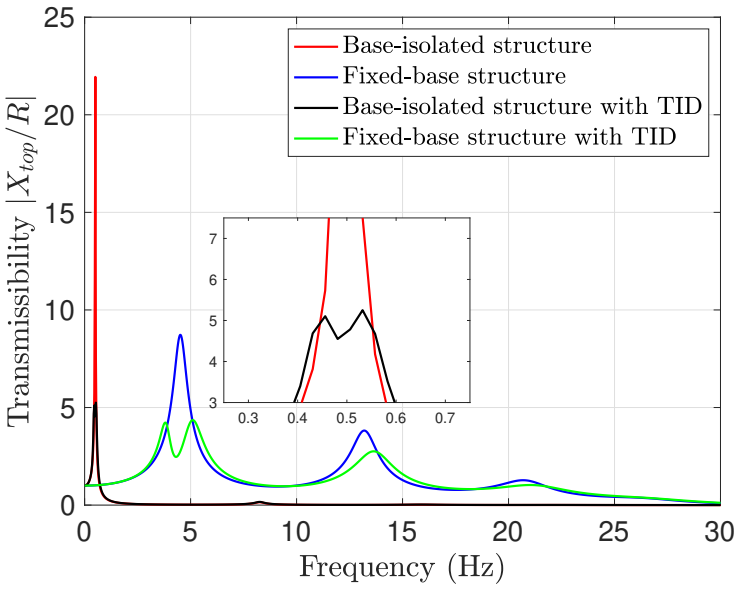

(a)

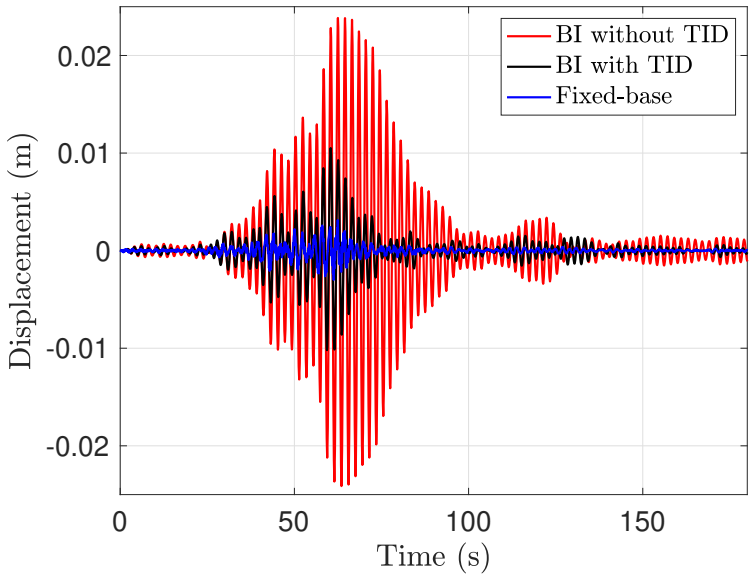

(b)

Figure 2.10: (a) Transmissibility (b) Time history response to Mexico City 1985 ground motion. Due to the low frequency content of the earthquake, the fixed-base structure performs better than both BI and BI with TID.

In this work, the performance of a TID on a multi-storey BI structure was investigated. For simulation, the Mexico City earthquake of 1985 was used, which was a long-period earthquake with pre-dominant frequency around 0.33-0.58Hz. One structural system adopted from [134] was used in this analysis. The structure is a five-storey base-isolated building as shown in Figure 2.9(b). The properties of mass, stiffness, and damping for each floor of the superstructure are assumed to be the same, m_i= 3500 kg, k_i= 35000 kN/m, and c_i= 35 kNs/m, where i={2,3,4,5,6}. The mass m_b and stiffness k_b of the base isolation system are given as 3500 kg and 210 kN/m. These values are zero for the case of a fixed-base structure as shown in Figure 2.9(a).

Figure 2.10(a) shows the transmissibility response of the considered structure. With base isolation, the first natural frequency of the structure is shifting to the left-hand side and now the response is dominated by this first natural frequency only. As a result, the response at high frequencies is very low. However, if the frequency of the base excitation is low and close to the first natural frequency of the structure, the response could be very high. The TID in this case was designed to solve this issue.

The response of the considered structure subject to a long period Mexico City earthquake is presented in Figure 2.10(b). Due to the low frequency content of the earthquake, the response of the fixed-base structure is the best among all. In this case, using the base isolation makes it worse. The TID is used to reduce the response of the BI structure. As can be seen in this figure, the structural response with the TID is significantly reduced.

2.8 Summary

An inerter is capable of generating inertance several times higher than its physical mass. This important feature has attracted researchers in many areas of study including mechanical, aerospace and civil engineering. In the earthquake engineering community, inerters are often combined with the other two mechanical elements – spring and damper – to form a TIBD to be used as a seismic protection device in civil structures such as buildings and bridges. There are several possible configurations and the three best established are the TVMD; TID; and TMDI.

To date, TVMD is the only one that has been used in a real civil structure. Many studies have been published presenting the use of TID and TMDI for mitigating structures from earthquakes. A published article from this thesis discussing the effectiveness of TID for protecting BI structures from long-period earthquake ground motions has also been discussed in this chapter. However, research on both TID and TMDI are still in a conceptual stage. Therefore, this thesis aims to propose novel and more realistic analytical models for both TID and TMDI and to provide experimental data as proof of concept via shake table experiments.

One thing in common between the three TIBDs is that each has two elements in

parallel. The three TIBDs assume that their three elements can be varied independently of one another. Hence, each can be individually optimised. However, some experimental results have shown that the two elements in parallel are coupled and may exhibit hysteresis, for examples, see [54, 55].

In this thesis, for the first time, the possibilities of the TIBDs exhibiting hysteresis through the two elements in parallel and their effect on the TIBDs performance are explored in detail. In particular, two linear hysteretic damping concepts are discussed: (1) complex damping; and (2) complex stiffness (see Chapter 3). Based on the complex stiffness model, two novel inerter-based-dampers are introduced in Chapter 5, namely the tuned-inerter-hysteretic-damper (TIhD) and the tuned-mass-hysteretic-damper-inerter (TMhDI).

Chapter 3

Linear Hysteretic Damping Models

3.1 Introduction

The objective of this chapter is to develop two linear hysteretic damping models for inerter and damper in parallel and for spring and damper in parallel. The first model has been motivated by the recent experimental results from [136] showing that the helical fluid inerter has hysteresis in its force-velocity relationship. As has been discussed in [137], the helical fluid inerter has two parameters in parallel, inertance and damping. A complex damping model is proposed in this chapter to capture the hysteretic behaviour of the fluid inerter. Later in Chapter 4, the fluid inerter will be proposed for use as a TVMD by connecting the device with a spring element in series.

The second model representing both stiffness and damping in parallel has been well known as a complex stiffness model, given by $k(1 + i\eta)$, usually used to model the frequency independence of a material. Here k is the stiffness of the spring, $i = \sqrt{-1}$ and η is the loss factor of the material. This model will be used later in Chapter 5 to model a material damping which is connected in series with an inerter device. This system will be representing the TID with linear hysteretic damping, or TIhD. If the mass of the inerter is included, it becomes TMDI with linear hysteretic damping, or TMhDI.

3.2 Complex Damping: Linear Hysteretic Damping Model For Inertance and Damping in Parallel

3.2.1 Analytical Model

This section seeks to develop a hysteretic model for a device having an inertance and a damping in parallel. This model can be developed by assuming that the device force,

F, is approximated by

$$F = b\ddot{x} + c\dot{x} \tag{3.1}$$

where x is the relative displacement of the inerter, an overdot represents differentiation with respect to time, b is the inertance (in kg) and c is the viscous damping (in kg/s). Note that both x and F are function of time. Now assume a harmonic solution for Equation 3.1 of the form

$$x = \bar{X}\sin(\omega t + \phi), \quad \text{so} \quad \dot{x} = \omega\bar{X}\cos(\omega t + \phi), \quad \text{and} \quad \ddot{x} = -\omega^2\bar{X}\sin(\omega t + \phi), \tag{3.2}$$

where ω is the circular frequency and ϕ is the phase shift. This leads to

$$\begin{aligned} F &= -b\omega^2\bar{X}\sin(\omega t + \phi) + c\omega\bar{X}\cos(\omega t + \phi) \\ &= c\dot{x} \pm b\omega\sqrt{\omega^2\bar{X}^2 - \dot{x}^2} \end{aligned} \tag{3.3}$$

where $\bar{X}^2 = \bar{X}^2\sin^2(\omega t + \phi) + \bar{X}^2\cos^2(\omega t + \phi)$ has been used.

Eq. 3.3 is now in terms of F and $\dot{x}$ only, and so can be plotted as a hysteresis loop in the force vs velocity plane as shown in Figure 3.1. The model forms an ellipse in

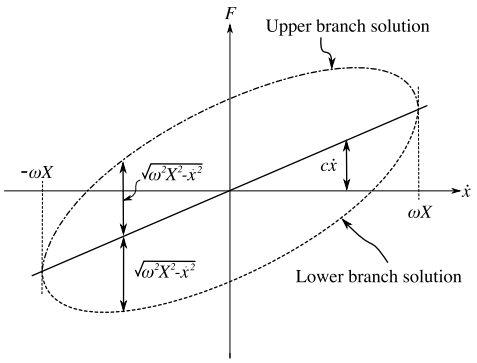

Figure 3.1: Schematic diagram showing the idealised linear hysteresis model for inertance and damping in parallel.

the F vs $\dot{x}$ plane. The orientation of the ellipse is governed by c.

The area inside the loop is given by

$$\begin{aligned} \Delta P = \int_0^{\frac{2\pi}{\omega}} F d\dot{x} &= \int_0^{\frac{2\pi}{\omega}} (c\bar{X}\omega\cos(\omega t + \phi) - b\omega^2\bar{X}\sin(\omega t + \phi))(-\omega^2\bar{X}\sin(\omega t + \phi))dt \\ &= \pi\omega^3 b\bar{X}^2. \end{aligned} \tag{3.4}$$

Eq. 3.4 demonstrates that the area inside the hysteretic loop (ΔP) is strongly affected by the frequency ω and amplitude $\bar{X}$ of the excitation. The area inside the loop has the units of power and is related to the rate at which energy is transferred between kinetic and potential forms. However the precise physical significance of this measurement is unclear and could be the focus of future research.

Finally, the model can be generalised using an assumed exponential solution to Eq. 3.1. So if $x = \bar{X}\mathrm{e}^{\mathrm{i}(\omega t+\phi)}$ is assumed, then substituting into Equation 3.1 gives

$$F = (\mathrm{i}c\omega - b\omega^2)\bar{X}\mathrm{e}^{\mathrm{i}(\omega t+\phi)} \rightsquigarrow F = c(1+\mathrm{i}\omega\frac{b}{c})\mathrm{i}\omega\bar{X}\mathrm{e}^{\mathrm{i}(\omega t+\phi)} \tag{3.5}$$

where the relationship between force and velocity is now called "complex damping" of $c(1+\mathrm{i}\omega\frac{b}{c})$. This is analogous to the well-known concept of complex stiffness $k(1+i\omega\frac{c}{k})$.

In the complex stiffness concept, $\frac{\omega c}{k}$ is defined as equivalent to (for one specific frequency of interest) a loss factor η which is a constant value. This equivalence is known as equivalent viscous damping; for example, see [138]. From Equation 3.5, a hypothesis rises that there is a constant term τ which can be defined as equivalent to $\frac{\omega b}{c}$. To prove this, some experimental results on helical fluid inerters are discussed in the next section.

3.2.2 Helical Fluid Inerter

The complex damping model proposed in Equation 3.5 aims to capture the hysteretic behaviour of a device having an inertance and damping in parallel. Particularly in this section, the helical fluid inerter is discussed. A schematic diagram of the fluid inerter system considered in this section is shown in Figure 3.2. The first experimental work on the helical fluid inerter was conducted by Swift et al. [123] in 2013, then in 2016 by Smith and Wagg [136]. The inerter system was designed with a central fluid-filled cylinder, radius r_2, which is attached to a helical coil on the outside of the cylinder. The helical coil has an internal radius of r_3, and the helix radius is r_4. The fluid is driven through the cylinder using a plunger of radius r_1. This mechanism generates inertance proportional to the helix radius. This will be further discussed in detail in the next chapter Section 4.1. Particularly, the influence of the helical fluid inerter dimensions to the generated inertance is given by Equation 4.2.

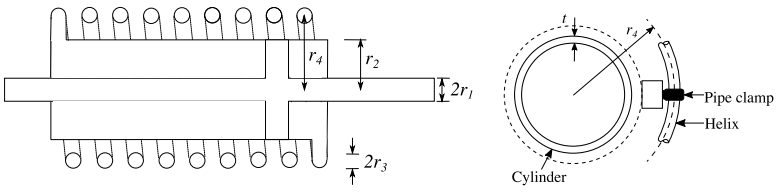

(a) (b)

Figure 3.2: Schematic diagram of the helical fluid inerter showing the (a) longitudinal cross section, and (b) the top view of the system [55]

The helical fluid inerter has been experimentally tested by Smith and Wagg [136]. The data of the experimental results were obtained from [139]. Examples of the experimentally obtained hysteresis loops are shown in Figure 3.3 and 3.4, for two different values of the helix radius r_4, defined as Tests 2 and 3 in [139].

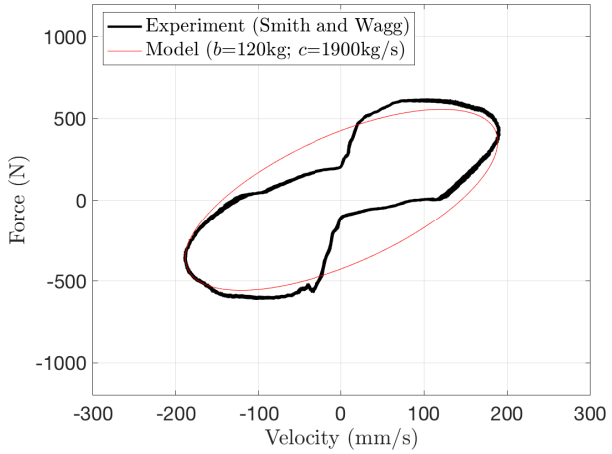

(a)

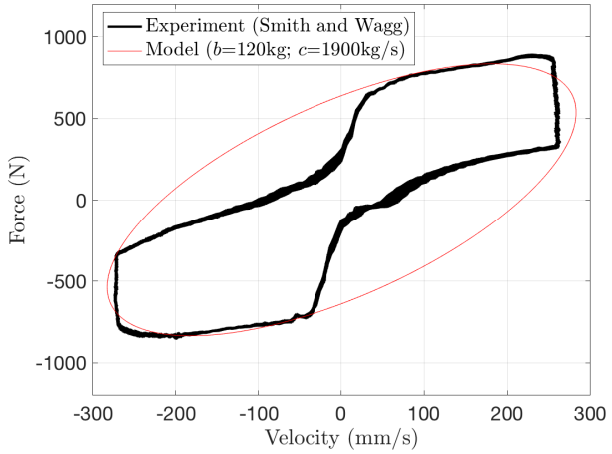

(b)

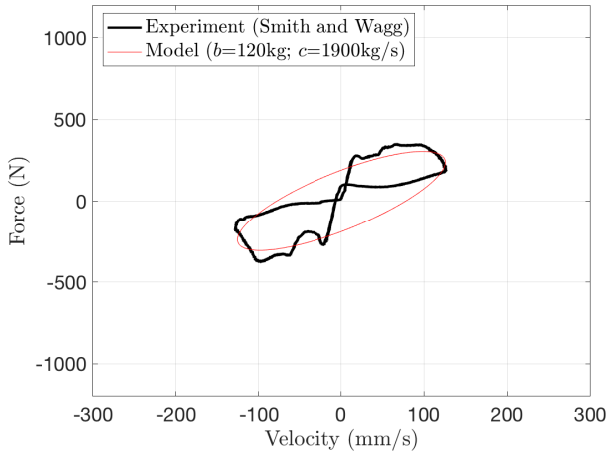

(c)

Figure 3.3: Hysteretic loops generated from experimental Test 2 [139], for (a) amplitude 10mm; frequency 3Hz (b) amplitude 15mm; frequency 3Hz (c) amplitude 10mm; frequency 2Hz

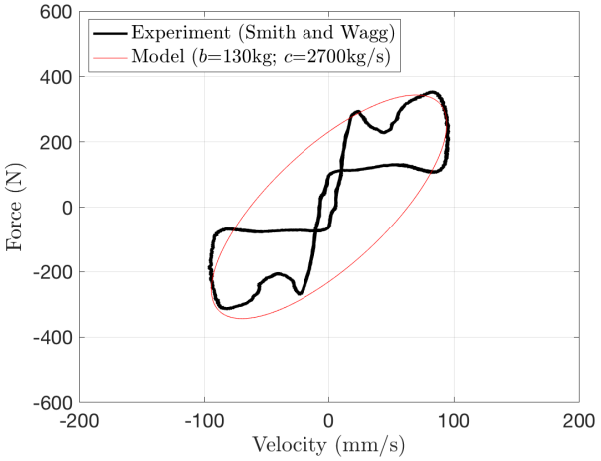

(a)

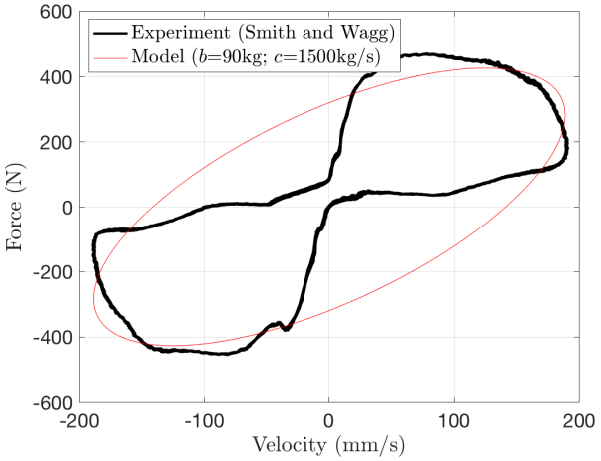

(b)

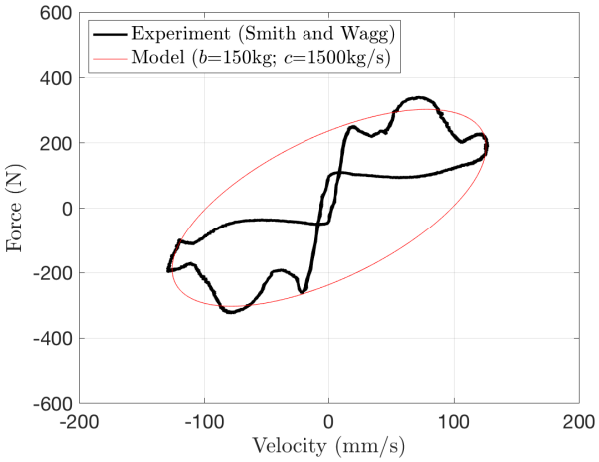

(c)

Figure 3.4: Hysteretic loops generated from experimental Test 3 [139], for (a) amplitude 5mm; frequency 3Hz (b) amplitude 10mm; frequency 3Hz (c) amplitude 10mm; frequency 2Hz

The complex damping model given in Equation 3.5 is proposed in this section to capture the hysteretic behaviour of the helical fluid inerter. Some comparisons between the model and the experiment are shown in Figure 3.3 and 3.4. It can be seen from these Figures that the proposed model cannot accurately capture the hysteretic behaviour of the device. It is because the devices clearly show nonlinearity due to friction, while the elliptical hysteresis model represents a limited approximation, because it does not include any nonlinear effects. This has also been reported in [49] that strong friction has affected the result as shown in Figure 3.5. The centre of the loops also tend to get smaller which cannot be captured by the model.

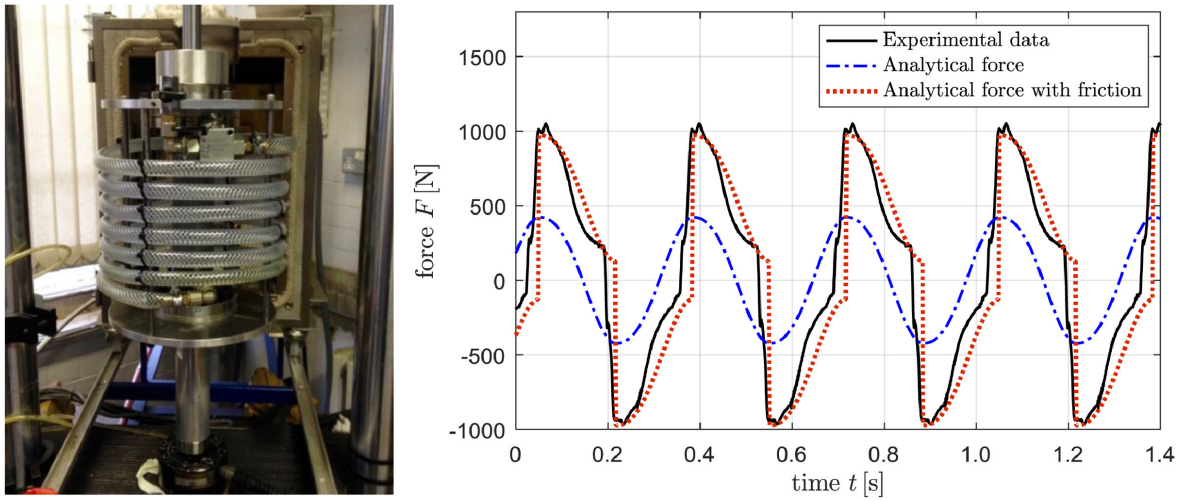

Figure 3.5: Analytical vs experimental force of the helical fluid inerter [49].

However, the approximation by the models in Figure 3.3 gives the same inertance and viscous damping constant value for all cases. Compared to Figure 3.3(a), either when the amplitude of excitation is increased (Figure 3.3(b) or when the frequency is decreased (Figure 3.3(c)), the b and c values do not change. This fact supports the hypothesis of the term τ which is a constant and is equivalent to $\frac{\omega b}{c}$. However, unlike Figure 3.3, the b and c values given by the models in Figure 3.4 are different for each case which does not support this hypothesis.

Overall, it can be concluded that the helical fluid inerter tested in [136] shows a strong nonlinearity that comes from friction which is not included in the complex damping model. Although the model has failed to capture the data from the experiment, the model can be used as a linear approximation to the real behaviour. The helical fluid inerter can be used to form a PVID (another name for the TVMD) by connecting the device with a spring element in series. The design of the helical fluid inerter for the PVID is discussed next in Chapter 4.

3.3 Complex Stiffness: Linear Hysteretic Damping Model for Stiffness and Damping In Parallel

Complex stiffness is discussed in this section as an analytical model for a material damper having a coupled stiffness and damping. The concept of complex stiffness was motivated by the fact that the energy loss per cycle in most materials is independent of excitation frequency and proportional to amplitude squared. As previously mentioned, the concept of complex stiffness has been widely used in the literature. Although it is a noncausal model, it has been proven to be accurate if used appropriately [97, 98].

In the literature, the analysis of complex stiffness is often carried out only in the frequency domain. In the time domain analysis, an equivalent viscous damping approach [138] is often used. This is because using a standard numerical integration method for the complex stiffness model in the time domain leads to unstable results due to the unstable poles [98]. However, using the equivalent viscous damping approach will only be accurate for one specific frequency of interest which is usually the natural frequency of the system. Therefore, the complex stiffness term must be treated as its original form and as a result, a new time-domain method is required.

The aims of this section are: (1) to investigate the differences between the complex stiffness model and the equivalent viscous damping model in the frequency domain; and (2) to propose a new-time domain method for the complex stiffness model. The method is based on that proposed by Inaudy and Makris [98]. Instead of using a zero-order hold method as in [98], the current method uses a standard numerical integration ode45 based on the Runge-Kutta method which is available in MATLAB. Next the use of the proposed method will be also demonstrated for both SDOF and MDOF structures.

3.3.1 Frequency-domain Analysis

Consider a mass m supported by a material damper subjected to a base excitation $r(t)$ as shown in Figure 3.6. The equation of motion of the system can be written as

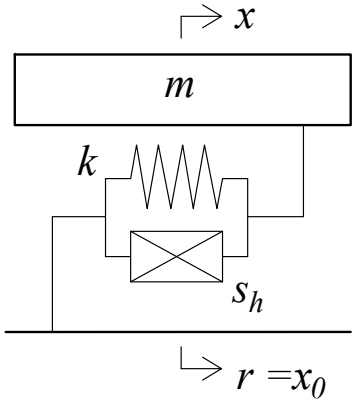

Figure 3.6: SDOF structure with a complex stiffness

$$m\ddot{x}(t) = k(1 + j\eta)(r(t) - x(t)) \tag{3.6}$$

here the complex stiffness $k(1 + j\eta)$ represents the material damper, k and η denote the stiffness and the loss factor respectively, and $j = \sqrt{-1}$. s_h is a parameter with a unit of stiffness, such that $\eta = s_h/k$.

In the Laplace domain, the Equation 3.6 can be written as

$$(ms^2)X = k(1 + j\eta)(R - X) \tag{3.7}$$

where X represents the Laplace transform of the storey displacement and R represents the Laplace transform of the base displacement. Initial conditions are assumed to be zero.

The transfer function X/R can be written in the frequency domain as

$$\frac{X}{R} = \frac{k(1 + j\eta)}{ms^2 + k(1 + j\eta)} \tag{3.8}$$

where s represents the Laplace transform variable.

A common approach in the literature for dealing with the complex stiffness is to use a equivalent viscous damping, given by $\zeta_{eq} = \frac{\eta}{2}$ or $c_{eq} = \frac{k\eta}{\omega_n}$, where ζ_{eq} and c_{eq} are the equivalent viscous damping ratio and the equivalent viscous damping coefficient, respectively. This approach assumes that the energy loss per cycle given by the complex stiffness is equivalent to that of viscous damping at a frequency of interest, which is usually the natural frequency ω_n. As a result, it is expected that using this approach will lead to some discrepancy in the frequency domain response especially in the frequencies away from resonance. To show this effect, first the transfer function X/R can be written in the frequency domain in the case of using the equivalent viscous damping approach, such that

$$\frac{X}{R} = \frac{c_{eq}s + k}{ms^2 + c_{eq}s + k} \tag{3.9}$$

The comparison between the Equation 3.8 and 3.9 is plotted in Figure 3.7 considering the SDOF structure given in Figure 3.6. The mass m and stiffness k were assumed to be 0.6kg and 23.6871N/m respectively, such that its natural frequency is 1Hz. Note that the equivalent viscous damping $\zeta_{eq} = \frac{\eta}{2}$ is used to plot Figure 3.7(b). As can be seen in these Figure 3.7(a) and 3.7(b) that the response around resonance is very similar between the complex stiffness and the equivalent viscous damping. However, at the higher frequencies, the equivalent viscous damping shows a higher response than the complex stiffness. It is even more obvious if the damping ratio is increased as shown in Figure 3.7(b), which shows, that the structural response using the equivalent viscous damping in the higher frequencies is amplified by the increase of the damping ratio. On the other hand, less amplification is shown in case of complex stiffness, as can be seen in Figure 3.7(a). Therefore it can be concluded that using the equivalent viscous

damping approach to model the material damper in an SDOF system could lead to overestimation of the response at higher frequencies of excitation.

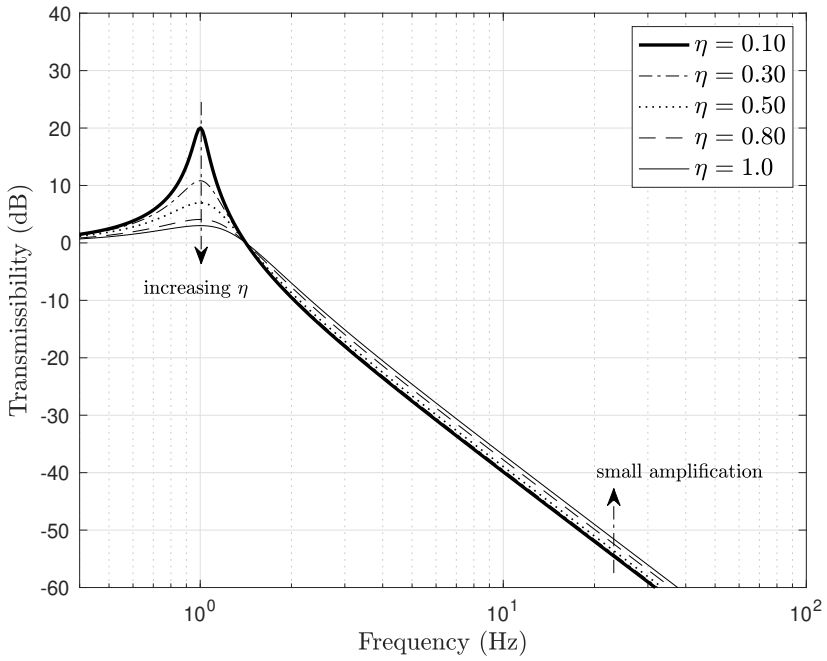

(a)

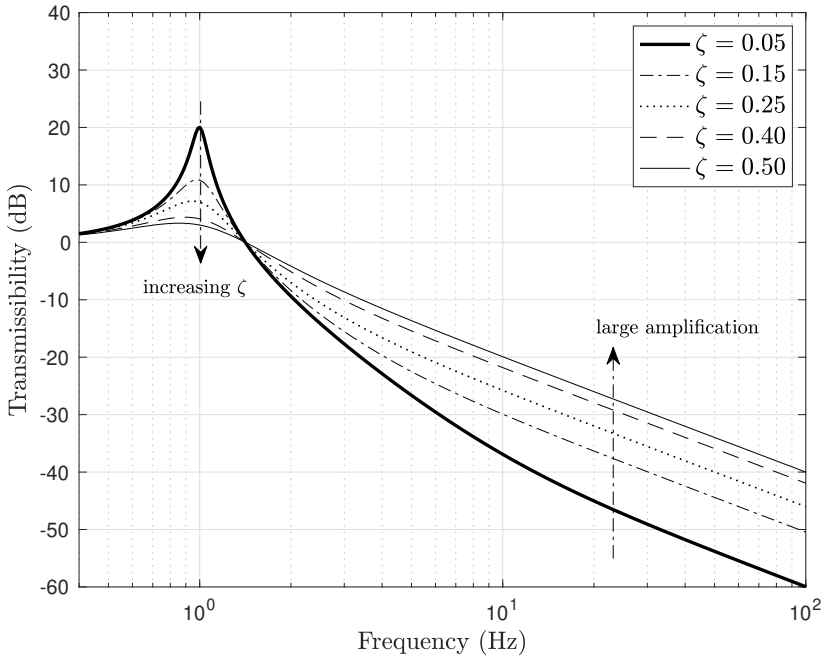

(b)

Figure 3.7: X/R of SDOF structure (a) complex stiffness (b) equivalent viscous damping

3.3.2 Time-domain Analysis

From the cases of SDOF and MDOF structures given above, it is obvious that using the equivalent viscous damping approach to simplify the complex stiffness model could only be accurate around the frequency of interest. Therefore, it is suggested that the complex stiffness term must be treated in its original form when conducting a frequency response analysis. This should not be any problem because the complex stiffness term can be easily included in the analytical formulation of the frequency response analysis. However, treating the complex stiffness in its original form in a standard numerical integration method for the time domain analysis could lead to unstable responses [98]. To solve this problem, a new time-domain method is proposed based on that proposed by Inaudi and Makris [98] involving analytic signals and the Hilbert transform.

3.3.2.1 Analytic Signals

Inaudi and Makris [98] were the first to introduce a time-domain method for a system with complex stiffness involving a time-reversal technique and Hilbert transform. The force of the complex stiffness model can be written as a sum of the force of the spring and the hysteretic damper

$$f_{hys}(t) = kx(t) + s_h H[x(t)] \tag{3.10}$$

where s_h is a constant with a unit of stiffness such that $\eta = \frac{s_h}{k}$ and $H[\ ]$ denotes the Hilbert transform.

The complex stiffness generates complex-parameter mechanical networks in the time domain and therefore, the input excitation in the time-domain needs to be complex-valued (analytic signal) since the imaginary part of the excitation when it operates on the imaginary part of the constitutive model contributes to the real part of the response. Here an analytic signal $y_a(t)$ is defined as $y_a(t) = y(t) + jH[y(t)]$.

Applying the Hilbert transform to Equation 3.10, we obtain

$$H[f_{hys}(t)] = kH[x(t)] - s_h x(t) \tag{3.11}$$

where $H[H[x(t)]] = -x(t)$ has been used. Multiplying Equation 3.11 with $-j$ and summing the result to Equation 3.10, we obtain

$$f_{hys_a}(t) = k(1 + j\eta)x_a(t) \tag{3.12}$$

Equation 3.12 represents the force generated by the complex stiffness. This will be used further in the time domain analysis.

The current time-domain method also adopted the time-reversal technique from Inaudi and Makris [98] that will be further discussed next.

3.3.2.2 Time reversal technique

In general, the dynamic equation of motion for a multi DOFs system with complex stiffness can be expressed in matrix form as

$$\mathbf{M}\ddot{\mathbf{x}} + \mathbf{K}(1 + j\mathbf{G})\mathbf{x} = \mathbf{F} \tag{3.13}$$

where $\mathbf{G}$ is the matrix of damping coefficients which represent the loss factor of each element of the system.

The sizes of the matrices in Equation 3.13 are defined by the number of DOFs, n. The first and second derivatives with respect to the time are denoted by dot, $[\dot{\ }]$, and double dots, $[\ddot{\ }]$. Here, $\mathbf{x}$ $(n \times 1)$ and $\mathbf{F}$ $(n \times 1)$, respectively, are the displacement and force vectors. Whereas $\mathbf{M}$ $(n \times n)$ and $\mathbf{K}$ $(n \times n)$ represent the mass, and stiffness matrices.

Inaudi & Makris [98] suggested that the displacements and the forces can be evaluated in analytic forms, i.e., complex signals constructed by real and imaginary components. Hence,

$$\mathbf{x_a}(t) = \mathbf{x}(t) + j\ H[\mathbf{x}(t)] \tag{3.14}$$

and

$$\mathbf{F_a}(t) = \mathbf{F}(t) + j\ H[\mathbf{F}(t)] \tag{3.15}$$

These analytic signals satisfy the boundary conditions of $\mathbf{x_a}(-\infty) = \mathbf{x_a}(\infty) = 0$ and $\mathbf{F_a}(-\infty) = \mathbf{F_a}(\infty) = 0$. Therefore, in a state-space form, Equation 3.13 can be rewritten as

$$\dot{\bar{\mathbf{x}}}_\mathbf{a}(t) = \mathbf{A}\ \bar{\mathbf{x}}_\mathbf{a}(t) + \mathbf{B}\ r_a(t) \tag{3.16}$$

where

$$\bar{\mathbf{x}}_\mathbf{a}(t) = \begin{bmatrix} \mathbf{x_a}(t) \\ \dot{\mathbf{x}}_\mathbf{a}(t) \end{bmatrix} \quad , \quad \mathbf{A} = \begin{bmatrix} \mathbf{0} & \mathbf{I} \\ -\mathbf{M^{-1}}\ \mathbf{K}(1 + j\mathbf{G}) & \mathbf{0} \end{bmatrix} \quad , \quad \mathbf{B} = \begin{bmatrix} \mathbf{0} \\ \mathbf{M^{-1}L_F} \end{bmatrix} \tag{3.17}$$

and

$$\mathbf{F_a}(t) = \mathbf{L_F}\ r_a(t) \tag{3.18}$$

It is important to note that the vectors and matrices denoted by $\bar{\mathbf{x}}_\mathbf{a}$ $(2n \times 1)$, $\mathbf{x_a}$ $(n \times 1)$, $\mathbf{A}$ $(2n \times 2n)$, $\mathbf{B}$ $(2n \times 1)$ and $\mathbf{L_F}$ $(n \times 1)$ are all in complex form. The force vector in analytic form, $\mathbf{F_a}$, is defined as the product of the complex time function, r_a, with a coefficient vector of elements' load factor, $\mathbf{L_F}$. Whereas $\mathbf{0}$ $(n \times 1)$ and $\mathbf{I}$ $(n \times 1)$ are the zeros and identity vectors, respectively.

Despite it seeming that Equation 3.16 can be solved directly involving a standard integration procedure, i.e., convolution integral, the eigenvalues of $\mathbf{A}$ are pairs of stable

and unstable roots [98]. Therefore, a special treatment is required to obtain the stable solutions of Equation 3.16. Inaudi & Makris [98] introduced a backward integration technique that reverses the independent variable (time) in the modal coordinate of the unstable parts. The analytic vector $\mathbf{x_a}$ can be rewritten by defining analytic modal coordinates, $\mathbf{q_{k_a}}$ and $\mathbf{q_{l_a}}$, for the stable and unstable parts, respectively.

$$\mathbf{x_a}(t) = \mathbf{\Phi} \begin{bmatrix} \mathbf{q_{k_a}}(t) \\ \mathbf{q_{l_a}}(t) \end{bmatrix} \tag{3.19}$$

where $\mathbf{q_{k_a}} = \mathbf{q_k} + j\ H[\mathbf{q_k}]$ and $\mathbf{q_{l_a}} = \mathbf{q_l} + j\ H[\mathbf{q_l}]$. While $\mathbf{\Phi}$ $(2n \times 2n)$ is the eigenvector matrix of $\mathbf{A}$.

By introducing a reversed time, $z = -t$, and a function $\tilde{\mathbf{q}}_\mathbf{l}(z) = \mathbf{q_l}(t)$; hence,

$$\dot{\mathbf{q}}_\mathbf{l}(t) = -\tilde{\mathbf{q}}'_\mathbf{l}(z) \tag{3.20}$$

where [$'$] defines the derivative in the reversed time. Therefore, Equation 3.16 can be rewritten as

$$\begin{bmatrix} \dot{\mathbf{q}}_{\mathbf{k_a}}(t) \\ -\tilde{\mathbf{q}}'_{\mathbf{l_a}}(z) \end{bmatrix} = \mathbf{A}^* \begin{bmatrix} \mathbf{q_{k_a}}(t) \\ \tilde{\mathbf{q}}_{\mathbf{l_a}}(z) \end{bmatrix} + \mathbf{B}^* \begin{bmatrix} r_a(t) \\ \tilde{r}_a(z) \end{bmatrix} \tag{3.21}$$

where $\mathbf{A}^* = \mathbf{\Phi}^{-1}\mathbf{A}\mathbf{\Phi}$ and $\mathbf{B}^* = \mathbf{\Phi}^{-1}\mathbf{B}$. To be noted here, $\mathbf{A}^*$ is a diagonal matrix; thus, Equation 3.21 becomes uncoupled. Hence, components of $\mathbf{q_{k_a}}$ and $\mathbf{q_{l_a}}$ can be evaluated separately using forward time integration and backward time integration, respectively.

Inaudi & Makris [98] numerically solved both an SDOF and a 2-DOF problem by applying discrete-time sampling to the analytical integral solutions of Equation 3.21. However, this approach may be difficult to implement in a more complex and higher DOFs system as it requires the analytical integral solution for each different system. Therefore, in the present work, a more robust computational approach is proposed. Herein, a variable separation procedure is applied to separate the real and imaginary components in Equation 3.21; hence,

$$\begin{bmatrix} \dot{\mathbf{q}}_\mathbf{k}(t) \\ H[\dot{\mathbf{q}}_\mathbf{k}(t)] \\ -\tilde{\mathbf{q}}'_{\mathbf{l_a}}(z) \\ -H[\tilde{\mathbf{q}}'_{\mathbf{l_a}}(z)] \end{bmatrix} = \begin{bmatrix} \mathbf{A}^{**} & \mathbf{0} \\ \mathbf{0} & \tilde{\mathbf{A}}^{**} \end{bmatrix} \begin{bmatrix} \mathbf{q_{k_a}}(t) \\ H[\mathbf{q_{k_a}}(t)] \\ \tilde{\mathbf{q}}_{\mathbf{l_a}}(z) \\ H[\tilde{\mathbf{q}}_{\mathbf{l_a}}(z)] \end{bmatrix} + \begin{bmatrix} \mathbf{B}^{**} \\ \tilde{\mathbf{B}}^{**} \end{bmatrix} \begin{bmatrix} r_a(t) \\ \tilde{r}_a(z) \end{bmatrix} \tag{3.22}$$

which can be evaluated separately for forward integration

$$\begin{bmatrix} \dot{\mathbf{q}}_\mathbf{k}(t) \\ H[\dot{\mathbf{q}}_\mathbf{k}(t)] \end{bmatrix} = \mathbf{A}^{**} \begin{bmatrix} \mathbf{q_{k_a}}(t) \\ H[\mathbf{q_{k_a}}(t)] \end{bmatrix} + \mathbf{B}^{**} r_a(t) \tag{3.23}$$

and backward integration

$$\begin{bmatrix} -\tilde{\mathbf{q}}'_{\mathbf{l_a}}(z) \\ -H[\tilde{\mathbf{q}}'_{\mathbf{l_a}}(z)] \end{bmatrix} = \tilde{\mathbf{A}}^{**} \begin{bmatrix} \tilde{\mathbf{q}}_{\mathbf{l_a}}(z) \\ H[\tilde{\mathbf{q}}_{\mathbf{l_a}}(z)] \end{bmatrix} + \tilde{\mathbf{B}}^{**}\tilde{r}_a(z) \tag{3.24}$$

In Equations 3.23 and 3.24, the matrices $\mathbf{A}^{**}$ $(2n \times 2n)$, $\tilde{\mathbf{A}}^{**}$ $(2n \times 2n)$, $\mathbf{B}^{**}$ $(2n \times 1)$, and $\tilde{\mathbf{B}}^{**}$ $(2n \times 1)$ consisted of components that provide coupling between the real and imaginary parts of each modal coordinate.

The key aspect in the present work is that Equations 3.23 and 3.24 are sets of ordinary differential equations (ODEs); thus, they can be straightforwardly solved via a standard numerical procedure, i.e., by using the Runge-Kutta method. Therefore, it provides a more robust approach to evaluate any structural system as long as the mass, stiffness, damping matrices and the force vector are known.

3.3.2.3 Validation

The proposed method in this section is validated with the zero-order hold method by Inaudi and Makris [98]. First, a simple SDOF structure is assumed with a mass of 0.6kg is supported by a material damper having stiffness and loss factor of 23.69N/m and 0.1 respectively. The transmissibility of the mass is plotted in Figure 3.7(a). The MATLAB code for this example can be found in Appendix A.

Attention is given at the frequency of resonance, $\omega = \omega_n$, and away from resonance ($\omega = 10\omega_n$ and $\omega = 30\omega_n$). The plots of the responses are given in Figure 3.8 which shows that the results from the current method are very close to those of the zero-order hold method. The benefit of the current method is as mentioned above, that it can be straightforwardly solved via a standard numerical procedure, i.e., using the built-in ode45 in MATLAB which is based on the Runge-Kutta method. Therefore, it provides a more robust approach to evaluate any structure system as long as the mass, stiffness, damping matrices and the force vector are known. It is also means that it can be used for even a more complex structure such as an MDOF structure subject to random and nonstationary base excitation.

It can also be seen from Figure 3.8 that treating the complex stiffness as its original form in the time domain gives a close result to the one given by the equivalent viscous damping approach at $\omega = \omega_n$ as shown in Figure 3.8(a). However, when the frequency of the excitation is increased, for examples when $\omega = 10\omega_n$ in Figure 3.8(b) and $\omega = 30\omega_n$ in Figure 3.8(c), the response of the complex stiffness becomes much lower than that of equivalent viscous damping. The difference will become more obvious if the damping ratio is increased.

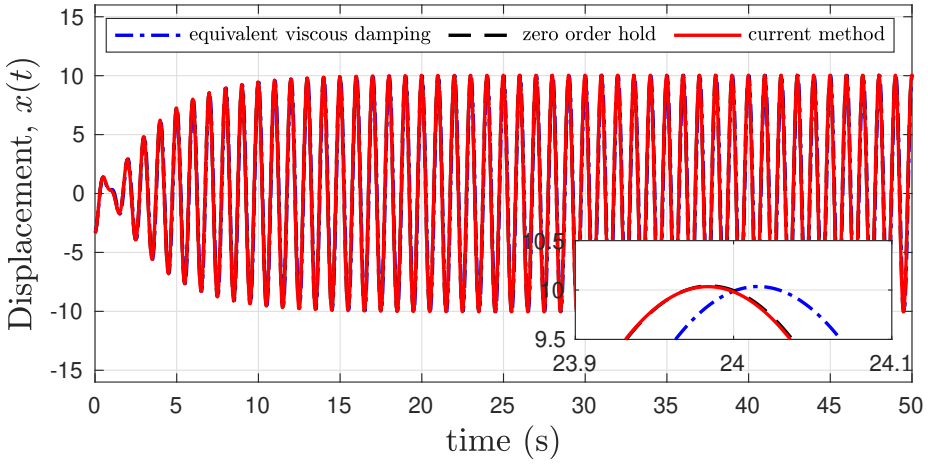

(a)

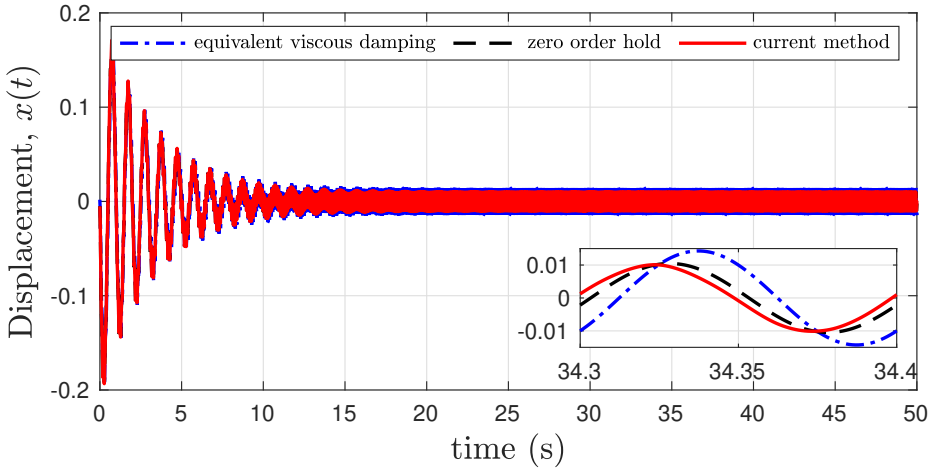

(b)

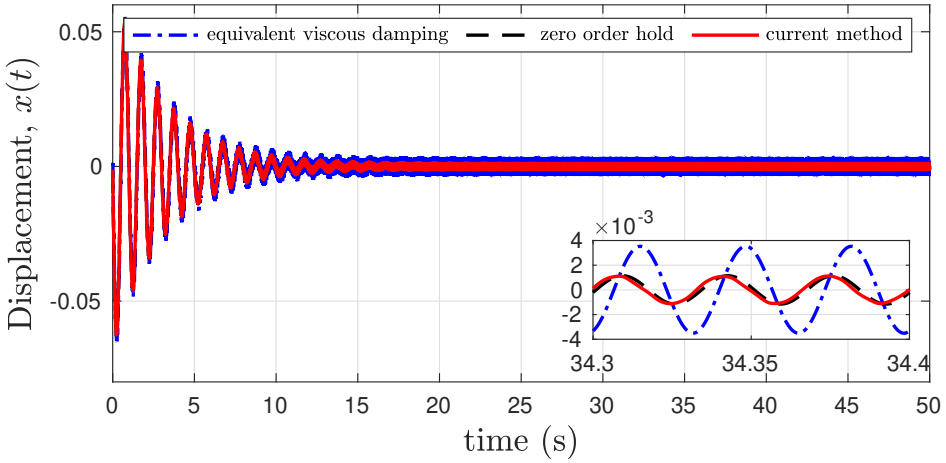

(c)

Figure 3.8: Time history responses of SDOF structure (a) ω=ω_n (b) ω=10ω_n (c) ω=30ω_n subjected to sine-wave ground displacement with amplitude R=1 unit length.

3.3.2.4 Example 1: MDOF structure

A generalised n-DOF structure subjected to base excitation $r(t)$ is given in Figure 3.9. The structure is separated into three parts: bottom storey, $i = 1$; middle storeys, i^{th}, where $i \in [2 : n-1]$; and top storey, $i = n$.

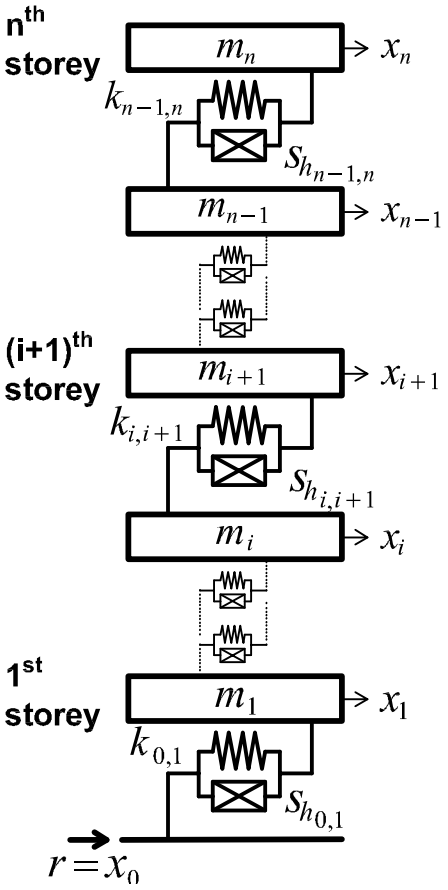

Figure 3.9: n-DOF structure with hysteretic damping

The equation of motion of the above structure can be written using analytic functions, given that $x_{i_a}(t) = x_i(t) + jH[x_i(t)]$, the equations can be written as follows:

$$\begin{cases} m_1\ddot{x}_{1_a}(t) + k_{0,1}(1+j\eta_{0,1})(x_{1_a}(t) - r_a(t)) - k_{1,2}(1+j\eta_{1,2})(x_{2_a}(t) - x_{1_a}(t)) = 0 \\ \vdots \\ m_i\ddot{x}_{i_a}(t) + k_{i-1,i}(1+j\eta_{i-1,i})(x_{i_a}(t) - x_{(i-1)_a}(t)) - k_{i,i+1}(1+j\eta_{i,i+1})(x_{(i+1)_a}(t) - x_{i_a}(t)) = 0 \\ \vdots \\ m_n\ddot{x}_{n_a}(t) + k_{n-1,n}(1+j\eta_{n-1,n})(x_{n_a}(t) - x_{(n-1)_a}(t)) = 0 \end{cases} \tag{3.25}$$

where m_i and $x_i(t)$ represent the mass concentrated on the i^{th} storey and its displacement response; $H[x_i(t)]$ is the Hilbert transform of $x_i(t)$; $k_{i-1,i}$ and $s_{h_{i-1,i}}$, $i \in [1 : n]$

represent the stiffness and a parameter with a unit of stiffness characterising the damping between storeys $i-1$ and i; $\eta_{i-1,i}$ is the loss factor of the linear hysteretic damping between storey $i-1$ and i, given by $\eta_{i-1,i} = \frac{s_{h_{i-1,i}}}{k_{i-1,i}}$; $r(t)$ represents ground displacement input signal; subscript a denotes an analytic signal; and $j = \sqrt{-1}$. In state-space formulation, Equation 3.25 can be expressed as:

$$\dot{\mathbf{x}}_a(t) = \mathbf{A}\mathbf{x}_a(t) + \mathbf{B}r_a(t) \tag{3.26}$$

where

$$\mathbf{x}_a(t) = \begin{bmatrix} x_{1_a}(t) \\ \dot{x}_{1_a}(t) \\ \vdots \\ x_{n_a}(t) \\ \dot{x}_{n_a}(t) \end{bmatrix} \quad ; \quad \mathbf{A} = \begin{bmatrix} a_{1,1} & a_{1,2} & \dots & a_{1,n-1} & a_{1,n} \\ a_{2,1} & a_{2,2} & \dots & a_{2,n-1} & a_{2,n} \\ \vdots & \vdots & \vdots & \vdots & \vdots \\ a_{n-1,1} & a_{n-1,2} & \dots & a_{n-1,n-1} & a_{n-1,n} \\ a_{n,1} & a_{n,2} & \dots & a_{n,n-1} & a_{n,n} \end{bmatrix} \quad ; \quad \mathbf{B} = \begin{bmatrix} B_1 \\ B_2 \\ \vdots \\ B_{n-1} \\ B_n \end{bmatrix} \tag{3.27}$$

The eigenvalues of $\mathbf{A}$ are given by s_z, where $z = 1, 2, ..., n-1, n$. Note also that

$$s_z = s_{z_{re}} + s_{z_{im}} j \tag{3.28}$$

Here, im stands for "imaginary" and re for "real". Defining the analytic modal coordinates $q_{z_a}(t)$

$$\dot{\mathbf{x}}_a(t) = \mathbf{\Phi} \begin{bmatrix} q_{1_a}(t) \\ q_{2_a}(t) \\ \vdots \\ q_{(n-1)_a}(t) \\ q_{n_a}(t) \end{bmatrix} \quad ; \quad \mathbf{\Phi} = \begin{bmatrix} \phi_{1,1} & \phi_{1,2} & \dots & \phi_{1,n-1} & \phi_{1,n} \\ \phi_{2,1} & \phi_{2,2} & \dots & \phi_{2,n-1} & \phi_{2,n} \\ \vdots & \vdots & \vdots & \vdots & \vdots \\ \phi_{n-1,1} & \phi_{n-1,2} & \dots & \phi_{n-1,n-1} & \phi_{n-1,n} \\ \phi_{n,1} & \phi_{n,2} & \dots & \phi_{n,n-1} & \phi_{n,n} \end{bmatrix} \tag{3.29}$$

where $\mathbf{\Phi}$ is the modal matrix, and $\phi_{l,z} = \phi_{l,z_{re}} + \phi_{l,z_{im}} j$, where $l = 1, 2, ..., n-1, n$. Now we have

$$\mathbf{\Phi} \begin{bmatrix} \dot{q}_{1_a}(t) \\ \dot{q}_{2_a}(t) \\ \vdots \\ \dot{q}_{(n-1)_a}(t) \\ \dot{q}_{n_a}(t) \end{bmatrix} = \mathbf{A}\mathbf{\Phi} \begin{bmatrix} q_{1_a}(t) \\ q_{2_a}(t) \\ \vdots \\ q_{(n-1)_a}(t) \\ q_{n_a}(t) \end{bmatrix} + \mathbf{B}r_a(t) \tag{3.30}$$

Using

$$\mathbf{\Phi}^{-1}\mathbf{A}\mathbf{\Phi} = \begin{bmatrix} s_1 & \dots & \dots & 0 \\ \vdots & s_2 & & \vdots \\ \vdots & & \ddots & \vdots \\ \vdots & & s_{n-1} & \vdots \\ 0 & \dots & \dots & s_n \end{bmatrix} \quad ; \quad \mathbf{\Phi}^{-1}\mathbf{B} = \begin{bmatrix} B_1 \\ B_2 \\ \vdots \\ B_{n-1} \\ B_n \end{bmatrix} \tag{3.31}$$

where

$$B_z = B_{z_{re}} + B_{z_{im}} j \tag{3.32}$$

we obtain

$$\begin{cases} \dot{q}_{1_a}(t) = s_1 q_{1a}(t) + B_1 r_a(t) \\ \dot{q}_{2_a}(t) = s_2 q_{2a}(t) + B_2 r_a(t) \\ \vdots \\ \dot{q}_{(n-1)_a}(t) = s_{n-1} q_{(n-1)_a}(t) + B_{n-1} r_a(t) \\ \dot{q}_{n_a}(t) = s_n q_{n_a}(t) + B_n r_a(t) \end{cases} \tag{3.33}$$

Separating Equation (3.33) into real and imaginary parts, one can obtain

$$\begin{cases} \dot{q}_1(t) = s_{1_{re}} q_1(t) - s_{1_{im}} H[q_1(t)] + B_{1_{re}} r(t) - s_{1_{im}} H[r(t)] \\ H[\dot{q}_1(t)] = s_{1_{re}} H[q_1(t)] + s_{1_{im}} q_1(t) + B_{1_{im}} r(t) + B_{1_{re}} H[r(t)] \\ \dot{q}_2(t) = s_{2_{re}} q_2(t) - s_{2_{im}} H[q_2(t)] + B_{2_{re}} r(t) - s_{2_{im}} H[r(t)] \\ H[\dot{q}_2(t)] = s_{2_{re}} H[q_2(t)] + s_{2_{im}} q_2(t) + B_{2_{im}} r(t) + B_{2_{re}} H[r(t)] \\ \vdots \\ \dot{q}_{n-1}(t) = s_{(n-1)_{re}} q_{n-1}(t) - s_{(n-1)_{im}} H[q_{n-1}(t)] + B_{(n-1)_{re}} r(t) - s_{(n-1)_{im}} H[r(t)] \\ H[\dot{q}_{n-1}(t)] = s_{(n-1)_{re}} H[q_{n-1}(t)] + s_{(n-1)_{im}} q_{n-1}(t) + B_{(n-1)_{im}} r(t) + B_{(n-1)_{re}} H[r(t)] \\ \dot{q}_n(t) = s_{n_{re}} q_n(t) - s_{n_{im}} H[q_n(t)] + B_{n_{re}} r(t) - s_{n_{im}} H[r(t)] \\ H[\dot{q}_n(t)] = s_{n_{re}} H[q_n(t)] + s_{n_{im}} q_n(t) + B_{n_{im}} r(t) + B_{n_{re}} H[r(t)] \end{cases} \tag{3.34}$$

The MATLAB code for solving equation 3.34 can be found in Appendix B. From Equation (3.29), $\dot{\mathbf{x}}_a(t)$ can be written as:

$$\dot{\mathbf{x}}_a(t) = \begin{bmatrix} \phi_{1,1} & \phi_{1,2} & \cdots & \phi_{1,n-1} & \phi_{1,n} \\ \phi_{2,1} & \phi_{2,2} & \cdots & \phi_{2,n-1} & \phi_{2,n} \\ \vdots & \vdots & \vdots & \vdots & \vdots \\ \phi_{n-1,1} & \phi_{n-1,2} & \cdots & \phi_{n-1,n-1} & \phi_{n-1,n} \\ \phi_{n,1} & \phi_{n,2} & \cdots & \phi_{n,n-1} & \phi_{n,n} \end{bmatrix} \begin{bmatrix} q_{1a}(t) \\ q_{2a}(t) \\ \vdots \\ q_{(n-1)_a}(t) \\ q_{na}(t) \end{bmatrix} \tag{3.35}$$

Separating the real and imaginary parts, this equation now can be solved using:

$$\begin{bmatrix} x_1(t) \\ \dot{x}_1(t) \\ \vdots \\ x_n(t) \\ \dot{x}_n(t) \end{bmatrix} = \begin{bmatrix} \phi_{(1,1)_{re}} & \phi_{(1,2)_{re}} & \cdots & \phi_{(1,n-1)_{re}} & \phi_{(1,n)_{re}} \\ \phi_{(2,1)_{re}} & \phi_{(2,2)_{re}} & \cdots & \phi_{(2,n-1)_{re}} & \phi_{(2,n)_{re}} \\ \vdots & \vdots & \vdots & \vdots & \vdots \\ \phi_{(n-1,1)_{re}} & \phi_{(n-1,2)_{re}} & \cdots & \phi_{(n-1,n-1)_{re}} & \phi_{(n-1,n)_{re}} \\ \phi_{(n,1)_{re}} & \phi_{(n,2)_{re}} & \cdots & \phi_{(n,n-1)_{re}} & \phi_{(n,n)_{re}} \end{bmatrix} \begin{bmatrix} q_1(t) \\ q_2(t) \\ \vdots \\ q_{n-1}(t) \\ q_n(t) \end{bmatrix} + \begin{bmatrix} \phi_{(1,1)_{im}} & \phi_{(1,2)_{im}} & \cdots & \phi_{(1,n-1)_{im}} & \phi_{(1,n)_{im}} \\ \phi_{(2,1)_{im}} & \phi_{(2,2)_{im}} & \cdots & \phi_{(2,n-1)_{im}} & \phi_{(2,n)_{im}} \\ \vdots & \vdots & \vdots & \vdots & \vdots \\ \phi_{(n-1,1)_{im}} & \phi_{(n-1,2)_{im}} & \cdots & \phi_{(n-1,n-1)_{im}} & \phi_{(n-1,n)_{im}} \\ \phi_{(n,1)_{im}} & \phi_{(n,2)_{im}} & \cdots & \phi_{(n,n-1)_{im}} & \phi_{(n,n)_{im}} \end{bmatrix} \begin{bmatrix} H[q_1(t)] \\ H[q_2(t)] \\ \vdots \\ H[q_{n-1}(t)] \\ H[q_n(t)] \end{bmatrix} \tag{3.36}$$

where $q_z(t)$ and $H[q_z(t)]$ were obtained from Equation (3.34).

Figure 3.10 (a) shows an example of a 2-storey structure with linear hysteretic damping on each storey. The accuracy of the proposed time-domain method can be

seen in Figure 3.10 (b). Here the response of the structure in the time domain at steady-state is plotted in the same plot with the analytical frequency domain. It is obvious that the proposed numerical time-domain method is in good agreement with the analytical frequency response.

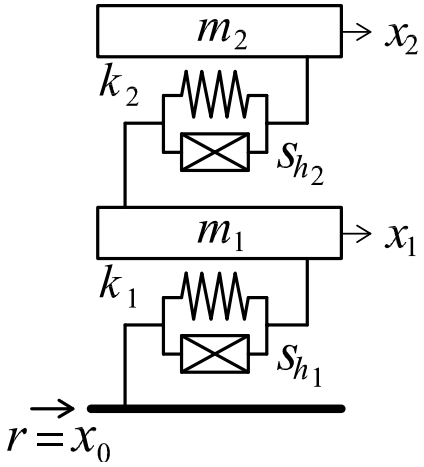

(a)

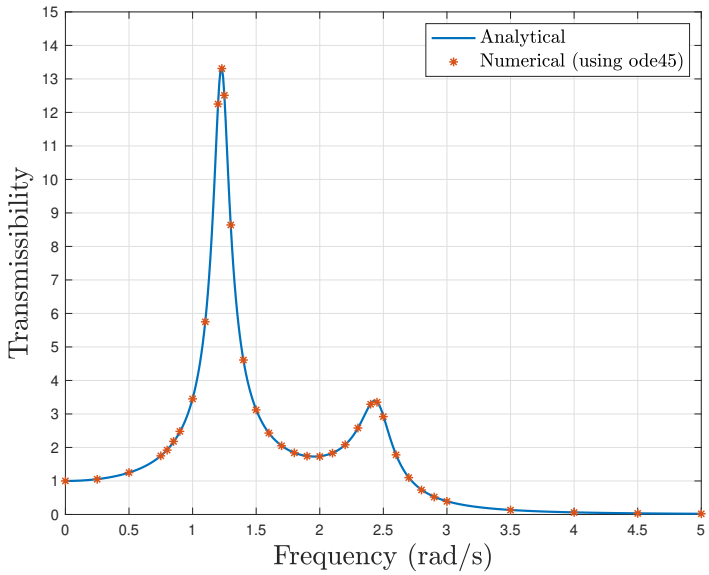

(b)

Figure 3.10: (a) 2-storey structure with hysteretic damping, $m_1 = 2$tonne, $m_2 = 1$tonne, $k_1 = 6$kN/m, $k_1 = 3$kN/m, $\eta = 0.1$. and (b) its top storey transmissibility when the structure is subjected to base displacement $r(t)$

3.3.2.5 Example 2: Hysteretic TMD (HTMD)

Many strategies have been introduced for protecting structures from unwanted vibrations. Using the tuned-mass-damper (TMD) is one of the established strategies that has been used in many structures. Wong [107] has investigated the TMD with hys-

teretic damping and shown how the tuning procedure based on fixed-point theory in the frequency domain can be used. However, an equivalent time-domain analysis had not yet been presented.

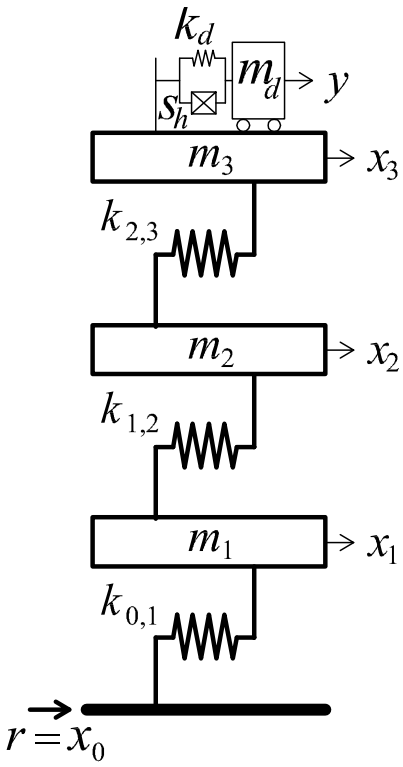

Figure 3.11: 3-storey structure with a HTMD at the top storey

This gap in knowledge is now addressed. A 3-storey undamped structure is equipped with a HTMD at the top storey subjected to base displacement as shown in Figure 3.11, and is then investigated in the time-domain. The optimum parameters of the HTMD are found to be $m_d = 0.102\text{kNs}^2/\text{m}$, $k_d = 27.6\text{kN/m}$ and $\eta = s_h/k_d = 0.2336$. m_d and k_d represent the mass and stiffness of the HTMD, and η is the loss factor of the linear hysteretic damping of the HTMD. The equation of motions of the system can be written as:

$$\begin{cases} \ddot{x}_{1_a}(t) = \dfrac{-(k_{0,1}+k_{1,2})x_{1_a}(t) + k_{1,2}x_{2_a}(t) + k_{0,1}r_a(t)}{m_1} \\ \ddot{x}_{2_a} = \dfrac{-(k_{1,2}+k_{2,3})x_{2_a}(t) + k_{2,3}x_{3_a}(t) + k_{1,2}x_{1_a}(t)}{m_2} \\ \ddot{x}_{3_a} = \dfrac{-(k_{2,3}+k_d(1+j\eta)x_{3_a}(t)) + k_{2,3}x_{2_a}(t) + kd(1+j\eta)y_a(t)}{m_3} \\ \ddot{y}_a(t) = \dfrac{-k_d(1+j\eta)(y_a(t)-x_{3_a}(t))}{m_d} \end{cases} \tag{3.37}$$

Figure 3.12 shows the performance of the structure with a HTMD on the top storey in the frequency domain by assuming the base displacement input is harmonic. The

performance of the HTMD is compared with the TMD with viscous damping obtained via an equivalent viscous damping, where $c_{eq} = \frac{k_d \eta}{\omega_{n_1}}$. It is obvious that the response of the HTMD is different from the TMD, particularly around the second and third resonances. This implies that modelling the HTMD by using an equivalent viscous damping would lead to an underestimation of the level of damping around the higher resonances.

The accuracy of the proposed time-domain method can also be seen in Figure 3.12. The steady-state responses from the time domain response across frequencies are in a good agreement with the frequency domain response of the HTMD.

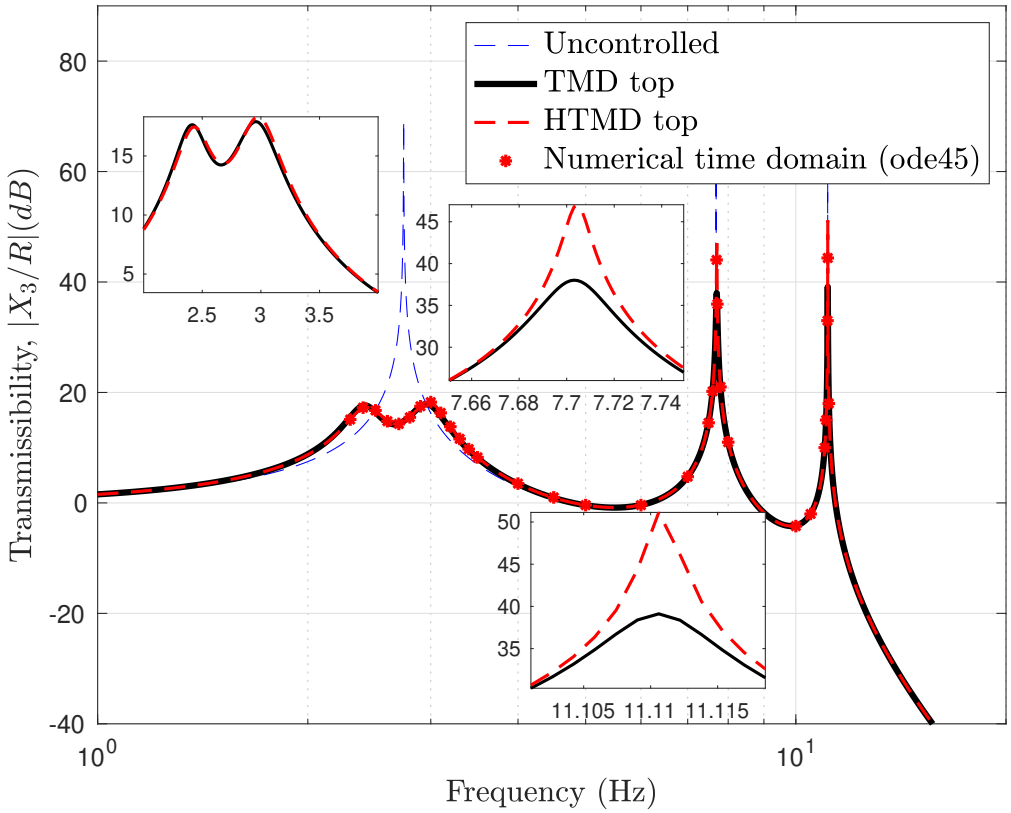

Figure 3.12: 3-storey structure with a HTMD at the top storey, $m_1 = m_2 = m_3 =$ 1tonne, $k_{0,1} = k_{1,2} = k_{2,3} =$ 1500kN/m, $k_d =$ 27.6kN/m,$c_d =$ 0.38kNs/m,$m_d =$ 0.102tonne and $\eta = 0.2336$.

3.4 Summary

In this chapter, two linear hysteretic models were presented: complex damping and complex stiffness. The first is motivated by the helical fluid inerter that has been shown in the literature to have inertance and viscous damping in parallel, see [55].

The second is a well-known concept to represent a material damper. The complex damping model is analogous to the complex stiffness model. In the complex stiffness, the term $\frac{\omega c}{k}$ is defined as equivalent to a constant loss factor, η. Likewise, in the concept of complex damping introduced in this chapter, further experiments are still needed in order to investigate the term $\frac{\omega b}{c}$, whether it is constant or not.

Complex stiffness is a well-known model to represent a material damper. although this is a noncausal model, it has been proven to be accurate [98] and widely used in practice [97]. However, the analysis of complex stiffness is often carried out only in the frequency domain. In the time domain analysis, an equivalent viscous damping approach is often used. This is because using a standard numerical integration method for the complex stiffness model in the time domain leads to unstable results due to the unstable poles [98]. However, from the cases of SDOF and MDOF structures given in this chapter, it is obvious that using the equivalent viscous damping approach to simplify the complex stiffness model could only be accurate around the frequency of interest. Therefore, it is suggested that the complex stiffness term must be treated in its original form when conducting a time domain analysis. Therefore, a new time-domain method is proposed in this chapter based on that proposed by Inaudi and Makris [98] involving analytic signals and the Hilbert transform. This proposed method has been validated and shown to be accurate. However, it should be noted that the method is only valid for linear models. Also, the initial conditions of both input and output signals must be zero when the time is both minus and plus infinity. An article from this chapter specifically discussing about this time domain method has also been published in [140, 141].

The concept of complex damping is a simple linear model assuming both inertance and viscous damping are in parallel as given in Equation 3.1. This model can capture some of the most important aspects of real hysteresis, but nonlinear effects such as friction are excluded from the scope of the thesis, and so would need to be a future development of the modelling approach. It was decided that this will remain as an open discussion for the future work, hence the helical fluid inerter will not be used for any experiment later in this study, especially for the shake table experiment.

The design of the helical fluid inerter is interesting. In the literature, as mentioned above, the helical fluid inerter has been shown to have both inertance and damping in parallel. This is interesting because it can be used to build a TVMD. In another study, see [132], a similar layout of the TVMD is also called as a parallel-viscous-inerter-damper (PVID). The helical fluid inerter can be used to build a PVID just by connecting the device with a spring element in series. However, because both inertance and damping parameters are coupled, it is difficult to know how best to design the device to achieve the targeted parameters from the TVMD/PVID optimum design, something that is addressed in the next chapter. In particular, an new design method will be proposed for the helical fluid inerter design.

Chapter 4

Tuned-Inerter-Based-Dampers with Helical Fluid Inerters

4.1 Introduction

Helical fluid inerter has been shown in the previous chapter to have both inertance and damping in parallel. These damping and inertance parameters are produced by the viscosity of the fluid inside the chamber and the acceleration of the fluid inside a helical pipe coiled around the outside of the chamber.

Theoretically, this device can be easily used to form a PVID by adding one spring element in series. However, it is a particular challenge to tune both inertance and damping parameters to fit with optimised values resulting from a design analysis because both parameters are coupled to each other. This chapter presents a new analysis that demonstrates how a helical fluid inerter can be designed to achieve the targeted PVID optimum parameters.

Most literature recently focusses on the application of both mechanical geared inerters and ball screw inerters for realization of TIBD concepts. Examples of this can be found in [135] and [14]. This is due to simplicity of the design processes when using such an inerter.

Fluid inerters on the other hand, require a complicated design processes involving the consideration of many parameters of the device. The derived formula for calculating damping and inertance of the device is given by [123]:

$$F_{damper} = 0.03426\frac{2\rho l A_1}{\sqrt{D_h R_h}}\left(\frac{A_1}{A_2}\right)^2 \dot{x}^2 + 17.54\frac{2\bar{\mu} l A_1}{D_h^2}\left(\frac{A_1}{A_2}\right)\dot{x} \tag{4.1}$$

and by [55]:

$$b = \frac{m_{hel}}{1 + \left(\frac{h}{2\pi r_4}\right)^2}\left(\frac{A_1}{A_2}\right)^2 \tag{4.2}$$

where $\bar{\mu}$ and ρ are the viscosity and density of the fluid, in this study these are assumed to be 1×10^6 kPa s and 1000 kg/m^3. l is the length of the channel, D_h and R_h are the channel hydraulic diameter and its bend radius. m_{hel} is the mass of the fluid inside the helical channel. A_1 and A_2 are the area of the piston and the channel, given by $A_1 = 2\pi(r_2 - r_1)^2$ and $A_2 = 2\pi r_3^2$.

As can be seen in Equations 4.1 and 4.2, that both damping and inertance parameters are functions of many other parameters. Therefore, a new design approach is proposed in this chapter to practically design the dimensions of the helical fluid inerter such that both targeted damping and inertance parameters can be achieved. This proposed design approach relies on the fact that both damping and inertance are insensitive to changes in some parameters. Consequently, these parameters can be chosen based upon practical design considerations, so that the number of unknown parameters in Equations 4.1 and 4.2 can be reduced.

Three examples of different scenarios are presented to show the effectiveness of the proposed method. The first example is for a simple SDOF structure. Here the mass of the structure is connected to a helical fluid inerter via a bracing. One end of the helical fluid inerter is connected to the bracing and its other end is grounded. The layout of this system is similar to that of TVMD or PVID. Therefore, a fixed-point theory approach can be used to obtain the targeted optimised damping and inertance parameters.

The second example is for an MDOF structure. A 10-storey structure is considered where the helical fluid inerter is installed on each of the storey via bracings. The targeted optimised damping and inertance of the helical fluid inerters are obtained based on the fixed-point theory approach.

The third example is for an MDOF structure equipped with a helical fluid inerter on its base. In this example, the helical fluid inerter is assumed to be nonlinear. The discussion focuses on how practically the helical fluid inerter dimensions can be designed. While the targeted optimum parameters of damping and inertance parameters of the device have been extensively discussed in [49].

4.2 Design of The Helical Fluid Inerter For Use As A PVID

4.2.1 Example 1: SDOF structure

The displacement transmissibility of an SDOF structure with a PVID subjected to base excitations as shown in Figure 4.1, can be expressed as

$$\left|\left(\frac{X}{R}\right)^2\right| = \frac{[1-\mu q^2(\lambda+1)]^2 + [2\zeta(\lambda+1)q]^2}{[1-q^2(\lambda\mu+1+\mu)+\lambda\mu q^4]^2 + [2\zeta(1-\lambda q^2+\lambda)q]^2} \tag{4.3}$$

where X and R are the Laplace transform of the main mass displacement and the base displacement, $\mu = \frac{b}{m}$, is the inertance-to-mass ratio, $q = \frac{\omega}{\omega_n}$, is the frequency ratio, $\omega_n = \sqrt{\frac{k}{m}}$, is the natural frequency of the system $\lambda = \frac{k}{k_d}$, is the stiffness ratio, and $\zeta = \frac{c_d}{2m\omega_n}$, is the damping ratio of the device. In this example the damping of the structure is selected as 2%, which is relatively small and has therefore been neglected in the frequency domain analysis.

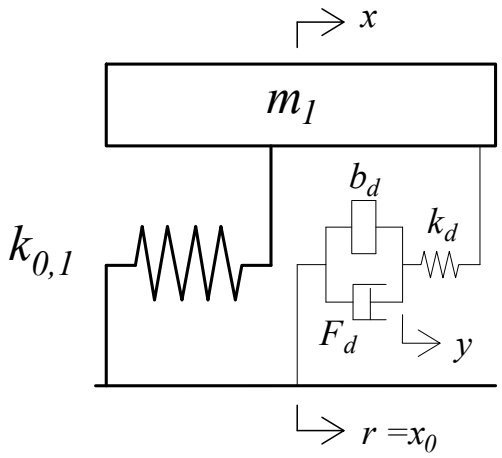

Figure 4.1: SDOF structure with a PVID

Table 4.1: Optimum parameters of the PVID

Inertance, b (kg)	Stiffness, k_d (kN/m)	Damping, c_d (kNs/m)
500	17.79	0.83
1000	38.82	2.48
1500	64.21	4.86
2000	95.71	8.05
2500	136.23	12.23
3000	191.13	17.78

The structural mass and stiffness are 10^4kg and 328.89kN/m, respectively. It should be noted that F_d is originally nonlinear as shown in Equation 4.1, and the damping parameter of the PVID, c_d, is the linearisation of F_d. Here, the PVID, was optimised using the analysis presented in [42]. The optimisation aims to minimise the response ampliude x around the resonance frequency. The optimum parameters were computed for a range of inertance values and are presented in Table 4.1. The transmissibility of the structure with optimised PVID parameters obtained by this method for a selection of inertance-to-mass ratio is shown in Figure 4.2(a). As would be expected, increasing the inertance-to-mass ratio will decrease the amplitude of response of the SDOF system and increase the width of the peaks. As a result, the cut-off frequency moves to the

right for larger inertance-to-mass ratios.

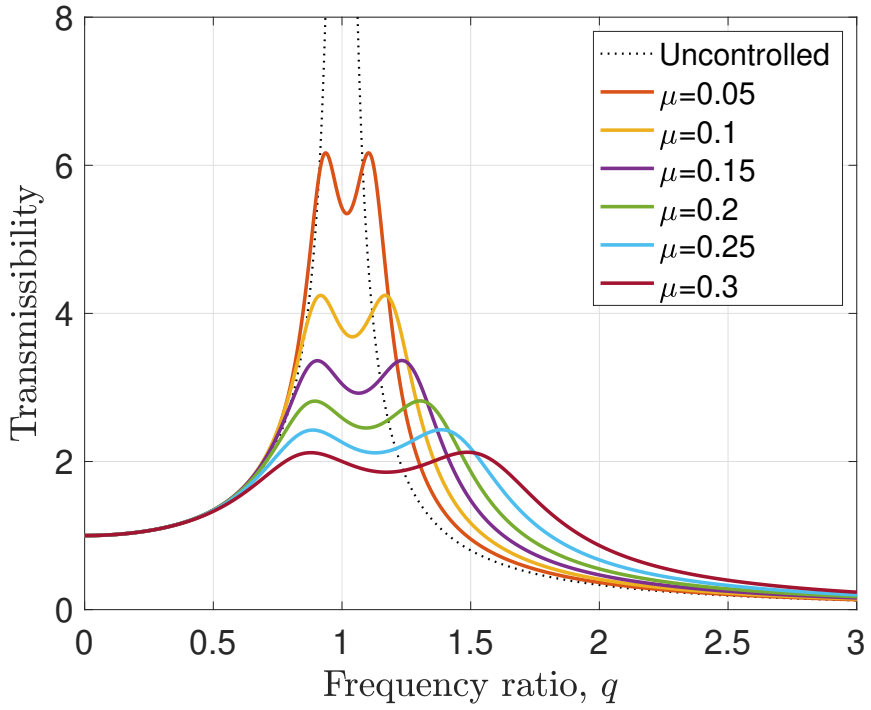

(a)

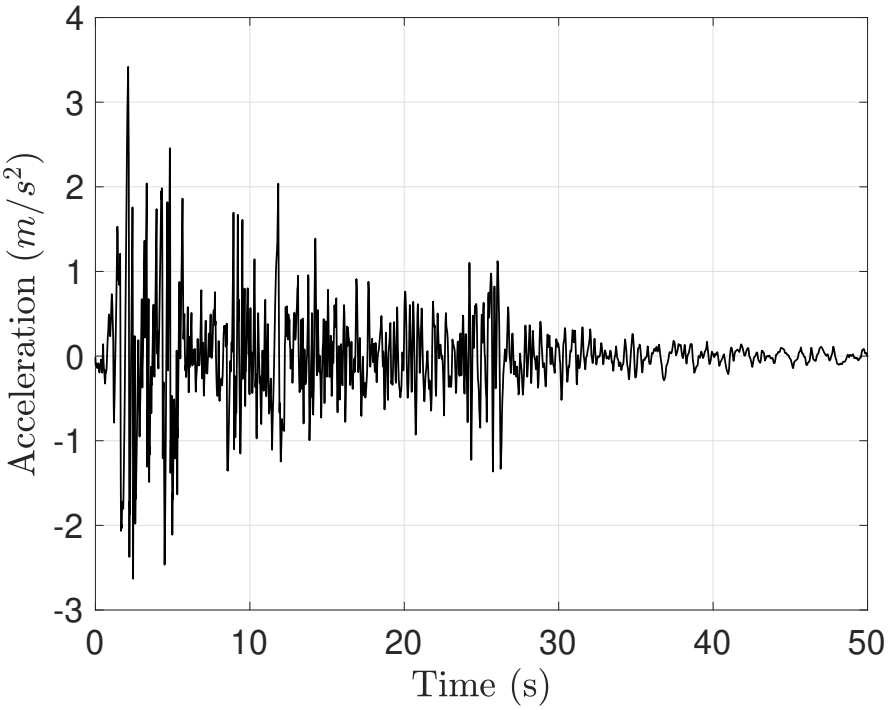

(b)

Figure 4.2: (a) Optimized PVID with various mass-ratios for an SDOF structure (b) El Centro ground motion.

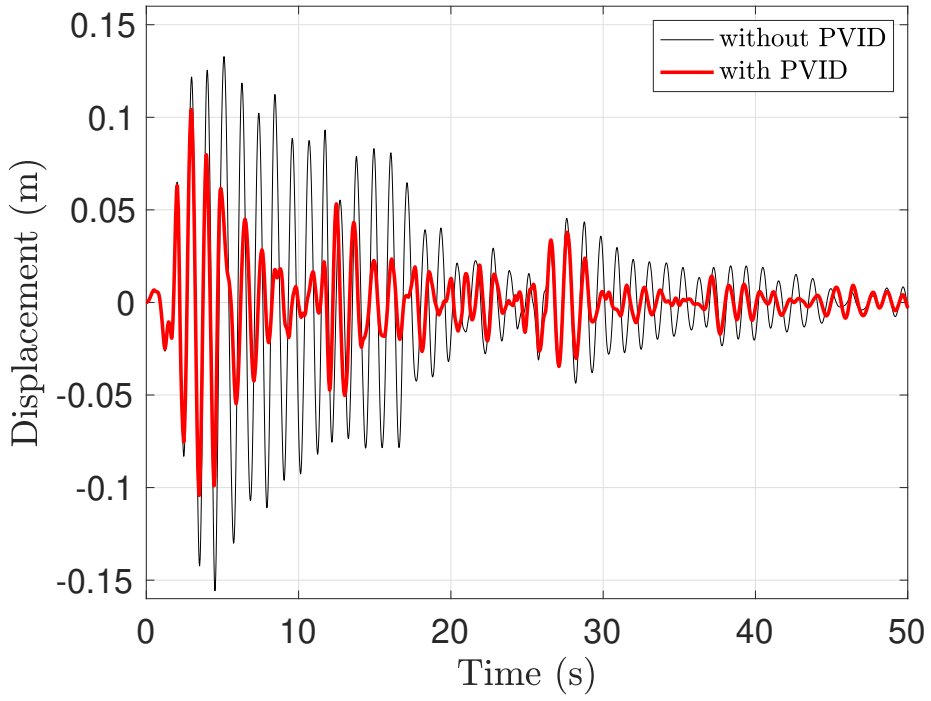

(a)

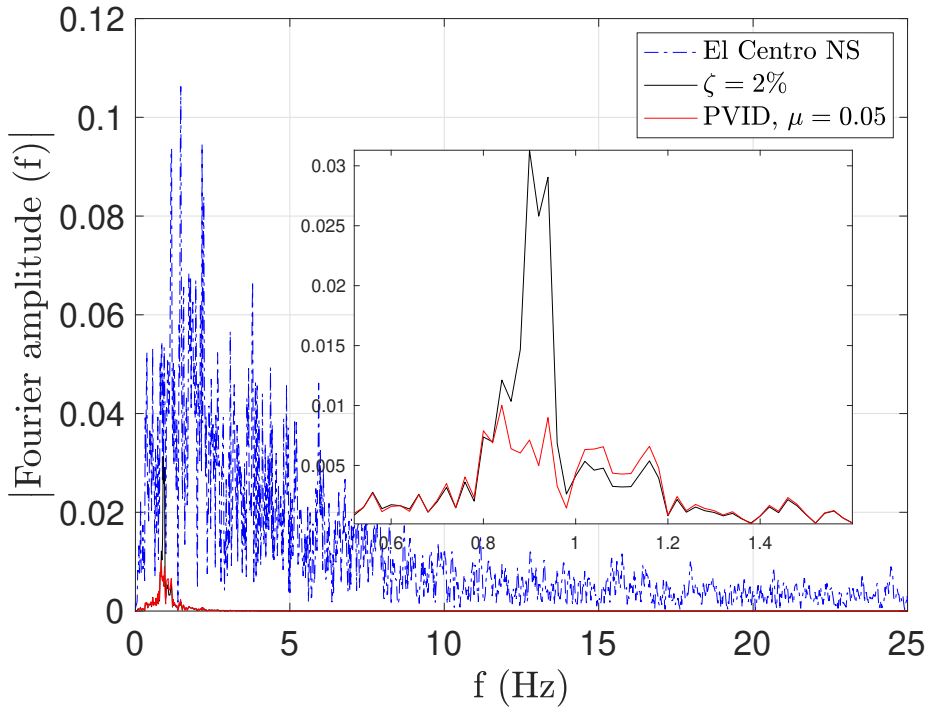

(b)

Figure 4.3: (a) Response of an SDOF structure equipped with a PVID (b) Fourier Transform of the earthquake input and the structural time history response.

To evaluate the performance of the structure subjected to non-sinusoidal signals,

an El Centro ground motion shown in Figure 4.2(b), was used.

As expected, using $\mu = 0.05$, the response of the structure is significantly reduced, as shown in Figure 4.3(a). Furthermore, a frequency response analysis, shown in Figure 4.3(b), also demonstrates that the PVID gives a significant reduction of the response of the SDOF mass close to the natural frequency at $f = 0.91Hz$.

Next a parametric study was performed to determine the physical parameters of the fluid inerter that gives inertance b and damping c_d close enough to the required optimal values when using $\mu = 0.05$ as shown in the 4.1. The spring element is provided by a bracing system which can be easily adjusted. However, the design of the fluid inerter is quite challenging due to the inertance and the damping parameters being coupled to each other.

In the design process, the helical channel is assumed to cover all the surface of the tube, with no space in between ($h = 2r_3$). Hence, the total length of the channel is calculated using $l = 2n\pi r_4$, where n is the number of turns in the helix, given by $n = L_t/2r_3$, where L_t is the length of the tube, and r_3 is the radius of the helix. The distance between the outer surface of the tube and the outer surface of the helical channel,r_d, is given by $r_d = r_4 - (r_3 + r_2)$, where r_2 is the distance from the center to the outer surface of the tube.

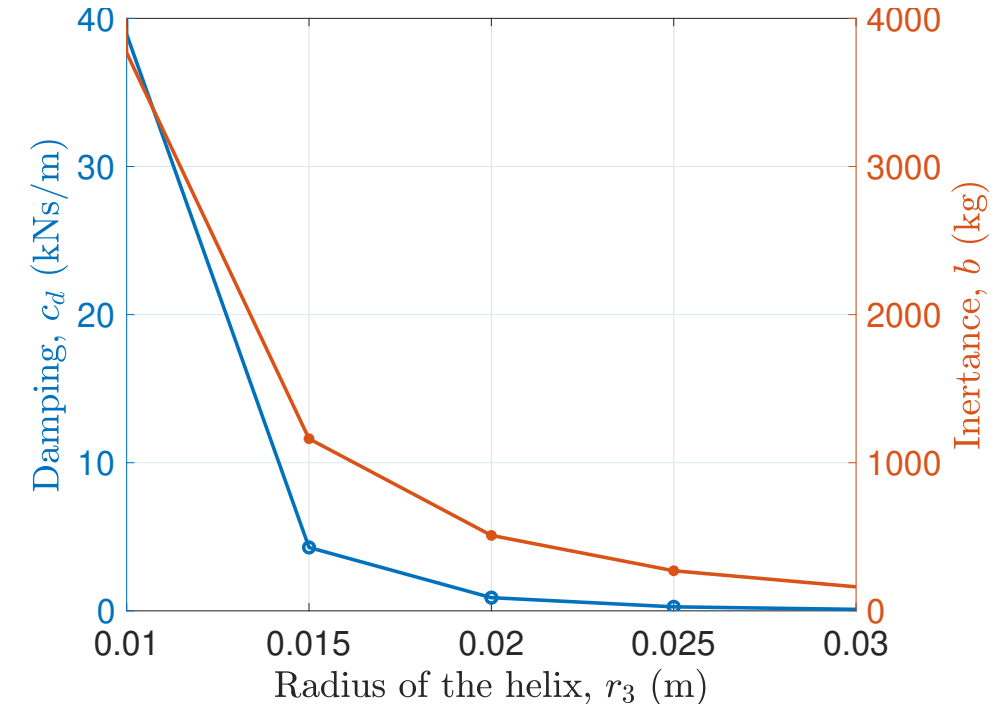

(a)

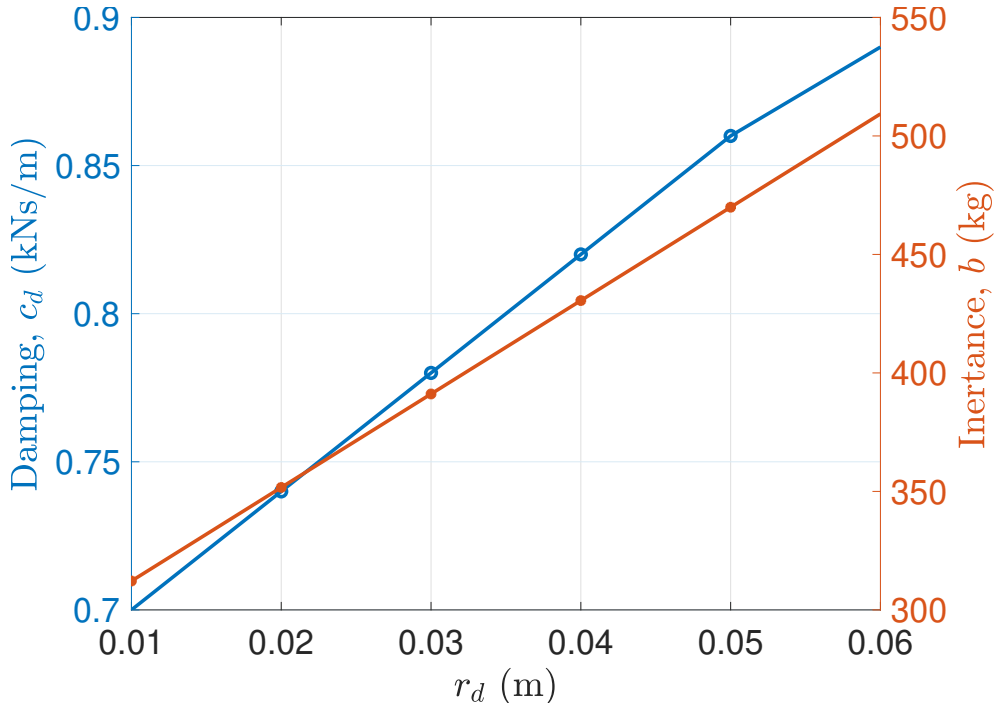

(b)

Figure 4.4: The influence of changing (a) r_3 (radius of the helix) and (b) r_d (distance between the outer surface of the tube and the outer surface of the helical channel) on damping and inertance values

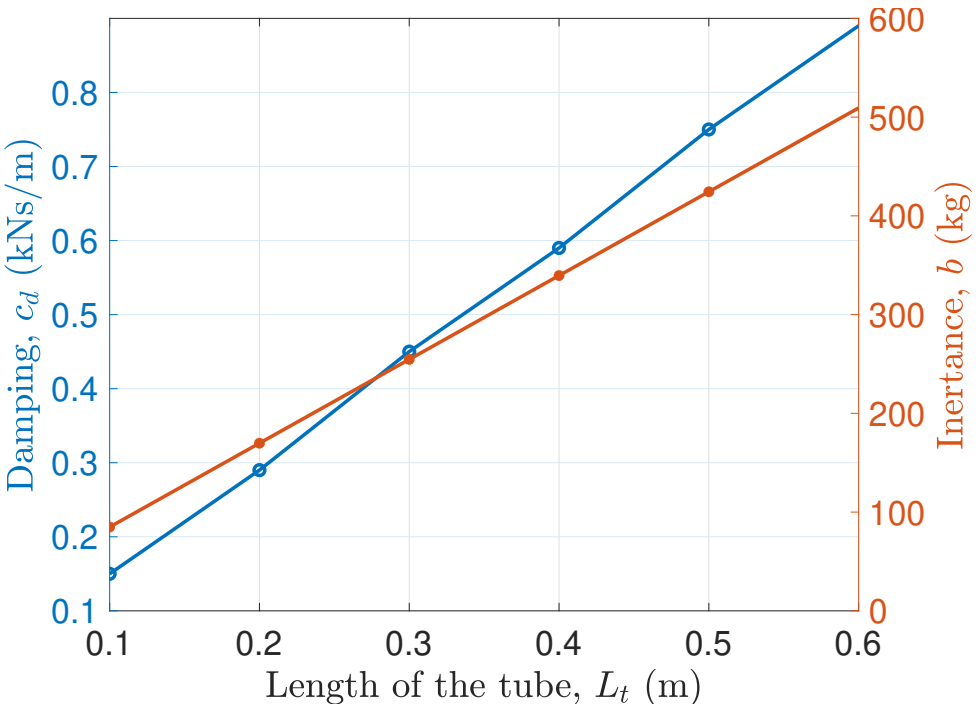

(a)

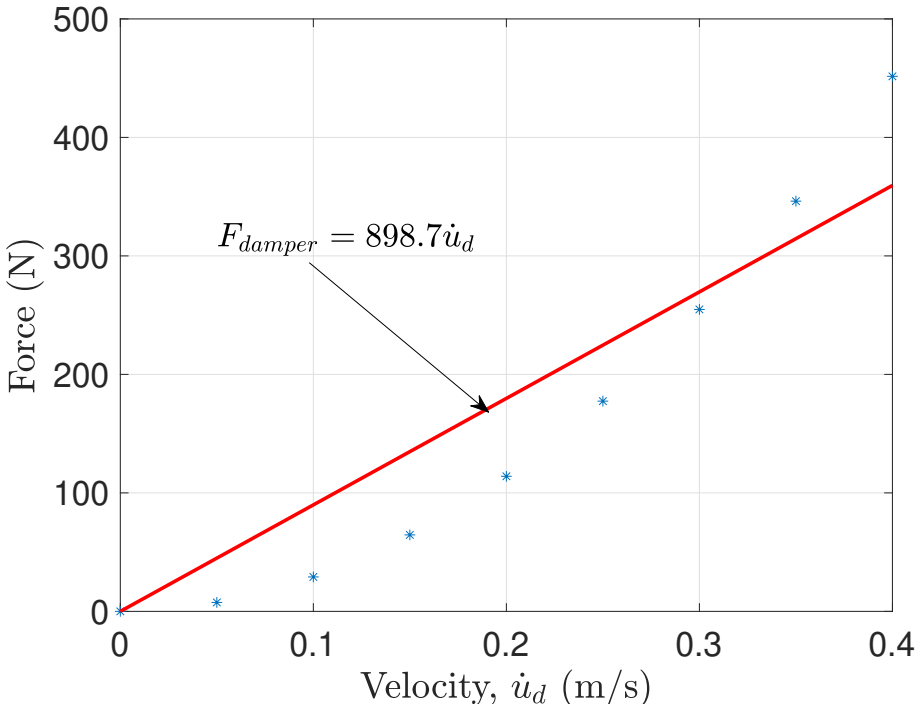

(b)

Figure 4.5: (a) The influence of changing L_t to damping and inertance values, and (b) Force versus velocity of the damper when $r_3 = 0.02m$, $r_d = 0.06m$, and $L_t = 0.6m$. Asterisk markers are the F_{damper} given by Equation 4.1

Note that in Equations 4.1 and 4.2 both inertance and damping are strongly influenced by the area of the helical channel A_1 and the channel length l. Thus, determine

Table 4.2: Fixed parameters

Property	Value	Units
Helix pitch, h	0.04	m
r_1	0.014	m
r_2	0.05	m
r_4	0.13	m
Oil density	802	kg/m^3

the design requirements, three parameters were studied: r_3, r_d, and L_t. The other parameters were fixed as given in Table 4.2.

Figure 4.4(a) show that, when both r_d and L_t are fixed to 0.06m and 0.6m, both inertance and damping parameters of the fluid inerter decrease as the helix radius increases. It should be noted that the damping force is nonlinear as is given in Equation 4.1, however for simplification, it was considered as linear as presented in Figure 4.5(b). It was found that when the radius of the helix is $0.02m$, both inertance and damping were close enough to the required values, which are 500kg and 0.83kNs/m given in Table 4.1.

Figures 4.4(b) and 4.5(a) show the influence of changing the r_d when r_3 and L_t are fixed to 0.02m and 0.6m, and the influence of changing the L_t when r_3 and r_d are fixed to 0.02m and 0.06m. It can be seen that both r_d and L_t are less sensitive to the changing of inertance and damping compared to r_3, as also can be seen in Figure 4.4(a).

It is finally found that parameters obtained in order to achieve the targeted parameters of b and c_d are : $r_3 = 0.02m$, $r_d = 0.06m$, and $L_t = 0.6m$. The final plot of force versus velocity relationship of the fluid inerter using the optimised parameters is given in Figure 4.5(b). It can be seen although the actual device is nonlinear, the linear approximation by the model is acceptable for a velocity range of maximum 0.4m/s.

4.2.2 Example 2: MDOF structure

As with the previous example, the helical fluid inerter here is designed and placed on each of the storeys of the MDOF structure via bracing. This concept is adopted from [14] for the design of tuned viscous mass damper (TVMD). Similarly, this concept also has been used for the design of a gyromass-viscous damper-brace (GVB) in [135]. The benefit of this concept is that the optimum stiffness of the system can be easily achieved through the design of the bracing system. The installation of the fluid inerter via bracing forms an analytical layout consisting of an inertance and a damping in parallel-connected to a spring in series. This layout is also called a parallel viscous inerter damper (PVID) [132].

Due to the similarity of the layout between TVMD and the PVID, the optimum parameters of the fluid inerter can be obtained by adopting the proposed simple design procedure given in [142] summarised as follows:

- choose the mass ratio, $\mu = B_b/M$, where M is the generalised modal mass for the undamped primary structure, and B_b is the effective modal mass of the inertance as described in [142]. In this study, the mass ratio of 0.1 was chosen.
- calculate the eigenvector ϕ_p of the characteristic equation of the primary structure (damping matrix is neglected)
- calculate the natural frequency of the first mode of the primary structure ω_{p1}
- calculate the inertance of the damper system at each storey by assuming that it is proportional to the stiffness of the primary structure at each storey,

$$b_i = \alpha k_i \tag{4.4}$$

  α is the constant ratio, given by

$$\alpha = \frac{\mu . {}_1\phi_p^T \mathbf{M}_{p1} \phi_p}{{}_1\phi_p^T \mathbf{K}_{p1} \phi_p} \tag{4.5}$$

- calculate the optimum natural frequency of the PVID system, given by

$$\omega_d^{opt} = \frac{1 - \sqrt{1 - 4\mu}}{2\mu} . {}_1\omega_p \tag{4.6}$$

- calculate the optimum stiffness of the damper system

$$k_{d,i} = (\omega_d^{opt})^2 . b_i \tag{4.7}$$

- calculate the optimum damping value of the damper system

$$c_{d,i} = 2\zeta_d^{opt} \omega_d^{opt} b_i \tag{4.8}$$

  where ζ_d^{opt} is the optimum damping ratio of the damper, given by [35]

$$\zeta_d^{opt} = \frac{\sqrt{3(1 - \sqrt{1 - 4\mu})}}{4} \tag{4.9}$$

In this example, a helical fluid inerter was designed for a 10-storey building studied in [142]. Here, the optimum design parameters of the TVMDs were obtained by following the steps above are used for the PVIDs with the fluid inerter, as given in Table 4.3.

Similar to the previous example, four parameters were varied in order to achieve the target damper characteristics on each storey. The varied parameters were the radius

Table 4.3: Optimum parameters of the PVID for 10-story building [142]

story	b_i [ton]	$k_{d,i}$ [kN/m]	c_d [kNs/m]
1	2147	74709	5207
2	2087	72643	5063
3	2002	69684	4857
4	1891	65809	4586
5	1752	60986	4250
6	1585	55171	3845
7	1388	48299	3366
8	1157	40254	2805
9	885	30814	2148
10	558	19407	1353

of the helix (r_3), space between the outer surface of the tube and the outer surface of the helical channel (r_d), which is $r_d = r_4 - (r_3 + r_2)$, and the length and radius of the tube (L_t and r_2).

In general, the design process is described as follows:

- Approximate the initial length of the tube. The helical channel is designed to turn around and along the length of the tube with helix pitch $h = 2r_3$ (no space in between the coils).
- Iterate r_3 and r_2. Both parameters have a significant effect on the inertance and damping as given in Equation 4.1 and 4.2.
- Increase r_d to reduce the required r_3 and r_2 from the previous step.
- The total length of the helical channel l is given by $2n\pi r_4$. n is number of turns in the helix, which is $n = L_t/2r_3$.

Based on the design process above, the helical fluid inerter dimensions were designed with the design inertance and damping parameters are close to the targeted optimized PVIDs parameters for each storey as shown in Figures 4.6(a) and 4.6(b).

The dimensions of the fluid inerters obtained from the design process are given in Table 4.4. It is obvious that the size of the fluid inerters is feasible for the considered structure. The size of the device is 1.5m length and 0.7-0.8m height for the first 8 storeys, and the length is reduced to 1.1 m for the top two. These sizes give the inertance and damping close to the targeted parameters as presented in Figure 4.6.

It should be noted that in the design process, the damping constant c_d is obtained based on linear regression of the nonlinear quadratic damping force resulting from Equation 4.1. As a result, the design is strongly influenced by the velocity range of the

Table 4.4: Design of the fluid inerter for 10-storey building

storey	$r_2[m]$	$r_3[m]$	$r_d[m]$	$r_4[m]$	$L_t[m]$	$D_h[m]$	$b[ton]$	$c_d[kNs/m]$
1	0.615	0.0930	0.10	0.8080	1.5	0.186	2121.10	5214
2	0.606	0.0920	0.10	0.7980	1.5	0.184	2039.92	5033
3	0.601	0.0915	0.10	0.7925	1.5	0.183	1992.08	4918
4	0.580	0.0890	0.10	0.7690	1.5	0.178	1821.81	4557
5	0.568	0.0875	0.10	0.7555	1.5	0.175	1732.27	4374
6	0.551	0.0863	0.10	0.7373	1.5	0.172	1560.22	3885
7	0.530	0.0846	0.10	0.7146	1.5	0.169	1373.92	3379
8	0.500	0.0820	0.10	0.6820	1.5	0.164	1140.34	2726
9	0.524	0.0855	0.07	0.6795	1.1	0.171	886.61	2129
10	0.443	0.0760	0.07	0.5890	1.1	0.152	558.62	1382

damper. However, despite of this limitation, it is obvious that the fluid inerter can be designed to fit the targeted parameters obtained from the optimisation processes.

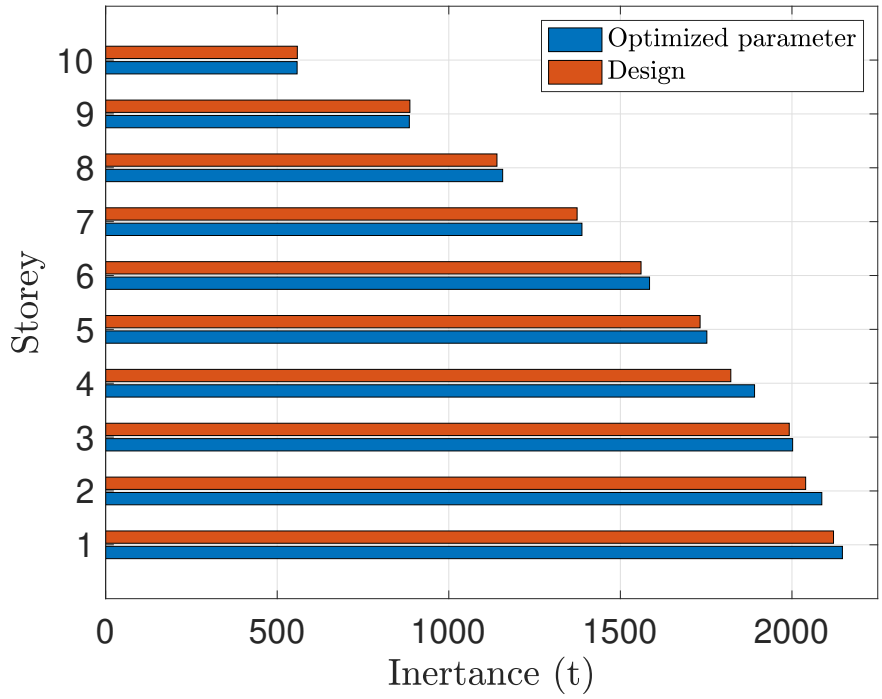

(a)

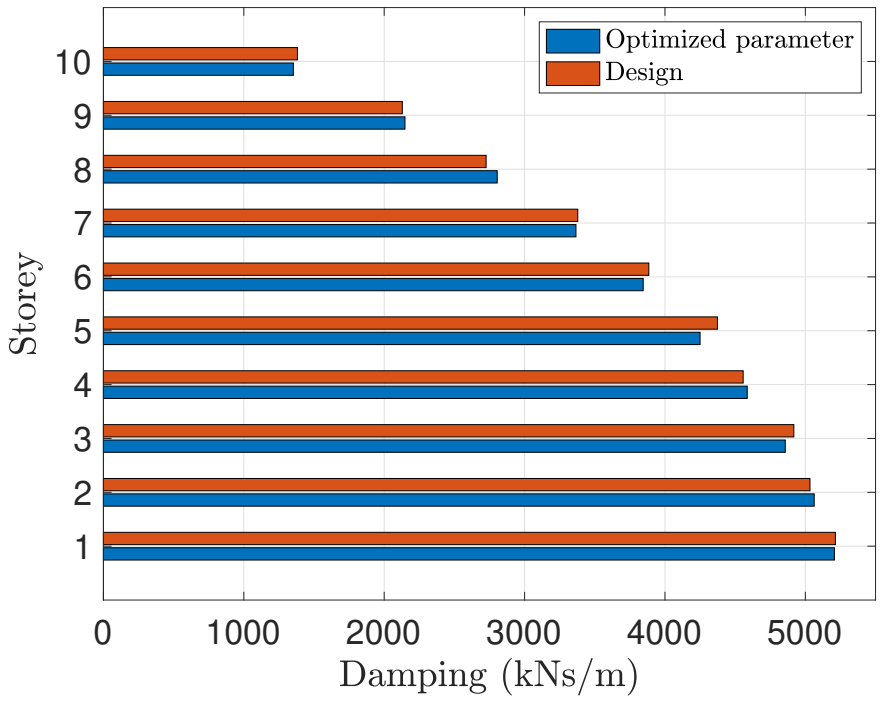

(b)

Figure 4.6: Optimized parameters versus design parameters (a) inertance (b) damping

4.2.3 Example 3: Nonlinear helical fluid inerter

In this example, the damping force of the helical fluid inerter was considered as nonlinear as given in [49]. The schematic figure is given in Figure 4.7. The inerter was optimised for use in a multi-storey structure. The targeted optimised inertance and nonlinear damping coefficient parameters were obtained from [49], which are $b = 452380kg$ and ${c_p}^{NL} = 737760^{1.75} Ns/m$. The proposed design approach was implemented here to achieve the helical fluid inerter dimensions such that both inertance and damping parameters were as close as possible to the targeted values. Two parameters were selected as free variables: r_2 and r_3 as they were found to be the most sensitive to the changing of b and ${c_p}^{NL}$ values. The other parameters were fixed to reasonable values given in Table 4.5.

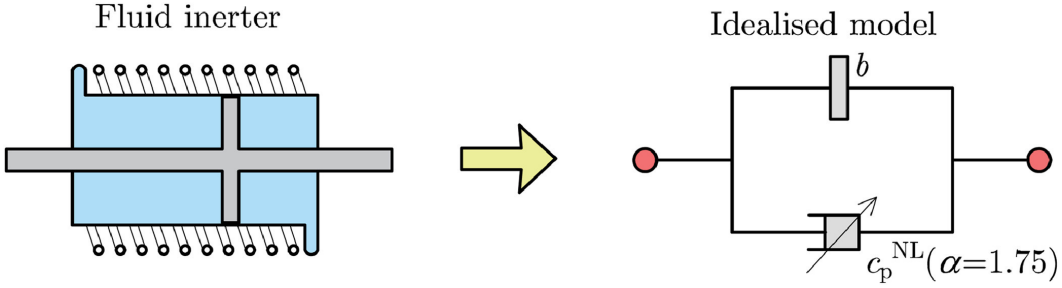

Figure 4.7: Simplified model of nonlinear helical fluid inerter

Table 4.5: Fixed parameters of the helical fluid inerter

Property	Value	Units
r_1	0.1	m
r_d	0.06	m
L	1.0	m
Oil density	1000	kg/m^3
μ_f	0.001	Pa s

Figures 4.8(a) and 4.8(b) show how both r_2 and r_3 parameters can significantly affect the system performance. These two parameters are directly related to the dimensions of the fluid inerter device –inner radius of the cylinder and inner radius of the helical channel. It can be seen that $r_2 = 0.357$ intersects at line $r_3 = 0.05$ for the given optimum band ${c_p}^{NL}$ values in both graphs. The actual b and ${c_p}^{NL}$ values given from the actual dimensions of the fluid inerter are $457,689$kg and $730,234^1.75$ Ns/m.

Figure 4.9 compares the force-vs-velocity relationship between the design and actual values of the fluid inerter. Both total force (F_{total}) and damping force ($F_{d-helix}$) from the actual fluid inerter are very close to the design specifications with the percentage of errors around 1%.

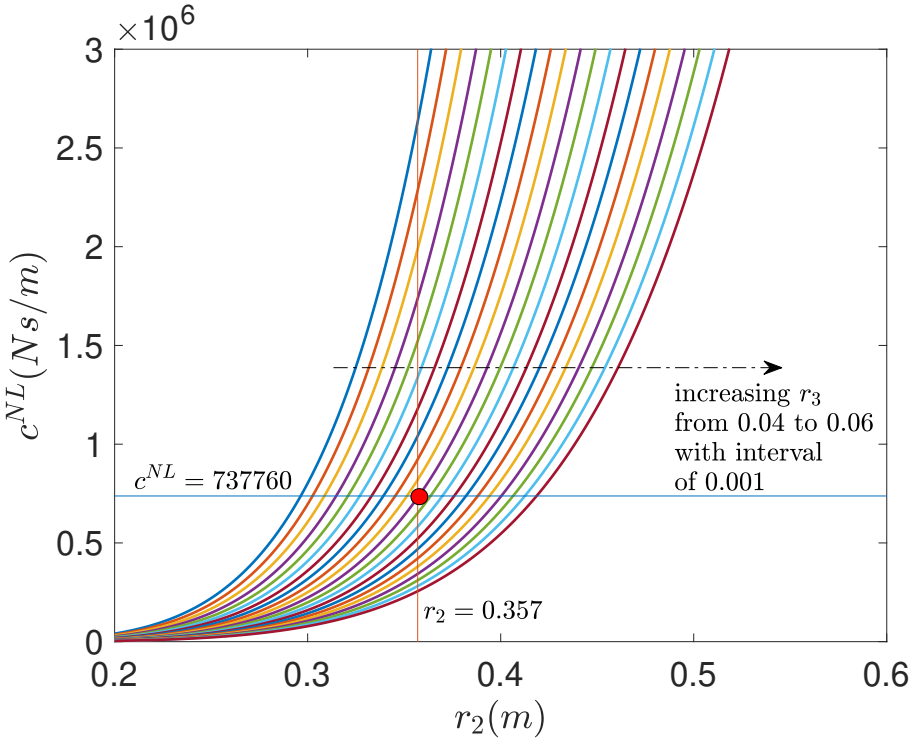

(a)

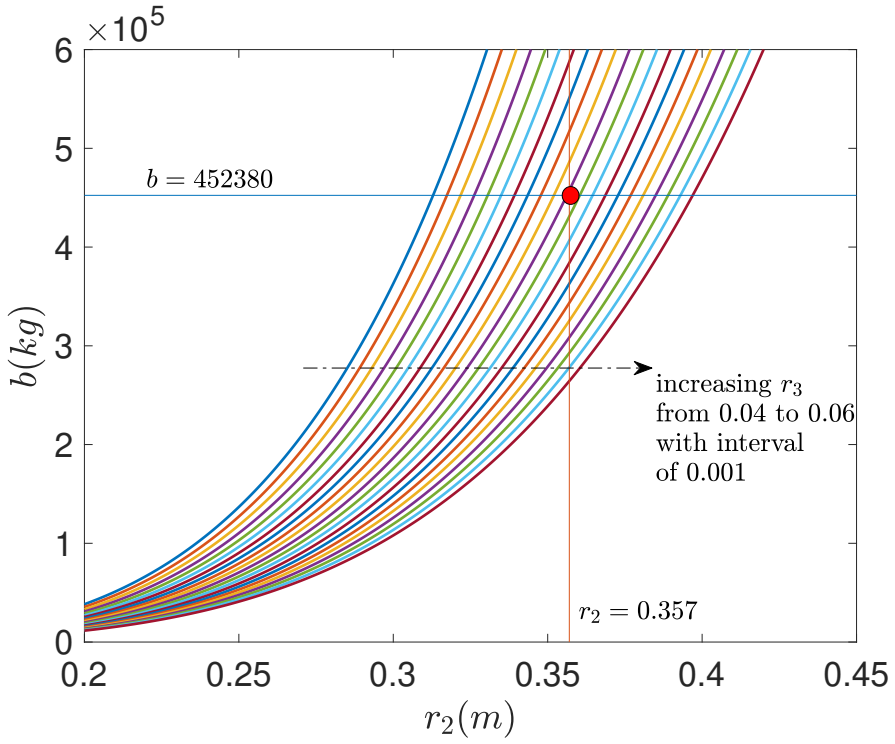

(b)

Figure 4.8: Design parameters identification via parametric approach: (a) nonlinear damping coefficient vs r_2 for a family of r_3 curves; (b) inertance vs r_2 for a family of r_3 curves. b and r_3 are in kg and m, respectively.

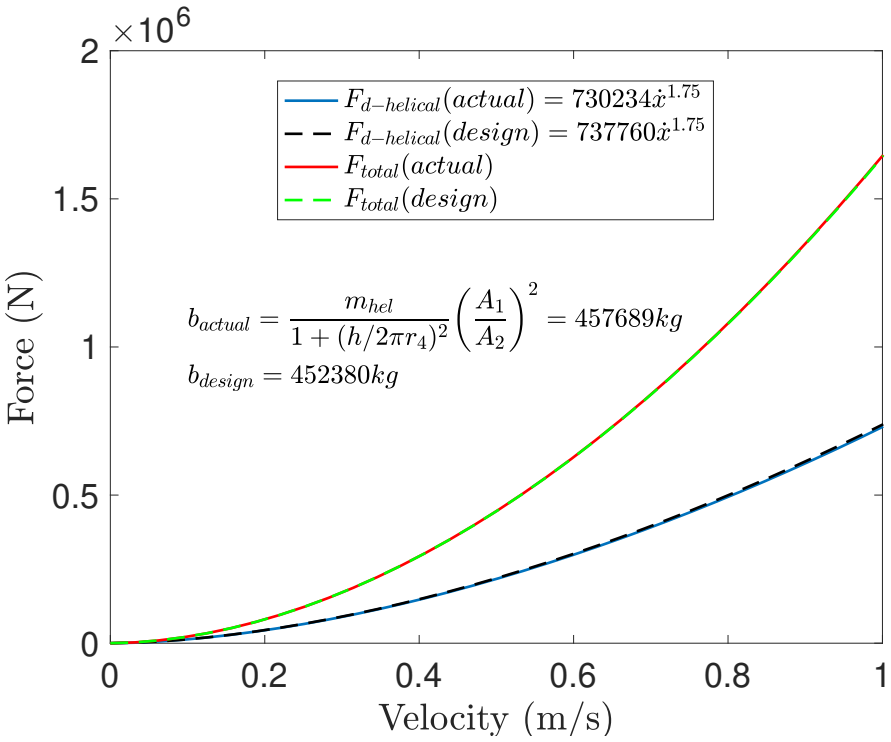

Figure 4.9: Force vs velocity curve for the fluid inerter with the design parameters compared to the optimal (target) parameters.

4.3 Summary

In this chapter, the feasibility of the fluid inerter to build a PVID was discussed. The fluid inerter has both inertance and damping in parallel. For this reason, it can be used to build a PVID by adding one spring in series.

One of the challanges of the helical fluid inerter design is that its damping and inerter parameters are coupled. Therefore, it is difficult to design both inertance and damping separately. In this chapter, a new design approach is proposed to simplify the design of a helical fluid inerter for use as a PVID. The design approach relies on the fact that the damping and inertance are insensitive to changes in some parameters. Consequently, these parameters can be chosen based on practical design considerations, so that the number of unknown parameters can be reduced.

Three examples have been presented, for both SDOF and MDOF building structures, and also in a nonlinear helical fluid inerter. The results show that the the helical fluid inerter can be accurately and practically designed to achieve the targeted inerter and damping parameters for all the three examples of different cases. An article from this thesis has also been published based on these results, see [143] and [49].

Despite of the successful implementation of the design method, the nonlinear effects such as friction and fluid compressibility, see [49], are beyond the scope of this thesis. Therefore, they are not chosen for the next stages of this thesis because they might

be difficult to use to achieve the objectives set in Chapter 1, especially for shake table experiments. It is decided that this will remain as an open discussion for the future work.

Chapter 5

Tuned-Inerter-Based-Dampers with Complex Stiffness

5.1 Introduction

In this chapter, a novel concept of using linear hysteretic damping represented by a complex stiffness in passive tuned-inerter-devices is proposed. Specifically, two devices are introduced namely the tuned-inerter-hysteretic-damper (TIhD) and the tuned-mass-hysteretic-damper-inerter (TMhDI). These two devices were designed based on the well established existing concepts of tuned-inerter-damper (TID) and tuned-mass-damper-inerter (TMDI).

In this study, the parallel connected stiffness and viscous damping element in the inerter dampers are replaced by a linear hysteretic damping element which has coupled stiffness and loss factor. The rationale is that, as discussed in detail in Section 3.3, the realisation technique based on this form of damping model is considered to be more realistic. It has been reported to accurately capture the real physical behaviour of a range of damper elements [144] and has been widely used in practice [97].

It is well known that viscous damping can be directly related to the loss factor of an equivalent hysteretic damping element using the well established analysis based on equivalent viscous damping, see Section 3.3 . However, it is shown analytically that this process underestimates the response amplitudes at the higher modes of vibration of multi-degree-of-freedom structures due to the frequency-dependency associated with the viscous damping element. This has also been addressed and discussed in Section 3.3 for the case of HTMD.

Furthermore, results showing the optimum performance comparison of the devices in suppressing an n-degree-of-freedom structure highlight the differences in performance that would be expected compared to a viscous damping model. Specifically the regions of the frequency domain where significant differences are obtained between the two damping models for harmonic and selected earthquake inputs. In addition, the non-

causality associated with the hysteretic damping is solved in the time domain by using the method discussed in Section 3.3 involving the time reversal technique and the Hilbert transform that is now extended to work with multi-degree-of-freedom systems.

5.2 Analytical Modelling

In order to assess the tuned-inerter-damper devices and their effect on the structural performance, a generalised model of a n-DOF lumped mass system is used as a benchmark system as shown in Figure 5.1(a). The structure is separated into three parts: bottom storey, $i = 1$; middle storeys, i^{th}, where $i \in [2 : n-1]$; and top storey, $i = n$. The structural performance was examined and compared for each of the inertial damper systems in Figure 5.1(b)-(e) when placed at the bottom story level.

The TID is one of the first established concepts of inerter dampers and therefore it is used here as a benchmark. The TID is considered to be an idealized concept where a pure inerter is attached to a parallel-connected spring-damper system in series. If a mass element is present between the inerter and the spring-damper system, then it is called a TMDI. It is considered to be more realistic than the TID because the physical mass of the inerter element can be included to represent the mass of the device itself although in most cases this is very small compared to the inertance. Two inerter-damper systems are introduced in this chapter, namely the TIhD and TMhDI. Each of them is studied to gain insight into the effect of hysteretic damping.

The equations of motion of the n-DOF structure as shown in Figure 5.1 in absolute coordinates can be written as

$$\begin{cases} (m_1 s^2 + k_{0,1} + k_{1,2})X_1 = k_{1,2}X_2 + k_{0,1}R + F_{1,0} \\ \vdots \\ (m_i s^2 + k_{i-1,i} + k_{i,i+1})X_i = k_{i-1,i}X_{i-1} + k_{i,i+1}X_{i+1} \\ \vdots \\ (m_n s^2 + k_{n-1,n})X_n = k_{n-1,n}X_{n-1} \end{cases} \tag{5.1}$$

where m_i and $k_{i-1,i}$, $i \in [1 : n]$ represent the mass and stiffness between storeys $i-1$ and i; X_i represents the Laplace transform of the ith storey displacement, when $i = 0$, then $X_0 = R$ which represents the Laplace transform of the base displacement; s represents the Laplace transform variable and $F_{1,0}$ represents the force transferred to the structure by the inerter damper systems in the Laplace domain.

The next two sections will discuss both the TIhD and TMhDI separately in detail. In particular, the discussion will specifically assess the effect of the linear hysteretic damping in the inerter-damper systems.

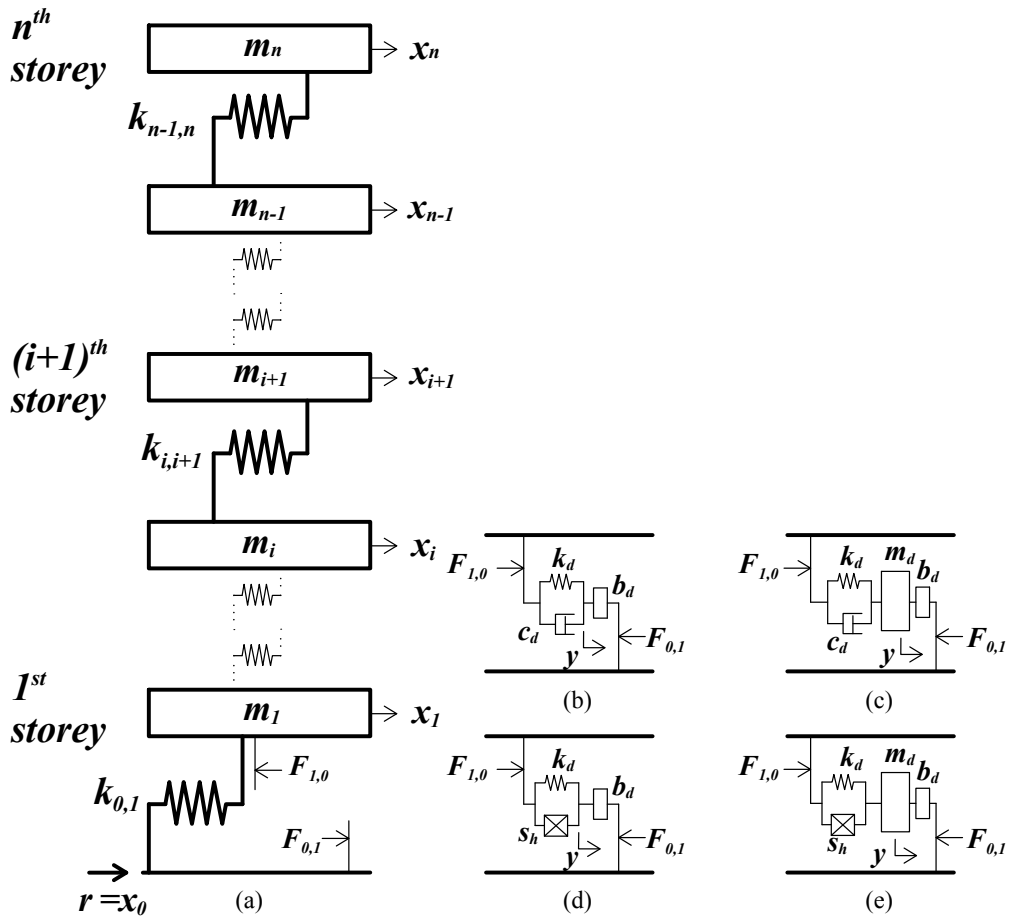

Figure 5.1: (a) n-DOF structure (b) TID (c) TMDI (d) TIhD (e) TMhDI

5.3 TIhD (Tuned-Inerter-hysteretic-Damper)

As previously mentioned, the TID is one of the first established concepts of inerter-damper systems. It consists of an inerter in series connection with a parallel-connected spring-damper system. In this section, the linear hysteretic damping represented by a complex stiffness is proposed to replace the parallel-connected spring-damper system. The device with this layout now is called the TIhD. This concept is motivated by the fact that often material dampers are employed in civil engineering applications. The energy dissipated per cycle by material dampers can be assumed frequency independent [54] if viscoelasticity is insignificant. For this reason, the parallel-connected spring-viscous damping model cannot accurately predict the real behaviour of the dampers due to the frequency depedency of the viscous damping element. Therefore, a complex stiffness is proposed here to represent the material damper.

In this section the TIhD is studied and compared to the TID. Here it is assumed that the mass of the inerter device is neglected.

5.3.1 Force Transferred To The Host Structure

The equation of motion of the TIhD as shown in Figure 5.1(d) can be written in the Laplace domain as

$$b_d s^2(R - Y) = k_d(1 + j\eta)(Y - X_1) \tag{5.2}$$

where b_d, k_d and η are the device inertance, stiffness and hysteretic damping loss factor respectively and $j = \sqrt{-1}$. Hence

$$Y = \frac{b_d s^2 R + k_d(1 + j\eta)X_1}{b_d s^2 + kd(1 + j\eta)} \tag{5.3}$$

The force transferred to the structure by the TIhD is

$$F_{1,0} = k_d(1 + j\eta)(Y - X_1) \tag{5.4}$$

Substituting Equation 5.3 into Equation 5.4 leads to

$$F_{1,0} = \frac{b_d s^2(k_d(1 + j\eta))}{b_d s^2 + k_d(1 + j\eta)}(R - X_1) \tag{5.5}$$

To illustrate the Equation 5.5, a 3-DOF structure adopted from [145] is assessed when equipped with a TIhD. Figure 5.3.1 shows the comparison between the force transferred by the TID and by the TIhD. Here, the parameters of the TID are: b_d=21kg; k_d=22kN/m; and c_d=356.87Ns/m, and the parameters of the TIhD are: b_d=21kg; k_d=22kN/m; and η=0.53. As can be seen in this Figure, the force transferred to the structure by the TIhD is larger than that of TID in the second and the third modes. This is due to the fact that the energy dissipated by the linear hysteretic damper is frequency indepedent.

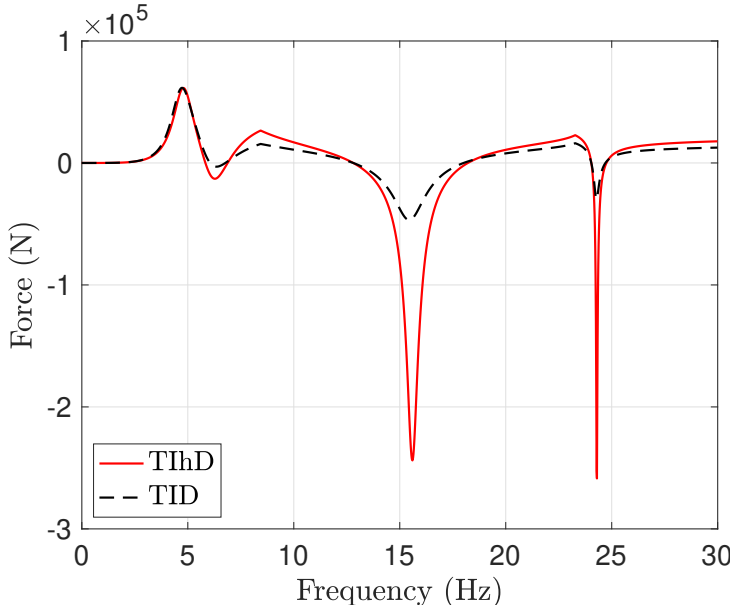

Figure 5.2: Force transferred to the structure by the TID and the TIhD

5.3.2 Optimum Tuning Procedure

The optimum tuning procedure derived in this section is based on the fixed-point-theory by Den Hartog [38] proposed for a TMD. This theory says that for an undamped structure, regardless of the choice of TMD stiffness and damping parameters, all displacement response curves in the frequency response diagram pass through two fixed points, P and Q. These two points are then made equal by selecting an optimum stiffness value of the TMD. For a TID applied to a SDOF structure, Hu et al [146] proposed an algebraic solution to analytically determine the frequencies where these two equal-in-amplitude points occur. For the TIhD, this algebraic solution is adapted in this section by simply replacing the viscous damping ratio with a loss factor of the linear hysteretic damping.

Considering a TIhD from Figure 5.1(d) is attached to a 1-DOF structure as shown in Figure 5.1(a) for $n = 1$. The transfer function X/R can be derived analytically and written in the frequency domain as

$$\left|\left(\frac{X}{R}\right)\right| = \sqrt{\frac{[(1-\mu q^2)-\lambda\mu q^2]^2 + [\eta(1-\mu q^2)]^2}{[(1-(1+\mu)q^2)-\mu\lambda q^2(1-q^2)]^2 + [\eta(1-(1+\mu)q^2)]^2}} \tag{5.6}$$

where η is the loss factor of the hysteretic damping, $\mu = b_d/m_1$ is the inertance-to-mass ratio, $q = \omega/\omega_n$ is the frequency ratio, $\lambda = k_{0,1}/k_d$ is the stiffness ratio, ω is the forcing frequency (assuming a sine wave input) and $\omega_n = \sqrt{k_{0,1}/m_1}$.

The approximate optimum parameters of the TIhD can be analytically obtained based on fixed-point theory via an algebraic solution. This technique has been derived by Hu *et al.* [42] for the TID optimisation. Following the same procedure, and by replacing the viscous damping ratio ζ with the loss factor η, one obtains the η optimum for the TIhD as

$$\eta_{opt} = \sqrt{\frac{\eta_P^2 + \eta_Q^2}{2}} \tag{5.7}$$

η_P and η_Q are given by

$$\eta_{P.Q}^2 = \frac{A - BCD}{E} \tag{5.8}$$

where

$A = (2\mu(1-(1+\mu)q_{P.Q}^2)^2(\mu q_{P.Q}^2(\lambda_{opt}+1)-1)(\lambda_{opt}+1))$

$B = (2(1-\mu q_{P.Q}^2)^2$

$C = ((1-(1+\mu)q_{P.Q}^2 - \lambda_{opt}\mu q_{P.Q}^2(1-q_{P.Q}^2))$

$D = (\lambda_{opt}\mu q_{P.Q}^2 - \lambda_{opt}\mu(1-q_{P.Q}^2) - \mu - 1)$

$E = (2\mu(1-(1+\mu)q_{P.Q}^2)^2(1-\mu q_{P.Q}^2)) - (2(1-\mu q_{P.Q}^2)^2(1+\mu)(1-(1+\mu)q_{P.Q}^2))$

The frequency ratio at the first two fixed-points P and Q are the solution of the

following equation

$$q^4 - \left(\frac{2}{\lambda_{opt}\mu}(1 + \lambda_{opt} + \mu + \lambda_{opt}\mu) - q_R^2\right)q^2 + \frac{2}{\mu^2\lambda_{opt}q_R^2} = 0. \tag{5.9}$$

The optimum stiffness ratio (λ_{opt}) can be obtained by using either

$$\lambda_{opt} = \frac{2(1 + \mu q_R^4(1 + \mu) - q_R^2(1 + 2\mu))}{\mu q_R^4(\mu q_R^4 - 2q_R^2(1 + \mu) + 2)} \tag{5.10}$$

or

$$\lambda_{opt} = \frac{2(q_R^2(3\mu + 2\mu^2 + 1) - 2(1 + \mu))}{q_R^2(\mu q_R^2(1 + 2\mu) - 2(1 + 2\mu + 2\mu^2))} \tag{5.11}$$

where q_R is the frequency ratio at the third fixed-point R given by

$$q_R^2 = \frac{3}{2} + \frac{1}{\mu} + \sqrt{\left(\frac{3}{2} + \frac{1}{\mu}\right)^2 - \frac{2}{\mu}}. \tag{5.12}$$

This fixed-point R was firstly identified by Lazar *et.al.* [37] for the TID. The fixed-point R is the third fixed-points in addition to the fixed-point P and Q located away from the resonance frequency as shown in Figure 5.3. It should be noted that in Figure 5.3(a), the ζ_P, ζ_Q and ζ_{opt} lines are plotted using ζ_P, ζ_Q and ζ_{opt} values obtained from the optimisation process based on Hu *et al.* [42]. While for η_P, η_Q and η_{opt} lines in Figure 5.3(b) are plotted using η_P, η_Q and η_{opt} values obtained from Equation 5.8 and 5.7, respectively.

Figure 5.3(a) and 5.3(b) show the difference between the optimised TID and TIhD using fixed-point theory. It can be seen that for viscous damping, Figure 5.3(a), the underlying peaks of ζ_P and ζ_Q are quite low in amplitude and therefore the peaks of the combined optimal curve are very close to the fixed points P and Q. However, in the hysteretic damping case, Figure 5.3(b), the underlying peaks of η_P and η_Q are now quite high in amplitude and therefore the peaks of the combined optimal curve are much further away from the fixed points P and Q. It is therefore suggested that the optimised TIhD will require a further fine tuning process to make both peaks closer to equal amplitude.

In this example, μ is increased from 0.3 to 0.9 to obviously see the effect of the mass ratio as shown in Figure 5.4. When μ is increased, a potential benefit in the high frequency region can be seen from the TIhD compared to the TID although the level of response amplitude around resonance is quite similar. The TID shows a higher amplification due to the increase of μ, while on the other hand the TIhD shows very small amplification. This is in line with what has been discussed in Chapter 3.3 where a structure with complex stiffness has a lower amplification of response in the high frequency region. This is interesting to note, because this is the reason why a complex damping should be treated as its original form both in the frequency and time domain analyses. Although an equivalent viscous damping [138] is often used, but it fails

to accurately predict the real behaviour of a linear hysteretic damping in the high frequency region, particularly when the mass ratio is large.

Table 5.1 is presented to summarise the optimum ζ and η of both devices obtained via the process above. As previously mentioned, equivalent viscous damping is often used to obtain an approximation for the response of a hysteretically damped system. However this kind of approximation will not persist after the optimisation process. In this case, the equivalent viscous damping relationship $\eta = 2\zeta$ given in [138] cannot be used for the TIhD. The approximate relationship can instead be expressed as $\eta = 2\lambda\zeta$. It should be noted that this expression does not give the exact optimum solution — a point that was also noted by Wong [107] for the HDVA system. Therefore it is important to derive the optimum η of the TIhD separately from the derivation of ζ of the TID.

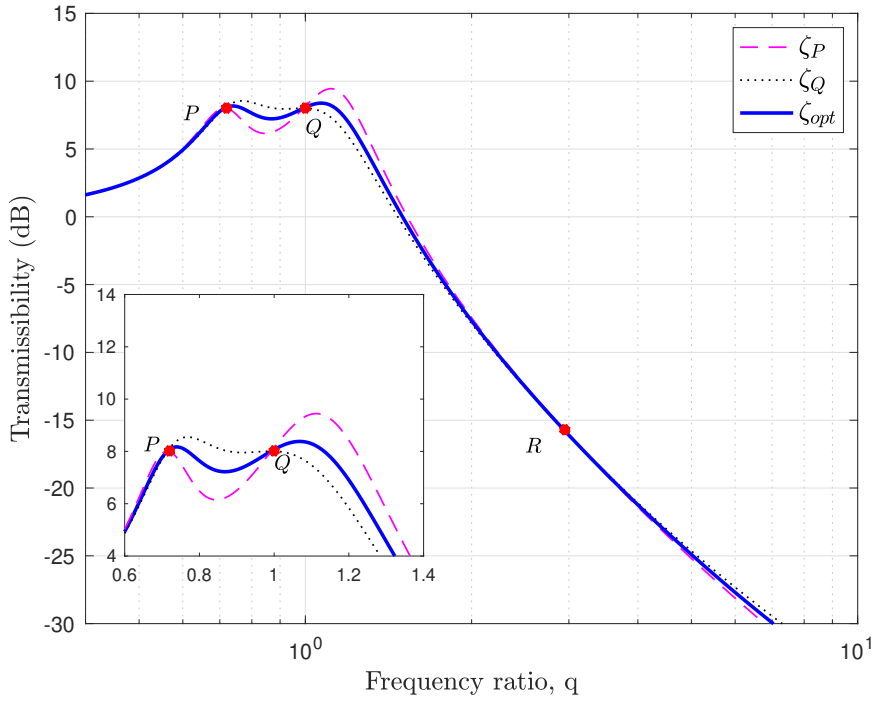

(a)

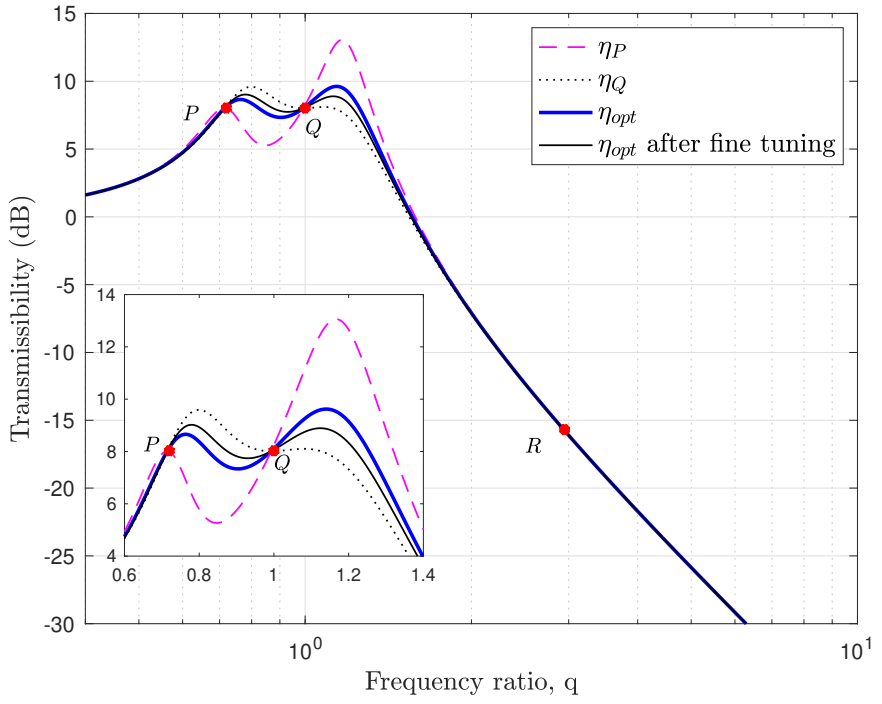

(b)

Figure 5.3: Optimisation process for 1-DOF structure equipped with (a) TID (b) TIhD. Here $\mu = 0.3$.

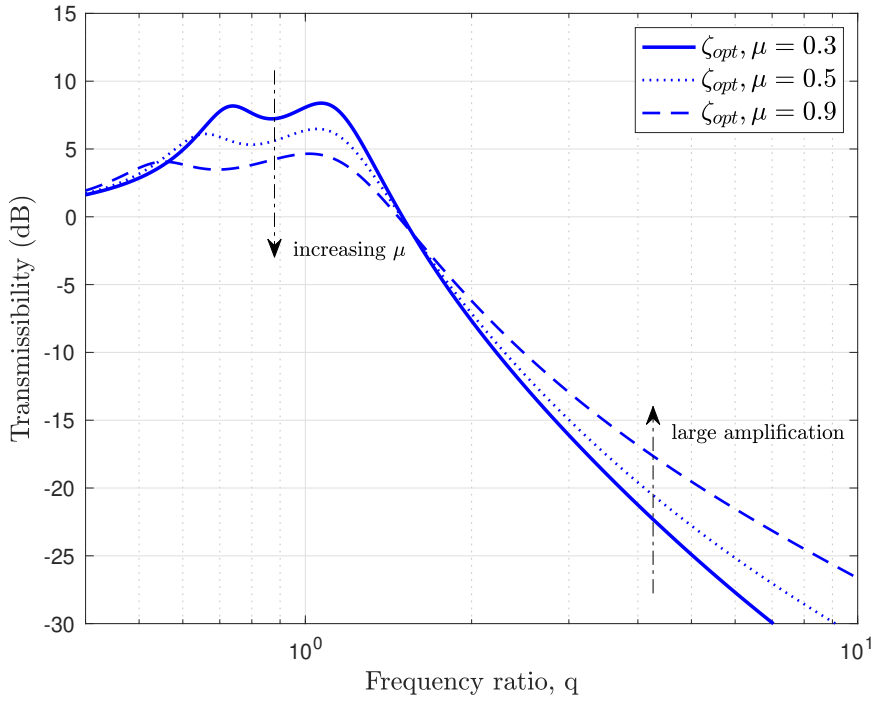

(a)

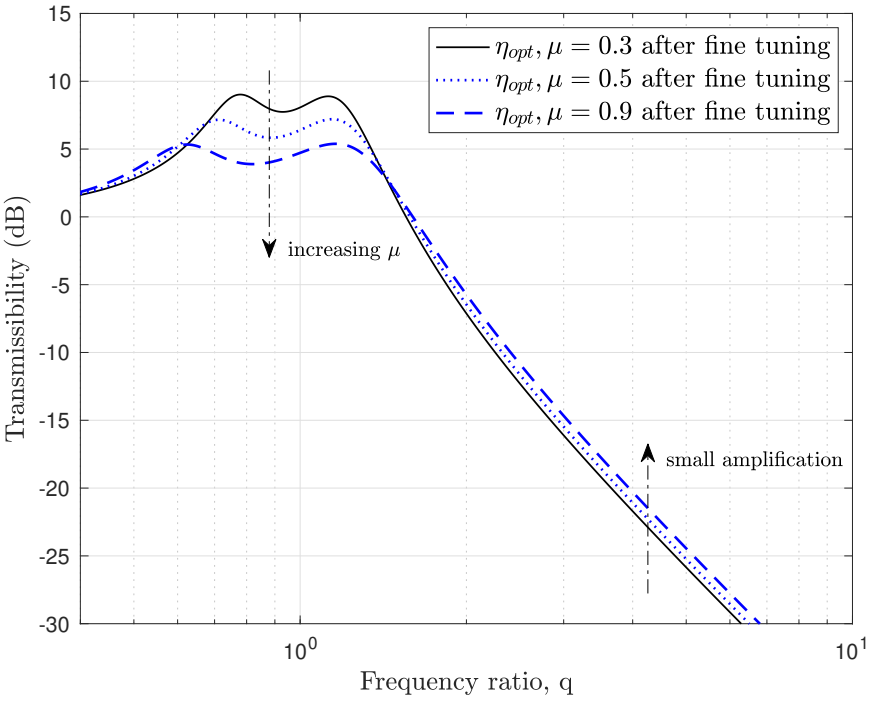

(b)

Figure 5.4: Transmissibility of a 1-DOF structure equipped with (a) TID (b) TIhD for various μ.

The optimum tuning procedure derived for a TIhD in this Section, which is based on the fixed-point theory via algebraic solution proposed in [42], shows that the optimum tuning procedure for a TID can be used to approximate the optimum parameters of the

Table 5.1: Optimum damping ratio and loss factor of the inerter dampers

μ	ζ_{opt} of the TID	η_{opt} of the TIhD
0.3	0.0713	0.71
0.5	0.1264	0.92
0.9	0.2221	1.26

TIhD in SDOF structures. It is simply just replacing the viscous damping ratio of the TID with a loss factor of the TIhD. Another approach based on the fixed-point theory for the TID is derived by Lazar et al. [37] where they show how the TID optimum tuning can be approximated by the TMD tuning procedure by Den Hartog [38]. The optimum tuning of the TIhD for MDOF system can also be approximated by the TID optimum tuning proposed in [37]. As in the case of SDOF structure discussed in this section, a fine tuning is also required to make the two peaks equal in the frequency response amplitude.

5.3.3 Time domain analysis

Here in this section, the performance of a structure with a TIhD is analyzed in the time domain. Due to the presence of linear hysteretic damping, a standard numerical integration method cannot be used to solve the structure in this domain. Therefore, the newly developed method discussed in the Section 3.3.2 is adopted.

Considering a three storey structure with a TIhD in the ground floor as shown in Figure 5.1(a) where $n = 3$, $m_1 = m_2 = m_3 = 1$ tonne and $k_{0,1} = k_{1,2} = k_{2,3} =$ 1500kN/m, the governing equation of motion of the considered strucure in the absolute coordinate can be written using analytic functions as follows:

$$\begin{cases} m_1\ddot{x}_{1_a}(t) + k_{0,1}(x_{1_a}(t) - r_a(t)) + k_d(1+j\eta)(y_a(t) - r_a(t)) - k_{1,2}(x_{2_a}(t) - x_{1_a}(t)) = 0 \\ m_2\ddot{x}_{2_a}(t) + k_{1,2}(x_{2_a}(t) - x_{1_a}(t)) - k_{2,3}(x_{3_a}(t) - x_{2_a}(t)) = 0 \\ m_3\ddot{x}_{3_a}(t) + k_{2,3}(x_{3_a}(t) - x_{2_a}(t)) = 0 \\ \ddot{y}_a(t) = \ddot{x}_{1_a}(t) - \dfrac{k_d}{b_d}(y_a(t) - r_a(t)) \end{cases} \tag{5.13}$$

where m_i and $x_i(t)$ represent the mass concentrated on the i^{th} storey and its displacement response. Subscription $_a$ denotes an analytic signal which is a pair of real and imaginary components. The imaginary component of the analytic signal $x_{ia}(t)$ is given by the Hilbert transform of the real signal $x_i(t)$, such that $x_ia(t) = x_i(t) + jH[x_i(t)]$, where $H[x_i(t)]$ is the Hilbert transform of $x_i(t)$. $k_{i-1,i}$ and $s_{h_{i-1,i}}$, $i \in [1:n]$ represent the stiffness and a parameter with unit of stiffness characterising the damping between storeys $i-1$ and i; $\eta_{i-1,i}$ is the loss factor of the linear hysteretic damping between storey $i-1$ and i, given by $\eta_{i-1,i} = \frac{s_{h_{i-1,i}}}{k_{i-1,i}}$; $r(t)$ represents ground displacement input signal; subscript a denotes an analytic signal; and $j = \sqrt{-1}$. In state-space

formulation, Equation 5.13 can be expressed as:

$$\dot{\mathbf{x}}_a(t) = \mathbf{A}\mathbf{x}_a(t) + \mathbf{B}r_a(t) \tag{5.14}$$

where

$$\mathbf{x}_a(t) = \begin{bmatrix} x_{1_a}(t) \\ \dot{x}_{1_a}(t) \\ x_{2_a}(t) \\ \dot{x}_{2_a}(t) \\ x_{3_a}(t) \\ \dot{x}_{3_a}(t) \\ y_a(t) \\ \dot{y}_a(t) \end{bmatrix} \quad ; \quad \mathbf{A} = \begin{bmatrix} 0 & 1 & 0 & 0 & 0 & 0 & 0 & 0 \\ \frac{-k_{0,1}-k_{1,2}}{m_1} & 0 & \frac{k_{1,2}}{m_1} & 0 & 0 & 0 & \frac{-k_d}{m_1}(1+j\eta) & 0 \\ 0 & 0 & 0 & 1 & 0 & 0 & 0 & 0 \\ \frac{k_{1,2}}{m_2} & 0 & \frac{-k_{1,2}-k_{2,3}}{m_2} & 0 & \frac{k_{2,3}}{m_2} & 0 & 0 & 0 \\ 0 & 0 & 0 & 0 & 0 & 1 & 0 & 0 \\ 0 & 0 & \frac{k_{2,3}}{m_3} & 0 & \frac{-k_{2,3}}{m_3} & 0 & 0 & 0 \\ 0 & 0 & 0 & 0 & 0 & 0 & 0 & 1 \\ \frac{-k_{0,1}-k_{1,2}}{m_1} & 0 & \frac{k_{1,2}}{m_1} & 0 & 0 & 0 & \frac{k_d(m_1-b_d)}{m_1 b_d}(1+j\eta) & 0 \end{bmatrix} \tag{5.15}$$

and

$$\mathbf{B} = \begin{bmatrix} 0 \\ \frac{k_{0,1}}{m_1} + \frac{k_d}{m_1}(1+j\eta) \\ 0 \\ 0 \\ 0 \\ 0 \\ 0 \\ \frac{k_{0,1}}{m_1} + \frac{k_d(m_1-b_d)}{m_1 b_d}(1+j\eta) \end{bmatrix}$$

The next steps follow the Equations 3.18 to 3.24 in Chapter 3.3.2. The MATLAB code for this example can be found in Appendix D. Some plots obtained by using this method will be presented in Chapter 5.5.

5.4 TMhDI (Tuned-Mass-hysteretic-Damper-Inerter)

As previously mentioned, the TMDI is considered to be a more realistic model for the TID. The same logic also applies for the TMhDI as a realistic model of the TIhD. Since the TMhDI has a mass element between the hysteretic damper and the inerter. The layout of the TMhDI is very similar to that of TMDI with the viscous damping element replaced by a loss factor of a linear hysteretic damping as shown in Figure 5.1(e).

5.4.1 Force Transferred To The Host Structure

The equation of motion of the TMhDI as shown in Figure 5.1(e) can be written in the Laplace domain as

$$m_d s^2 Y + b_d s^2 (Y - X_1) = k_d(1+j\eta)(R - Y) \tag{5.16}$$

where m_d is the mass element of the TMhDI. Hence

$$Y = \frac{b_d s^2 X_1 + k_d(1 + j\eta)R}{(m_d + b_d)s^2 + kd(1 + j\eta)} \tag{5.17}$$

The force transferred to the structure by the TMhDI is

$$F_{1,0} = b_d s^2 (Y - X_1) \tag{5.18}$$

Substituting Equation 5.17 into Equation 5.18 leads to

$$F_{1,0} = \frac{b_d s^2 k_d(1 + j\eta)(R - X_1) - b_d s^2 m_d s^2 X_1}{(m_d + b_d)s^2 + k_d(1 + j\eta)} \tag{5.19}$$

It can be seen from Equation 5.19 that when $m_d = 0$ the Equation 5.19 becomes the same as Equation 5.5 since the layout of the TMhDI becomes the same as the layout of the TIhD.

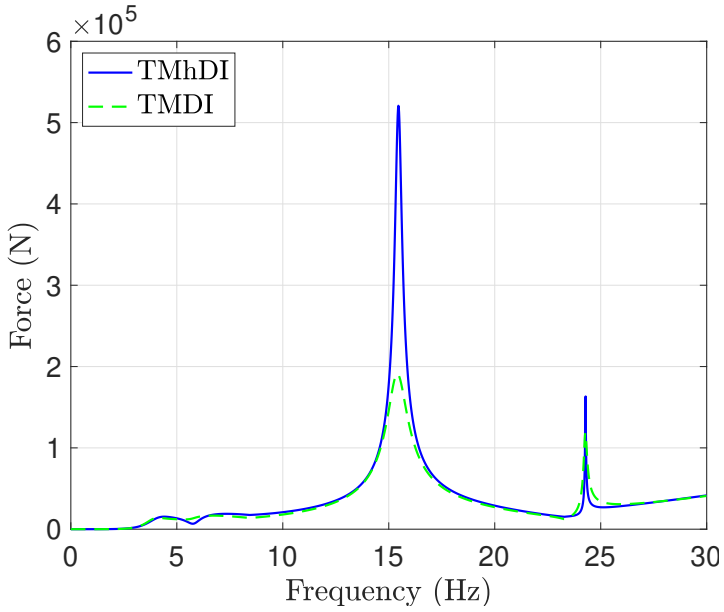

Figure 5.5: Force transferred to the structure by the TMDI and the TMhDI

To illustrate Equation 5.19, a 3-DOF structure adopted from [145] is assessed when equipped with a TMhDI. Figure 5.5 shows the comparison between the force transferred by the TMDI and by the TMhDI. Similar to the previous case between the TID and the TIhD, as can be seen in Figure 5.5 the force transferred to the structure by the TMhDI is larger than that of TMDI in the second and the third modes due to the frequency indepedency of the linear hysteretic damping. Here the TMDI and TMhDi parameters are the same with the TID and the TIhD parameters discussed earlier in Section 5.3 with an auxiliary mass m_d=10kg.

5.4.2 Optimum Placement

It is well known that the optimal location for a TMD is at the top of a MDOF structure, and that the TID is optimum at the base of the structure [37]. Here the optimum location for the TMDI is derived assuming the secondary mass m_d is small, which is in this case 5% of the inertance b_d. Later, the same logic is applied to the optimum location of the TMhDI. The passive control forces in the Laplace domain can be written as follows when a TMDI is mounted at the i^{th} storey level of the considered structure in Figure 5.1(a).

$$F_{i,i+1} = b_d s^2 (X_{i+1} - Y) \tag{5.20a}$$

$$F_{i+1,i} = (c_d s + k_d)(Y - X_i) \tag{5.20b}$$

where X_i represents the Laplace transform of the displacement of mass m_i, and b_d is the inertance. The equation of motion for the y-DOF TMDI system can be written as

$$Y = \frac{b_d s^2 X_{i+1} + (c_d s + k_d) X_i}{(m_d + b_d)s^2 + c_d s + kd} \tag{5.21}$$

Substituting Equation 5.21 into Equation 5.20a gives

$$F_{i,i+1} = \frac{(b_d s^2 m_d s^2) X_{i+1} + b_d s^2 (c_d s + k_d)(X_{i+1} - X_i)}{(m_d + b_d)s^2 + c_d s + kd} \tag{5.22a}$$

$$F_{i+1,i} = F_{i,i+1} = T_m X_{i+1} + T_d (X_{i+1} - X_i) \tag{5.22b}$$

where

$$T_d = \frac{b_d s^2 (c_d s + k_d)}{(m_d + b_d)s^2 + c_d s + k_d} \quad \text{and} \tag{5.23a}$$

$$T_m = \frac{b_d s^2 m_d s^2}{(m_d + b_d)s^2 + c_d s + k_d}. \tag{5.23b}$$

Now the optimum placement of the TMDI in a n-DOF structure (as shown in Figure 5.1) is discussed. In matrix form, the equation of motion of the system can be written as

$$\mathbf{M}s^2 + \mathbf{K}Z = -\mathbf{M} \begin{bmatrix} 1 \\ 1 \\ \vdots \\ 1 \\ 1 \end{bmatrix} s^2 R + \begin{bmatrix} F_{1,0} - F_{1,2} \\ F_{2,1} - F_{2,3} \\ \vdots \\ F_{n-1,n-2} - F_{n-1,n} \\ F_{n,n-1} \end{bmatrix} \tag{5.24}$$

where $\mathbf{M}$ and $\mathbf{K}$ are the mass and stiffness matrices, $Z = X_i - R$ represents the vector of relative storey displacement. The above equation can also be written in form of

modal matrices

$$\mathcal{M}s^2 + \mathcal{K}Z = -\Phi^T\mathbf{M}\begin{bmatrix}1\\1\\\vdots\\1\\1\end{bmatrix} s^2R + \Phi^T\begin{bmatrix}F_{1,0} - F_{1,2}\\F_{2,1} - F_{2,3}\\\vdots\\F_{n-1,n-2} - F_{n-1,n}\\F_{n,n-1}\end{bmatrix} \tag{5.25}$$

where Φ is the eigenvector matrix, $\mathcal{M} = \Phi^T\mathbf{M}\Phi$ and $\mathcal{K} = \Phi^T\mathbf{K}\Phi$ are the modal mass and stiffness matrices, respectively.

Now, consider the cases where the TMDI is mounted at either the bottom or top storey level. Assuming that only the first vibration mode is significant, the following transfer functions can be obtained

TMDI at bottom storey level

$$\frac{Q_1}{R} = \frac{-\sum_{i=1}^{n}(m_1\Phi_{i,1})s^2 + \Phi_{1,1}T_m}{m_{m_1}s^2 + k_{m_1} + T_d\Phi_{1,1}^2} \tag{5.26}$$

TMDI at top storey level

$$\frac{Q_1}{R} = \frac{-\sum_{i=1}^{n}(m_1\Phi_{i,1})s^2 + (\Phi_{n,1} - \Phi_{n-1,1})T_m}{m_{m_1}s^2 + k_{m_1} + T_d(\Phi_{n-1,1} - \Phi_{n,1})^2 - T_m\Phi_{n-1,1}(\Phi_{n,1} - \Phi_{n-1,1})} \tag{5.27}$$

It is obvious that when the mass element of the TMDI is small or close to zero, the above equations will be identical to the TID transfer functions given in Lazar *et al.* [37].

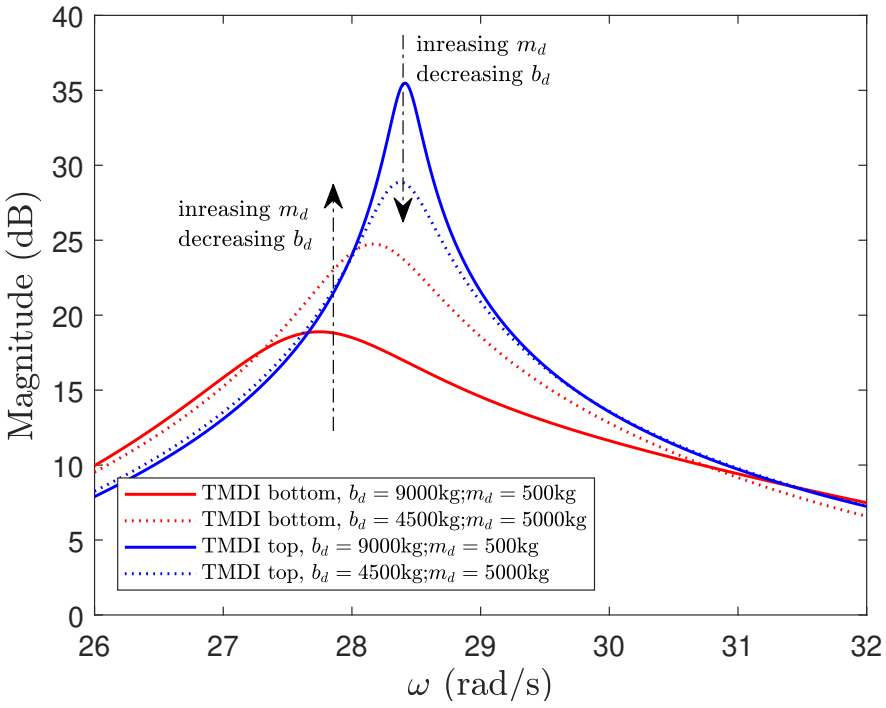

(a)

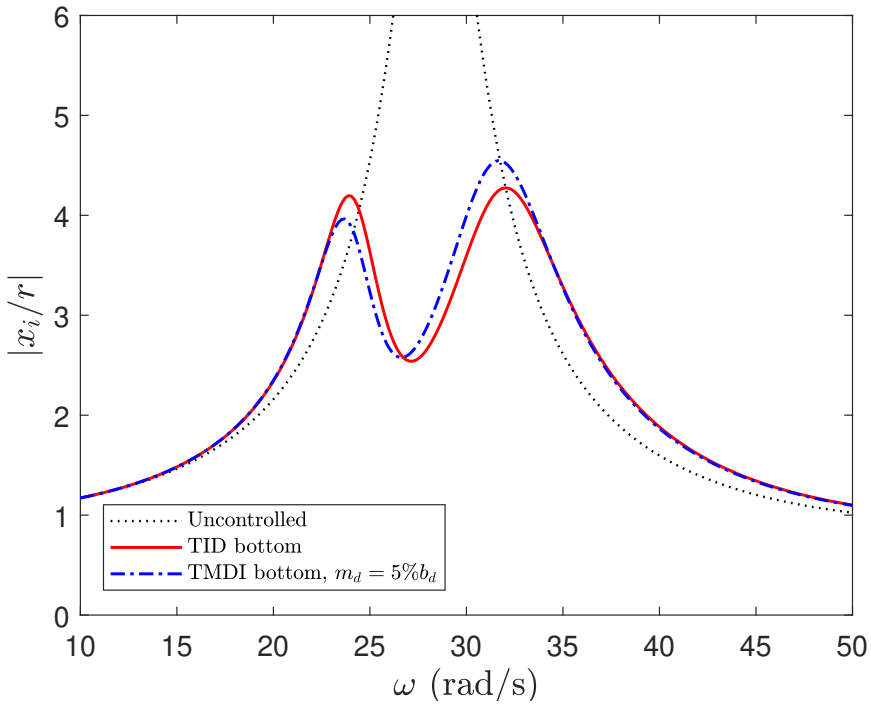

(b)

Figure 5.6: (a) The effect of increasing m_d to the TMDI optimum location (b) Frequency response function (1^{st} mode) when $m_d = 5\%b_d$, $\mu = 0.62$.

Figure 5.6(a) shows how the optimum location of the TMDI changes between top and bottom story level by increasing m_d and decreasing b_d at the same time using Equation 5.26 and 5.27. It can be seen that increasing m_d will make the TMDI at the

bottom story less effective. Conversely, decreasing m_d makes its performance better when placed on the bottom story. This aligns with the assumption of making the m_d only 5% of the device inertance, to represent the mass of the inerter device.

Furthermore, Figures 5.3(a), 5.3(b) have already demonstrated that the tuning procedure of the TID can be used for estimating the optimum parameters of the TIhD. Therefore, it is also applied to the TMDI and TMhDI assuming the m_d is only 5% of the inertance, as can be seen in Figure 5.6. However, as previously noted additional fine tuning is required to get the actual optimum values for these three systems, and this is also the case for MDOF systems.

5.4.3 Optimum Tuning Procedure

TMhDI is basically a TIhD with a small secondary mass element m_d between the inerter b_d and the complex-stiffness element as illustrated in Figure 5.1(d). The TMhDI model can potentially be used to represent an even more realistic device than the TIhD device. This is because it has both secondary mass element m_d and loss factor η of material damping. In this analysis the inertance is designed to be dominant, where m_d is assumed to be just 5% of the inertance to represent the mass of the inertial device. Therefore, the tuning of the TMhDI follows the TIhD tuning rule based on fixed point analysis presented in the previous subsection.

Figure 5.7 shows the performance comparison in the frequency domain between the four considered inertial damper systems in an SDOF structure subjected to harmonic base displacement. Although the response at low frequencies are close for all four devices, it is clear from Figure 5.7(a) that the devices with hysteretic damping give significantly lower amplitude responses at higher frequencies. In this higher frequency range, the hysteretic damping also changes the phase angle as can be seen in Figure 5.7(b).

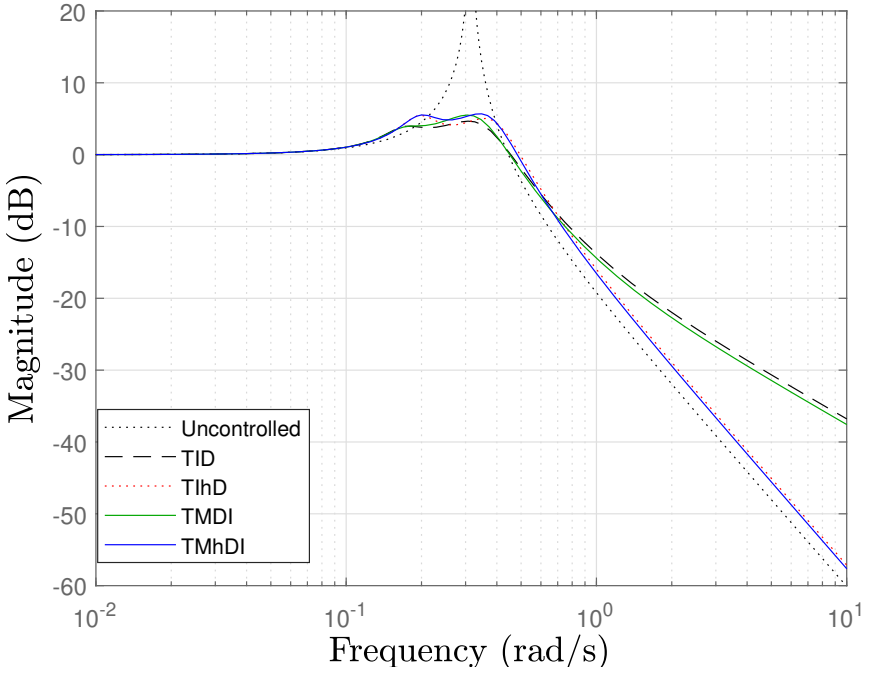

(a)

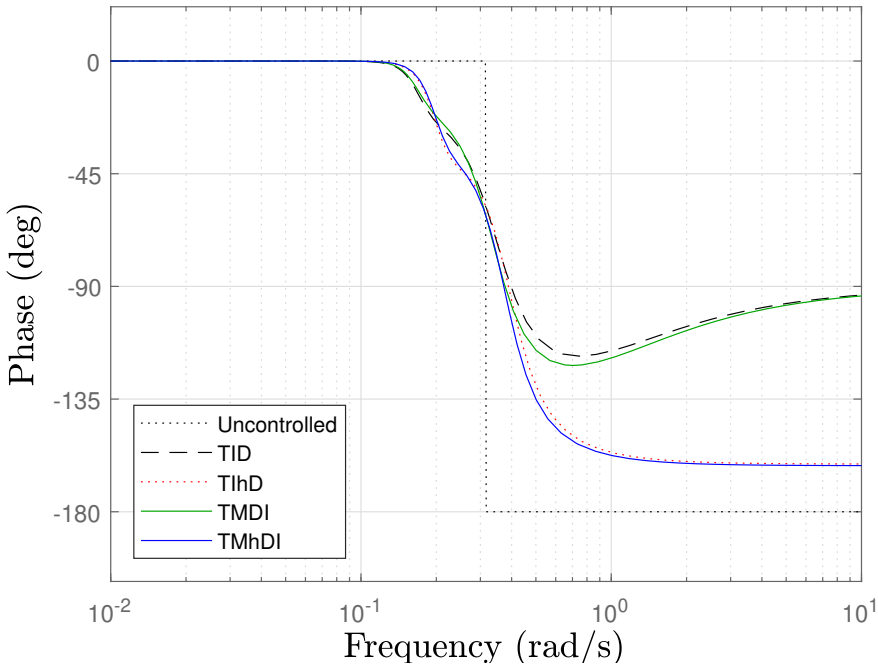

(b)

Figure 5.7: (a) Frequency response of a 1-DOF structure with optimised inertial damper systems (b) Phase angle , $\mu = 0.9$ and $m_d = 5\%b_d$. High μ was chosen to clearly see the difference between the structural response with hysteretic and viscous damping above the resonance frequency.

5.4.4 The effect of the grounded inerter

In this section, the effect of grounded and non-grounded inerter within the TMhDI is explored. As previously mentioned, the TMDI is considered to be a more realistic model for the TID. The same logic also applies for the TMhDI as a realistic model of the TIhD. In the case of TIhD, the force transferred to the primary structure when the inerter is attached to the primary mass of the structure can be expressed by

$$f_{t_{TIhD}} = b_d(\ddot{y} - \ddot{x}_1) \tag{5.28}$$

The Equation 5.29 below is also valid when the inerter is attached to the ground (grounded),

$$f_{t_{TIhD}} = k_d(1 + j\eta)(r - y) \tag{5.29}$$

where

$$b_d(\ddot{y} - \ddot{x}_1) = k_d(1 + j\eta)(r - y) \tag{5.30}$$

Here r is the ground displacement, y and x_1 are the displacement of the TIhD and the structural mass, respectively.

Unlike the TIhD, the force transferred by the TMhDI to the primary structure is different when the inerter is grounded and when it is not, since the TMhDI has a mass element between the hysteretic damper and the inerter. The difference between both cases are depicted in Figure 5.8.

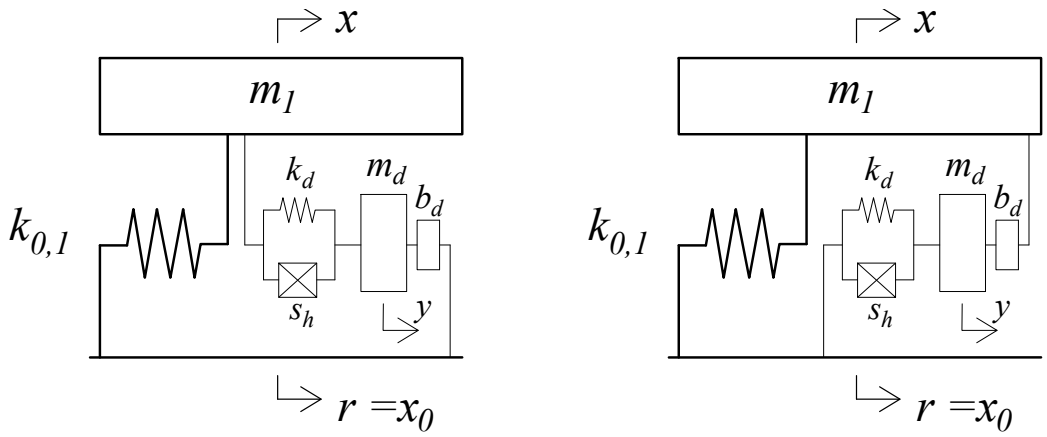

(a) (b)

Figure 5.8: SDOF structure equipped with a TMhDI with (a) grounded inerter, and (b) nongrounded inerter

In the case where the inerter is attached to the primary structure, the force is expressed by

$$f_{t_{TMhDI}} = b_d(\ddot{y} - \ddot{x}_1) \tag{5.31}$$

However, this Equation 5.32 is not valid when the inerter is attached to the ground (grounded), which is expressed by

$$f_{t_{TMhDI}} = k_d(1 + j\eta)(r - y) \tag{5.32}$$

where

$$b_d(\ddot{y} - \ddot{x}_1) \neq k_d(1 + j\eta)(r - y) \tag{5.33}$$

In the case of nongrounded inerter, the force transferred by the TMhDI to the structure is given by Equation 5.19. For comparison, in the case of grounded inerter, the equation of motion of the TMhDI system is given by

$$b_d(\ddot{y} - \ddot{x}_1) = m_d\ddot{y} + k_d(1 + j\eta)(r - y) \tag{5.34}$$

in the Laplace domain, this Equation can be written as

$$((m_d + b_d)s^2 + k_d(1 + j\eta))Y = b_d s^2 R + k_d(1 + j\eta)X_1 \tag{5.35}$$

hence we obtain

$$Y = \frac{b_d s^2 R + kd(1 + j\eta)X_1}{(m_d + b_d)s^2 + k_d(1 + j\eta)} \tag{5.36}$$

The force transferred by the TMhDI to the structure in the Laplace domain can be written as

$$F_{1,0} = kd(1 + j\eta)(Y - X_1) \tag{5.37}$$

Substituting Equation 5.36 into Equation 5.37 we obtain

$$F_{1,0} = \frac{k_d(1 + j\eta)b_d s^2 R - (m_d + b_d)s^2(kd(1 + j\eta))X_1}{(m_d + b_d)s^2 + kd(1 + j\eta)} \tag{5.38}$$

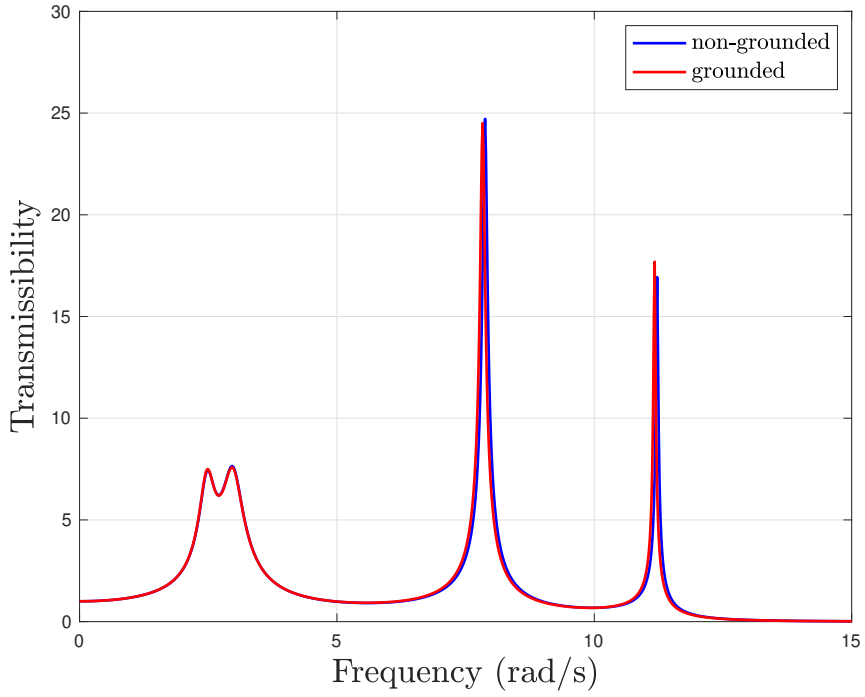

(a)

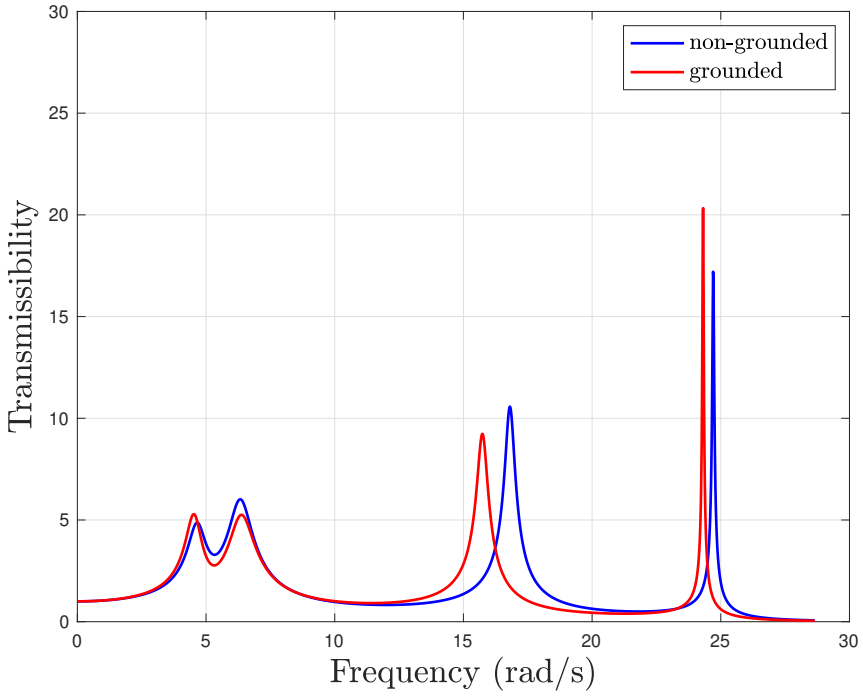

(b)

Figure 5.9: 3-DOF structure with TMhDI in case of inerter is grounded and non-grounded (a) uniform structure (b) non-uniform structure

As can be seen from Equation 5.19 and 5.38 the force transferred by the TMhDI system to the structure is different when the inerter is grounded and non-grounded.

Figure 5.9 shows how the grounded inerter affected performance of two different

structures. Here two 3-storey structures from [37] and [145] are used for examples. The parameters of the first structure are: $m_1 = m_2 = m_3 = 1$ tonne, and $k_{0,1} = k_{1,2} = k_{2,3} = 1500$kN/m, and for the second structure are: $m_1 = 33.15$kg, $m_2 = m_3 = 24.15$kg, and $k_{0,1} = 140.48$kN/m, $k_{1,2} = 168.58$kg, $k_{2,3} = 207.92$kN/m.

Figure 5.9(a) is the case for the first 3-storey structure from [37] with uniformaly distributed mass and stiffness on each floor (mass and stiffness for each floor are all the same). In another case, Figure 5.9(b) shows the effect of the grounded inerter on the second structure which is a non-uniform structure (mass and stiffness for each floor are different) taken from [145]. From these figures, it can be concluded that there is almost no difference between grounded and nongrounded inerter if the mass and stiffness of the host structure is uniformaly distributed on each floor. However, the grounded inerter shows a slightly better performance when the structural mass and stiffness parameters are not uniform, particularly around the first and second resonances. This is very important to note because commonly in the structural analysis, the structure is assumed to be a lumped mass system, meaning the structural mass and stiffness parameters are assumed to be uniformaly distributed on each floor. However, in the reality, this is not the case.

Based on these results, it is suggested that when a TMhDI is employed, the inerter element must always be directly connected to the ground. However, it is important to note that this conclusion is only based on these two specific considered structures. Future study is required in order to make a more general and universal conclusion.

5.4.5 Time domain analysis

In this section, the performance of structure with a TMhDI is analyzed in the time domain. Similar to the TIhD, due to the presence of linear hysteretic damping, a standard numerical integration method cannot be used to solve the structure in the time domain. Therefore, the newly developed method discussed in the Chapter 3.3.2 is adopted.

Considering a three storey structure as shown in Figure 5.1(a) with a TMhDI in the ground floor where $n = 3$, $m_1 = m_2 = m_3 = 1$ tonne and $k_{0,1} = k_{1,2} = k_{2,3} = 1500$kN/m, the govering equation of motion of the considered strucure in the absolute coordinate system can be written using analytic functions as follows:

$$\begin{cases} m_1\ddot{x}_{1_a}(t) + b_d(\ddot{x}_{1_a}(t) - \ddot{y}_a(t)) + k_{0,1}(x_{1_a}(t) - r_a(t)) - k_{1,2}(x_{2_a}(t) - x_{1_a}(t)) = 0 \\ m_2\ddot{x}_{2_a}(t) + k_{1,2}(x_{2_a}(t) - x_{1_a}(t)) - k_{2,3}(x_{3_a}(t) - x_{2_a}(t)) = 0 \\ m_3\ddot{x}_{3_a}(t) + k_{2,3}(x_{3_a}(t) - x_{2_a}(t)) = 0 \\ m_d\ddot{y}_a(t) + kd(1 + j\eta) - b_d(\ddot{x}_{1_a}(t) - \ddot{y}_a(t)) = 0 \end{cases} \tag{5.39}$$

In state-space formulation, Equation 5.39 can be expressed as:

$$\dot{\mathbf{x}}_a(t) = \mathbf{A}\mathbf{x}_a(t) + \mathbf{B}r_a(t) \tag{5.40}$$

where

$$\mathbf{x}_a(t) = \begin{bmatrix} x_{1_a}(t) \\ \dot{x}_{1_a}(t) \\ x_{2_a}(t) \\ \dot{x}_{2_a}(t) \\ x_{3_a}(t) \\ \dot{x}_{3_a}(t) \\ y_a(t) \\ \dot{y}_a(t) \end{bmatrix} \quad ; \quad \mathbf{A} = \begin{bmatrix} 0 & 1 & 0 & 0 & 0 & 0 & 0 & 0 \\ \frac{(k_{0,1}+k_{1,2})(m_d+b_d)}{\Gamma} & 0 & \frac{-k_{1,2}(m_d+b_d)}{\Gamma} & 0 & 0 & 0 & \frac{(b_d k_d)+(j b_d s_h)}{\Gamma} & 0 \\ 0 & 0 & 0 & 1 & 0 & 0 & 0 & 0 \\ \frac{k_{1,2}}{m_2} & 0 & \frac{-k_{1,2}-k_{2,3}}{m_2} & 0 & \frac{k_{2,3}}{m_2} & 0 & 0 & 0 \\ 0 & 0 & 0 & 0 & 0 & 1 & 0 & 0 \\ 0 & 0 & \frac{k_{2,3}}{m_3} & 0 & \frac{-k_{2,3}}{m_3} & 0 & 0 & 0 \\ 0 & 0 & 0 & 0 & 0 & 0 & 0 & 1 \\ \frac{-k_{1,2}b_d-k_{0,1}b_d}{\Upsilon} & 0 & \frac{k_{1,2}b_d}{\Upsilon} & 0 & 0 & 0 & \frac{-k_d(m_1+b_d)-j s_h(m_1+b_d)}{\Upsilon} & 0 \end{bmatrix} \tag{5.41}$$

and

$$\mathbf{B} = \begin{bmatrix} 0 \\ \frac{-k_{0,1}(m_d+b_d)-b_d k_d - j s_h b_d}{\Gamma} \\ 0 \\ 0 \\ 0 \\ 0 \\ 0 \\ \frac{k_{0,1}b_d+k_d(m_1+b_d)+j s_h(m_1+b_d)}{\Upsilon} \end{bmatrix}$$

where $\Gamma = b_d^2 - (m_1 + bd)(m_d + b_d)$ and $\Upsilon = -\Gamma = (m - 1 + b_d)(m_d + b_d) - b_d^2$.

Next steps follow the Equations 3.18 to 3.24 in Section 3.3.2. The MATLAB code for this example can be found in Appendix E. Some plots obtained by using this method will be presented in Section 5.5.

5.5 Example: Performance Comparison

5.5.1 Harmonic Excitations

An undamped SDOF structure as shown in Figure 5.1 (a) for $n = 1$, mass m and stiffness $k_{0,1}$ set to 1 tonne and 0.0987kN/m respectively was used in this example. Figure 5.10(a) shows the performance comparison between the four inerter-based damper systems applied to an SDOF structure. Their optimised parameters are given in Table 5.2. It can be seen from this figure that the performance of the TID and the TMDI is similar. This can be understood because the effect of m_d which is only 5% of the inertance is small across the frequencies. However, the TMDI has slightly higher response around the resonant frequency after the optimisation. Its time domain response

is given in Figure 5.11(a) and 5.11(b) obtained by using the method presented in the previous Section. A similar result also can be seen for the TIhD compared to the TMhDI which indicates that the effect of m_d is very small.

Although the response amplitude around the resonant frequency is slightly higher with the hysteretic damping, it has a potential benefit in the higher frequency region as previously discussed. The attenuation difference between TID/TMDI and TIhD/TMhDI in the high frequency region is 20dB/dec respectively. In civil engineering applications, especially for low frequency structures such as base-isolated structures, this is a valuable benefit because the response around the resonance frequency needs to be reduced to deal with long-period earthquakes, while at the same time also maintaining lower response at the higher frequency region.

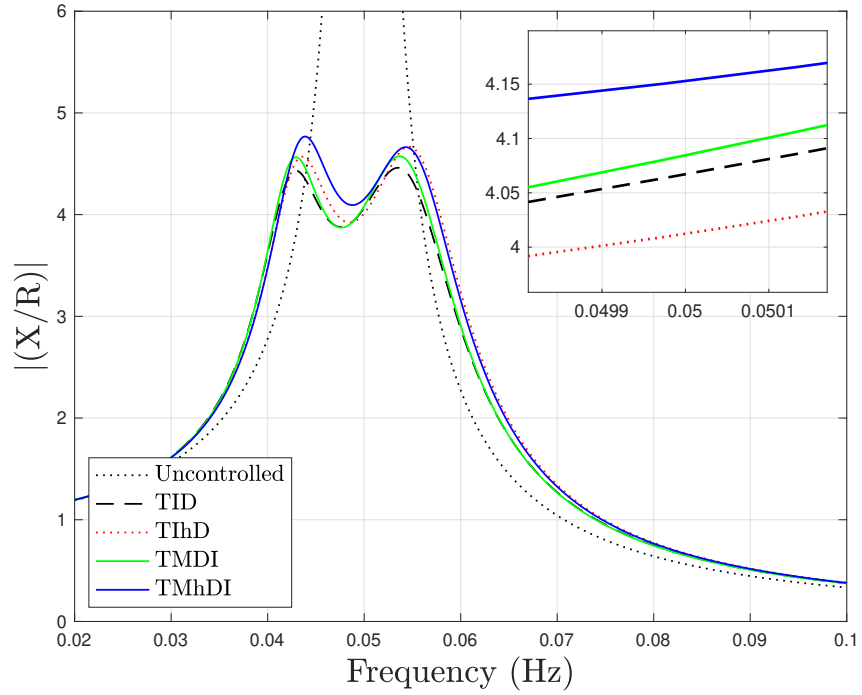

(a)

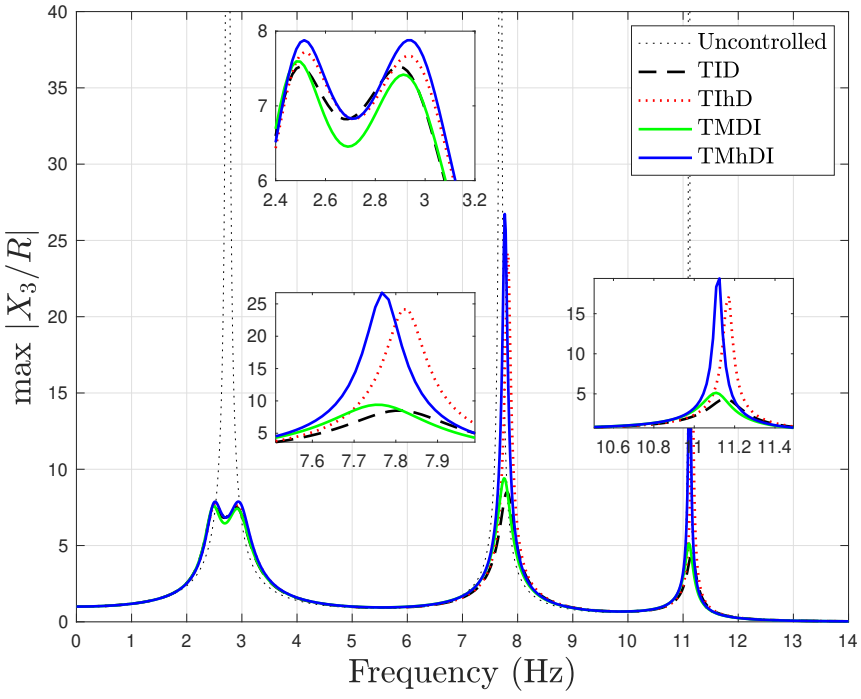

(b)

Figure 5.10: Transmissibility of (a) SDOF structure, $\mu = 0.1$ (b) 3-DOF structure, $\mu = 0.18$

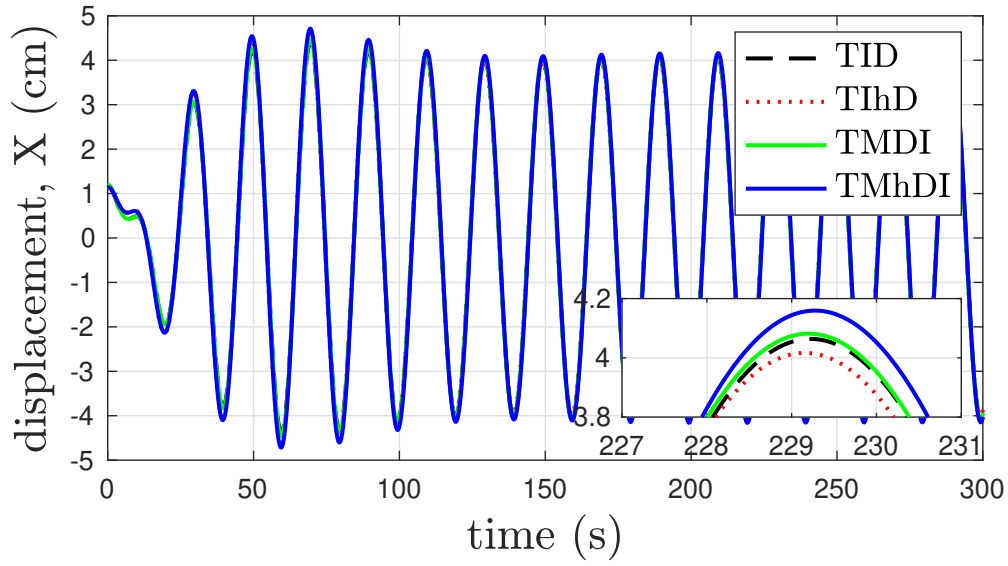

(a)

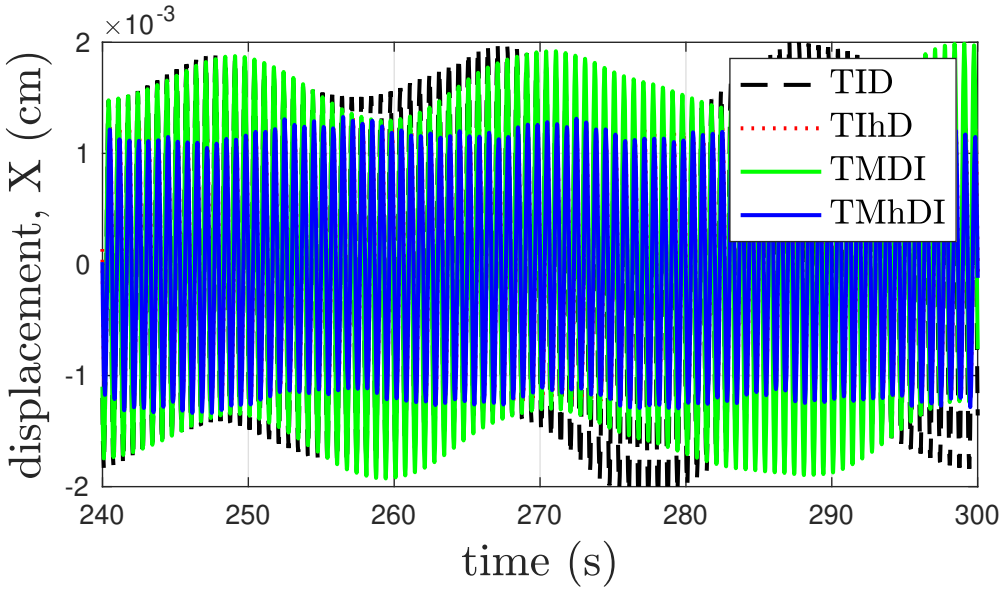

(b)

Figure 5.11: Time history responses at steady state of SDOF structure, $\mu = 0.1$, ω=0.05Hz (a) and ω=30ω_n (b) subjected to sine wave ground displacement with amplitude R=1 cm

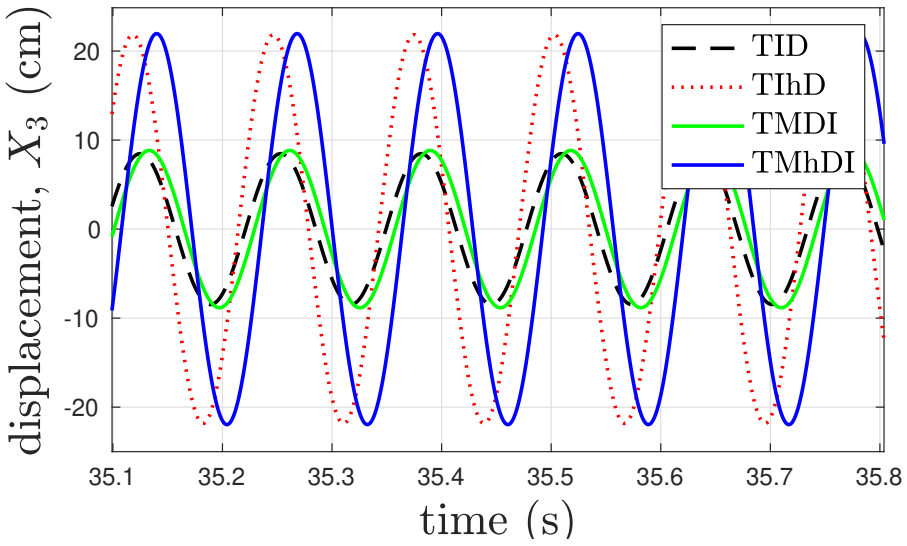

(a)

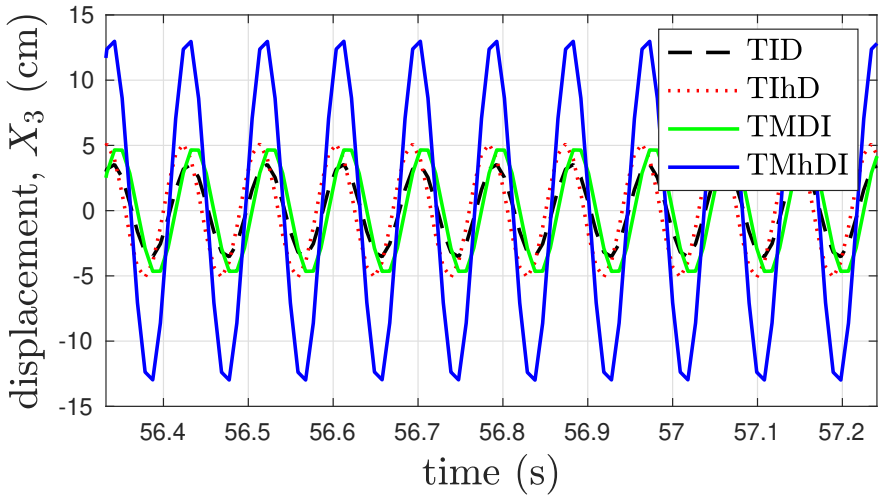

(b)

Figure 5.12: Time history responses at steady state of a 3-DOF structure, $\mu = 0.18$, ω=7.8Hz (a) and ω=11.1Hz (b) subjected to sine wave ground displacement with amplitude R=1 cm

To explore MDOF structures, a 3-DOF structure as shown in Figure 3.9(a) for $n = 3$ was selected for a case study. The parameters of the structure were designed to be the same as the 3-DOF structure presented in Lazar *et al.* [37], where $m_1 = m_2 = m_3 = 1\text{kNs}^2/\text{m}$ and $k_{0,1} = k_{1,2} = k_{2,3} = 1500\text{kN/m}$. All of the inerter-damper devices shown in Figure 3.9 (b) – (d) were located at the bottom storey as this is their optimum location.

Figure 5.10(b) shows the transfer function X_3/R of a 3-DOF structure in the frequency domain. Its time domain response is given in Figure 5.12(a) and 5.12(b). The optimised parameters of the inerter-damper devices are given in Table 5.3. These were

Table 5.2: Optimum parameters of the inertial damper systems for SDOF structure

Parameters	SDOF structure, $\mu = 0.1$			
	TID	TMDI	TIhD	TMhDI
Inertance, b_d(kNs^2/m)	0.1	0.1	0.1	0.1
Stiffness, k_d(kN/m)	0.0085	0.0091	0.0085	0.0091
Viscous damping, c_d(kNs/m)	0.0107	0.0107	–	–
Loss factor, η	–	–	0.3848	0.3848
Secondary mass, m_d(kNs^2/m)	–	0.005	–	0.005

Table 5.3: Optimum parameters of the inertial damper systems for MDOF structure

Parameters	3-DOF structure, $\mu = 0.18$			
	TID	TMDI	TIhD	TMhDI
Inertance, b_d(kNs^2/m)	0.48	0.48	0.48	0.48
Stiffness, k_d(kN/m)	138.6	146	138.6	146
Viscous damping, c_d(kNs/m)	2.5	2.5	–	–
Loss factor, η	–	–	0.3060	0.2905
Secondary mass, m_d(kNs^2/m)	–	0.024	–	0.024

derived based on a fixed value of $\mu = 0.18$. The structural response amplitude around the first resonance frequency are similar for all cases. As mentioned previously for SDOF structures, the hysteretic damping gives a slightly higher response after the optimisation. However, around the 2^{nd} and 3^{rd} resonance frequencies, the response of the structure with TIhD and TMhDI is significantly higher when compared to the TID and TMDI with no hysteretic damping. This is because the force transferred to the structure by the TIhD and the TMhDI is larger than that of TID and TMDI. This also indicates that modelling a system that has hysteretic damping with a viscous damping model may significantly overestimate the level of damping that can be achieved in higher modes of vibration. As a result using the model proposed in this study may have considerable benefits for modelling physical systems of this type.

5.5.2 Seismic Excitations

A further benefit of the proposed time domain method for linear hysteretic damping presented in Chapter 3.3 is its ability to be used for non-sinusoidal and non-periodic forcing functions such as earthquakes. In this section, the time domain response comparison is presented among the four inerter-based-damper devices shown in Figure 5.1(b)-(e) when installed in the ground floor of a 3-DOF structure.

Two optimum tuning approaches are used to obtain the optimum parameter of the four devices. The first approach is based on the fixed-point theory (FPT) approach discussed in the previous section assuming a harmonic input signal, which is not directly

applicable to seismic applications where the excitations are not harmonic in nature. The second approach is a numerical optimisation approach using the Self-Adaptive Differential Evolution algorithm (SADE) [147]. For this second approach, MATLAB is employed to apply the algorithm. The SADE algorithm is an improved Differential Evolution (DE) algorithm [148] that is capable of adaptively choosing the learning strategy to obtain a global optimum solution of the defined objective function. In this algorithm, a parameter candidate pool is generated for each generation. The number of generations was defined based on at which the result was converged. The detailed procedure of the SADE algorithm can be found in [147].

The four tuned-inerter devices were optimised for a SDOF structure as shown in Figure 3.9 (a) for $n = 1$. Mass m and stiffness $k_{0,1}$ were assumed to be 1kNs^2/m and 1kN/m respectively. The objective chosen was to find the optimum values of b_d, k_d and c_d or η that gives minimum average root-mean-square (RMS) value of the top displacement response for all considered earthquakes. This condition can be expressed as

$$min \left| \frac{\sum_{\ell=1}^{N_e} \mathrm{RMS}(x_\ell(t))}{N_e} \right| \tag{5.42}$$

where N_e is the number of earthquake input signals considered. Note that the upper and lower limits of the parameter values for inertance, stiffness, and damping must be set to realistic values. In this study the limits are selected to be $0.1 \leq b_d \leq 0.9; 0.1 \leq k_d \leq 1; 0.1 \leq \eta \leq 2$; and $0.1 \leq c_d \leq 3$.

Three design response spectra were selected: (1) Arrete 2010-2011, representing high-frequency earthquakes; (2) NTC2004 - a, representing low-frequency earthquakes; and (3) NTC2004 - b, representing mid-frequency earthquakes. The following assumptions were made: (1) for Arrete 2010-2011: seismic zone 1; ground type A; and building class 3, (2) for NTC2004 - a : ground type IIIc, for (3) NTC2004 - b: ground type II. Ten artificial earthquakes were generated using the SeismoArtif software for each of the corresponding design spectra as shown in Figure 5.13. Earthquakes 1-10 correspond to Arrete 2010-2011, Earthquakes 11-20 correspond to NTC2004 - a, and Earthquakes 21-30 correspond to NTC2004 - b. This enabled the effect of the hysteretic damping and the small mass element m_d which was assumed to be 5% of the inertance b_d to be observed. In order to try and make meaningful comparisons, the results are presented in terms of normalised RMS of the seismic displacement response histories of the structural system.

The optimum parameters obtained for the devices using the SADE algorithm and FPT are given in Table 5.4. As can be seen from this Table, there is no obvious correlation between the optimum η of the TIhD and TMhDI with the optimum c_d of the TID and TMDI. This implies that equivalent viscous damping cannot be used, because each of the devices needs to be individually optimised.

Figure 5.14 shows the performance comparison between the SADE and FPT opti-

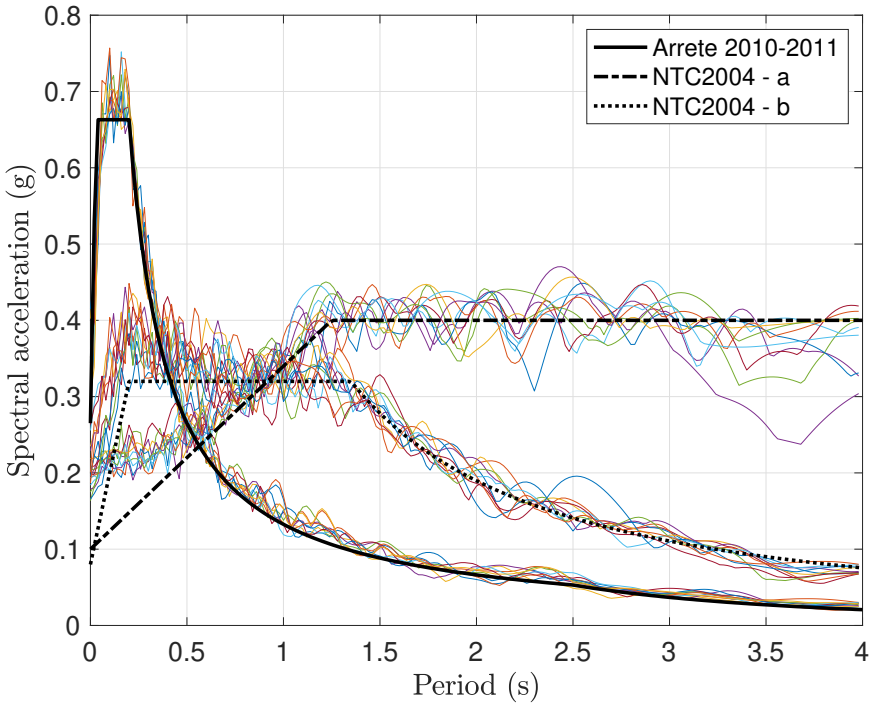

Figure 5.13: Design response spectrums and 30 generated artificial earthquakes

misations. Each bar in the figure represents the difference between FPT and SADE for each device for that specific earthquake with FPT taken as 0% for the sake of comparison. If no bar is shown, then there is a negligible difference between FPT and SADE. As would be expected, almost all of the bars for SADE are below the FPT line. The average is -3.64% for case (1) Arrete 2010-2011 (high-frequency) earthquakes 1-10, -44.38% for case (2) NTC2004 - a (low-frequency) earthquakes 11-20, and -10.42% for case (3) NTC2004 - b (mid-frequency) earthquakes 21-30. It should be noted that the natural frequency of the considered SDOF structure is 0.16Hz, which is in this case in the range of the low-frequency earthquakes.

From Figure 5.14 it can be observed that overall the optimisation by SADE algorithm works better than the FPT, particularly for low-frequency earthquakes (earthquakes 11-20). For earthquakes 9, 29 and 30, the FPT is actually better than SADE. It is not clear what the reason for this is, but one possible explanation is that the objective function given in Equation 5.42 is designed to seek for the minimum overall average, not the minimum for each of the earthquakes. Overall, the average is -24.66% for the bars below FPT and 5.18% for the bars above the FPT. This means that the optimisation using the SADE algorithm gives a much better response compared to the FPT across all 30 earthquake cases. In terms of applications, computations of this type can be used during the design stage, in order to give estimates of the level of displacement responses in a structure where the damping in the inerter device is hysteretic.

Table 5.4: Optimum parameters of the inertial damper systems for an SDOF structure. The optimum parameters obtained by the SADE algorithm for each of the device in the table are based on the objective function given in Equation 5.42.

	Fixed-Point Theory				SADE algorithm			
Parameters	TID	TMDI	TIhD	TMhDI	TID	TMDI	TIhD	TMhDI
b_d(kNs^2/m)	0.9	0.9	0.9	0.9	0.9	0.9	0.9	0.9
k_d(kN/m)	0.38	0.43	0.35	0.36	0.85	0.88	0.91	0.89
c_d(kNs/m)	0.44	0.44	–	–	1.64	1.74	–	–
η	–	–	1.26	1.26	–	–	1.73	1.83
m_d(kNs^2/m)	–	0.045	–	0.045	–	0.045	–	0.045

Figure 5.15 shows a comparison of the performance of the four devices for each earthquake, for the three different cases considered. Each of the devices was optimised by using the SADE algorithm. The comparison was made relative to the TID performance, which was the best overall. So in this figure, each bar represents the difference between each device and TID (which is taken as 0%) for each earthquake.

An example of the time domain response is given in Figure 5.16 for both SADE and FPT optimisations. The trends observed in both Figures 5.14 & 5.15 can also be observed in these time domain plots. Specifically, the overall amplitudes in Figure 5.16 (b) for SADE are significantly less that the amplitudes in Figure 5.16 (a) for FPT. It is also possible to see that the hysteretic damping devices have higher amplitude responses than the TID or TMDI in both plots.

From Figures 5.15 it can be inferred that the effect of the secondary mass m_d is small due to the fact that the TMDI performance is only up to 6% different to the TID performance. The effect of the hysteretic damping was much larger, because the TIhD and TMhDI were up to 33% different to the TID results. This implies that when the physical damping behaviour in an inerter-based device is hysteretic, then the viscous damping approximation could lead to results that over-estimate the effectiveness of the device.

5.6 Summary

In this chapter, two novel inerter-based dampers are discussed in detail, namely the TIhD and the TMhDI. The layout of the TIhD is similar to that of TID with the viscous damping element replaced by a linear hysteretic damping represented by a complex stiffness. Similarly, the layout of the TMhDI is also similar to that of TMDI with the presence of linear hysteretic damping.

Both the TID and TMDI have been well established in the literature and have been shown to be effective in protecting structures against earthquakes, for example

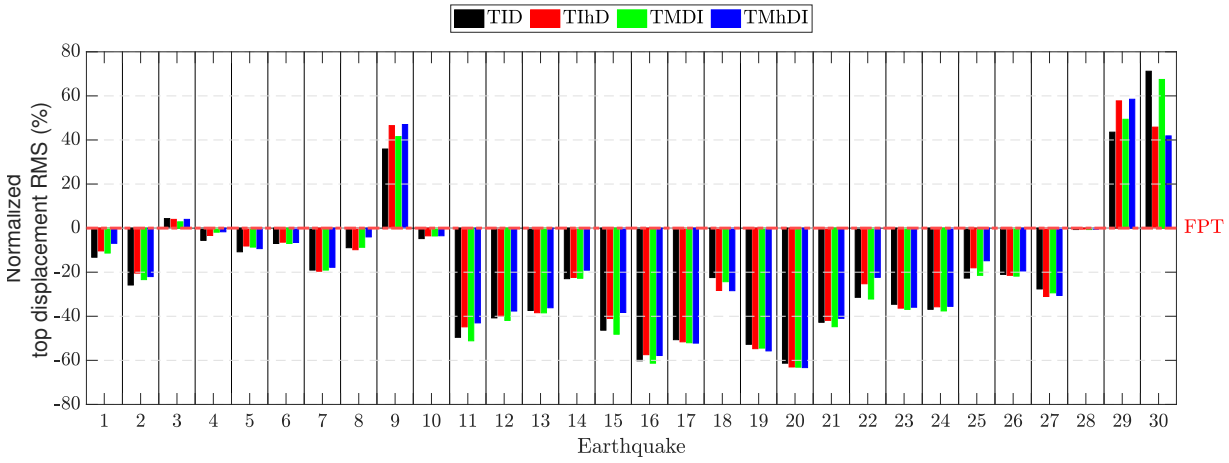

Figure 5.14: Performance comparison between the SADE and FPT optimisations. Any bars that are very close to the FPT values are not shown, and can be assumed to be approximately the same as the FPT value. Earthquakes 1 to 10 correspond to Case (1): Arrete 2010-2011, earthquakes 11 to 20 correspond to Case (2): NTC2004 - a, and earthquakes 21 to 30 correspond to Case (3) NTC2004 - b.

see [37, 41, 49]. The TID is considered to be an idealised model which is very difficult to realise due to the parasitic mass of the inerter device. The TMDI appears to be pratically more realistic due to the presence of the secondary mass element m_d.

In this chapter, both TIhD and TMhDI are considered to be a more realistic models of the TID and TMDI respectively, when a material damping is used. It is common in practice to convert the hysteretic damping to viscous damping via an equivalent viscous damping, for example see [97, 138]. It has been demonstrated in this chapter how this practice cannot be used for the TIhD and TMhDI analyses because it leads to inaccurate response at higher frequencies of excitation for SDOF structure, and for MDOF structure it leads to over-estimation of damping level around the higher modes of vibration. Therefore, the complex damping must be treated in its original form. A time domain method as discussed in Section 3.3.2 is adopted here to analyze both TIhD and TMhDI in the time domain.

It has been shown in this chapter that the response of structure with TIhD is different compared to the structure with TID, especially in the high frequency region in the frequency domain. For SDOF structures, the TIhD gives a lower amplification of response in the high frequency excitations when the mass ratio is increased. Moreover, for MDOF structures, the TIhD gives a higher response around the higher resonant modes. This is because the force transferred by the TIhD to the structure is higher than that by TID. Similar conclusion is also reached for the TMhDI in comparison with the TMDI.

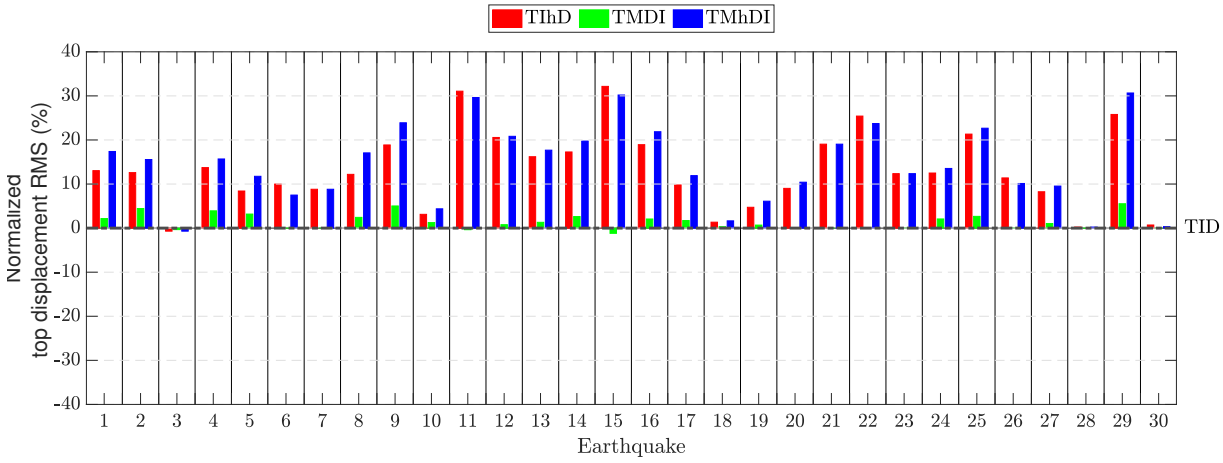

Figure 5.15: Performance comparison between the four devices. Any bars that are very close to the TID values are not shown, and can be assumed to be approximately the same as the TID value. Earthquakes 1 to 10 correspond to Case (1): Arrete 2010-2011, earthquakes 11 to 20 correspond to Case (2): NTC2004 - a, and earthquakes 21 to 30 correspond to Case (3) NTC2004 - b.

The newly developed time domain method in Section 3.3.2 has enabled the analysis of both TIhD and TMhDI in the time domain for both harmonic and random excitations such as earthquakes. This time domain method has also enabled the numerical optimisation for both TIhD and TMhDI for seismic base excitations. This numerical optimisation is based on the SADE algorithm with an objective function of minimisation of the structural response RMS in the time domain. The results showed that the numerical optimisation gives a better structural performance compared to the fixed-point approach.

With reference to Section 1.2, this chapter has demonstrated new design concepts for TIBDs with linear hystereitc damping (Objective 2) based upon idealised lumped parameter models, namely the TIhD and TMhDI. These design concepts have also been published in [149]. Meanwhile, in Chapter 4 it was argued that helical fluid devices could not easilty designed according to the hysteretic lumped parameter concepts. Consequently, the following chapters will investigate an alternative practical design of TIBD that can provide hysteretic damping. Therefore, a TMhDI is considered to be a feasible option. However, first the TMhDI needs to be effectively designed. The next chapter will discuss a novel concept of design for the realisation of the TMhDI. This concept is aiming to effectively realise an TMhDI concept with minimum friction in the inerter device. A material damping made of gel is employed to represent the complex stiffness model.

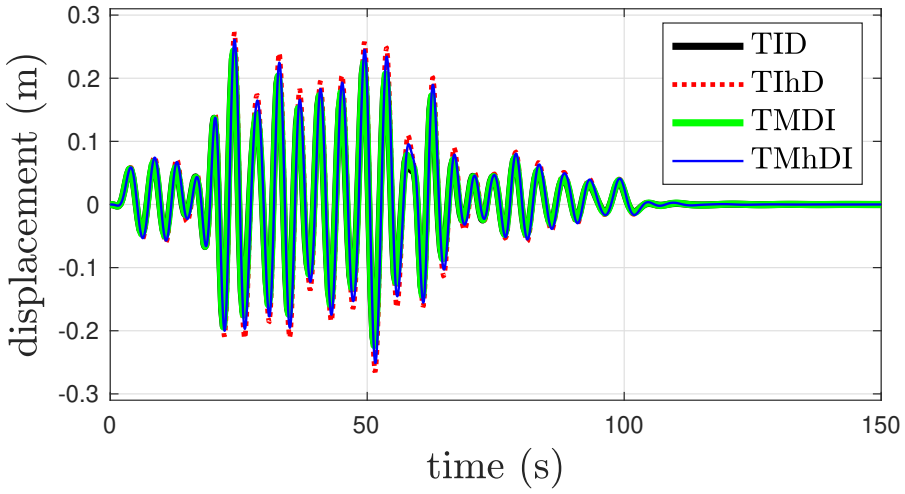

(a)

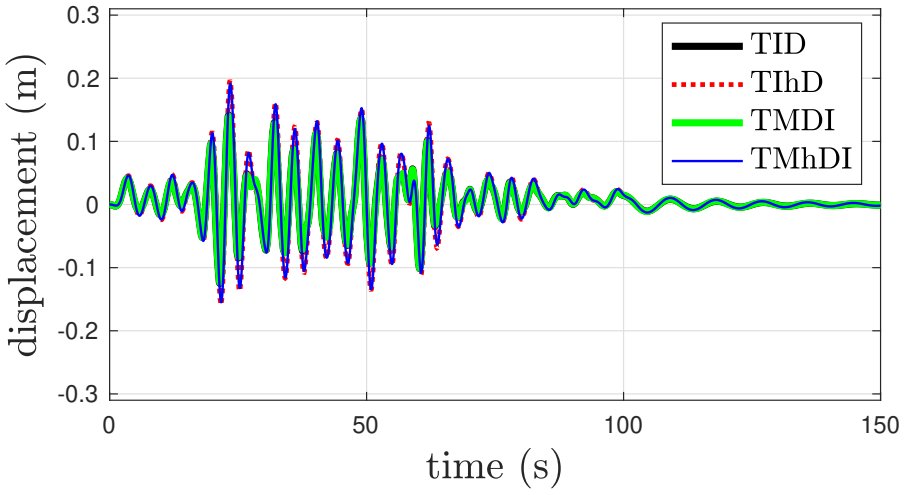

(b)

Figure 5.16: Time history responses of the structure subjected to Earthquake 15 base motion optimised by (a) FPT (b) SADE

Chapter 6

Novel Concept of Designs For The Realisation of A Tuned Inerter Based Damper System

6.1 Introduction

In the previous chapter, the concept of using linear hysteretic damping for tuned-inerter-based-damper system has been discussed in detail. In particular the TIhD and TMhDI were studied in both frequency and time domain.

This chapter proposes a new concept of designs for the TMhDI and the TMDI to be used for shake table experiments next in Chapter 7. In particular, this chapter discusses the realisation of linear hysteretic damping, inertance, stiffness, and viscous damping of both systems.

The linear hysteretic damping of the TMhDI was realised by gel dampers having a coupled stiffness and damping parameter. The inertance parameter was realised by a flywheel inerter. For the TMDI system, the viscous damping and stiffness parameters were realised by Eddy Current Dampers (ECDs) and several leaf springs made of steel profile.

Each components of both TMhDI and TMDI proposed in this chapter were tuned to the targeted optimised parameters for use in the base storey of a 3-storey steel structure. The detailed information about this structure is presented in chapter 7.

6.2 Gel Damper

6.2.1 Design of the Gel Damper

In order to realise the linear hysteretic damping, the silicone gel (Magic Power Gel, from Raytech) was used as shown in Figure 6.1. This gel is normally used as an

insulating gel in electrical equipment and is made by reacting two liquids - the blue and white. The design of this gel damper is based on the mechanical properties given in [150]. The shear modulus of the gel is given by

$$G = \frac{E}{2(1+v)} \tag{6.1}$$

where E is the Young's modulus and v is the Poisson's ratio.

In this design, G was assumed to be $0.33E$ estimated from Equation 6.1. The mixing ratio of white and blue components of the gel used in this experiment was 1:1.058 to achieved the targeted values of loss factor and stiffness of 0.7 and 14N/mm. These targeted values were based on the optimised parameters of the TMhDI for used in the shake table experiment of 3-storey fixed-based structure which will be discussed next in Chapter 7.

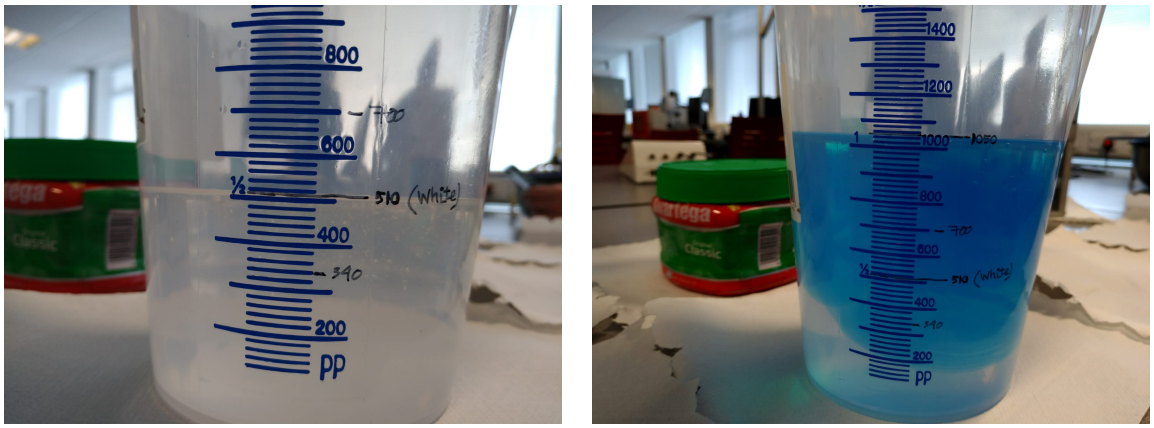

(a) (b)

Figure 6.1: (a) white liquid (b) blue liquid

The mixing process was very simple, first 510ml of the white liquid was poured into the measurement jug followed by 540ml of the blue liquid as shown in Figure 6.1. The mixing process created some bubbles inside the gel. To remove these bubbles, a degassing chamber was used. The process of removing the bubbles is given in Figure 6.2. The clean gel was then poured into the aluminium mould as can be seen in Figure 6.3.

The gel was made in two layers. The dimension of each was 150 mm x 150 mm which was estimated by using

$$A = \frac{kh}{2G} \tag{6.2}$$

where h is the thickness of each of the gel layer which was designed as 30mm. The two layers were separated by an aluminium plate of 150 mm x 190 mm with 5mm thickness.

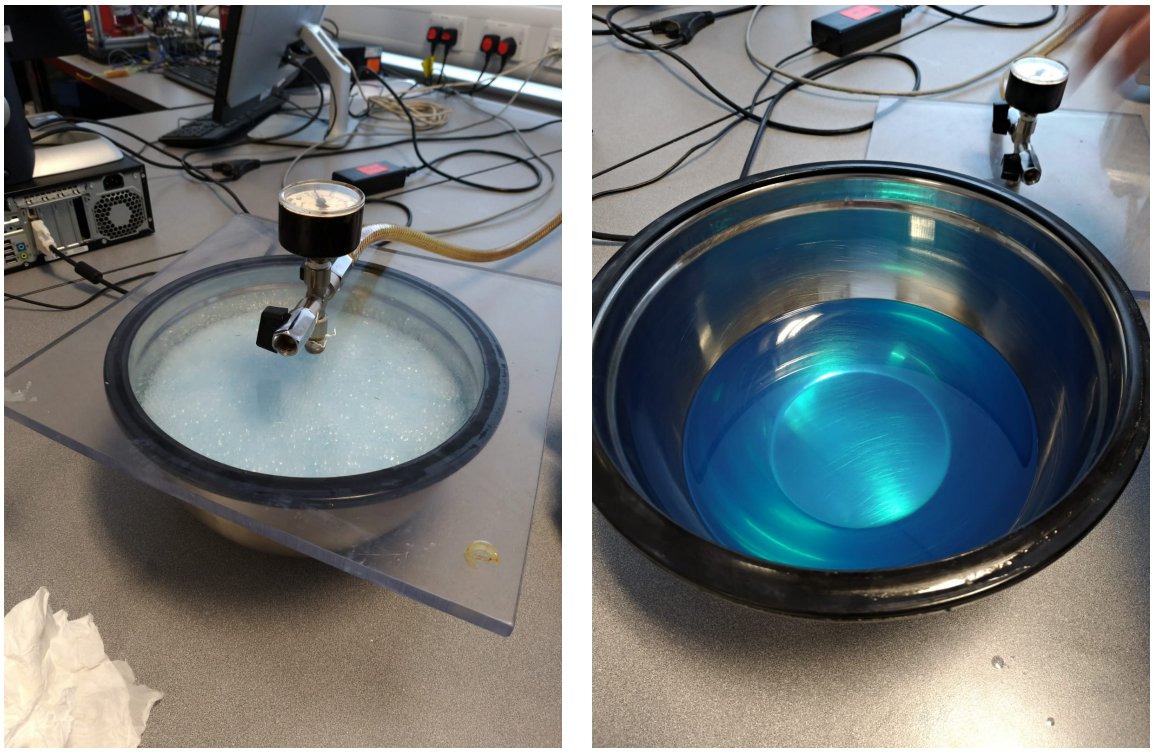

(a) (b)

Figure 6.2: (a) Removing bubles (b) Clean gel

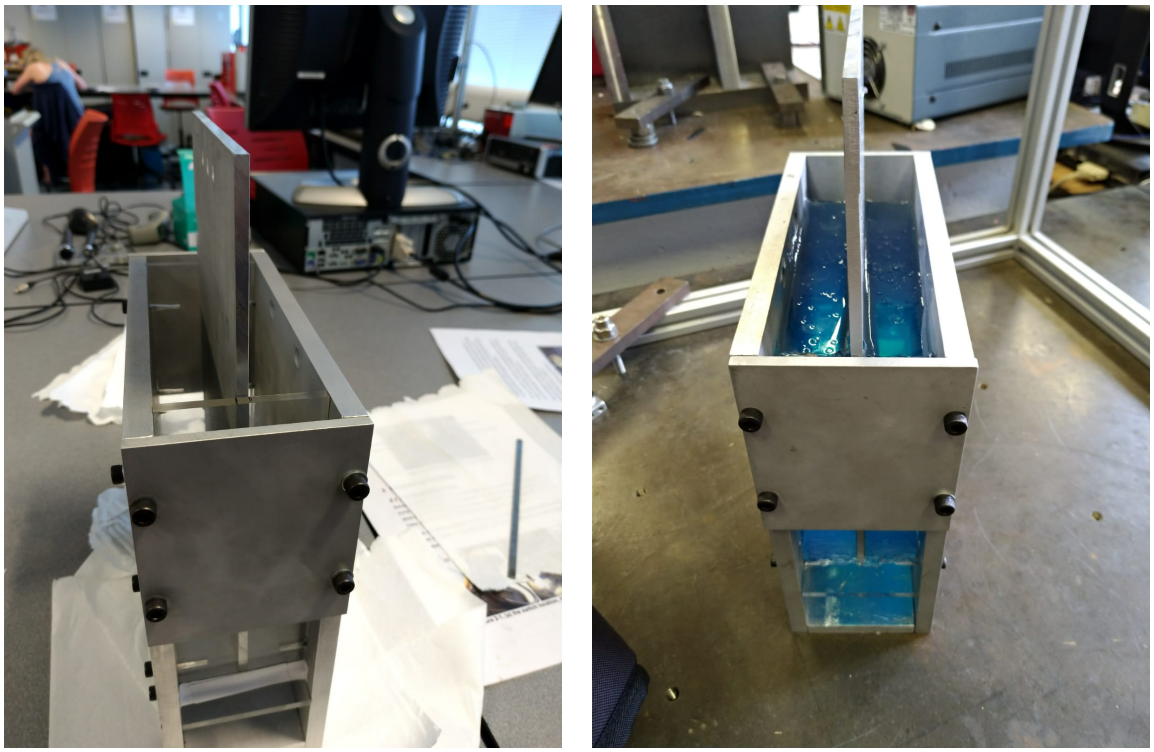

(a) (b)

Figure 6.3: (a) Empty mould (b) Mould with the gel inside

The gel that had been poured into the mould was then left at room temperature for 48 hours to ensure it had perfectly formed. Two identical gel dampers were made and each was then tested in the Damping Lab, University of Sheffield using a servohydraulic test machine (Figure 6.4) to obtain the loss factor and stiffness of the gel damper. Fifty cyclic displacement sinusoidal tests were performed for each gel damper specimen.

6.2.2 Experiment and Results

The complete results of the experiments are given in Figure 6.5 for gel damper 1 and 6.6 for gel damper 2. The area inside the hysteresis loops as given in Table 6.1 and 6.2 were obtained by using MATLAB. The analytical estimation of the area inside the loop is given by

$$\Delta W = \pi \eta k X^2 \tag{6.3}$$

where η is the loss factor, k is the stiffness, and X is the amplitude of oscillation.

Firstly, the stiffness k of each hysteresis loop was obtained by measuring the slope of the loop. Then the loss factor η for each hysteresis loop is obtained by

$$\eta = \frac{\Delta W}{\pi k_{avg} X^2} \tag{6.4}$$

where k_{avg} is the average of the stiffness of all hysteresis loops.

Finally, resulting loss factor and stiffness were 0.53 and 11N/mm which are the average of all hysteresis loops. These values are slightly below the designed values which could be due to the inaccurate estimation of the shear modulus of the gel.

Table 6.1: Area inside the hysteresis loops of gel damper 1

Amplitude (mm)	Frequency (Hz)				
	3	4	5.6	7	8
	Area (Nmm)				
2	79.98	89.34	97.28	102.06	105.98
3	172.91	192.68	211.99	228.95	231.28
4	301.49	331.61	373.58	398.31	399.46
5	464.62	515.32	581.06	606.78	609.09
6	666.13	744	833.54	853.2	852.77
7	907.87	1012.4	1110.6	1133.3	1124.3
8	1184.4	1311.8	1420.3	1432.8	1418.2
9	1489.1	1644.1	1759.4	1767.9	1732.7
10	1817.8	1993.3	2142.4	2123.9	2066.8
12	2526.6	2772.5	2944.3	2803.2	2342.6

Table 6.2: Area inside the hysteresis loops of gel damper 2

Amplitude (mm)	Frequency (Hz)				
	3	4	5.6	7	8
	Area (Nmm)				
2	77.91	88.42	95.55	101.52	104.21
3	170.62	192.34	212.73	227.34	231.53
4	301.1	339.57	375.62	399.65	407.55
5	470.65	526.32	588.88	617.64	625.11
6	679.94	752.28	840.33	873.64	868.9
7	923.74	1022.4	1127.90	1160.40	1152.50
8	1192.1	1331.90	1462.40	1471.90	1460.10
9	1531.3.1	1676.50	1877.40	1824.90	2004.00
10	1864.7	2043.10	2296.90	2190.20	2463.30
12	2587.9	2881.60	3220.10	3413.00	3496.40

Figure 6.4: Servohydraulic test machine machine used for the cyclic displacement sinusoidal tests of the gel dampers

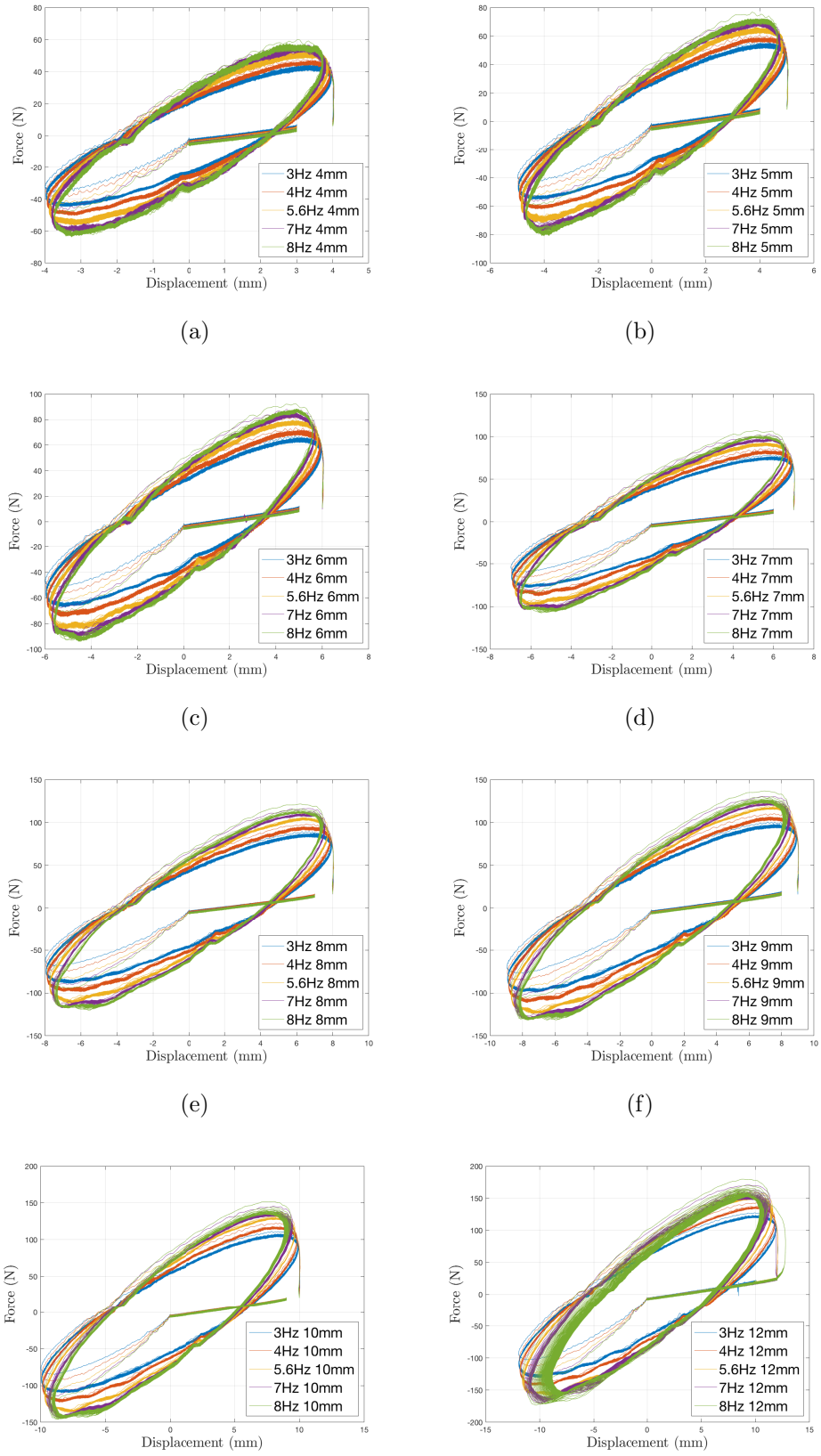

Figure 6.5: Hystereses loops of the gel damper 1

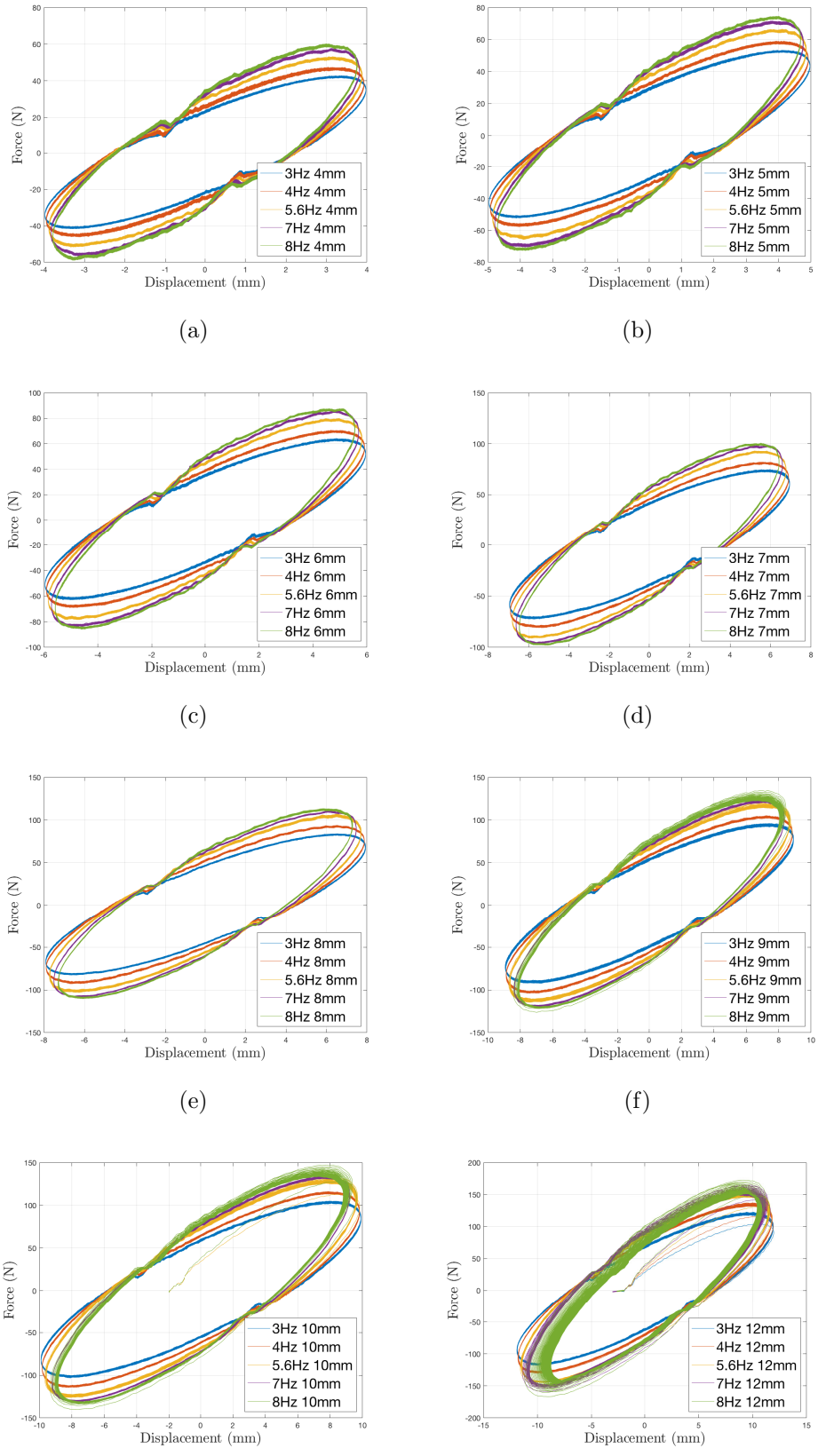

Figure 6.6: Hystereses loops of the gel damper 2

The results indicate that the energy dissipated per cycle by the gel damper was slightly changed by increasing of the excitation frequency, as can be seen in Table 6.1 for gel damper 1 and in Table 6.2 for gel damper 2. Theoretically the energy dissipated by the linear hysteretic damping is independent of the excitation frequency. The changing of the dissipated energy per cycle could be because of the changing of the stiffness as can be seen in Figure 6.5 and 6.6. Despite this discrepancy, the area inside the loop does change proportionally to the ratio of the square of excitation amplitude $(X_2/X_1)^2$ approximately. This is theoretically correct because the energy dissipated by the linear hysteretic damping is only dependent on the excitation amplitude given by Equation 6.3.

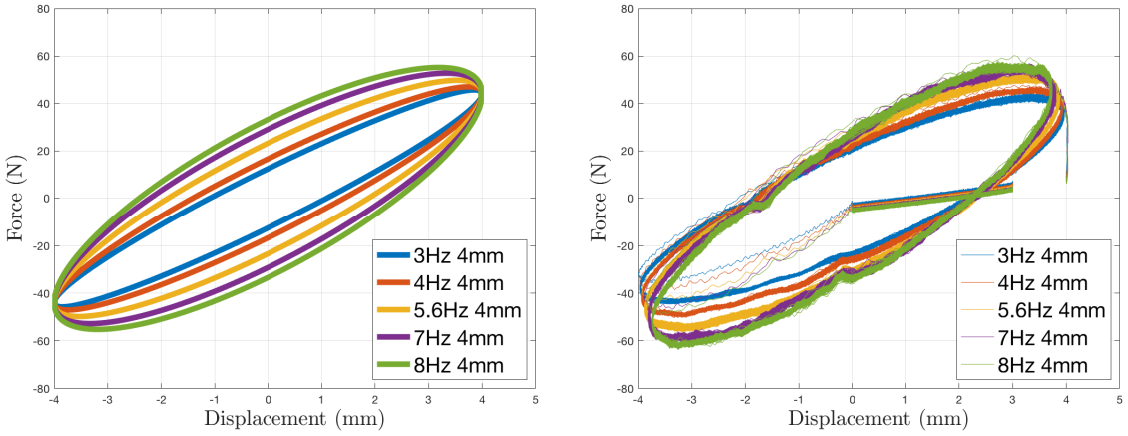

(a) (b)

Figure 6.7: (a) Model of viscous damping and stiffness in parallel, $F = c\dot{x} + kx$, where $c = 0.1657$Ns/mm and $k = 11$N/mm (b) Experiment.

Compared to the viscous damping model, the area inside the loops observed in Figure 6.5 and 6.6 only increases slightly. For example, Figure 6.7 shows the comparison between hysteretic loops by the model of viscous damping and stiffness in parallel and the experiment, for amplitude of 4mm. As can be seen in this figure, the area inside the loops shown by the model significantly increase with the increasing of frequency. While for the experiment, the area of the loops is only increasing slightly. This implies that the model is frequency dependent which is not suitable for the gel damper model. Therefore, the complex stiffness model is more suitable because it can represent the frequency indepedency of the damper.

6.3 Eddy Current Damper

6.3.1 Design of The Eddy Current Damper

To realise a TMDI system, a pure viscous damper is needed. For this purpose, an eddy current damper is proposed. The damper made of some permanent magnets as shown in Figure 6.8. The damping forces are generated by the relative motion between the permanent magnets and the aluminium sliding plates. To provide a sufficient amount of damping, 39 Neodymium Halbach Array Magnets 10 x 10 x 10mm were used for each of the dampers.

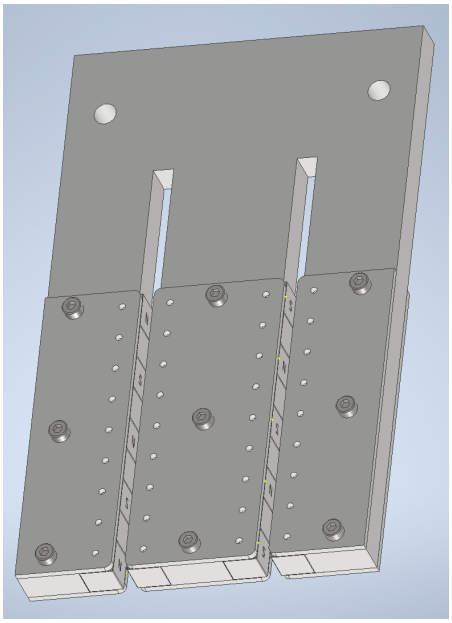

(a)

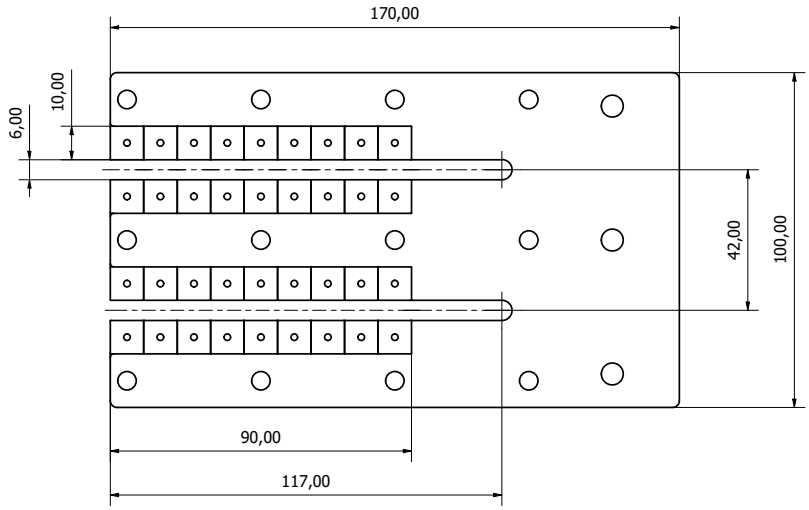

(b)

Figure 6.8: Design drawing of the Eddy Current Damper (a) 3D view (b) 2D view with dimensions (unit in mm)

6.3.2 Experiment and Results

This experiment aimed to characterise the properties of the damper. For this purpose, the damper was installed on a servohydraulic test machine as shown in Figure 6.9. The damper was fixed on a stiff frame connected to a force transducer. The sliding plate was attached to the actuator where the harmonic input signals were applied. A frictionless plastic sliding system as shown in Figure 6.10(a) was designed to ensure the sliding plate does not rotate. The damping forces are generated based on the relative motion between the permanent magnets and the aluminium sliding plate with 2mm thickness as shown in Figure 6.10(b).

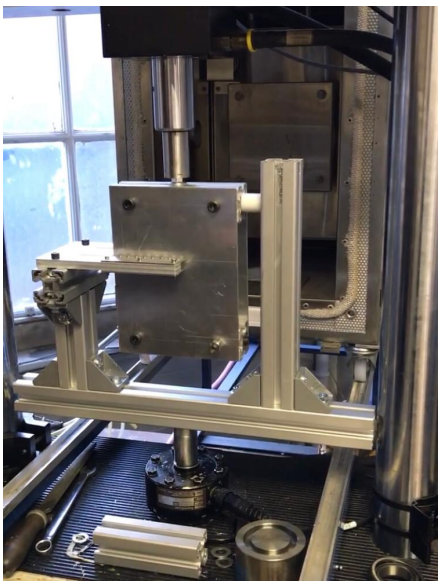

Figure 6.9: Experimental set up on a servohydraulic test machine

(a) (b)

Figure 6.10: (a) Frictionless plastic sliding system (b) Damper gaps

To characterise the damper, 50 harmonic sinewave input signals were applied via the actuator. Each signal was applied for a 100 seconds. The frequencies used were 3Hz, 4Hz, 5.6Hz, 7Hz and 8Hz with 10 amplitudes for each frequency.

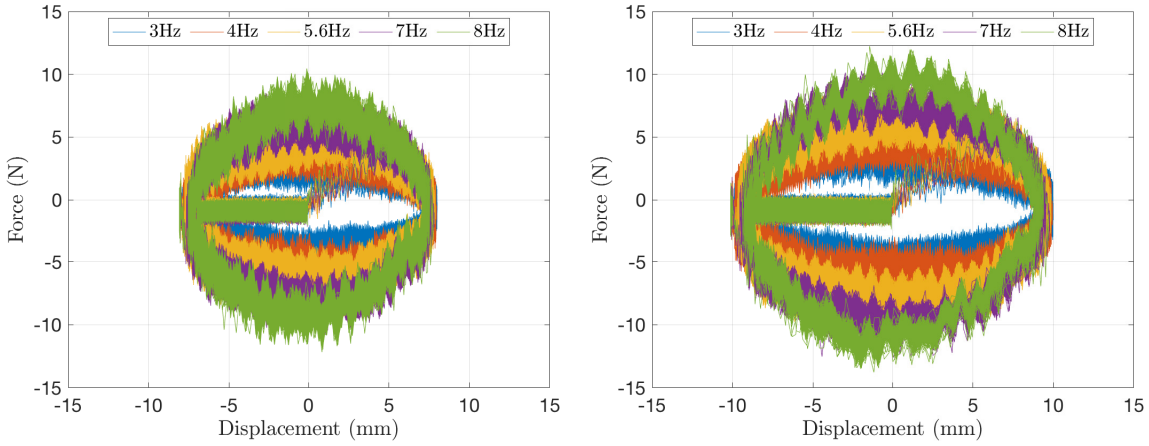

Figure 6.11: Hysteretic loops of the ECD for amplitude of oscillation: (a) 8mm (b) 10mm.

Fifty hysteresis loops were plotted to obtain the viscous damping coefficient of the damper. Some examples of these hysteretic loops are given in Figure 6.11(a) for an amplitude of 8mm and Figure 6.11(b) for an amplitude of 10mm.

As can be seen from Figure 6.11, the area inside the hysteresis loops of the ECD is highly dependent on the frequency and amplitude of the oscillation. It is unlike the gel damper which is almost frequency-independent. Another important finding is that the ECD damper has a pure linear viscous damping with no stiffness involved. It is unlike the gel damper having coupled stiffness-damping properties. The noise observed in these tests are probably caused by the friction between the siding plate and the magnets.

The area inside the loops represents the energy dissipated by the damper per cycle. The area was calculated by using MATLAB The viscous damping coefficient for each loop was calculated based on Equation 6.5.

$$\Delta W = \pi c_d \omega X^2 \tag{6.5}$$

where c_d is the viscous damping coefficient of the damper, ω is the frequency of the harmonic input signal, and X is the amplitude of oscillation.

Taking the average value of the viscous damping coefficient of the 50 hysteretic loops, it was found that the viscous damping coefficient of the ECD was 0.024Ns/mm. Based on this result, 12 ECDs are required to achieve the equivalent damping of the two gel dampers. However, due to the limited stock of magnets, only 4 ECD were used in the shake table experiment presented in Chapter 7.

Figure 6.12 shows the comparison between the hysteresis loops given by the viscous damping model and the experiment for various frequency for amplitude of 10mm. As can be seen in this figure, the model can accurately predict the real behaviour of the damper.

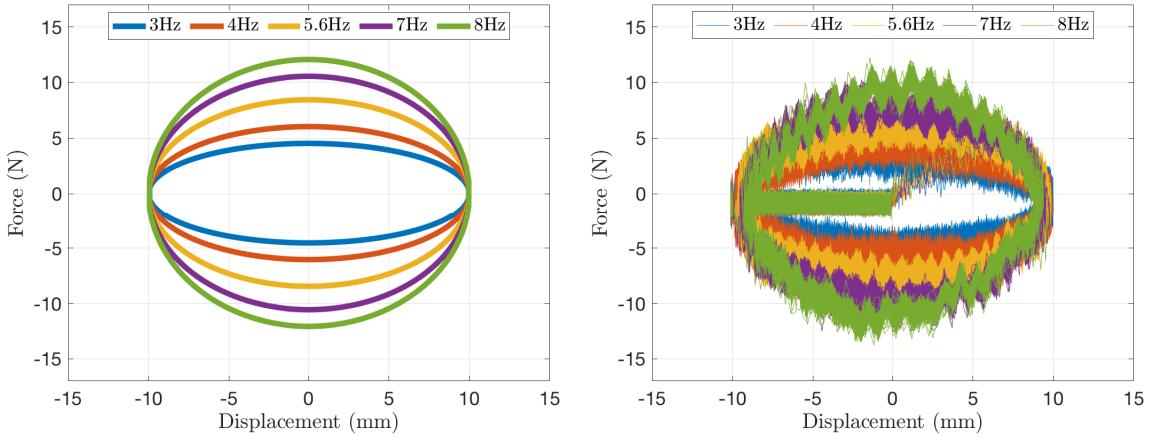

(a) (b)

Figure 6.12: Hysteresis loops for excitation amplitude 10mm (a) Model of viscous damping, $F = c\dot{x}$, where $c = 0.025$Ns/mm (b) Experiment.

6.4 Flywheel Inerter

6.4.1 Design of the Flywheel Inerter

The concept of inerter has been converted to a real device via several mechanisms. In this study a new design of the inerter is proposed based on the concept of the flywheel inerter studied by John and Wagg [151] as shown in Figure 6.13, which stated that the force generated by the flywheel inerter is proportional to the inertia and angular acceleration of the flywheel given by

$$F = \frac{I\ddot{\theta}}{l_a} \tag{6.6}$$

where I is the inertia of the flywheel, θ is the angle of rotation of the flywheel, l_a is the distance between the two terminals of the inerter, and the overdot denotes the differentiation with respect to time, t.

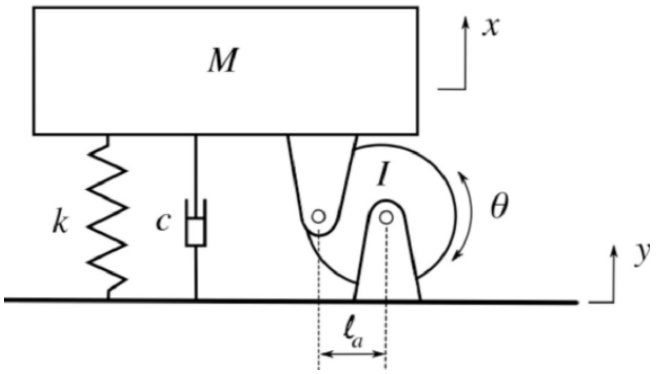

Figure 6.13: Flywheel inerter in an SDOF structure [151]. *Image reproduced with permission of the rights holder, Elsevier.*

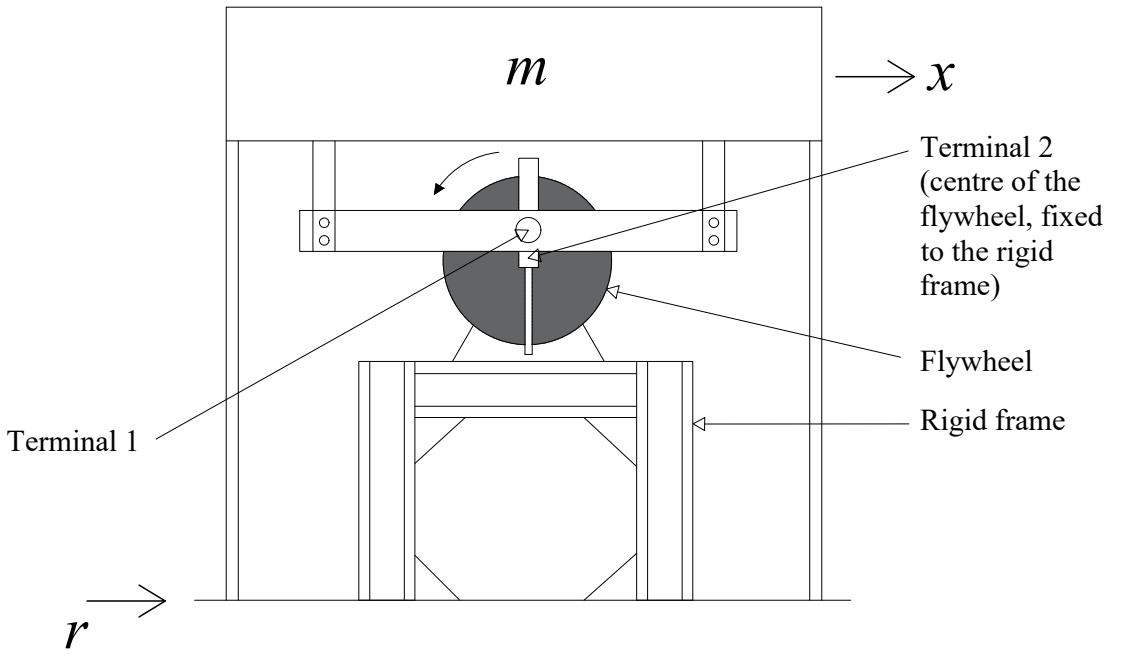

Figure 6.14: Flywheel inerter considered in this thesis

Figure 6.14 is the schematic configuration of a flywheel inerter mounted on a single-degree-of-freedom (SDOF) structure subjected to ground displacement, r. Here one terminal of the inerter is connected to the ground and another terminal is connected to the mass, m. Given that the force generated by the inerter is $F = b_d(\ddot{r} - \ddot{x})$, Hence the inertance b_d can be expressed as

$$b_d = \frac{I\ddot{\theta}}{l_a(\ddot{r} - \ddot{x})} \tag{6.7}$$

with $I = \frac{1}{2}m_d r_d^2$, where r_d is the radius of the flywheel and m_d is the mass of the

flywheel. Equation 6.7 can be further simplified for the case of a small angle of rotation, $\theta < 10.4^{\circ}$ as follows [151]

$$b_d = \frac{m_d r_d^2}{2{l_a}^2} \tag{6.8}$$

The key part of the flywheel inerter design is that it must be a mechanism to convert the translational motion of the two terminals into rotational motion of the flywheel to generate inertance. The design of the flywheel inerter in [151] used a living hinge mechanism for this purpose. The living hinge must be flexible enough for the flywheel to rotate. The use of this type of living hinge design is challenging for a larger scale devices due to the large rotation of the flywheel inerter.

In this study, a combined linear bearing and slider were used as can be seen in Figure 6.15. This mechanism allow some rotation at the joint between the inerter and the damper and at the same time also allows this joint to have translation motion.

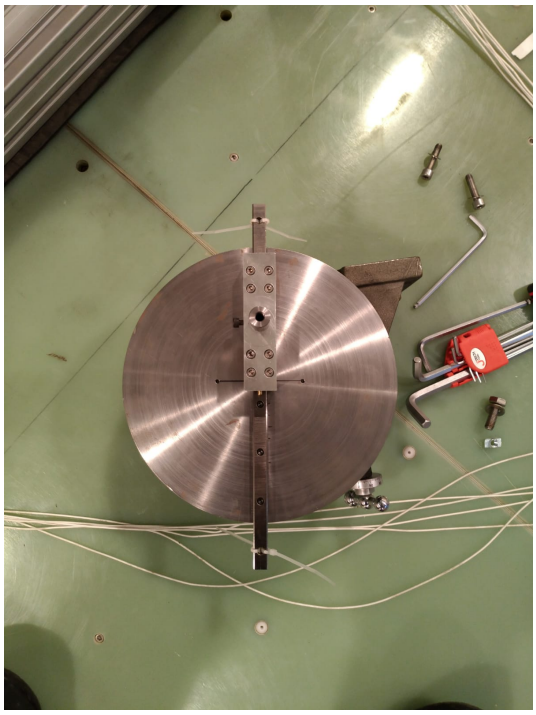

Figure 6.15: Flywheel inerter

6.4.2 Experiment and Results

The pivoted flywheel inerter was tested in the Jonas Lab at the University of Sheffield. The test objective was to find the inertance of the flywheel. The setup of the experiment is shown in Figure 6.16. The centre of the flywheel was acting as an inerter terminal and was fixed during the experiment. The other terminal of the inerter was connected to a shaker.

The shaker generated forces to activate the inerter. The force needed to produce a rotational motion of the flywheel with angle θ is given by Equation 6.7, where $\ddot{x}$, in this case, is zero and $\ddot{y}$ is the acceleration at terminal 2 which is the point where the shaker was attached, measured by the accelerometer. $\ddot{\theta}$ is the angular acceleration given by

$$\tan(\ddot{\theta}) = \frac{\ddot{y} - \ddot{x}}{l_a} \tag{6.9}$$

From the Equation 6.7, the inertance of the flywheel is influenced by the distance between its two terminals, l_a. The inertance generated is inversely proportional to l_a. In this design, l_a can be adjusted by changing the flywheel support position which is also acting as terminal 1 of the inerter, to tune the inertance to the targeted value.

In Figure 6.16, the shaker applies several sinusoidal forces $F(t)$ with different frequencies to the flywheel measured by the force transducer. The second terminal of the flywheel will oscillate with an acceleration of $\ddot{y}$ measured by the accelerometer. The linear guide mechanism has made it possible for the second terminal of the flywheel inerter to oscillate. Finally, the actual inertance of the inerter was obtained by using the averaged values of b_d from each frequency of input signals, given by

$$b_d = \sum_{n=1}^{m_m} \frac{F(t)_n}{\ddot{y}_n} \tag{6.10}$$

where m_m is number of test frequency.

The results from the experiment were compared with the predicted inertance value given by Equation 6.8. Figure 6.17 shows the comparison between the predicted and the obtained inertance from experiment accross frequency tested for various l_a. Figure 6.18 shows the plot of b_d against l_a. The predicted results were obtained by Equation 6.8 and the experimental results were obtained by Equation 6.10. Overall the prediction and experiment are in a reasonably good agreement, particularly when l_a is large. Some discrepancies can be seen when l_a is small. This is logical, because θ becomes large when l_a is small, hence the small-angle assumption relating to Equation 6.8 is no longer satisfied. It is also obvious from this figure that the inerter is capable of generating inertance of up to 25kg for the range of values tested. It should be noted that the actual mass of the flywheel was only 9kg which means that the inerter can generate inertance of up to almost 3 times its actual mass.

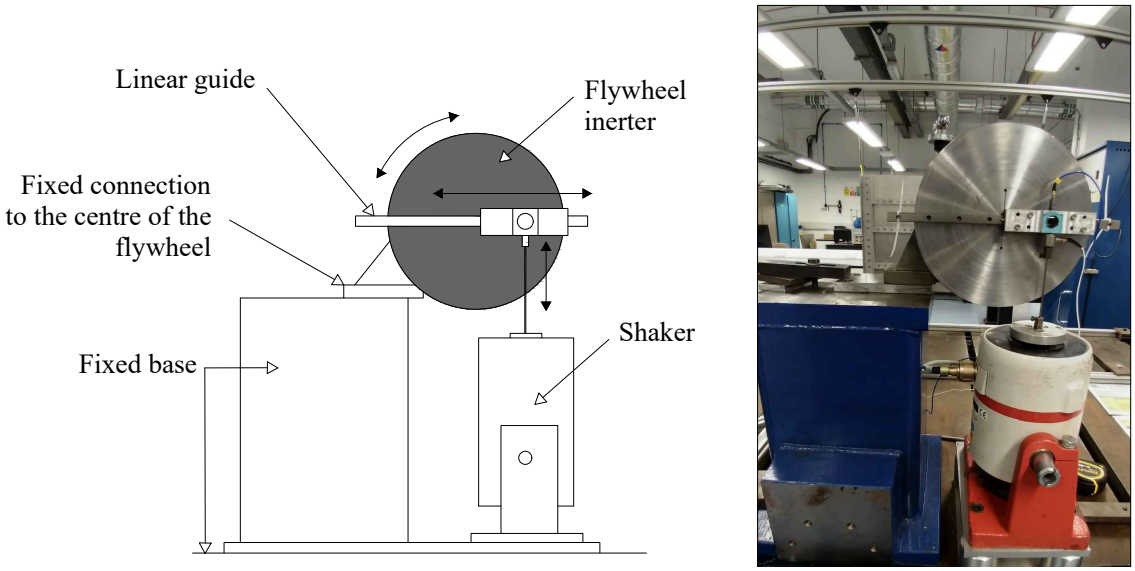

Figure 6.16: Flywheel inerter experimental set-up

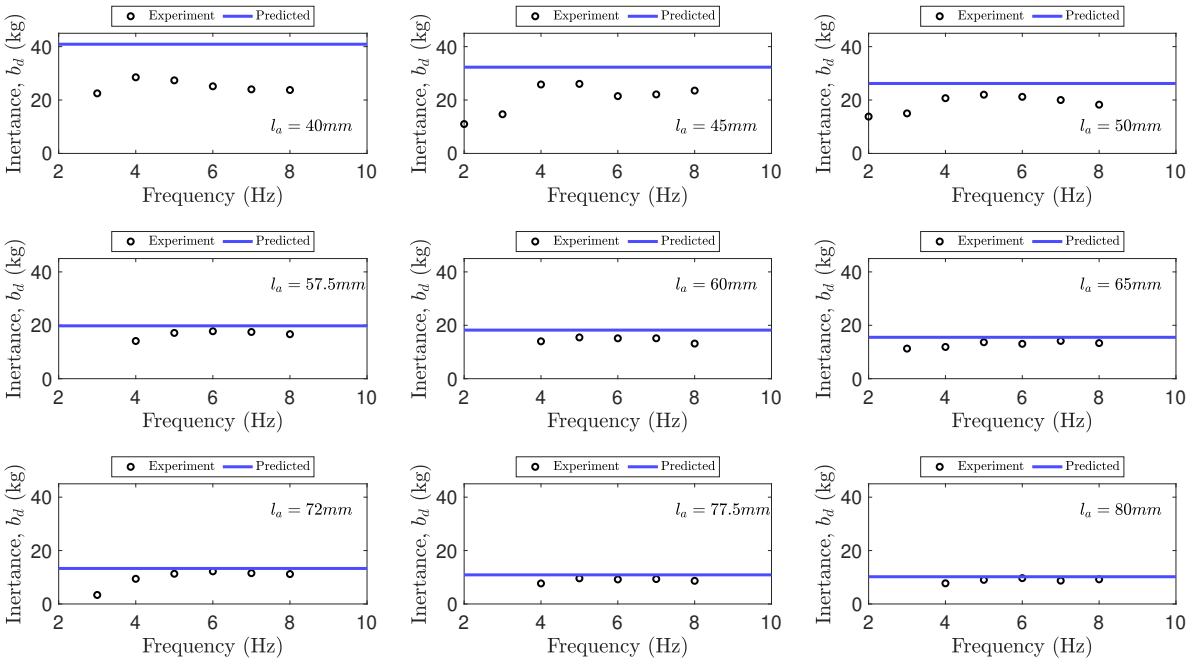

Figure 6.17: Inertance accross frequency tested for various l_a

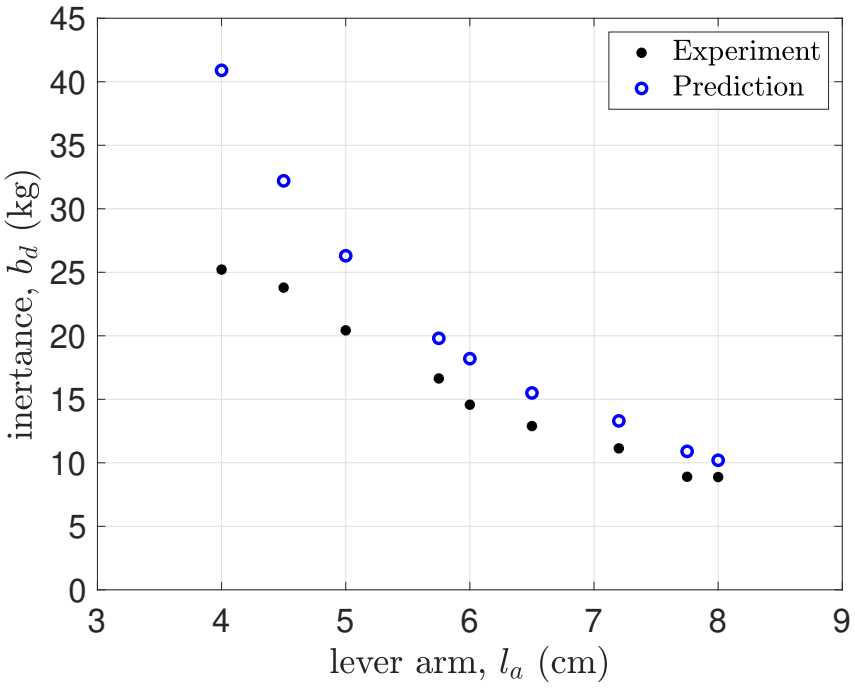

Figure 6.18: b_d versus l_a. The predicted values are obtained from Equation 6.8 and the experiment values are obtained from Equation 6.10 based on the experimental results.

6.5 Series Connected Dampers and Flywheel Inerter

A series connected inerter-damper is the key to realise both TMhDI and TMDI. Figure 6.19 shows the mechanism of the flywheel inerter when connected to a parallel spring-damper. The first terminal of the inerter was fixed to the stiff frame which was fixed on the shake table. The second terminal of the inerter was connected to a parallel spring-damper through an aluminium bar. For the TMhDI, this bar is connected to two gel dampers, and for the TMDI this bar is connected to a parallel-connected ECDs and flexible plates. Each systems will be discussed in detail below.

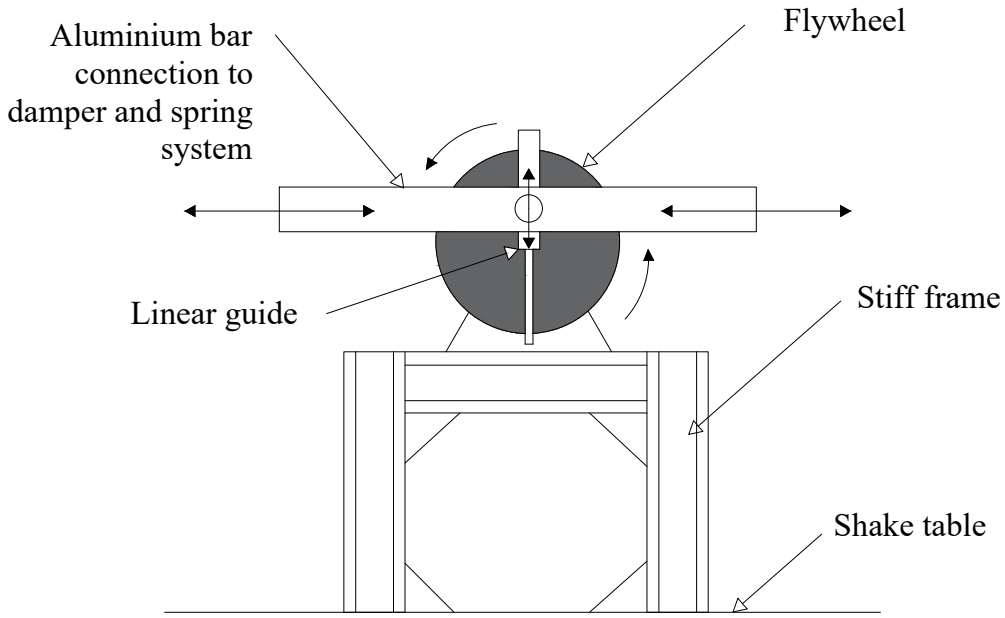

Figure 6.19: Mechanism of the Inerter in both TMhDI and TMDI

6.5.1 Realisation of the TMhDI

The TMhDI is one of the tuned-inerter-based-damper variants consisting of one inerter, one mass, and one linear hysteretic damper (coupled spring-damper) connected in series. It is basically a tuned-mass-damper-inerter (TMDI) with the parallel spring-dashpot replaced by a complex stiffness as discussed in Chapter 5.

In this study, the TMhDI was realised by using a flywheel inerter and gel dampers connected in series as can be seen in Figure 6.20. The first terminal of the flywheel inerter is its support connected to the ground (shake table). The other terminal of the inerter is connected to the gel dampers on both the right and left sides of the structure. The actual mass of the flywheel itself is acting as the TMhDI mass m_d. The inertance of the flywheel inerter is b_d, and the gel dampers are represented by a complex stiffness $k_d(1 + \eta j)$.

The flywheel inerter and gel dampers were designed for use as a vibration suppression device of a 3-storey scaled structure in the Laboratory for Verification and Validation (LVV), the University of Sheffield. The structure with the TMhDI was then experimentally tested on a shake table. The detailed shake table experiments will be further discussed in detail in Chapter 7.

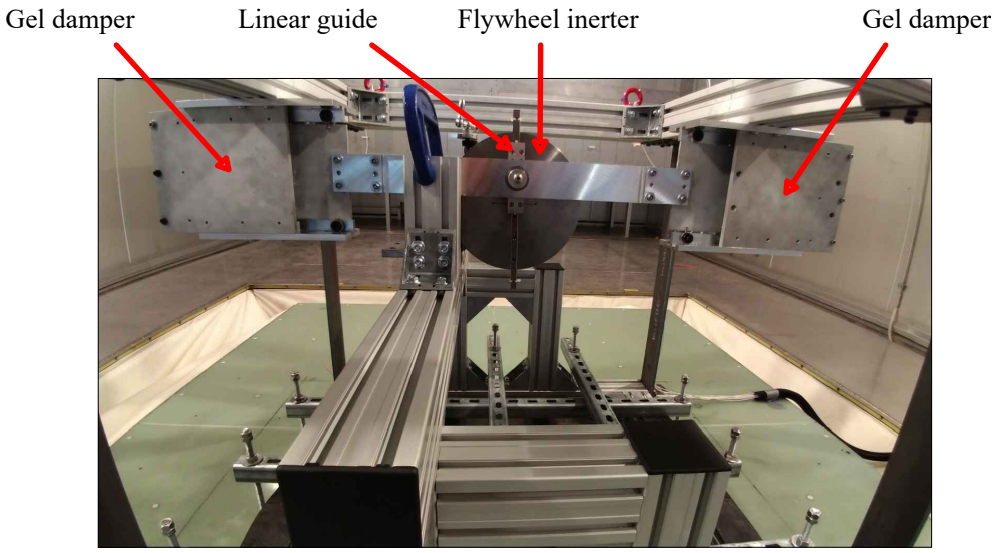

Figure 6.20: TMhDI

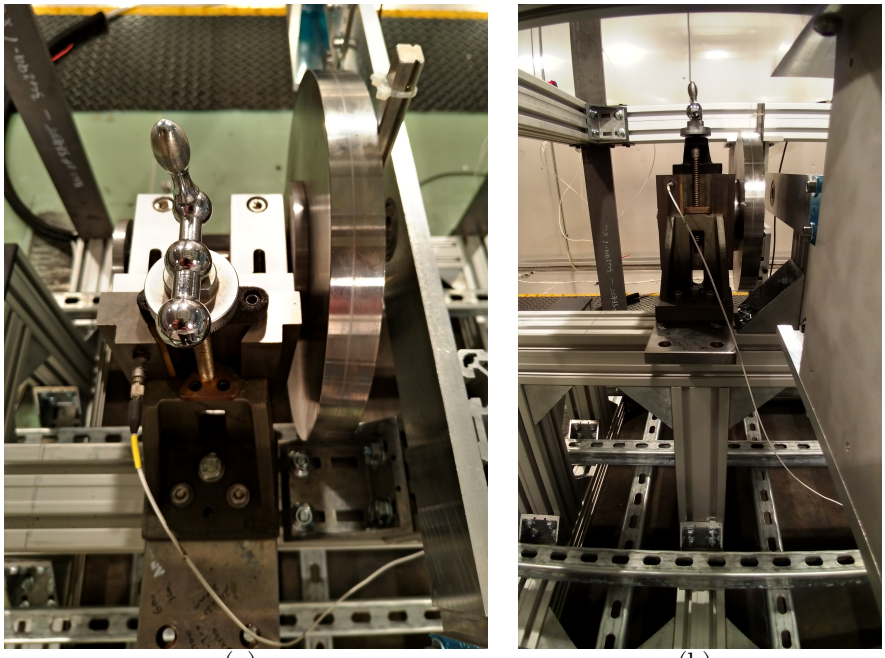

(a) (b)

Figure 6.21: Flywheel inerter connection detail (a) flywheel support (b) supported frame

The flywheel inerter was supported at its centre via a joint as can be seen in Figure 6.21(a). This joint was designed to allow the flywheel to be moved up and down. This mechanism makes it possible for the inertance to be adjusted by changing the distance between its two terminals before the experiment started. The flywheel support was fixed on a frame which was fixed on the shake table as shown in Figure 6.21(b).

The second terminal of the flywheel inerter was connected to the gel dampers on both sides via a beam as can be seen in Figure 6.5.1. The beam was fixed to the middle plates between the two gel layers. To prevent any rotation, each of the middle plates was supported by a linear bearing as shown in Figure 6.22.

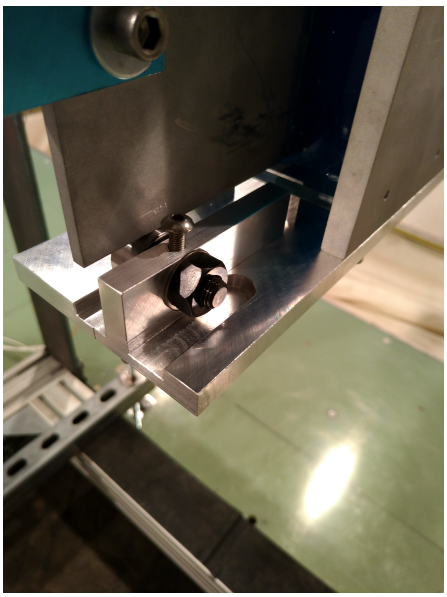

Figure 6.22: (a) Roller bearing on the gel damper

6.5.2 Realisation of the TMDI

The TMDI was realised by connecting the grounded flywheel inerter in series to a parallel spring-damper system as can be seen in Figure 6.23(a). The first terminal of the flywheel inerter, which is the central support of the flywheel was grounded through the stiff frame. The second terminal of the flywheel inerter was connected to both ECDs and flexible steel paltes via a rigid beam which is connected to two sliding plates. The translational motion of this rigid beam is the same as that of the two aluminium sliding plates because they were rigidly connected. The detailed parts of this system are shown in Figure 6.23(b).

Four ECDs were used to provide a sufficient damping to the structural system. The ECDs were activated by the translational motions of the two aluminium sliding plates which were connected to the four flexible steel plates which are the realisation of the TMDI stiffness k_d. The detail of the connection between the flexible plates and the ECDs is shown in Figure 6.24.

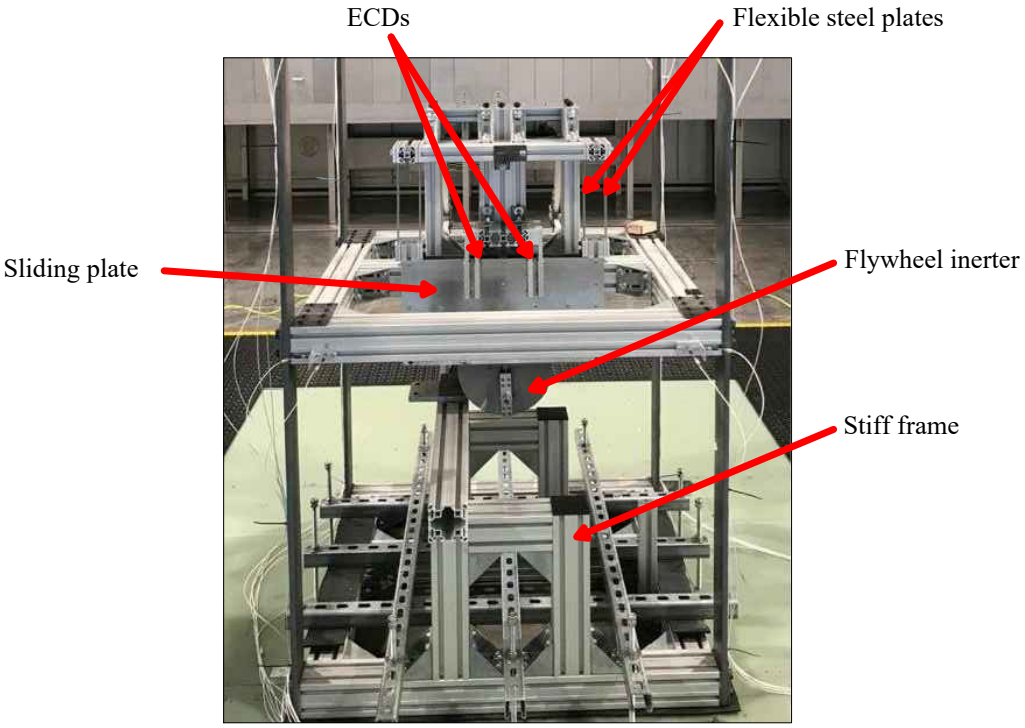

(a)

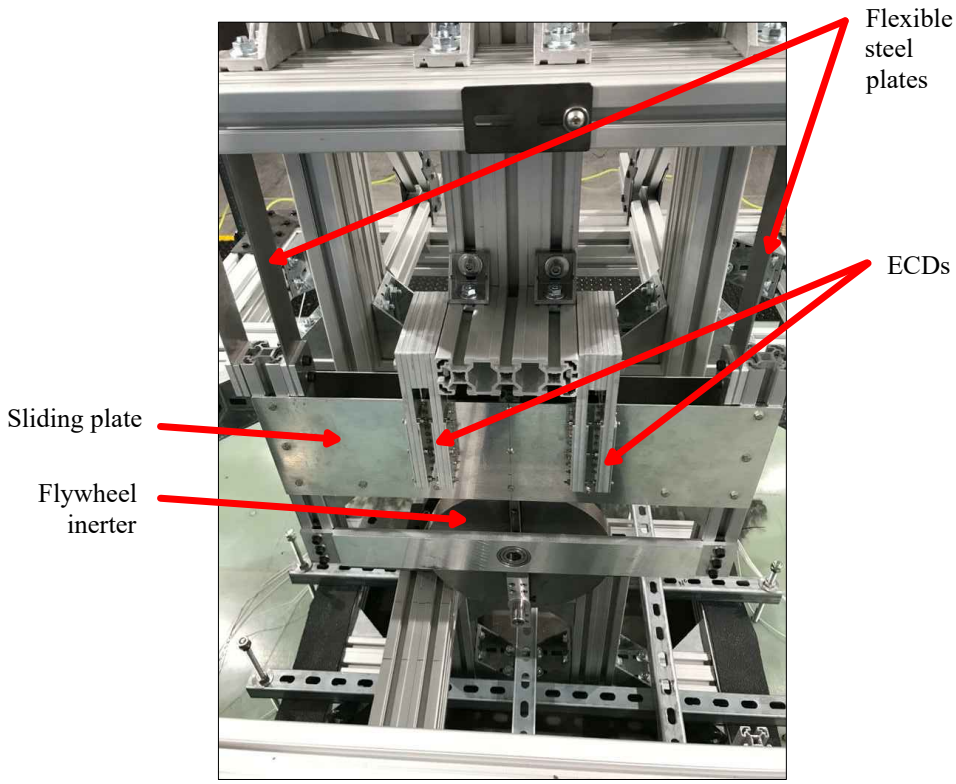

(b)

Figure 6.23: (a) Realisation of the TMDI (b) TMDI detailed parts

(a) (b)

Figure 6.24: (a) Flexible steel plates (b) ECDs

6.6 Summary

This chapter discusses a novel design of an inerter and the realisation of both TMhDI and TMDI. The linear hysteretic damping of the TMhDI is realised by the gel dampers, while for the TMDI, the viscous damping is realised by the ECDs.

A flywheel inerter was selected due to its simplicity and ease of manufacture. Although the design of this inerter is relatively simple, it allows the inertance to be tuned to a targeted value. This is made possible by changing the flywheel support position which is also acting as the first terminal of the inerter. The change of the support position will change the distance between the two terminals l_a giving a significant effect on the inertance value. Another important part of the proposed design of the flywheel inerter is the linear guide mechanism which allows a smooth conversion from the lateral motion of the rigid beam on the second terminal of the inerter to a rotational motion of the flywheel which will generate inertance.

The experimental results of the flywheel inerter show that the inertance generated by the inerter is in a good agreement with the prediction as can be seen in Figure 6.18. However, there were discrepancies for some small values of l_a, between the prediction and the experiment. This is because small l_a increases the angle of rotation θ of the flywheel. In effect, the predicted inertance values given by Equation 6.8 are no longer satisfied.

To realise the hysteretic damping properties of the TMhDI, two identical gel dampers were employed. The gel materials are made from silicone gel (Magic Power Gel, from Raytech). The gel dampers were manufactured to obtain the targeted values of loss factor η and stiffness k_d. They were tested using the servohydraulic test machine with sinusoidal displacement input signals. The obtained hysteretic loops were used to identify the loss factor and stiffness properties of the gel dampers.

For the realisation of the TMDI, some ECDs were employed to represent the viscous damping properties of the TMDI c_d. Unlike the gel dampers, ECDs exhibit pure linear viscous damping. Therefore, an additional stiffness element is required for the realisation of k_d. These dampers have been proven to have a pure linear viscous damping based on the results from a set of experiments using the servohydraulic test machine. The damper system consists of several magnetic dampers. The damping forces were generated by relative velocity between the two aluminium plates and the permanent magnets. From the obtained hysteretic loops, the viscous damping coefficient of the damper was obtained.

This chapter presents a new insight into the realisation of the inertance, damping and stiffness properties of both TMhDI and TMDI, which are simple and tuneable. Next in Chapter 7, a number of shake table experiments will be carried out. The structural performance comparison of a three storey structure subjected to ground displacements will be analysed when equipped with the TMDI and TMhDI.

Chapter 7

Shake Table Experiment

7.1 Introduction

This chapter discusses the shake-table experiments of a three-storey structure performed in the Laboratory For Verification and Validation (LVV), The University of Sheffield. The experiments were conducted on a fixed-base structure. The base of the structure was fixed on the table, hence the ground or soil condition was assumed to be solid rock. Therefore the base acceleration from the shake-table was directly transferred into the structure.

There are two parts of the experiments: (1) 3-storey structure equipped with a TMhDI, (2) 3-storey equipped with a TMDI. The purpose of these experiments is to investigate the effect of applying TMhDI and TMDI on the structural performance of a multi-storey structure. Firstly, the experiments were conducted with sinewave as the base acceleration input with frequency ranging from 3-26Hz. Secondly, earthquake ground accelerations were used as the base acceleration input.

7.2 Experimental Rig

A 3-storey structure was installed on a Multi-Axis Shaker Table (MAST) System in a chamber as shown in Figure 7.1. The shake table dimension is 3.2m $\times$ 2.2m with a useful frequency range of 5-70Hz. The MAST is connected to a system consisting of a 300 tonne concrete block and springs. This system has natural frequency around 0.8-1.4Hz. Therefore, for safety reason no test below 2Hz is allowed. In this experiment, the minimum testing frequency was 3Hz.

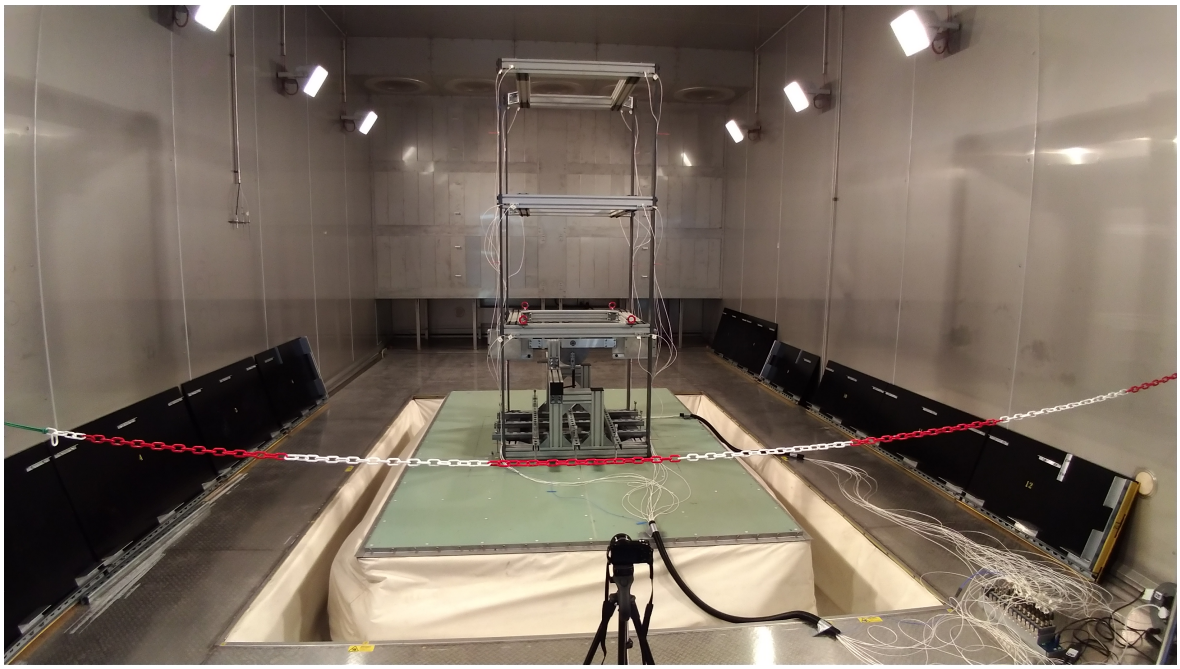

Figure 7.1: Experimental test setup

The structure is 900mm x 900mm in plan with a uniform inter-storey height of 780mm. The weight of each floor is 24.15kg. The cross section of the steel column is 80mm x 10mm that make it flexible in x-axis (direction from left hand side to right hand side of the chamber) and stiff in y-axis (direction from outside to inside). Therefore, the structure behave like a 2D structure. The ground floor of the structure is bolted on the shake table. Based on the specification of the structure, the inter-storey stiffness can be calculated as 1.35×10^5kN/mm in x direction.

The horizontal vibration response of the structure at each storey was measured using uniaxial accelerometers. The accelerometer type is PCB Piezotronics: 353B18 with a sensitivity around 10mV/g. The horizontal vibration of the ground floor was also measured using a tri-axial accelerometer (only the horizontal axials are recorded). The accelerometer type is PCB Piezotronics: 356B21 with a sensitivity around 10mV/g.

All accelerometer channels were sampled at 980Hz. For harmonic ground motion, the RMS of the signal was calculated at an update rate of 1Hz and this was used to calculate the peak acceleration and displacement at each location on the shear building. At each frequency step, the building was left to settle for a period of time. This was manually determined by monitoring the stability of the RMS value. Measurements were taken when the RMS had visually stabilised. Measurements were manually recorded at the ground level (MAST triaxial sensor), first storey level, second storey level and third storey level. At each frequency point, raw acceleration time domain data was captured for a period of 10 seconds.

The inerter-based-damper system was placed between the table and the first storey.

The experiments were performed in x-axis only. To analyse the effectiveness of the TMhDI and TMDI on reducing the vibration induced by the harmonic ground motion, a base-to-top-storey transmissibility X_3/R was plotted for both uncontrolled structure (a structure without TMDI or TMhDI) and the structure equipped with TMDI or TMhDI. For each frequency, the steady-state response at the top storey and the shake table were measured. For earthquake ground motions, the comparison are presented for top storey response of the two structural systems.

7.3 Experiment 1: 3-storey structure equipped with a TMhDI

As discussed in Chapter 6, the realisation of the TMhDI consists of two gel dampers connected in series to a grounded flywheel inerter as shown in Figure 6.20. This TMhDI is installed between the table and the first storey of the 3-storey structure as shown in Figure 7.2(b). The lumped-mass model of the structure with the TMhDI is presented in Figure 7.2(a). It should be noted that the structural damping is neglected in the model. The equations of motion of the structure in absolute coordinates can be written as

$$\begin{cases} (m_1 s^2 + k_{0,1} + k_{1,2})X_1 = k_{1,2}X_2 + k_{0,1}R + F_{1,0} \\ (m_i s^2 + k_{i-1,i} + k_{i,i+1})X_i = k_{i-1,i}X_{i-1} + k_{i,i+1}X_{i+1} \\ (m_3 s^2 + k_{2,3})X_3 = k_{2,3}X_2 \end{cases} \tag{7.1}$$

where m_i and $k_{i-1,i}$, $i \in [1:3]$ represent the mass and stiffness between storeys $i-1$ and i; X_i represents the Laplace transform of the ith storey displacement, when $i = 0$, then $X_0 = R$ which represents the Laplace transform of the base displacement; s represents the Laplace transform variable and $F_{1,0}$ represents the force transferred to the structure by the TMhDI in the Laplace domain, which is given by Equation 5.19.

Next detailed discussions are presented for the experiments which consists of two parts: (1) harmonic ground motion; (2) earthquake ground motion.

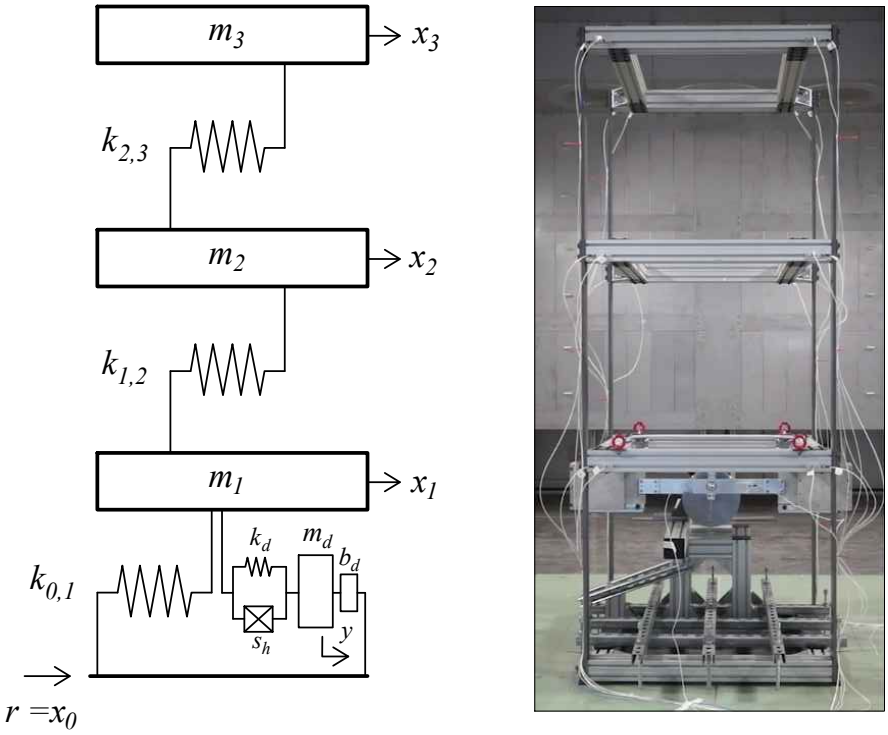

Figure 7.2: System layout: (a) lumped-mass model (b) 3-storey structure with TMhDI

7.3.1 Harmonic ground motion

The first part of the experiment was harmonic base accelerations. In this case, the structure was subjected to sine wave base acceleration. The frequency range of the sine wave acceleration input was 3-26Hz. This was based on the frequency of all the three resonant modes of the structure.

This first part of the experiments consisted of three cases as shown in Figure 7.3: (1) Uncontrolled structure (2) with Gel dampers only, and (3) with TMhDI. The first case is when the structure has no external damping device. The connection between the gel dampers and the flywheel inerter on the beam was removed. In the second case, the beam was fixed to the table while its connection to the flywheel was removed. In this case the vibration energy will be dissipated directly by the gel dampers. Finally in the third case the TMhDI was in place.

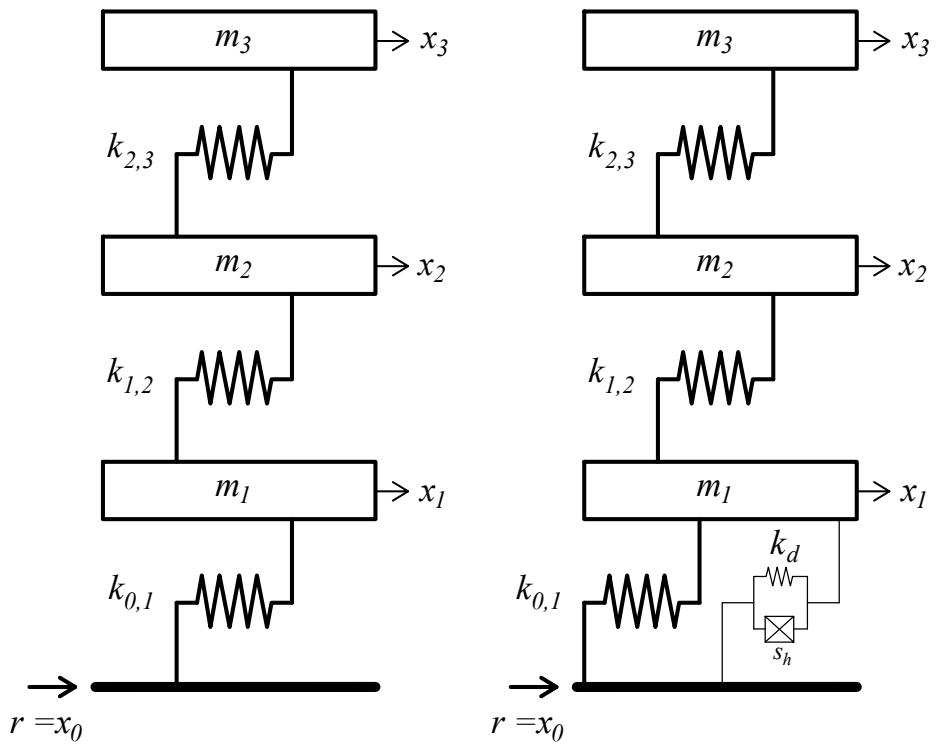

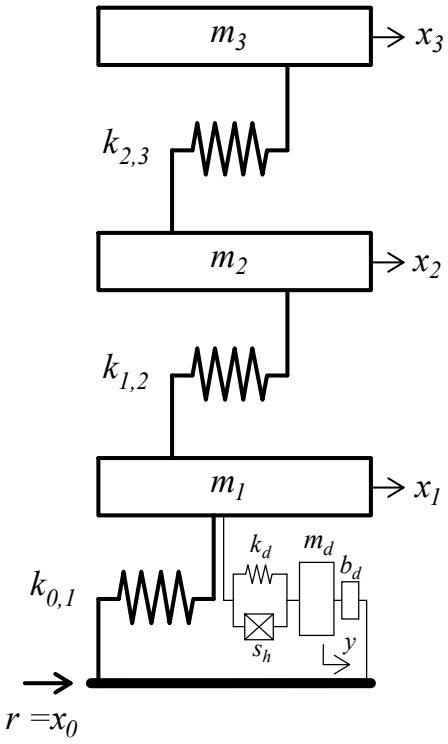

Figure 7.3: Lumped-mass model of the three cases: (a) uncontrolled (b) with gel dampers only (c) with TMhDI

The purpose of the uncontrolled structure experiment is to verify the stiffness and

mass properties of the structure. The storey mass of the structure was weighted directly before the experiment. The mass m_1,m_2 and m_3 are 33.15kg, 24.15kg and 24.15kg respectively. The storey stiffness of each of the storeys is estimated by

$$k = 12\frac{EI}{l^3} \tag{7.2}$$

where E is the Young's modulus of the column, I is the inertia of the column, and l is the effective length of the column. From this experiment, the stiffness of each of the storey was found to be $k_1 = 1.4048 \times 10^5$N/m, $k_2 = 1.6858 \times 10^5$N/m, and $k_3 = 2.0792 \times 10^5$ N/m.

As can be seen in Figure 7.4(a), the experiment and the analytical model are in a good agreeement. Therefore, the mass and stiffness properties of the structures can be used for optimisation of the TMhDI. Moreover, this figure also show that the natural damping of the structure is considerably low, so it can be excluded from the lumped mass model.

The second case was the 3-storey structure equipped with the gel dampers, without inerter. This experiment was performed to verify the loss factor and stiffness properties of the gel dampers obtained from the experiment discussed in Chapter 6. The result is presented in Figure 7.4(b). In this figure, two analytical models are proposed: (1) Hysteretic damping model; (2) Viscous damping model. In the first model, the gel dampers are represented by a complex stiffness $k_d(1 + j\eta)$, where the stiffness k_d and loss factor η properties of the gel dampers are obtained from Chapter 6. The second model assumes that the gel dampers have viscous damping and stiffness in parallel. In this case, the viscous damping property is obtained via an equivalent viscous damping method $c_{eq} = \frac{\eta k_d}{\omega_{n_1}}$.

Figure 7.4(b) clearly shows that the results from the experiment are very close to the hysteretic damping model. This suggests that the complex stiffness is a good representation of the gel dampers compared to the parallel viscous damping and stiffness. It also suggests that converting the hysteretic damping to viscous damping via an equivalent viscous damping method cannot be very accurate. Obvious differences can be observed around the second and third resonances. Around these resonances, the response with viscous damping model is far lower than both the hysteretic damping model and experiment. This result also supports the discussion in Chapter 5 that a hysteretic damping must be treated as its original form (complex stiffness) when performing both frequency and time-domain analyses.

The third case experiment was a 3-storey structure equipped with a TMhDI. As can be seen in Figure 7.2(b), the TMhDI was placed between the table and the first storey of the structure. The first terminal of the flywheel inerter was fixed to the stiff frame which was fixed to the table. The second terminal of the inerter is connected to the gel dampers which were mounted on the first storey of the structure. This way, the translational motion of the first storey induced by the shake table is converted to

a rotational motion of the flywheel to generate inertance. The analytical model of the TMhDI is depicted in Figure 7.2(a). The gel dampers are represented by the parallel k_d and s_h. b_d is the inertance of the flywheel, and m_d is the mass of the flywheel. Normally inertance is much larger than the physical mass of the inerter itself, hence m_d can be neglected. However in this case, m_d is too significant to be ignored.

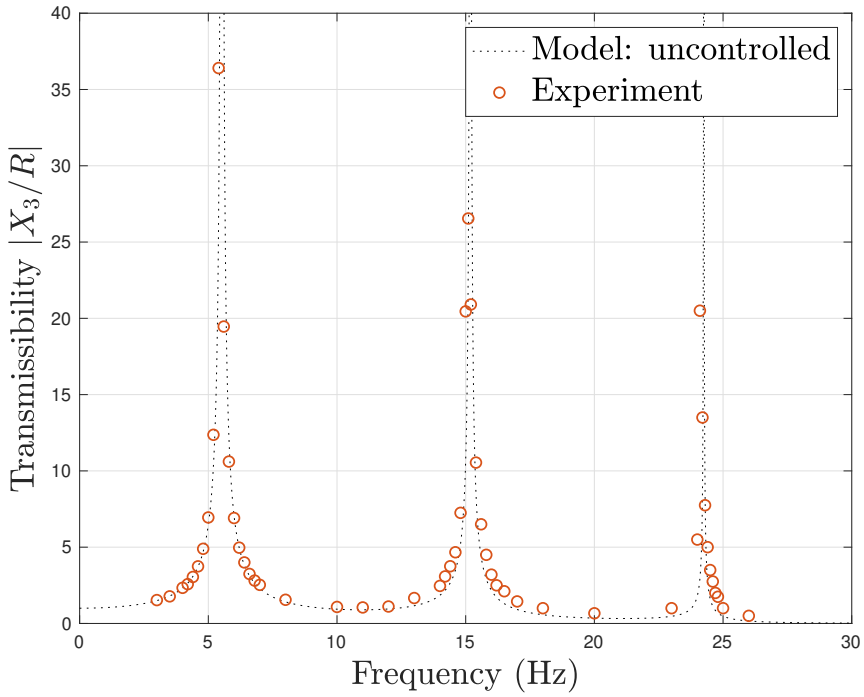

(a)

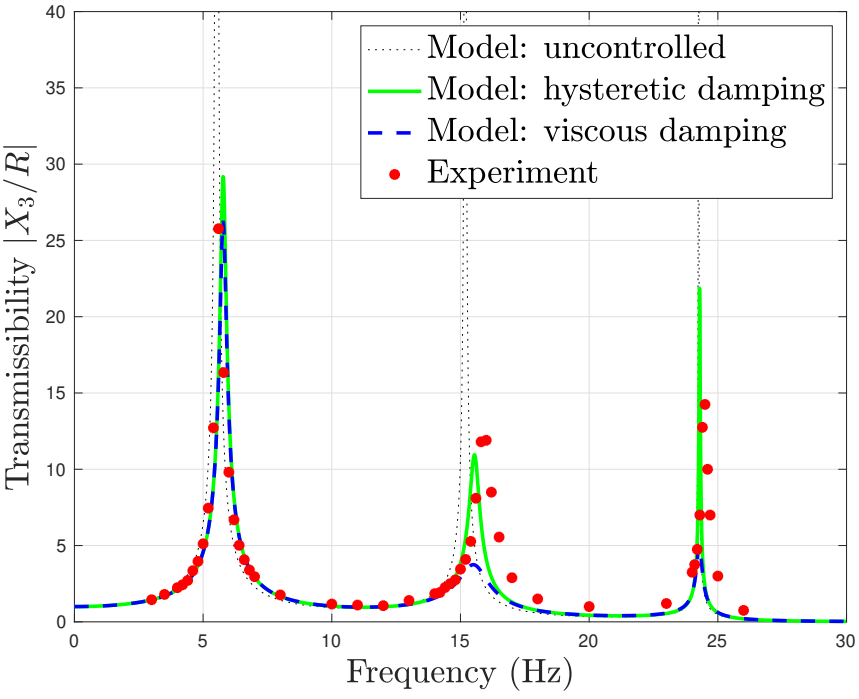

(b)

Figure 7.4: (a) The 3-storey structure's top storey transmissibility: uncontrolled structure, analytical vs experiment (b) The 3-structure's top storey transmissibility when equipped with hysteretic damping (green line) and with viscous damping (blue dash line) vs experiment with gel dampers only, without inerter

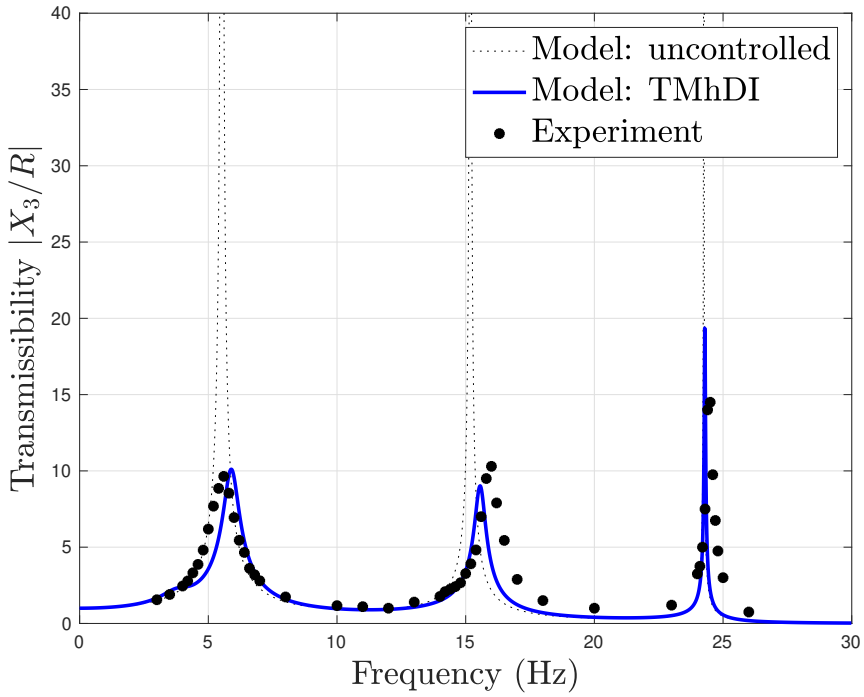

(a)

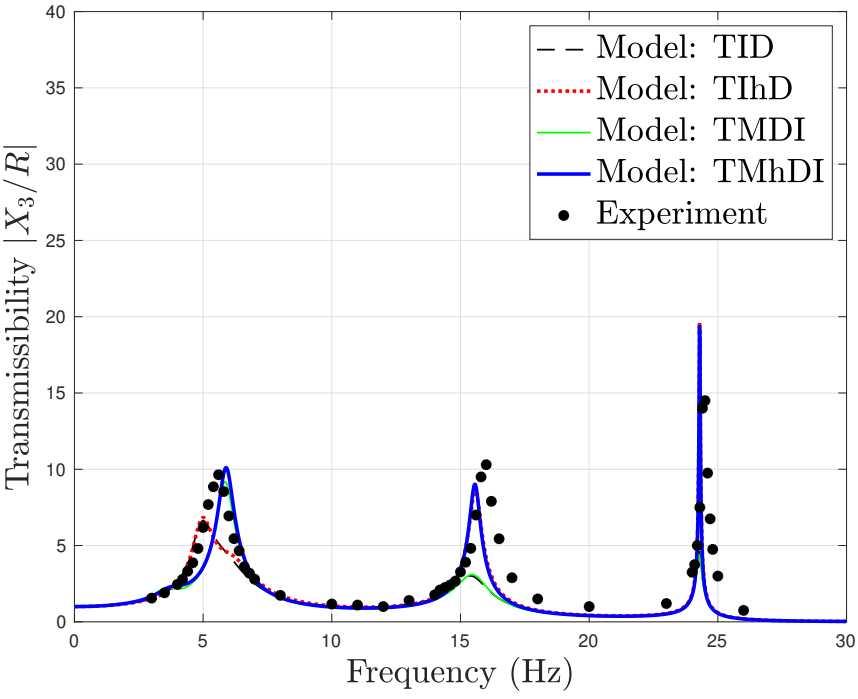

(b)

Figure 7.5: The 3-storey structure's top storey transmissibility (a) Experiment vs TMhDI model (b) Experiment vs all four analytical models (TID, TIhD, TMDI, TMhDI)

Table 7.1 presents the parameters of the uncontrolled 3-storey structure in Figure 7.4(a) and Table 7.2 presents the parameters of the models in Figure 7.4 and 7.5.

Table 7.1: Parameters of the 3-storey uncontrolled structue

Parameters	Storey 1	Storey 3	Storey 3
Mass, (kg)	33.15	24.15	24.15
Stiffness, (kN/m)	140.48	168.58	207.92

Table 7.2: Parameters of the TIBD systems

Parameters	TID	TMDI	TIhD	TMhDI
Inertance, b_d(Ns^2/m)	18	18	18	18
Stiffness, k_d(N/m)	21000	21000	21000	21000
Viscous damping, c_d(Ns/m)	340.65	340.65	–	–
Loss factor, η	–	–	0.53	0.53
Secondary mass, m_d(Ns^2/m)	–	16	–	16

The results of this experiment is presented in Figure 7.5(a) and 7.5(b). In Figure 7.5(a) the analytical model of the TMhDI is compared with the experiment. The result shows a good agreement between the model and the experiment. Figure 7.5(b) shows comparison between experiment and some analytical models of inerter-based-dampers: TID, TIhD, TMDI, and TMhDI. It is obvious from the first resonance that both the TIhD and TID are not in a good agreement with the experiment. This suggests that the mass of the flywheel m_d cannot be neglected in the model. The TMDI model shows a much lower response around the second and third resonances compared to the experiment. This suggets that the hysteretic damping model of the gel dampers must be treated in its original form and cannot be converted to a viscous damping.

From the above discussion, it is clear that the TMhDI model proposed in this chapter is accurate enough to capture the real behaviour of the structural system equipped with TMhDI device. Furthermore, the effectiveness of the TMhDI can be observed by comparing the structural response between the three cases: (1) Uncontrolled; (2) 3-storey structure equipped with gel dampers; (3) 3-storey structure equipped with a TMhDI. Comparing all the performance of the structure for all these three cases makes it obvious that the structural performance gets better with the gel dampers and is best with the TMhDI as can be seen in Figure 7.6(a). This is also shown in the time domain in Figure 7.6(b), it is obvious that with TMhDI, the structure achieves its best performance among all the scenarios considered.

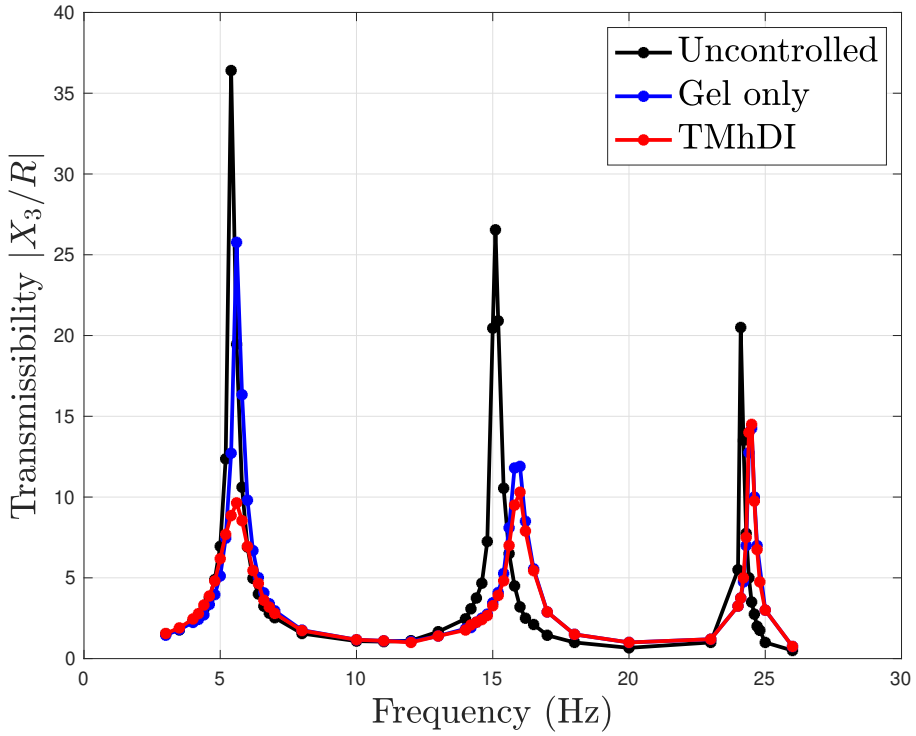

(a)

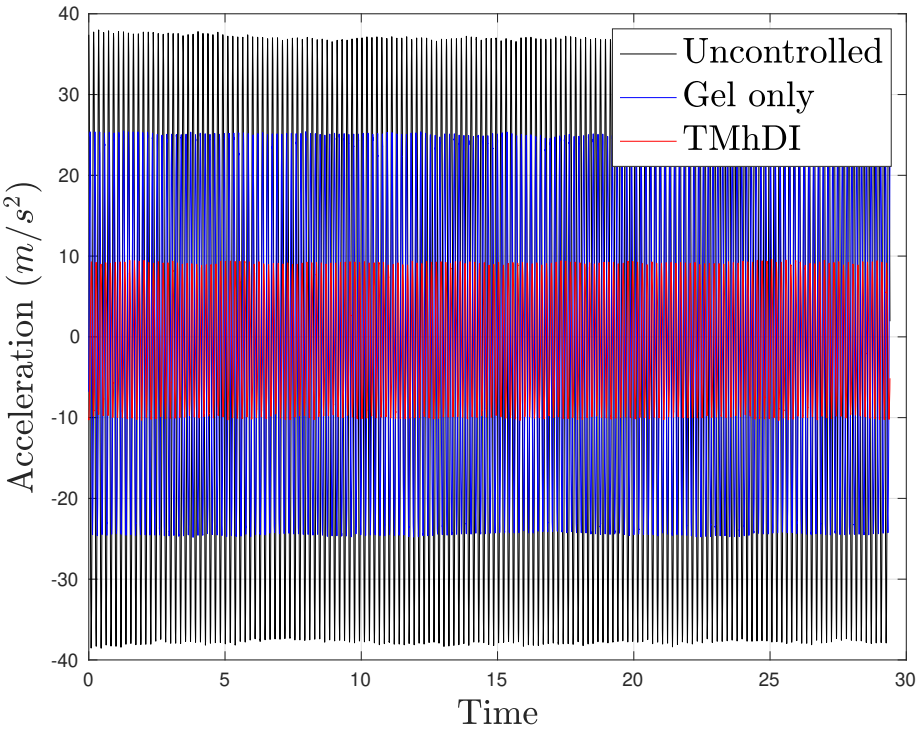

(b)

Figure 7.6: Experimental results (a) Transmissibility (b) Time domain response at first resonance, f=5.50Hz

7.3.2 Earthquake ground motion

The second part of the experiment is the earthquake ground motion. Nine selected earthquake ground motions were applied as the ground motion input. The earthquake ground motions data were taken from http://strongmotioncenter.org/.

Due to the limitation of the shake table equipment, the lowest allowable frequency of the input signal is 3Hz. Therefore the earthquake ground motion data was scaled so that the minimum frequency content of the earthquakes was 3Hz and the predominant frequency of the earthquakes was around 5Hz, which is close the first resonance frequency of the structure. The scaled earthquake ground motion data and their Fourier Transforms are given in Figure 7.7 and 7.8 respectively.

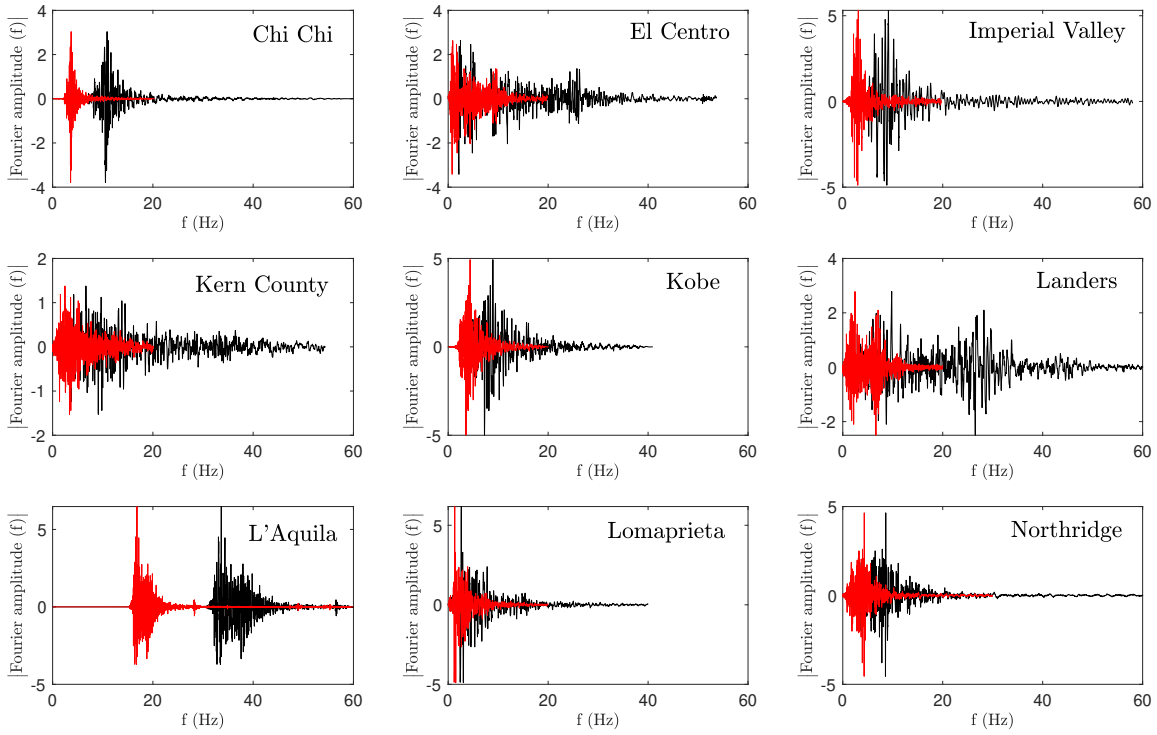

Figure 7.7: Acceleration data of the considered earthquakes. Before scaling (—), after scaling (—)

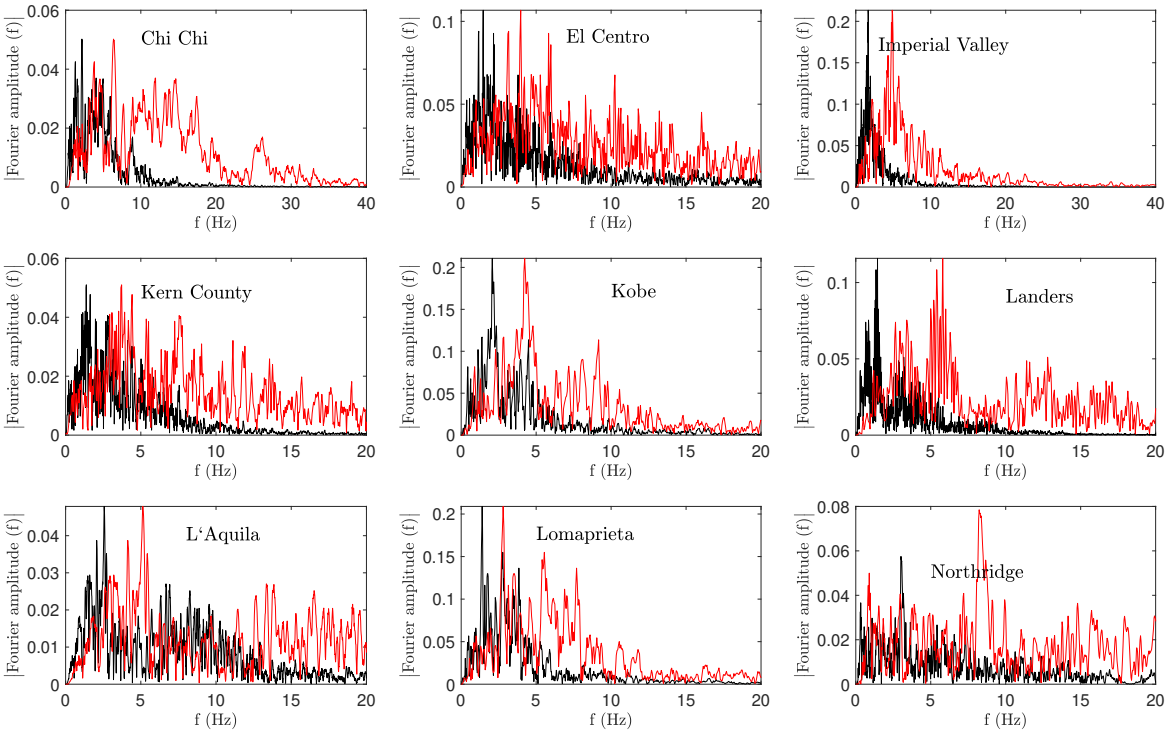

Figure 7.8: Fourier Spectrum of the considered earthquakes ground motion. Before scaling (—), after scaling (—)

To assess the effectiveness of the TMhDI, the top storey response of the structure wes obtained for each earthquake. The response comparison between the uncontrolled structure and the structure equipped with the TMhDI for all earthquakes is presented in Figure 7.9. For all cases, it is obvious that the TMhDI was capable of effectively reducing the response of the structure.

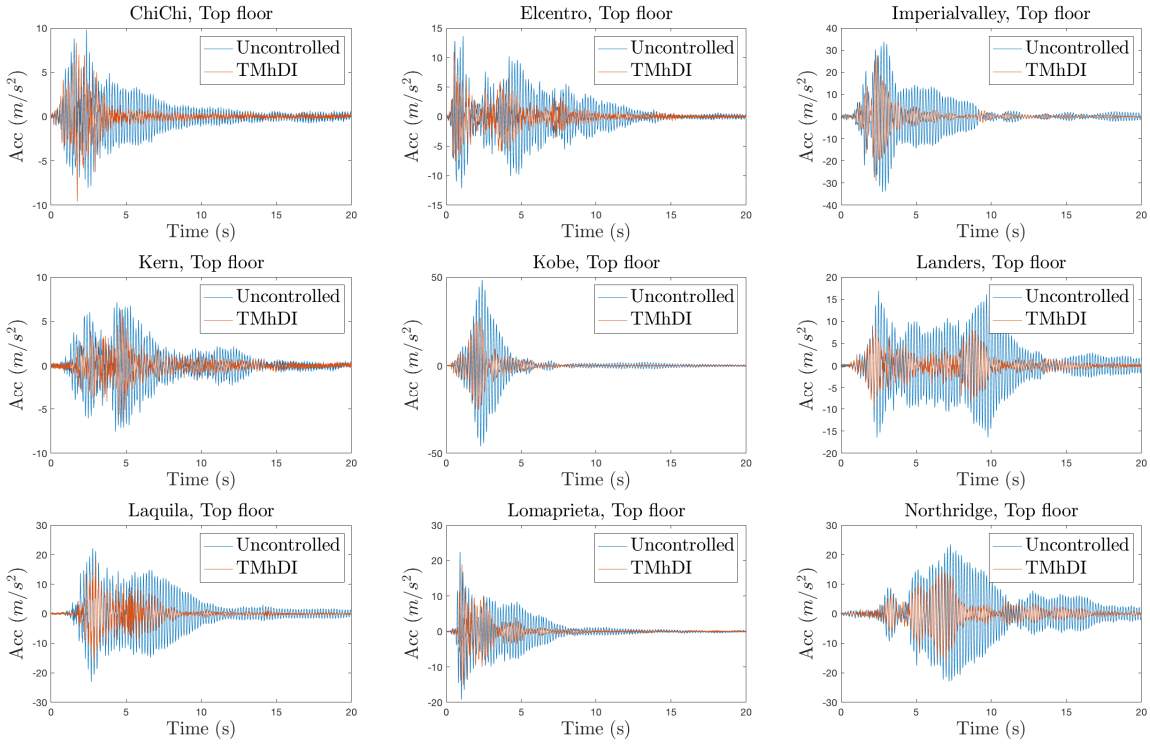

Figure 7.9: Top storey response of the 3-storey structure to all considered earthquakes ground motion

7.4 Experiment 2: 3-storey structure equipped with a TMDI

The second type of damper discussed in this thesis is the ECD made from a series of magnets and aluminium plates as discussed in detail in Chapter 6. These ECDs are the realisation of the viscous damping. To form a TMDI, these ECDs were connected in parallel to four flexible steel plates. A flywheel inerter was then connected in series to this parallel spring-dampers.

The lumped-mass model and photograph of the 3-storey structure equipped with a TMDI can be seen in Figure 7.10(a) and (b), respectively. It should be noted that the structural damping is neglected in the model. The equations of motion of the structure in absolute coordinates are given in Equation 7.1. The force transferred to the structure by the TMDI $F_{1,0}$ can be expressed similar to that in Equation 5.19 of the TMhDI with the complex stiffness is replaced by viscous damping and stiffness in parallel. Hence, the Equation becomes

$$F_{1,0} = \frac{b_d s^2 (c_d s + k_d)(R - X_1) - b_d s^2 m_d s^2 X_1}{(m_d + b_d)s^2 + (c_d s + k_d)} \tag{7.3}$$

Next, detailed discussions are presented for the experiments which again consisted

of two parts: (1) harmonic ground motion; (2) Earthquake ground motion.

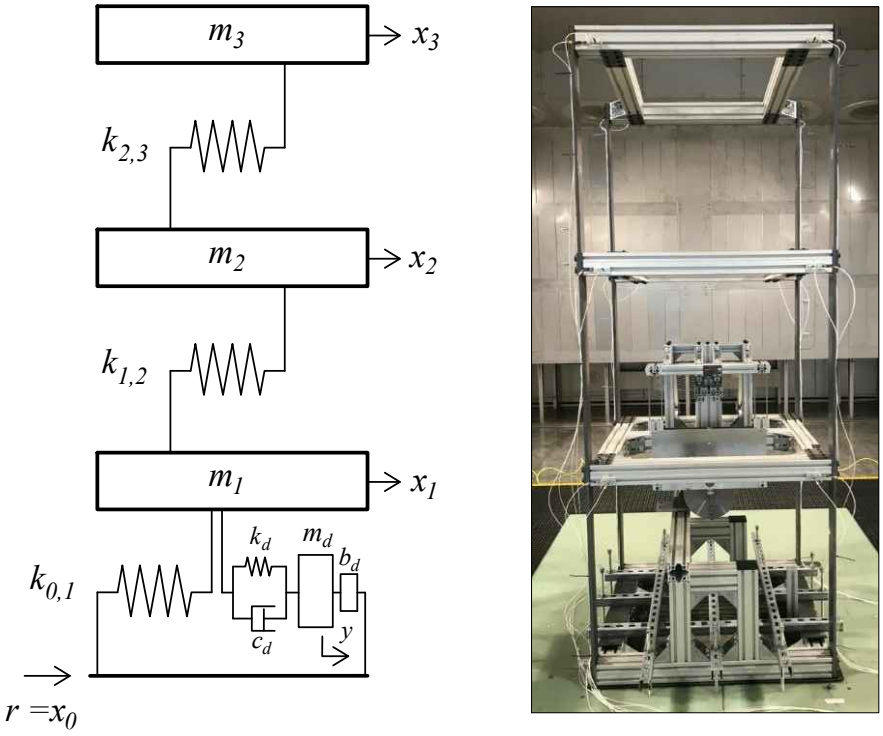

Figure 7.10: System layout: (a) lumped-mass model (b) 3-storey structure with TMDI

7.4.1 Harmonic ground motion

As shown in Figure 7.10(b), the installation of the TMDI adds some extra mass on the first storey of the structure. Therefore, this experiment is important to verify the mass and stiffness of each storey of the structure.

Similar to previous Section 7.3.1, this first part of the experiments consisted of three cases as shown in Figure 7.11: (1) Uncontrolled structure (2) with ECDs only, and (3) with TMDI. The first case was uncontrolled structure without any dampers. This experiment is necessary in order to verify the mass and stiffness parameters of the structure. In this experiment, the TMDI system was also mounted on the structure. However, the second terminal of the flywheel inerter is disconnected to the steel bar. Therefore, non of the dampers and inerter were mobilised.

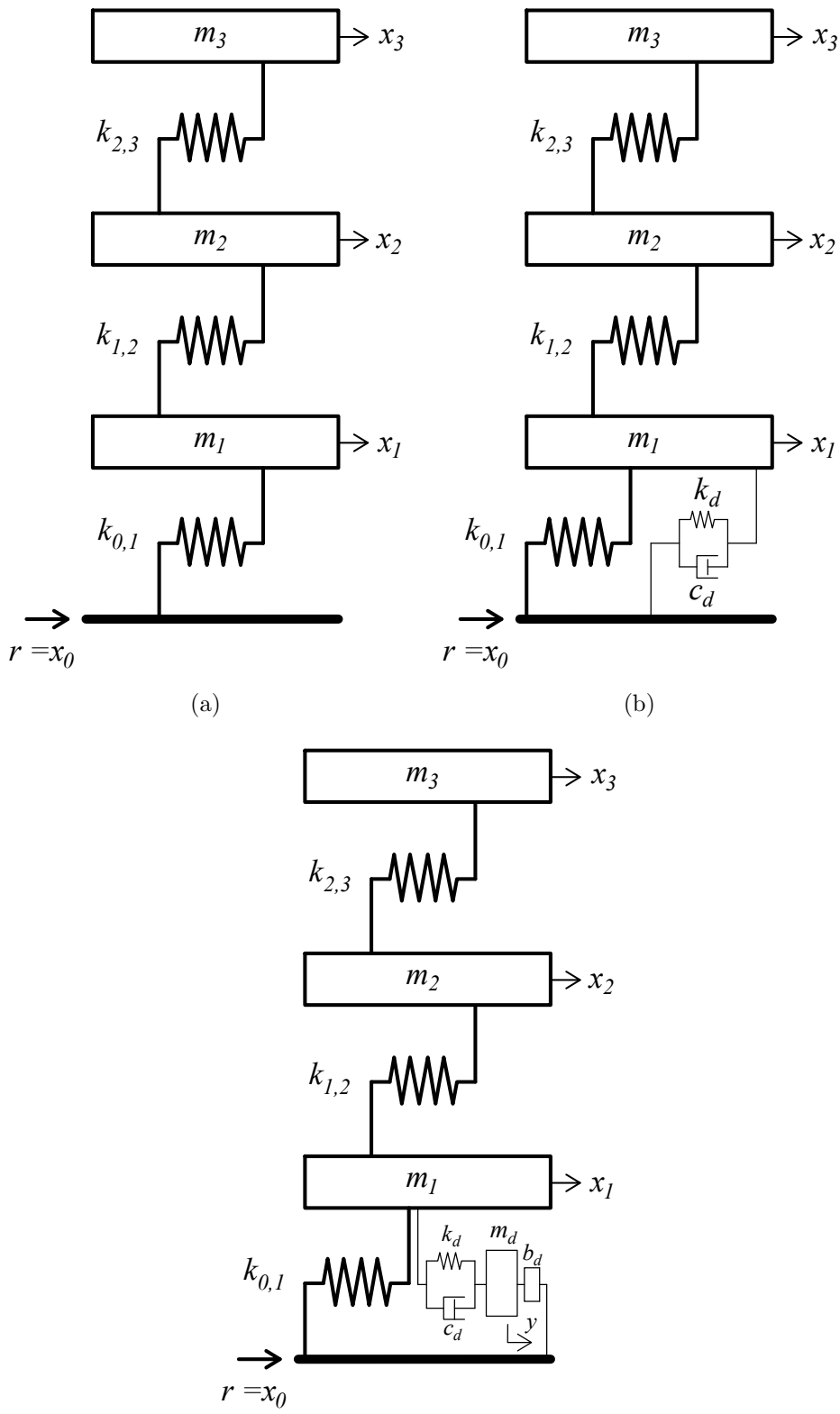

Figure 7.11: Lumped-mass model of the three cases: (a) uncontrolled (b) with ECDs only (c) with TMDI

The result of this uncontrolled structure experiment is presented in Figure 7.12(a).

As can be seen in this figure that the experiment and the analytical model are in good agreeement. Therefore, the mass and stiffness properties of the structures can be used for optimisation of the TMDI. Similar to the previous structure with the TMhDI system, it can be concluded from this figure that the damping of the structure is negligible.

The second case was the 3-storey structure equipped with the ECDs, without inerter. This experiment was performed to verify the viscous damping and stiffness properties of the ECDs obtained from the experiment discussed in Chapter 6. The result is presented in Figure 7.12(b). In this figure, two analytical models are proposed: (1) Hysteretic damping model; (2) Viscous damping model. In the first model, the ECDs are represented by a complex stiffness $k_d(1 + j\eta)$, where the loss factor η is obtained from an equivalent viscous damping. k_d is the stiffness of the four flexible plates connected in parallel to the ECDs. The second model assumes that the gel dampers have viscous damping and stiffness in parallel. The stiffness k_d and viscous damping c_d are obtained from Chapter 6.

Figure 7.12(b) clearly shows that the results from the experiment are very close to the viscous damping model. This suggests that viscous damping is a good representation of the ECDs. Obvious differences can be observed around the second and third resonances. Around these resonances, the response with hysteretic damping model is far higher than the viscous damping model and the experiment.

The third case was a 3-storey structure equipped with a TMDI. As can be seen in Figure 7.10(b), the TMDI was placed between the table and the first storey of the structure. The first terminal of the flywheel inerter was fixed to the stiff frame which was fixed to the table. The second terminal of the inerter is connected to the stiff bar which was connected to four flexible steel plates. These plates were connected in parallel to two sliding plates of the ECDs. The analytical model of the TMDI is depicted in Figure 7.10(a). The ECDs damping is represented by c_d. b_d is the inertance of the flywheel, and m_d is the mass of the flywheel.

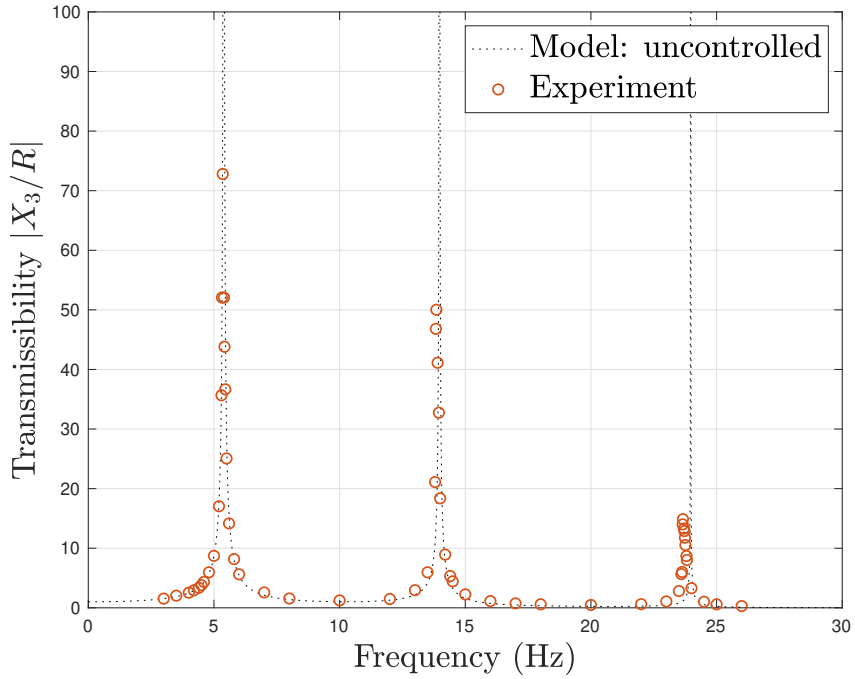

(a)

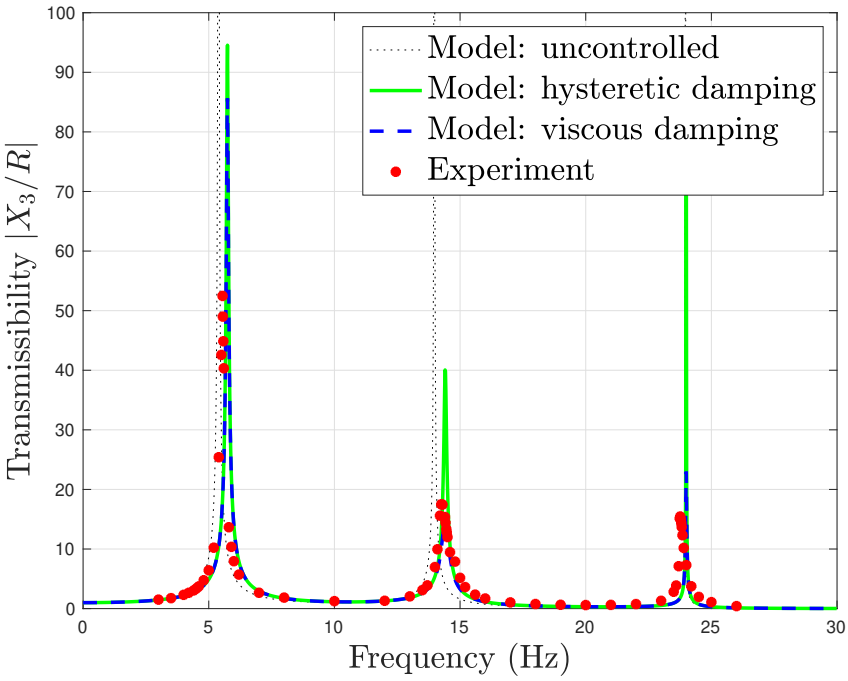

(b)

Figure 7.12: (a) The 3-storey structure's top storey transmissibility: uncontrolled structure, analytical vs experiment (b) The 3-storey structure's top storey transmissibility when equipped with hysteretic damping (green line) and with viscous damping (blue dash line) vs experiment with ECD only, without inerter

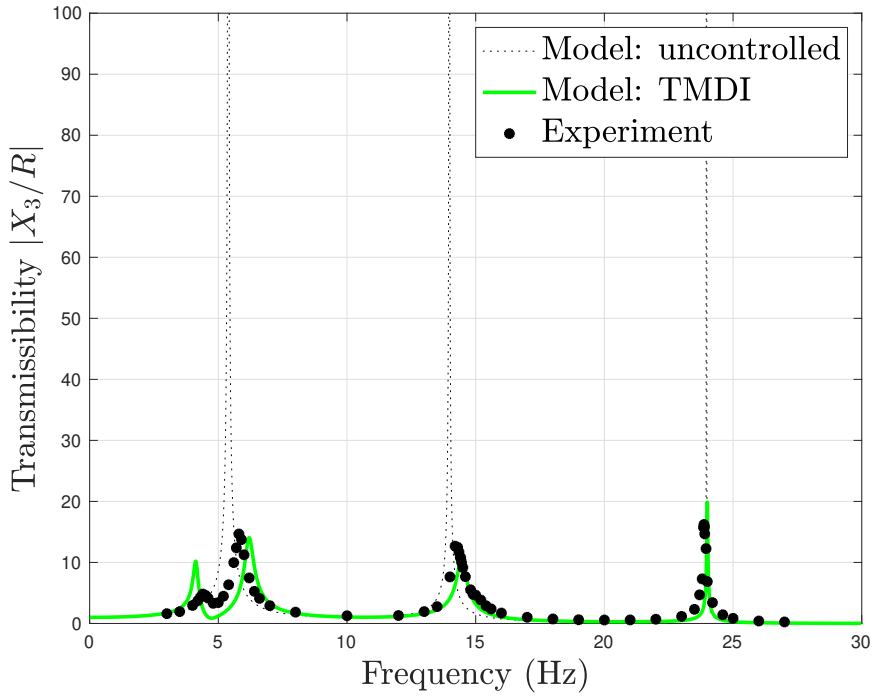

(a)

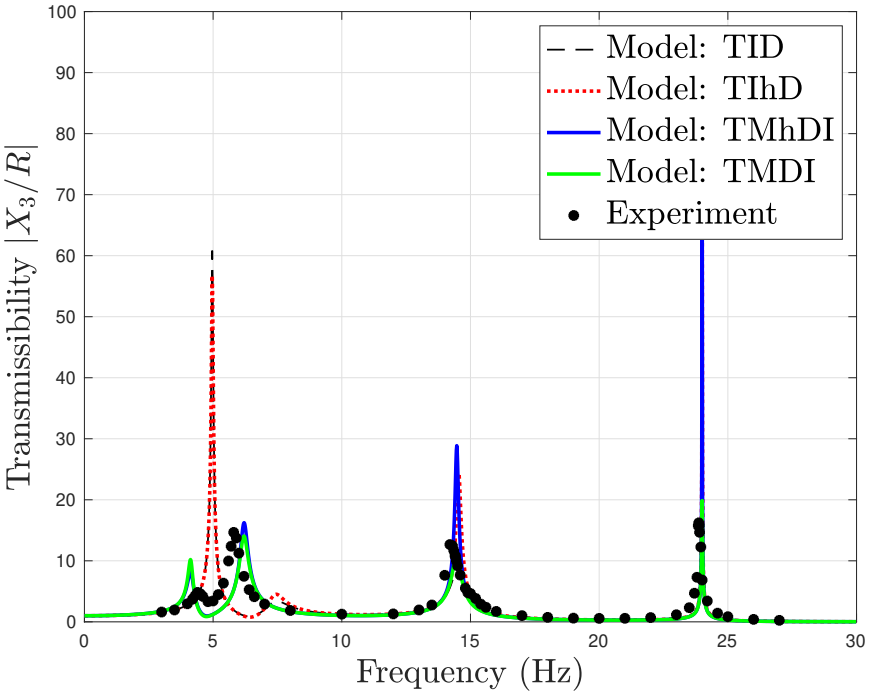

(b)

Figure 7.13: The 3-storey structure's top storey transmissibility (a) Experiment vs TMDI model (b) Experiment vs all four analytical models (TID, TIhD, TMDI, TMhDI)

Table 7.3 presents the parameters of the uncontrolled 3-storey structure in Figure

7.12(a) and Table 7.4 presents the parameters of the models in Figure 7.12 and 7.13.

Table 7.3: Parameters of the 3-storey uncontrolled structue

Parameters	Storey 1	Storey 3	Storey 3
Mass, (kg)	42.15	24.15	24.15
Stiffness, (kN/m)	140.48	168.58	207.92

Table 7.4: Parameters of the TIBD systems

Parameters	TID	TMDI	TIhD	TMhDI
Inertance, b_d(Ns^2/m)	15	15	15	15
Stiffness, k_d(N/m)	29700	29700	29700	29700
Viscous damping, c_d(Ns/m)	109	109	–	–
Loss factor, η	–	–	0.12	0.12
Secondary mass, m_d(Ns^2/m)	–	16	–	16

The results of this experiment are presented in Figure 7.13(a) and 7.13(b). In Figure 7.13(a) the analytical model of the TMDI is compared with the experiment. The result shows a good agreement between the model and the experiment. Figure 7.5(b) shows comparison between experiment and some analytical models of inerter-based-dampers: TID, TIhD, TMDI, and TMhDI. It is obvious from the first resonance that both the TIhD and TID are not in a good agreement with the experiment. It suggests that the mass of the flywheel m_d cannot be neglected in the model. The TMhDI model shows a much larger response around the second and third resonances compared to the experiment. It suggets that the ECDs behave as linear viscous rather than hysteretic, and therefore the TMDI model is a good representation of the device.

From the above discussion, it is clear that the proposed model in this chapter is accurate enough to capture the real behaviour of the structural system. Furthermore, the effectiveness of the TMDI can be observed by comparing the structural response between the three cases: (1) Uncontrolled; (2) 3-storey structure equipped with ECDs; and (3) 3-storey structure equipped with a TMDI. Comparing all the performance of the structure for all these three cases makes it obvious that the structural performance gets better with the ECDs and best with the TMDI as can be seen in Figure 7.14(a). Shown in Figure 7.14(b) is the structural response at the first resonance in the time domain. It is obvious that with TMDI the structure achieves its best performance among all the scenarios considered.

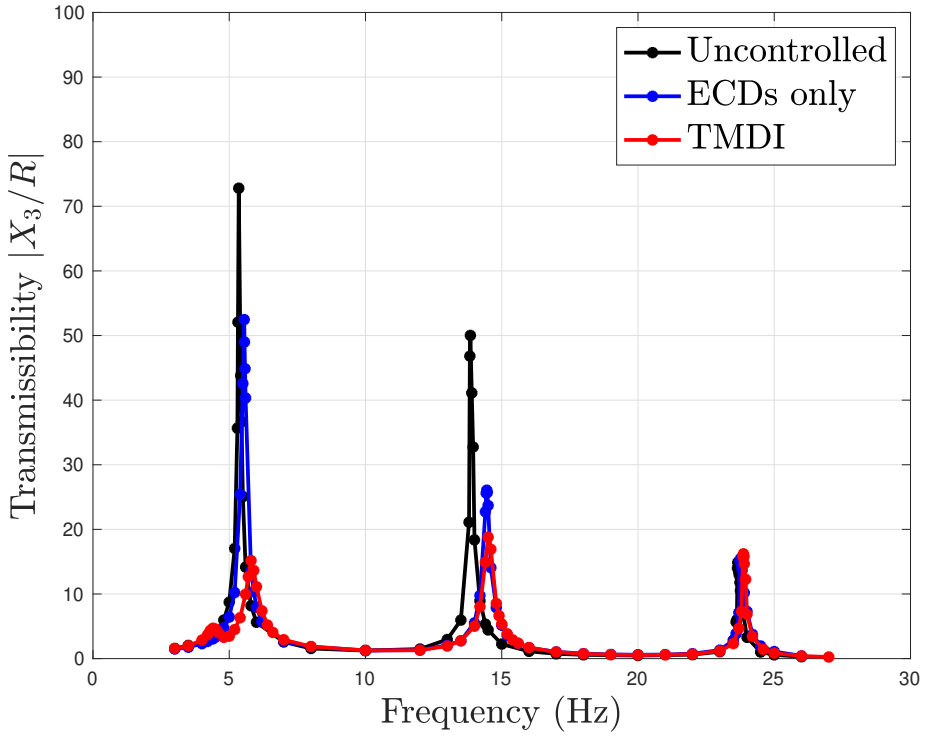

(a)

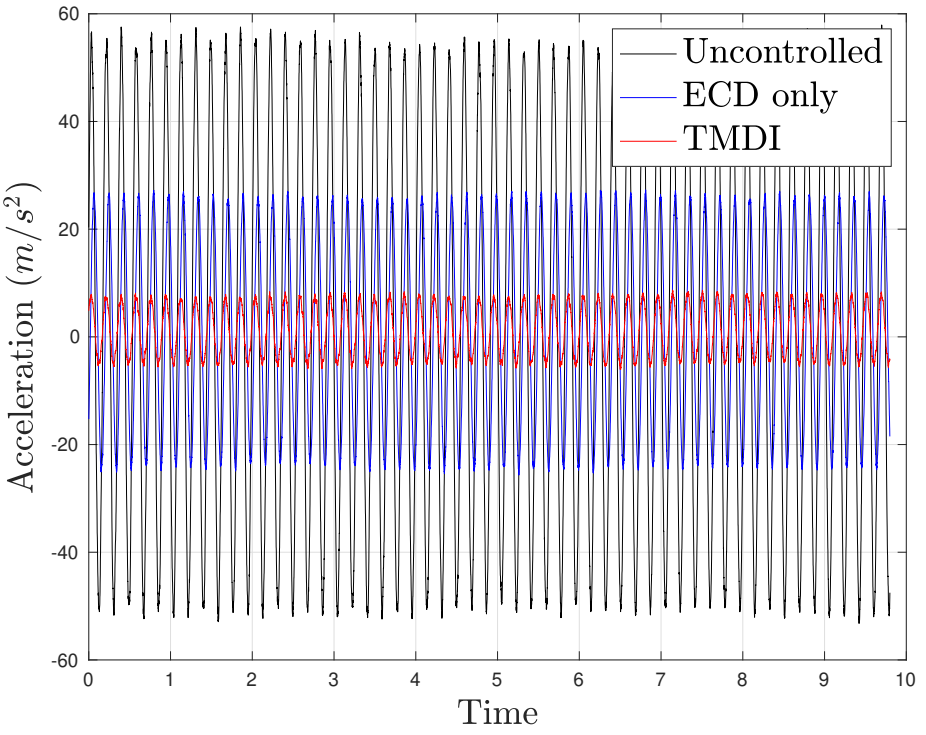

(b)

Figure 7.14: Experimental results (a) Transmissibility (b) Time domain response at f=5.40Hz

7.4.2 Earthquake ground motion

In this experiment, eight selected ground motions were selected as the base acceleration input: El Centro, Imperial Valley, Kern, Kobe, Landers, L'aquila, Loma Prieta, and Northridge. The acceleration data and their Fourier Transforms are given in Figure 7.7 and 7.8 respectively.

Figure 7.15 shows the top storey response of the 3-storey structure with and without TMDI. It clearly shows improvement on the structural response when the structure was equipped with the TMDI.

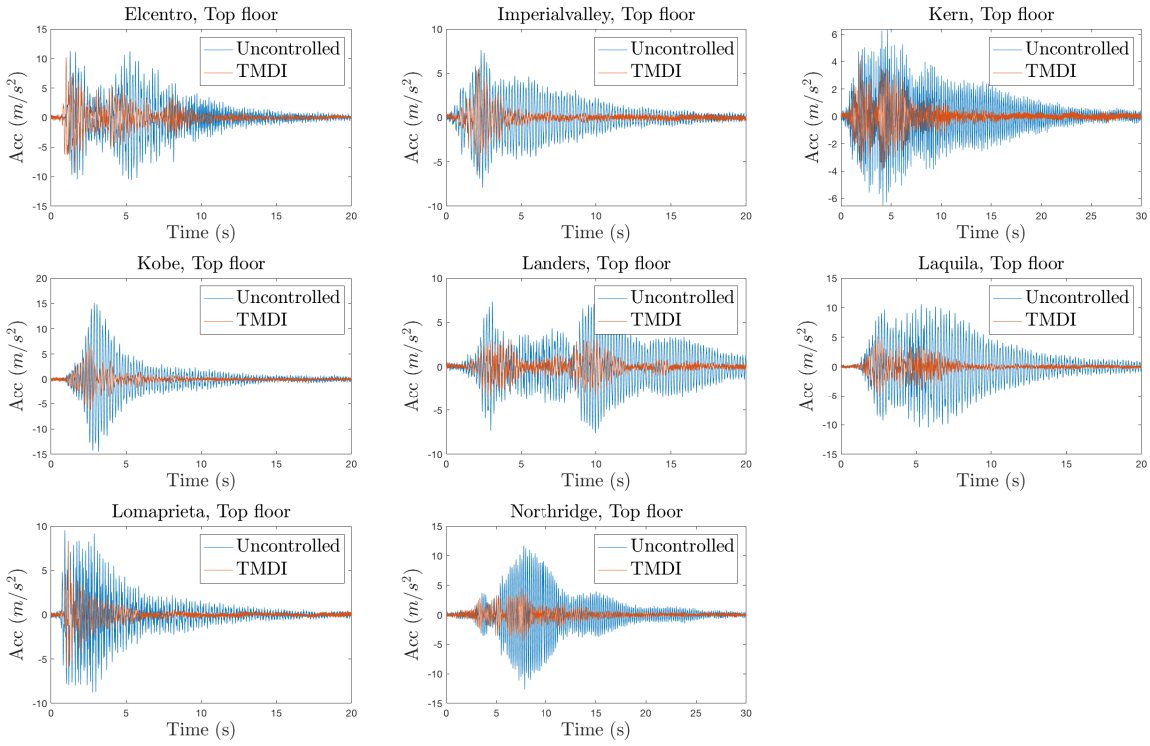

Figure 7.15: Top storey response of the 3-storey structure to all considered earthquakes ground motion

7.5 Experimental Errors

The experiments discussed in Section 7.3 and 7.4 have been successfully performed and the results have been shown to be in good agreement with the models. However, there are some possible source of errors that might occur during the experiments.

It should be noted that in the experimental results, discrepancies may occur around the third resonance because at high frequency the structural response is very low. It was observed from the experiments that the flywheel inerter was barely mobilised. Increasing the amplitude of input base acceleration might help, but it could damage the structure, and for this reason such tests where not carried out.

Another possible error is that, at high frequency of excitation, the gel dampers may exhibit nonlinearity which cannot be captured by the models. As discussed in Chapter 6 that the stiffness of the gel damper increases with the increasing of frequency. Similarly, the ECD may also exhibit nonlinearity due to friction between the sliding plate and the magnets.

7.6 Summary

This chapter presents a set of shake table experiments of a 3-storey structure. The first part of the experiments employed a TMhDI device consisting of two identical gel dampers and a flywheel inerter installed between the table and the first storey of the structure. The second part of the experiments employed TMDI device consisting of 4 ECDs in parallel with 4 flexible steel plates and in series with a flywheel inerter.

Four analytical models are proposed to be compared with the experimental results: TID, TIhD, TMDI, and TMhDI. The difference between these models has been extensively discussed in Chapter 5 and in [149], one of the published works from this Thesis.

The experiment with gel dampers and flywheel inerter shows that the proposed TMhDI model can accurately predict the real behaviour of the structural system. It suggests that the proposed complex stiffness model is a good representation of the damping and stiffness properties of the gel dampers.

The experiment with parallel-connected ECDs and flexible steel plates and flywheel inerter in series shows that the proposed TMDI model is in a good agreement with the experimental results. It also suggests that the damping properties of the ECDs can be accurately modelled by a linear viscous damping model.

Overall, the results from the shake table experiments presented in this chapter support the arguments and discussion presented in Chapter 5: (1) when dampers exhibit linear hysteresis, it must be treated as its original form, complex stiffness for analysis in both frequency and time-domain. (2) In MDOF structure, the structural response with TMDI compared to TMhDI is significantly different, particularly around the second and the third mode of vibrations. Therefore, the damping properties of both devices must be treated as its original form as the equivalent viscous damping method cannot be any accurate.

Chapter 8

Conclusions and Future Work

8.1 Key Summary of the Thesis

There has been a growing amount of research on inerters since the late nineties, exploring their potential use for various applications in mechanical, aerospace and civil engineering.

The use of inerters for protecting building structures against earthquakes has been the main focus of this thesis. Inerters are often combined with spring and damping elements to achieve an absorber-like effect, namely inerter-based dampers. The state of the art of the inerter applications for vibration suppression has led to three most commonly discussed inerter based dampers: TID, TMDI and TVMD.

8.1.1 TIBhD new models

Using linear hysteretic damping for both TID and TMDI is more practical since most damping in civil engineering applications is material damping using rubber and metal. Recent experimental results on a helical fluid inerter [55] demonstrated that the device has hysteresis in its force-velocity relationship. Based on these facts, the linear hysteretic damping in this thesis is defined as two models: (1) complex damping, linear hysteretic in its force-velocity; and (2) complex stiffness, linear hysteretic in its force-displacement.

In Chapter 3, the two linear hysteretic damping models were discussed. Firstly, a complex damping model represented by a parallel-connected inerter-damper was proposed. The model was compared to the helical fluid inerter experimental results. However, it was shown that the helical fluid inerter has strong nonlinearity as a result of friction which is not in the scope of this thesis. Therefore, the discussion on this model was left for future work.

Despite this phenomenon, the helical fluid inerter was also explored in the design perspective due to the coupled damping and inertance parameters. Both damping and inertance formulas have many coupled unknown parameters and so in Chapter

4, a new method was proposed to design the dimensions of the device such that both targeted damping and inertance can be achieved. The results show that the helical fluid inerter can be effectively designed to fit the targeted damping and inertance parameters obtained from the optimisation process. This design method relied on the fact that both inertance and damping parameters are insensitive to changes in some parameters. In effect, these parameters can be chosen based on practical design considerations and the number of unknown parameters reduced. To demonstrate the effectiveness of this approach, three design examples were presented for SDOF, MDOF and a nonlinear fluid inerter. For all these examples, the method was successfully used to design the helical fluid inerter with the targeted inertance and damping parameters.

The second model of the linear hysteretic damping is complex stiffness represented by $k(1+j\eta)$. This model was proposed to represent material dampers most-used in civil engineering applications. Unlike viscous dampers, material dampers are frequency-independent, meaning the energy dissipated per cycle is independent of frequency. Therefore, the complex stiffness is a more accurate model to represent the damping of material dampers. The complex stiffness model has also been reported [144] to be practically very accurate to design structures with a class of nonlinear dampers. Despite its non-causality, it is widely used in practice [97]. The problem with time-domain analysis due to the unstable poles was solved in Chapter 3 based on extending the time-reversal technique first proposed by Inaudi and Makris [98]. The newly developed time-domain method in this chapter has enabled the use of commercial software such as MATLAB to compute the structural response in the time domain, for example using ode45 which is based on the Runge-Kutta method. Moreover, the proposed method has also proven to be compatible with nonstationary random signals such as earthquakes.

The concept of complex stiffness models leads to two novel TIBhDs variants, namely the TIhD and the TMhDI as discussed in detail in Chapter 5. Inspired by the layout of the TID and the TMDI, both TIhD and TMhDI use complex stiffness to replace parallel stiffness-viscous damping. Compared to the TID and TMDI, both TIhD and TMhDI have a lower response at the high frequency excitations. In MDOF structures, the TIhD and TMhDI show less reduction on the higher mode of vibrations. This indicates that the level of damping at higher modes is less than that shown by the TID and TMDI. From a practical perspective, the TMhDI is considered to be the most realistic. This is because it has mass m_d representing the mass of the inerter and its connections to the dampers.

8.1.2 TIBhD realisation

For the first time, the TMhDI concept has been realised by using a material damper made of gel connected in series to a flywheel inerter. The gel dampers consist of gel layers and a steel plate in the middle which is connected to a flywheel via a rigid

beam. The flywheel is equipped with a linear bearing and linear slider mechanism that converts the transitional motion of the building to the rotational motion of the flywheel. The flywheel is grounded via a rigid frame. The flywheel support connects the centre of the flywheel to the rigid frame. This support can be used to adjust the position of the flywheel relative to the ground. Consequently, the terminal distance also changed. Via this mechanism, the inertance of the flywheel can be easily adjusted. This novel design of TIBhD for the realisation of the TMhDI is one of the key contributions of this thesis.

For a meaningful comparison, a TMDI was also built and experimentally tested. The TMDI consists of an eddy current damper in parallel with flexible plates providing stiffness. These two elements were connected in series to a grounded flywheel inerter. Both the damping and stiffness of this system are adjustable. The damping can be adjusted by adding or taking away the dampers or by changing the distance between the sliding plate and the damper fork. The stiffness element can be adjusted by changing the length of the flexible plates.

8.1.3 TIBhD shake table experiment

Chapter 7 presents the first-ever large-scale shake table experiment of tuned inerter-based dampers. In the first part, a device consisting of gel dampers and a flywheel inerter was proposed as a realisation of the TMhDI concept. In the second, the TMDI was built using the eddy current damper and a flywheel inerter. These devices were installed in the base of the structure, connecting the first storey and the ground.

The results from both experiments show good agreement with the analytical results and show that the structural response reduction around the untargeted modes (second and third modes) is less when the structure is equipped with the TMhDI than with the TMDI. These findings support the theory proposed in Chapter 5 that when a damper exhibits linear hysteretic rather than viscous damping, the equivalent viscous damping approach leads to inaccurate results. For this reason, linear hysteretic damping must be treated as its original form when performing both frequency and time-domain analysis.

8.2 Key Contributions of the Thesis

The key contributions of the thesis are as follows:

- The helical fluid inerter has been shown to have both inertance and damping in parallel. This is interesting because it can be used to build a TVMD or PVID by connecting the device with a spring element in series. However, because both inertance and damping parameters are coupled, it is difficult to know how best to design the device to achieve the targeted parameters from the TVMD/PVID optimum design. Therefore, a new design approach is proposed to simplify the

design of a helical fluid inerter for use as a PVID. The design approach relies on the fact that the damping and inertance are insensitive to changes in some parameters. Consequently, these parameters can be chosen based on practical design considerations, so that the number of unknown parameters can be reduced.

- Two novel inerter-based damper models are proposed in this thesis, namely the TIhD and the TMhDI, which represent both TID and TMDI when their damping exhibits linear hysteresis rather than viscous damping. When the damping of the TID or the TMDI exhibits hysteresis, the equivalent viscous damping approach is often used for simplification which, for the systems considered here, will lead to inaccurate results, particularly for the structural response around the untargeted modes. This was also shown when the damping device was made of gel. Therefore, the TIhD and TMhDI models were proposed as more realistic for both TID and TMDI when their damping is linear hysteretic.

- A challenge associated with the TIhD and the TMhDI time-domain analysis is addressed in this thesis. The complex stiffness in both TIhD and TMhDI is a noncausal model. In effect, using the traditional numerical integration method to solve a system with a complex stiffness leads to an unstable response. Therefore, a new formulation for the time-domain analysis of complex stiffness model is proposed which can solve the equation of motions of a system with complex stiffness in the time domain by using standard MATLAB ODE solvers based on the Runge-Kutta method.

- A novel design of TMhDI is presented in this thesis. The TMhDI was realised by connecting two gel dampers in series with a grounded flywheel inerter. The gel dampers represent the complex stiffness which is a coupled stiffness-damping. A set of characterisation tests was performed using a servohydraulic test machine to characterise the damping properties of the gel dampers. The results showed that the dampers exhibit linear hysteresis rather than viscous damping because the energy dissipated per cycle by the dampers is frequency-independent. The flywheel inerter was designed by using a linear guide mechanism to reduce friction and equipped with a base which can be used to change the centre of the flywheel position relative to the point where the gel dampers were connected so the distance between the two inerter terminals can be adjusted to change its inertance parameter.

- For the first time, a large scale shake table experiment was performed on a structure equipped with a TMhDI. A 2.3m three-storey structure was built on a 3.2 x 2.2m shake table. A set of ground motions were used as the base inputs. The structural response was measured by using accelerometers on each storey. The TMhDI was installed between the first storey and the table. The results show

good agreement between the analytical model and the experiment. In the second part of the experiment, the TMhDI was replaced with a TMDI consisting of an eddy current damper and a flywheel inerter. This second experiment was performed to give a new insight into the experimental data to distinguish between the TMhDI and the TMDI. As predicted by the analytical model, the TMDI showed less response around the untargeted modes. This suggests that the TMhDI cannot be simply converted to the TMDI via an equivalent viscous damping approach but must be treated as its original form with complex stiffness. The time-domain method proposed in this thesis is important in accurately solving such systems in the time domain representation.

8.3 Future Work

8.3.1 Tuned-Inerter-Based-Dampers

- The scope of this thesis has been limited to the linear system only. For future work, it will be important to include the nonlinear behaviour of both the structural and damper parameters as both exhibit nonlinearity due to factors such as friction, backlash and fluid flow. Including the nonlinearity in the models might be required for a more accurate result.

- The helical fluid inerter discussed in Chapter 3 shows an interesting phenomenon, especially on the force versus velocity graphs. The area inside the loop is in unit of power. However, it is still not clear what does it physically mean. Future study is required to learn more about this phenomenon.

- The use of gel in this thesis was found to achieve the targeted loss factor parameter of the TMhDI. However, for other structural systems or real-size building structures, the gel damper might not be suitable due to the required size. Investigation could be carried out to determine how these phenomena scale up to real buildings and structures.

- Finite Element Modelling (FEM) could be useful for modelling the inerter-based dampers. The FE model of the TIBD or TIBhD could simplify the analysis and increase accuracy. Via the FEM, a structure can be modelled with the TIBDs or TIBhDs attached. This would reduce the simplification required (e.g. lumped mass simplification) that may lead to inaccurate results.

8.3.2 Earthquake Protection Devices

- As discussed in Chapter 3, the nonlinear effects such as friction can be observed from the helical fluid inerter experimental results. Since this is beyond the scope

of this thesis, it was decided that this will remain as an open discussion for future work. The proposed method presented in Chapter 4 is accurate enough to design the dimensions of helical fluid inerters with the given optimised parameters. For future work, it would be interesting to develop both a helical fluid inerter device and the complex damping model so that the model can capture the nonlinear effects within the device.

- Larger scale shake table experiments might be useful for proof of the TIBD concept. The shake table experiments presented in this thesis are by far is the largest performed on a structure equipped with a TIBDs except for the TVMD. For future work, not only should larger-scale experiments be considered, but the 6 axists of the ground motions for a more realistic investigation. A new design and modelling of the TIBDs that works in all the 6-axists of the ground motions should also be considered.

- To date, only the TVMD that has been used in real buildings which are all located in Japan. This thesis provides a new insights into realistic TID and TMDI models when their damping exhibits hysteretic rather than viscous via the TIhD and TMhDI models. As a recommendation for the future works, these models should be considered for real application in buildings.

References

[1] A. Coburn and R. Spence, *Earthquake Protection, 2nd edition.* John Wiley and Sons, Ltd, Chichester, 2002. 1

[2] B. A. Bolt, *Earthquakes, 4th edition.* W.H. Freeman and Company, New York, 1999. 1

[3] V. Gioncu and F. Mazzolani, *Ductility of seismic-resistant steel structures.* CRC Press, 2003. 1

[4] "2020 [online] available at: https://www.bbc.co.uk/news/world-asia-38232611 [accessed 12 september 2020]," 1

[5] A. S. Elnashai and L. D. Sarno, *Fundamentals of Earthquake Engineering From Source to Fragility, 2nd edition.* John Wiley and Sons, Ltd, Chichester, 2015. 1

[6] P. Pan, D. Zamfirescu, M. Nakashima, N. Nakayasu, and H. Kashiwa, "Base-isolation design practice in japan: introduction to the post-kobe approach," *Journal of Earthquake Engineering*, vol. 9, no. 01, pp. 147–171, 2005. 2

[7] M. Cutfield, K. Ryan, and Q. Ma, "A case study cost-benefit analysis on the use of base isolation in a low-rise office building," 2014. 2

[8] A. Calabrese, M. Spizzuoco, G. Serino, G. Della Corte, and G. Maddaloni, "Shaking table investigation of a novel, low-cost, base isolation technology using recycled rubber," *Structural Control and Health Monitoring*, vol. 22, no. 1, pp. 107–122, 2015. 2

[9] D. Poon, S.-s. Shieh, L. Joseph, and C. Chang, "Structural design of taipei 101, the world's tallest building," in *Proceedings of the CTBUH 2004 Seoul Conference, Seoul, Korea*, pp. 271–278, 2004. 2, 12, 16

[10] R. Villaverde and L. A. Koyama, "Damped resonant appendages to increase inherent damping in buildings," *Earthquake engineering & structural dynamics*, vol. 22, no. 6, pp. 491–507, 1993. 2

[11] Okumura A, Japan Patent Koukai, H09-177875, 11 July 1997. 2, 16, 17

[12] M. C. Smith, "Synthesis of mechanical networks: The inerter," *IEEE Transactions on Automatic Control*, vol. 47, no. 10, pp. 1648–1662, 2002. 3, 16, 17

[13] F.-C. Wang, M.-F. Hong, and T.-C. Lin, "Designing and testing a hydraulic inerter," *Proceedings of the Institution of Mechanical Engineers, Part C: Journal of Mechanical Engineering Science*, vol. 225, no. 1, pp. 66–72, 2011. 3, 17

[14] K. Ikago, K. Saito, and N. Inoue, "Seismic control of single-degree-of-freedom structure using tuned viscous mass damper," *Earthquake Engineering & Structural Dynamics*, vol. 41, no. 3, pp. 453–474, 2012. 3, 16, 17, 19, 20, 48, 56

[15] Smith MC. 2001. Force-controlling mechanical device. US Patent 7,316,303. 3, 17

[16] W. Shen, A. Niyitangamahoro, Z. Feng, and H. Zhu, "Tuned inerter dampers for civil structures subjected to earthquake ground motions: optimum design and seismic performance," *Engineering Structures*, vol. 198, p. 109470, 2019. 3

[17] S. Nakaminami, H. Kida, K. Ikago, and N. Inoue, "Dynamic testing of a full-scale hydraulic inerter-damper for the seismic protection of civil structures," in *7th International Conference on Advances in Experimental Structural Engineering, AESE 2017*, pp. 41–54, EUCENTRE, 2017. 3

[18] A. Giaralis and F. Petrini, "Wind-induced vibration mitigation in tall buildings using the tuned mass-damper-inerter," *Journal of Structural Engineering*, vol. 143, no. 9, p. 04017127, 2017. 3

[19] R. Zhang, Z. Zhao, and K. Dai, "Seismic response mitigation of a wind turbine tower using a tuned parallel inerter mass system," *Engineering Structures*, vol. 180, pp. 29–39, 2019. 3

[20] Y. Wen, Z. Chen, and X. Hua, "Design and evaluation of tuned inerter-based dampers for the seismic control of mdof structures," *Journal of Structural Engineering*, vol. 143, no. 4, p. 04016207, 2017. 3

[21] Z. Zhao, R. Zhang, Y. Jiang, and C. Pan, "Seismic response mitigation of structures with a friction pendulum inerter system," *Engineering Structures*, vol. 193, pp. 110–120, 2019. 3

[22] D. De Domenico, G. Ricciardi, and R. Zhang, "Optimal design and seismic performance of tuned fluid inerter applied to structures with friction pendulum isolators," *Soil Dynamics and Earthquake Engineering*, vol. 132, p. 106099, 2020. 3

[23] L. Marian and A. Giaralis, "Optimal design of inerter devices combined with tmds for vibration control of buildings exposed to stochastic seismic excitation," in *Safety, Reliability, Risk and Life-Cycle Performance of Structures and Infrastructures-Proceedings of the 11th International Conference on Structural Safety and Reliability, ICOSSAR 2013*, pp. 1025–1032, CRC Press, 2013. 3

[24] F.-C. Wang, C.-H. Lee, and R.-Q. Zheng, "Benefits of the inerter in vibration suppression of a milling machine," *Journal of the Franklin Institute*, vol. 356, no. 14, pp. 7689–7703, 2019. 3

[25] A. Ogawa and K. Adachi, "Theoretical studies of function of planetary gear inerter on torsional vibration system of rotating machine train," *Transactions of Society of Automotive Engineers of Japan*, vol. 48, no. 5, 2017. 3

[26] F.-C. Wang, M.-K. Liao, B.-H. Liao, W.-J. Su, and H.-A. Chan, "The performance improvements of train suspension systems with mechanical networks employing inerters," *Vehicle System Dynamics*, vol. 47, no. 7, pp. 805–830, 2009. 3, 4

[27] F.-C. Wang and W.-J. Su, "Impact of inerter nonlinearities on vehicle suspension control," *Vehicle System Dynamics*, vol. 46, no. 7, pp. 575–595, 2008. 3

[28] Y. Li, J. Z. Jiang, and S. Neild, "Inerter-based configurations for main-landing-gear shimmy suppression," *Journal of Aircraft*, vol. 54, no. 2, pp. 684–693, 2017. 3

[29] X. Dong, Y. Liu, and M. Z. Chen, "Application of inerter to aircraft landing gear suspension," in *2015 34th Chinese Control Conference (CCC)*, pp. 2066–2071, IEEE, 2015. 3

[30] Y. Li, J. Z. Jiang, P. Sartor, S. A. Neild, and H. Wang, "Including inerters in aircraft landing gear shock strut to improve the touch-down performance," *Procedia engineering*, vol. 199, pp. 1689–1694, 2017. 3

[31] Y. Li, C. Howcroft, S. A. Neild, and J. Z. Jiang, "Using continuation analysis to identify shimmy-suppression devices for an aircraft main landing gear," *Journal of Sound and Vibration*, vol. 408, pp. 234–251, 2017. 3

[32] Y. Li, J. Z. Jiang, S. A. Neild, and H. Wang, "Optimal inerter-based shock–strut configurations for landing-gear touchdown performance," *journal of aircraft*, vol. 54, no. 5, pp. 1901–1909, 2017. 3

[33] M. T. Fox, J. M. Roach, and E. A. Howell, "Translational inerter assembly and method for damping movement of a flight control surface," Dec. 4 2018. US Patent 10,145,434. 3

[34] Y. Zhang, N. Hu, Z. Cheng, L. Zhang, and H. Chen, "Dynamic modeling of the aircraft landing gear based on isd mechanism," in *2018 Prognostics and System Health Management Conference (PHM-Chongqing)*, pp. 344–349, IEEE, 2018. 3

[35] K. Saito, Y. Sugimura, S. Nakaminami, H. Kida, and N. Inoue, "Vibration tests of 1-story response control system using inertial mass and optimized soft spring and viscous element," *Journal of Structural Engineering*, vol. 54, pp. 623–634, 2008. 3, 19, 57

[36] Y. Sugimura, W. Goto, H. Tanizawa, K. Saito, and T. Nimomiya, "Response control effect of steel building structure using tuned viscous mass damper," in *Proceedings of the 15th World Conference on Earthquake Engineering*, 2012. 3, 4, 17, 19

[37] I. Lazar, S. Neild, and D. Wagg, "Using an inerter-based device for structural vibration suppression," *Earthquake Engineering & Structural Dynamics*, vol. 43, no. 8, pp. 1129–1147, 2014. 3, 4, 17, 20, 22, 24, 70, 74, 77, 78, 85, 90, 95

[38] J. P. Den Hartog, *Mechanical vibrations*. Courier Corporation, 1985. 3, 11, 20, 21, 69, 74

[39] L. Marian and A. Giaralis, "Optimal design of a novel tuned mass-damper–inerter (tmdi) passive vibration control configuration for stochastically support-excited structural systems," *Probabilistic Engineering Mechanics*, vol. 38, pp. 156–164, 2014. 3, 20

[40] D. Pietrosanti, M. De Angelis, and M. Basili, "Optimal design and performance evaluation of systems with tuned mass damper inerter (tmdi)," *Earthquake Engineering & Structural Dynamics*, vol. 46, no. 8, pp. 1367–1388, 2017. 4, 20

[41] D. De Domenico and G. Ricciardi, "An enhanced base isolation system equipped with optimal tuned mass damper inerter (tmdi)," *Earthquake Engineering & Structural Dynamics*, vol. 47, no. 5, pp. 1169–1192, 2018. 4, 15, 24, 95

[42] Y. Hu, M. Z. Chen, Z. Shu, and L. Huang, "Analysis and optimisation for inerter-based isolators via fixed-point theory and algebraic solution," *Journal of Sound and Vibration*, vol. 346, pp. 17–36, 2015. 4, 21, 24, 50, 69, 70, 73

[43] S. Y. Zhang, J. Z. Jiang, and S. Neild, "Optimal configurations for a linear vibration suppression device in a multi-storey building," *Structural Control and Health Monitoring*, vol. 24, no. 3, p. e1887, 2017. 4

[44] A. Gonzalez-Buelga, I. F. Lazar, J. Z. Jiang, S. A. Neild, and D. J. Inman, "Assessing the effect of nonlinearities on the performance of a tuned inerter damper," *Structural Control and Health Monitoring*, 2016. 4

[45] X. Sun, L. Chen, S. Wang, X. Zhang, and X. Yang, "Performance investigation of vehicle suspension system with nonlinear ball-screw inerter," *International journal of automotive technology*, vol. 17, no. 3, pp. 399–408, 2016. 4

[46] Y. Shen, L. Chen, Y. Liu, and X. Zhang, "Modeling and optimization of vehicle suspension employing a nonlinear fluid inerter," *Shock and Vibration*, vol. 2016, 2016. 4

[47] F. de Haro Moraes, M. Silveira, and P. J. P. Gonçalves, "On the dynamics of a vibration isolator with geometrically nonlinear inerter," *Nonlinear Dynamics*, vol. 93, no. 3, pp. 1325–1340, 2018. 4

[48] I. Lazar, S. Neild, and D. Wagg, "Vibration suppression of cables using tuned inerter dampers," *Engineering Structures*, vol. 122, pp. 62–71, 2016. 4

[49] D. De Domenico, P. Deastra, G. Ricciardi, N. Sims, and D. Wagg, "Novel fluid inerter based tuned mass dampers for optimised structural control of base-isolated buildings," *Journal of the Franklin Institute*, vol. 356, no. 14, pp. 7626 – 7649, 2019. Special Issue on Inerter-based Systems. 4, 32, 49, 61, 63, 95

[50] Y. Hu, M. Z. Chen, S. Xu, and Y. Liu, "Semiactive inerter and its application in adaptive tuned vibration absorbers," *IEEE Transactions on Control Systems Technology*, vol. 25, no. 1, pp. 294–300, 2016. 4

[51] Y. Nakamura, A. Fukukita, K. Tamura, I. Yamazaki, T. Matsuoka, K. Hiramoto, and K. Sunakoda, "Seismic response control using electromagnetic inertial mass dampers," *Earthquake Engineering & Structural Dynamics*, vol. 43, no. 4, pp. 507–527, 2014. 4, 18

[52] P. Brzeski, M. Lazarek, and P. Perlikowski, "Experimental study of the novel tuned mass damper with inerter which enables changes of inertance," *Journal of Sound and Vibration*, vol. 404, pp. 47–57, 2017. 4, 20

[53] D. Pietrosanti, M. De Angelis, and A. Giaralis, "Experimental study and numerical modeling of nonlinear dynamic response of sdof system equipped with tuned mass damper inerter (tmdi) tested on shaking table under harmonic excitation," *International Journal of Mechanical Sciences*, vol. 184, p. 105762, 2020. 4

[54] A. L. Kimball and D. E. Lovell, "Internal friction in solids," *Phys. Rev.*, vol. 30, pp. 948–959, Dec 1927. 4, 26, 67

[55] N. Smith and D. Wagg, "A fluid inerter with variable inertance properties," in *6th European Conference on Structural Control, Sheffield, England*, 2016. 4, 16, 18, 26, 29, 46, 48, 144

[56] I. G. A. Susila, *Experimental and Numerical Studies of Masonry Wall Panels and Timber Frames of Low-rise Structures under Seismic Loadings in Indonesia*. PhD thesis, The School of Mechanical Aerospace and Civil Engineering, University of Manchester, 2014. 6, 8

[57] I. F. Lazar, *The Use of Inerters for Vibration Suppression in Structures*. PhD thesis, Department of Mechanical Engineering, University of Bristol, 2015. 6

[58] I. U. Khan, *Vibration Suppression in Flexible Structures using Hybrid Active and Semi-active Control*. PhD thesis, Department of Mechanical Engineering, University of Sheffield, 2017. 6

[59] N. Makris, "Seismic isolation: Early history," *Earthquake Engineering & Structural Dynamics*, vol. 48, no. 2, pp. 269–283, 2019. 7

[60] E. Staudacher, C. Habacher, and R. Siegenthaler, "Erdbebensicherung in baum," *Neue Zürcher Zeitung. Technikbeilage. Zürich. Switzerland*, 1970. 7

[61] J. Touaillon, "Improvement in buildings," Feb. 15 1870. US Patent 99,973. 7

[62] J. M. Kelly, "Earthquake-resistant design with rubber," 1993. 7

[63] W. H. Robinson, "Lead-rubber hysteretic bearings suitable for protecting structures during earthquakes," *Earthquake Engineering & Structural Dynamics*, vol. 10, no. 4, pp. 593–604, 1982. 8

[64] A. D. Shaw, S. A. Neild, D. J. Wagg, P. M. Weaver, and A. Carrella, "A nonlinear spring mechanism incorporating a bistable composite plate for vibration isolation," *Journal of Sound and Vibration*, vol. 332, no. 24, pp. 6265–6275, 2013. 8

[65] A. D. Shaw, S. A. Neild, and D. J. Wagg, "Dynamic analysis of high static low dynamic stiffness vibration isolation mounts," *Journal of Sound and Vibration*, vol. 332, pp. 1437–1455, 2013. 8

[66] J. Hwang and J. Chiou, "An equivalent linear model of lead-rubber seismic isolation bearings," *Engineering Structures*, vol. 18, no. 7, pp. 528–536, 1996. 8

[67] V. A. Zayas and S. A. Mahin, *The FPS earthquake resisting system experimental report*. Earthquake Engineering Research Center, 1987. 8

[68] A. Mokha, M. Constantinou, A. Reinhorn, and V. A. Zayas, "Experimental study of friction-pendulum isolation system," *Journal of Structural Engineering*, vol. 117, no. 4, pp. 1201–1217, 1991. 8

[69] M. C. Constantinou, P. Tsopelas, Y. Kim, and S. Okamoto, "Nceer-taisei corporation research program on sliding seismic isolation systems for bridges: experimental and analytical study of a friction pendulum system (fps)," 1993. 8

[70] Y.-P. Wang, M.-C. Teng, and K.-W. Chung, "Seismic isolation of rigid cylindrical tanks using friction pendulum bearings," *Earthquake engineering & structural dynamics*, vol. 30, no. 7, pp. 1083–1099, 2001. 8

[71] C. Tsai, "Finite element formulations for friction pendulum seismic isolation bearings," *International journal for numerical methods in engineering*, vol. 40, no. 1, pp. 29–49, 1997. 8

[72] P. Tsopelas, M. Constantinou, Y. Kim, and S. Okamoto, "Experimental study of fps system in bridge seismic isolation," *Earthquake engineering & structural dynamics*, vol. 25, no. 1, pp. 65–78, 1996. 8

[73] V. Quaglini, M. Bocciarelli, E. Gandelli, and P. Dubini, "Numerical assessment of frictional heating in sliding bearings for seismic isolation," *Journal of Earthquake Engineering*, vol. 18, no. 8, pp. 1198–1216, 2014. 8

[74] V. Panchal and R. Jangid, "Variable friction pendulum system for seismic isolation of liquid storage tanks," *Nuclear Engineering and Design*, vol. 238, no. 6, pp. 1304–1315, 2008. 8

[75] Y.-P. Wang, L.-L. Chung, and W.-H. Liao, "Seismic response analysis of bridges isolated with friction pendulum bearings," *Earthquake Engineering & Structural Dynamics*, vol. 27, no. 10, pp. 1069–1093, 1998. 8

[76] P. M. Calvi and G. M. Calvi, "Historical development of friction-based seismic isolation systems," *Soil Dynamics and Earthquake Engineering*, vol. 106, pp. 14–30, 2018. 8

[77] F. C. Ponzo, A. Di Cesare, G. Leccese, and D. Nigro, "Shake table testing on restoring capability of double concave friction pendulum seismic isolation systems," *Earthquake Engineering & Structural Dynamics*, vol. 46, no. 14, pp. 2337–2353, 2017. 8

[78] P. Deastra, "Numerical studies of rocker bearing seismic isolation," Master's thesis, School of Mechanical, Aerospace and Civil Engineering, University of Manchester, 2015. 8

[79] G. C. Lee, Y.-C. Ou, T. Niu, J. Song, and Z. Liang, "Characterization of a roller seismic isolation bearing with supplemental energy dissipation for highway bridges," *Journal of Structural Engineering*, vol. 136, no. 5, pp. 502–510, 2010. 8

[80] Y.-C. Ou, J. Song, and G. C. Lee, "A parametric study of seismic behavior of roller seismic isolation bearings for highway bridges," *Earthquake engineering & structural dynamics*, vol. 39, no. 5, pp. 541–559, 2010. 8

[81] M.-H. Tsai, S.-Y. Wu, K.-C. Chang, and G. C. Lee, "Shaking table tests of a scaled bridge model with rolling-type seismic isolation bearings," *Engineering structures*, vol. 29, no. 5, pp. 694–702, 2007. 8

[82] G. C. Lee and Z. Liang, "A sloping surface roller bearing and its lateral stiffness measurement," in *Proceedings ofthe 19th US–Japan bridge engineering workshop*, pp. 27–29, 2003. 8

[83] N. A. Ortiz, C. Magluta, and N. Roitman, "Numerical and experimental studies of a building with roller seismic isolation bearings," *Structural Engineering and Mechanics*, vol. 54, no. 3, pp. 475–489, 2015. 8

[84] P. S. Harvey Jr and K. C. Kelly, "A review of rolling-type seismic isolation: Historical development and future directions," *Engineering Structures*, vol. 125, pp. 521–531, 2016. 8

[85] G. C. Lee, Y.-C. Ou, Z. Liang, T. Niu, and J. Song, "Principles and performance of roller seismic isolation bearings for highway bridges," tech. rep., Report no. MCEER-07-0019, Multidisciplinary Center for Earthquake ..., 2007. 8

[86] D. Foti, "Rolling devices for seismic isolation of lightweight structures and equipment. design and realization of a prototype," *Structural Control and Health Monitoring*, vol. 26, no. 3, p. e2311, 2019. 8

[87] J. Wang, *Seismic isolation analysis of a roller isolation system*. State University of New York at Buffalo, 2005. 8

[88] M. Kasagi, K. Fujita, M. Tsuji, and I. Takewaki, "Automatic generation of smart earthquake-resistant building system: Hybrid system of base-isolation and building-connection," *Heliyon*, vol. 2, no. 2, p. e00069, 2016. 8, 22

[89] K. Mutō, *Earthquake resistant design of 36-storied Kasumigaseki building*. Muto Institute of Structural Mechanics, 1968. 9

[90] J. M. Kelly, R. Skinner, and A. Heine, "Mechanisms of energy absorption in special devices for use in earthquake resistant structures," *Bulletin of NZ Society for Earthquake Engineering*, vol. 5, no. 3, pp. 63–88, 1972. 9

[91] R. Skinner, J. Kelly, and A. Heine, "Hysteretic dampers for earthquake-resistant structures," *Earthquake engineering & structural dynamics*, vol. 3, no. 3, pp. 287–296, 1974. 9

[92] C. Christopoulus and A. Filiatrault, *Principle of Passive Supplemental Damping and Seismic Isolation*. IUSS Press, Pavia, 2006. 9

[93] R. Tyler, "Damping in building structures by means of ptfe sliding joints," *Bulletin of the New Zealand National Society for Earthquake Engineering*, vol. 10, no. 3, pp. 139–142, 1977. 9

[94] A. Pall, V. Verganelakis, and C. Marsh, "Friction dampers for seismic control of concordia university library building," in *Fifth Canadian Conference on Earthquake Engineering, Ottawa*, pp. 191–200, 1987. 9

[95] I. Aiken, "Dampers for seismic protection: 1. friction and viscous damper; 2. viscoelastic and metallic dampers," in *Technical seminar on seismic isolation and energy dissipation technology*, vol. 11, 1997. 9

[96] T. Soong and B. Spencer Jr, "Supplemental energy dissipation: state-of-the-art and state-of-the-practice," *Engineering structures*, vol. 24, no. 3, pp. 243–259, 2002. 9

[97] C. F. Beards, *Structural Vibrations: Analysis and Damping*. Halsted Press, 1996. 9, 10, 33, 47, 65, 95, 145

[98] J. A. Inaudi and N. Makris, "Time-domain analysis of linear hysteretic damping," *Earthquake engineering & structural dynamics*, vol. 25, no. 6, pp. 529–545, 1996. 9, 33, 36, 37, 38, 39, 47, 145

[99] P. Xiang and A. Nishitani, "Optimum design for more effective tuned mass damper system and its application to base-isolated buildings," *Structural Control and Health Monitoring*, vol. 21, no. 1, pp. 98–114, 2014. 11, 12, 13, 14, 15, 23

[100] H. Frahm, "Device for damping vibrations of bodies.," Apr. 18 1911. US Patent 989,958. 11

[101] L. Marian, *The Tuned Mass Damper Inerter for Passive Vibration Control and Energy Harvesting In Dynamically Excited Structural Systems*. PhD thesis, School of Engineering and Mathematical Sciences, City University London, 2015. 11

[102] G. Warburton, "Optimum absorber parameters for various combinations of response and excitation parameters," *Earthquake Engineering & Structural Dynamics*, vol. 10, no. 3, pp. 381–401, 1982. 11

[103] N. Carpineto, W. Lacarbonara, and F. Vestroni, "Hysteretic tuned mass dampers for structural vibration mitigation," *Journal of Sound and Vibration*, vol. 333, no. 5, pp. 1302–1318, 2014. 12

[104] F. Sadek, B. Mohraz, A. W. Taylor, and R. M. Chung, "A method of estimating the parameters of tuned mass dampers for seismic applications," *Earthquake engineering and structural dynamics*, vol. 26, no. 6, pp. 617–636, 1997. 12

[105] A. Leung and H. Zhang, "Particle swarm optimization of tuned mass dampers," *Engineering Structures*, vol. 31, no. 3, pp. 715–728, 2009. 12

[106] I. Kourakis, *Structural systems and tuned mass dampers of super-tall buildings: case study of Taipei 101.* PhD thesis, Massachusetts Institute of Technology, 2007. 12

[107] W. O. Wong, "Optimal design of a hysteretic vibration absorber using fixed-points theory," *The Journal of the Acoustical Society of America*, vol. 139, no. 6, pp. 3110–3115, 2016. 12, 44, 71

[108] B. Palazzo, L. Petti, and M. De Ligio, "Response of base isolated systems equipped with tuned mass dampers to random excitations," *Structural Control and Health Monitoring*, vol. 4, no. 1, pp. 9–22, 1997. 13, 14, 15, 23

[109] L. Petti, G. Giannattasio, M. De Iuliis, and B. Palazzo, "Small scale experimental testing to verify the effectiveness of the base isolation and tuned mass dampers combined control strategy," *Smart Structures and Systems*, vol. 6, no. 1, pp. 57–72, 2010. 13, 14, 23

[110] F. Sakai, S. Takaeda, and T. Tamaki, "Tuned liquid column damper-new type device for suppression of building vibrations," in *International Conference on Highrise Buildings, Nanjing, China, Mar*, pp. 25–27, 1989. 14

[111] K. Dai, J. Wang, R. Mao, Z. Lu, and S.-E. Chen, "Experimental investigation on dynamic characterization and seismic control performance of a tlpd system," *The Structural Design of Tall and Special Buildings*, 2016. 14

[112] K. Al-Saif, K. Aldakkan, and M. Foda, "Modified liquid column damper for vibration control of structures," *International Journal of Mechanical Sciences*, vol. 53, no. 7, pp. 505–512, 2011. 14

[113] S. Gur, K. Roy, and S. K. Mishra, "Tuned liquid column ball damper for seismic vibration control," *Structural Control and Health Monitoring*, vol. 22, no. 11, pp. 1325–1342, 2015. 14

[114] B. Palazzo and L. Petti, "Combined control strategy: base isolation and tuned mass damping," *ISET Journal of Earthquake Technology*, vol. 36, no. 2-4, pp. 121–137, 1999. 14, 15, 23

[115] M. Saitoh, "On the performance of gyro-mass devices for displacement mitigation in base isolation systems," *Structural Control and Health Monitoring*, vol. 19, no. 2, pp. 246–259, 2012. 15, 23

[116] T. Hashimoto, K. Fujita, M. Tsuji, and I. Takewaki, "Innovative base-isolated building with large mass-ratio tmd at basement for greater earthquake resilience," *Future Cities and Environment*, vol. 1, no. 1, p. 9, 2015. 15, 17, 22, 24

[117] F. A. Firestone, "A new analogy between mechanical and electrical systems," *The Journal of the Acoustical Society of America*, vol. 4, no. 3, pp. 249–267, 1933. 16

[118] F.-C. Wang, M.-F. Hong, and C.-W. Chen, "Building suspensions with inerters," *Proceedings of the Institution of Mechanical Engineers, Part C: Journal of Mechanical Engineering Science*, vol. 224, no. 8, pp. 1605–1616, 2010. 17

[119] I. Takewaki, S. Murakami, S. Yoshitomi, and M. Tsuji, "Fundamental mechanism of earthquake response reduction in building structures with inertial dampers," *Structural Control and Health Monitoring*, vol. 19, no. 6, pp. 590–608, 2012. 17

[120] S. Y. Zhang, J. Z. Jiang, and S. Neild, "Passive vibration suppression using inerters for a multi-storey building structure," in *Journal of Physics: Conference Series*, vol. 744, p. 012044, IOP Publishing, 2016. 17

[121] S. Y. Zhang, J. Z. Jiang, and S. Neild, "Optimal configurations for a linear vibration suppression device in a multi-storey building," *Structural Control and Health Monitoring*, 2016. 17, 22

[122] Glover AR, Smith MC,Houghton NE,Long PJG. 2009. Force-controlling hydraulic device. Int. PatentAppl. PCT/GB2010/001491. 17

[123] S. Swift, M. C. Smith, A. Glover, C. Papageorgiou, B. Gartner, and N. E. Houghton, "Design and modelling of a fluid inerter," *International Journal of Control*, vol. 86, no. 11, pp. 2035–2051, 2013. 17, 29, 48

[124] Y. Shen, L. Chen, Y. Liu, X. Zhang, and X. Yang, "2085. optimized modeling and experiment test of a fluid inerter.," *Journal of Vibroengineering*, vol. 18, no. 5, 2016. 18

[125] T. Arai, T. Aburakawa, K. Ikago, N. Hori, and N. Inoue, "Verification on effectiveness of a tuned viscous mass damper and its applicability to non-linear structural systems," *Journal of Structural and Construction Engineering, AIJ*, vol. 645, pp. 1993–2002, 2009. 19, 20

[126] T. Furuhashi and S. Ishimaru, "Response control of multi-degree system by inertial mass: Study on response control by inertial mass no. 2," *Journal of Structural and Construction Engineering*, no. 601, pp. 83–90, 2006. 19

[127] A. Gonzalez-Buelga, L. Clare, S. Neild, J. Jiang, and D. Inman, "An electromagnetic inerter-based vibration suppression device," *Smart Materials and Structures*, vol. 24, no. 5, p. 055015, 2015. 19

[128] K. Ikago, Y. Sugimura, K. Saito, and N. Inoue, "Modal response characteristics of a multiple-degree-of-freedom structure incorporated with tuned viscous mass dampers," *Journal of Asian Architecture and Building Engineering*, vol. 11, no. 2, pp. 375–382, 2012. 20

[129] T. Asai, K. Ikago, and Y. Araki, "Outrigger tuned viscous mass damping system for high-rise buildings subject to earthquake loadings," in *6AESE/11ANCRiSST Joint Conference*, 2015. 20

[130] Y. Watanabe, K. Ikago, N. Inoue, H. Kida, S. Nakaminami, H. Tanaka, Y. Sugimura, and K. Saito, "Full-scale dynamic tests and analytical verification of a force-restricted tuned viscous mass damper," in *Proceedings of the 15th World Conference on Earthquake Engineering, Lisbon, Portugal, Paper ID*, vol. 1206, 2012. 20

[131] P. Brzeski, E. Pavlovskaia, T. Kapitaniak, and P. Perlikowski, "The application of inerter in tuned mass absorber," *International Journal of Non-Linear Mechanics*, vol. 70, pp. 20–29, 2015. 20

[132] C. Pan, R. Zhang, H. Luo, C. Li, and H. Shen, "Demand-based optimal design of oscillator with parallel-layout viscous inerter damper," *Structural Control and Health Monitoring*, 2017. 21, 22, 47, 56

[133] P. Deastra, D. Wagg, and N. Sims, "The effect of a tuned-inerter-damper on the seismic response of base-isolated structures," in *16th European Conference on Earthquake Engineering*, pp. 18–21, Sheffield, 2018. 22

[134] H.-C. Tsai, "The effect of tuned-mass dampers on the seismic response of base-isolated structures," *International journal of solids and structures*, vol. 32, no. 8-9, pp. 1195–1210, 1995. 23, 25

[135] R. M. Hessabi and O. Mercan, "Investigations of the application of gyro-mass dampers with various types of supplemental dampers for vibration control of building structures," *Engineering Structures*, vol. 126, pp. 174–186, 2016. 23, 48, 56

[136] N. Smith and D. Wagg, "a fluid inerter with variable inertance properties," in *6th European Conference on Structural Control, Sheffield, England*, 2016. 27, 29, 32

[137] P. Deastra, D. Wagg, and N. Sims, "Modelling the hysteretic behaviour of a fluid inerter for use as a parallel-viscous-inerter-damper device," in *Accepted to appear in the proceeding of the 7th World Conference on Structural Control and Monitoring, Qingdao, China*, 2018. 27

[138] A. K. Chopra, *Dynamics of Structures, Theory and Applications to Earthquake Engineering, 4th edition.* Prentice Hall, 2012. 29, 33, 70, 71, 95

[139] Wagg D, "Helical Inerter Test Data from 2016," 11 -0001. Accessed on 2020/08/12. 29, 30, 31

[140] P. Deastra, D. Wagg, and N. Sims, "Time domain analysis of structures with hysteretic vibration suppression systems," in *Journal of Physics: Conference Series*, vol. 1264, p. 012032, IOP Publishing, 2019. 47

[141] P. Deastra, D. Wagg, and N. Sims, "Optimum design of a tuned-inerter-hysteretic-damper (tihd) for building structures subject to earthquake base excitations," in *EURODYN 2020: Proceedings of the XI International Conference on Structural Dynamics*, pp. 1501–1509, European Association for Structural Dynamics (EASD), 2020. 47

[142] K. Ikago, Y. Sugimura, K. Saito, and N. Inoue, "Simple design method for a tuned viscous mass damper seismic control system," in *Proceedings of the 15th World Conference on Earthquake Engineering, Lisbon, Portugal, Paper ID*, vol. 1575, 2012. 57, 58

[143] P. Deastra, D. J. Wagg, and N. D. Sims, "The realisation of an inerter-based system using fluid inerter," in *Dynamics of Civil Structures, Volume 2*, pp. 127–134, Springer, 2019. 63

[144] J. A. lnaudi and J. M. Kelly, *A friction mass damper for vibration control.* Report No. UCB/EERC-92/18, Earthquake Engineering Research Center, University of California at Berkeley, 1992. 65, 145

[145] P. Deastra, D. Wagg, N. Sims, and R. Mills, "Shake table tests of a three-storey structure with an inerter-based-hysteretic-damper," in *Accepted to appear in the proceeding of the 17th World Conference on Earthquake Engineering, Sendai, Japan*, 2020. 68, 76, 85

[146] Y. Hu, M. Z. Chen, Z. Shu, and L. Huang, "Analysis and optimisation for inerter-based isolators via fixed-point theory and algebraic solution," *Journal of Sound and Vibration*, vol. 346, pp. 17–36, 2015. 69

[147] A. Qin and P. Suganthan, "Self-adaptive differential evolution algorithm for numerical optimization," in *2005 IEEE Congress on Evolutionary Computation, 2–5 Sept, Edinburgh, Scotland, UK*, 2005. 92

[148] R. Storn and K. Price, "Differential evolution – a simple and efficient heuristic for global optimization over continuous spaces," *Journal of Global Optimization*, vol. 11, pp. 341–359, 1997. 92

[149] P. Deastra, D. Wagg, N. Sims, and M. Akbar, "Tuned inerter dampers with linear hysteretic damping," *Earthquake Engineering & Structural Dynamics*, vol. 49, no. 12, pp. 1216–1235, 2020. 96, 143

[150] A. A. Almagirby, *Understanding Vibration Transmitted to the Human Finger*. PhD thesis, University of Sheffield, 2016. 99

[151] E. D. John and D. J. Wagg, "Design and testing of a frictionless mechanical inerter device using living-hinges," *Journal of the Franklin Institute*, vol. 356, no. 14, pp. 7650–7668, 2019. 109, 110, 111

Appendix A: MATLAB code for time domain analysis of a SDOF structure with complex stiffness

```
%
% Analytic function integration INAUDI & MAKRIS 1996, but using ode45
%
close all
clear all
clc

%% Declare parameters and variables

eta = 0.1;      % loss factor
m = 0.6;        % mass in kg
k = 23.6871;    % stiffness in N/m
wn = sqrt(k/m);
fn = wn/(2*pi);
c=k*eta/wn;

%% calculation

A=[0 1;
   -wn^2*(1+eta*i) 0];
B=[0;wn^2*(1+eta*i)]; % base excitation
% Eigenvectors
[V,D] = eig(A);
%phi=V;
phi=[V(1,1)/V(1,1) V(1,2)/V(1,2);
    V(2,1)/V(1,1) V(2,2)/V(1,2)];
% teta^-1*A*teta
Q=inv(phi)*A*phi;
% teta^-1*B
b=inv(phi)*B;
% eigenvalues
```

```
s1=-Q(1,1);
s2=-Q(2,2);

%% Declare vectors to hold time series results

TT=50;      % total time in seconds
del=0.01;   % time interval and time vector
A0=1;        % amplitude of input signal
f=fn;
w=2*pi*f;        % frequency of input signal in rad/s

freq = w/(2*pi);
T = 1/freq;
cycle = ceil(TT/T); % round-up number of cycle
tendn = cycle*T;    % round-up end time

dt = ceil(T/del);
ht = T/dt;
tt = 0:ht:tendn;
n = numel(tt);

wr=A0*sin(w*tt);
dot_rt=w*A0*cos(w*tt);

%% construct the hilbert function with zero padding at start and finish

% length=2048;
tm = -ht:-ht:-tendn;
tp = tendn+ht:ht:(2*tendn);
ttt = [fliplr(tm) tt tp];
Pmi=-A0*exp(eta*wn*tm).*sin(w*tm);
% assumed force from t0 to -infinity
Ppi=A0*exp(-eta*wn*(tp-tendn)).*sin(w*(tp-tendn));
% assumed force from tend to +infinity

% pp=zeros(1,length);
% temp=[pp wr pp];
temp = [fliplr(Pmi) wr Ppi];
temp1 = [fliplr(Pmi) dot_rt Ppi];
wt=hilbert(temp);
% now define the analytic forcing function
wa=wt; % wt(length+1:length+npts+1);
wa_r=fliplr(wa);

%% Initial conditions for the modal displacements
qin1=0.0;
qin2=0.0;
```

```
%% ODE45 integration
wf=flip(wa);
% ode45 integration forwards
y0 = [0;0];
tspan=[-tendn 2*tendn];
[T1,Q1] = ode45(@(t,y)myode(t,y,s1,s2,b,wa,ttt),tspan,y0);
qvals1 = interp1(T1,Q1,ttt,'spline');

% ode45 integration backwards
y0 = [0;0];
tspan=[-tendn 2*tendn];
[T2,Q2] = ode45(@(t,y)myode2(t,y,s1,s2,b,wf,ttt),tspan,y0);
Qrev2 = interp1(T2,Q2,ttt,'spline');
qvals2 = flip(Qrev2);

x = phi*[(qvals1(:,1)+(1i*qvals1(:,2)))';
         (qvals2(:,1)+(1i*qvals2(:,2)))'];

%% Zero-Hold Order
%%% Initial and end conditions

qk=zeros(1,(3*n)-2);
ql=zeros(1,(3*n)-2);

qk(:,1)=0;
ql(:,(3*n)-2)=0;

%%% Numerical solutions

for j = 2:((3*n)-3)
   qk(1,j)=qk(1,j-1)*exp(s1*ht)
   + ((exp(s1*ht))-1)*(b(1)/s1)*(wa(j-1));
   ql(1,j)=ql(1,j-1)*exp(-s2*ht)
   + ((exp(-s2*ht))-1)*(b(2)/s2)*(wa_r((j-1)));
end
qrevl=fliplr(ql);
x_anly = phi*[(qk); (qrevl)];


%% Equivalent viscous damping
t  = ttt;
tdat = t;
y0 = [0;0];
tspan=[t(1):ht:t(end)];
[T,X] = ode45(@(t,y)Ceq_fun(t,y,c,k,m,tdat,temp1,temp),tspan,y0);
XCeq=X(:,1);

figure(12)
```

```
plot(T,XCeq,'-.b','Linewidth',1.5)
hold on
plot(tt,real(x_anly(1,n:(2*n)-1)),'--k','Linewidth',1.5)
hold on
plot(tt,real(x(1,n:(2*n)-1)),'-r','Linewidth',1.5)
grid on
i=legend({'equivalent viscous damping','zero order hold','current method'},
          'Orientation','horizontal');
j=xlabel(['time (s)']);
ij=ylabel(['Displacement, $x(t)$']);
set(i,'Interpreter','Latex','FontSize',9);
set(j,'Interpreter','Latex','FontSize',17);
set(ij,'Interpreter','Latex','FontSize',17);

% yticks([-16 -14 -12 -10 -8 -6 -4 -2 0 2 4 6 8 10 12 14 16]);
axis([0 50 -16 16]); % for f=fn
%axis([0 50 -0.08 0.06]); % for f=30fn

x01=10;
y01=10;
width=420;
height=220;
set(gcf,'position',[x01,y01,width,height]);

abc=real(x_anly(1,n:(2*n)-1));
def=real(x(1,n:(2*n)-1));
ghi=XCeq;

axes('position',[0.585 0.25 0.3 0.2]);
box on
index= 0<tt & tt<50;
index1= 0<T & T<50;
plot(T(index1),ghi(index1),'-.b','Linewidth',1.5)
hold on
plot(tt(index),abc(index),'--k','Linewidth',1.5)
hold on
plot(tt(index),def(index),'-r','Linewidth',1.5)
grid on

axis([23.9 24.1 9.5 10.5]); % for f=fn

%% Functions

function  ydot = myode(t,y,s1,s2,b,wa,ttt)
war = interp1(ttt,real(wa),t);
wai = interp1(ttt,imag(wa),t);
ydot = zeros(2,1);
ydot(1)=real(s1)*y(1)-imag(s1)*y(2)+real(b(1))*war-imag(b(1))*wai;
```

```
ydot(2)=real(s1)*y(2)+imag(s1)*y(1)+real(b(1))*wai+imag(b(1))*war;
end

function  ydot = myode2(t,y,s1,s2,b,wf,ttt)
war = interp1(ttt,real(wf),t);
wai = interp1(ttt,imag(wf),t);
ydot = zeros(2,1);
ydot(1)=-real(s2)*y(1)+imag(s2)*y(2)-real(b(2))*war+imag(b(2))*wai;
ydot(2)=-real(s2)*y(2)-imag(s2)*y(1)-real(b(2))*wai-imag(b(2))*war;
end

function ydot_vector = Ceq_fun(t,y,c,k,m,tdat,temp1,temp)
temp1 = interp1(tdat,temp1,t);
temp = interp1(tdat,temp,t);

ydot_vector=zeros(2,1);
ydot_vector(1) = y(2);
ydot_vector(2) = (-c/m)*y(2)-(k/m)*y(1)+(c/m)*temp1-(k/m)*temp;
% book 4 page 114
end
```

Appendix B: MATLAB code for time domain analysis of a MDOF structure with complex stiffness

```
clear all
close all
clc
% Book 4 page 142-143

%% Parameters
% main structure parameters
m1=2;
m2=1;
k1=6;
k2=3;

eta=0.1;
eta1=eta;
eta2=eta;

% natural frequencies in rad/s
wn1=1.22;
wn2=2.4;

%% calculation
A=[0 1 0 0;
   (-k1/m1)*(1+eta1*i)-(k2/m1)*(1+eta2*i) 0 (k2/m1)*(1+eta2*i) 0;
   0 0 0 1;
   (k2/m2)*(1+eta2*i) 0 -(k2/m2)*(1+eta2*i) 0 ];

B=[0;(k1/m1)*(1+eta1*i);0;0]; % base excitation (acceleration)
%B=[0;1/m1;0;1/m2]; % force on mass

% eigenvectors
[V,D] = eig(A);
```

```
% phi=V;
phi=[V(1,1)/V(3,1) V(1,2)/V(3,2) V(1,3)/V(3,3) V(1,4)/V(3,4);
     V(2,1)/V(3,1) V(2,2)/V(3,2) V(2,3)/V(3,3) V(2,4)/V(3,4);
     V(3,1)/V(3,1) V(3,2)/V(3,2) V(3,3)/V(3,3) V(3,4)/V(3,4);
     V(4,1)/V(3,1) V(4,2)/V(3,2) V(4,3)/V(3,3) V(4,4)/V(3,4)];

% teta^-1*A*teta
Q=inv(phi)*A*phi;
% teta^-1*B
b=inv(phi)*B;
% eigenvalues
s1=Q(1,1);
s2=Q(2,2);
s3=Q(3,3); % = -s1
s4=Q(4,4); % = -s2

%% Declare vectors to hold time series results

TT=500;      % total time in seconds
del=0.1;   % time interval and time vector
A0=1;        % amplitude of input signal
w=2.4;        % frequency of input signal in rad/s

freq = w/(2*pi);
T = 1/freq;
cycle = ceil(TT/T); % round-up number of cycle
tendn = cycle*T;    % round-up end time

dt = ceil(T/del);
ht = T/dt;
tt = 0:ht:tendn;
n = numel(tt);

wr=A0*sin(w*tt);

%% construct the hilbert function with zero padding at start and finish

% length=2048;
tm = -ht:-ht:-tendn;
tp = tendn+ht:ht:(2*tendn);
ttt = [fliplr(tm) tt tp];
Pmi=-A0*exp(eta*wn1*tm).*sin(w*tm);
% assumed force from t0 to -infinity
Ppi=A0*exp(-eta*wn1*(tp-tendn)).*sin(w*(tp-tendn));
% assumed force from tend to +infinity

% pp=zeros(1,length);
% temp=[pp wr pp];
```

```
temp = [fliplr(Pmi) wr Ppi];
wt=hilbert(temp);
% now define the analytic forcing function
wa=wt; % wt(length+1:length+npts+1);

% figure(1)
% plot([ttt],[temp])

%% ODE45 integration
wf=flip(wa);
% ode45 integration forwards
y0 = [0;0];
tspan=[-tendn 2*tendn];
[T1,Q1] = ode45(@(t,y)myode(t,y,s1,b,wf,ttt),tspan,y0);
Qrev1 = interp1(T1,Q1,ttt,'spline');
qvals1 = flip(Qrev1);
figure(2)
plot(ttt,qvals1(:,1))
figure(3)
plot(ttt,qvals1(:,2))

% ode45 integration forwards
y0 = [0;0];
tspan=[-tendn 2*tendn];
[T2,Q2] = ode45(@(t,y)myode2(t,y,s2,b,wf,ttt),tspan,y0);
Qrev2 = interp1(T2,Q2,ttt,'spline');
qvals2 = flip(Qrev2);
figure(4)
plot(ttt,qvals2(:,1))
figure(5)
plot(ttt,qvals2(:,2))

% ode45 integration backwards
y0 = [0;0];
tspan=[-tendn 2*tendn];
[T3,Q3] = ode45(@(t,y)myode3(t,y,s3,b,wa,ttt),tspan,y0);
qvals3 = interp1(T3,Q3,ttt,'spline');
figure(6)
plot(ttt,qvals3(:,1))
figure(7)
plot(ttt,qvals3(:,2))

% ode45 integration backwards
y0 = [0;0];
tspan=[-tendn 2*tendn];
[T4,Q4] = ode45(@(t,y)myode4(t,y,s4,b,wa,ttt),tspan,y0);
qvals4 = interp1(T4,Q4,ttt,'spline');
figure(8)
```

```
plot(ttt,qvals4(:,1))
figure(9)
plot(ttt,qvals4(:,2))

x = phi*[(qvals1(:,1)+(1i*qvals1(:,2)))';
         (qvals2(:,1)+(1i*qvals2(:,2)))';
         (qvals3(:,1)+(1i*qvals3(:,2)))';
         (qvals4(:,1)+(1i*qvals4(:,2)))'];

figure(10)
plot(tt,real(x(3,n:(2*n)-1)))
title('x(t)')
%saveas(gcf,'MDOF_x(t)_w8.fig')

%% Functions

function  ydot = myode(t,y,s1,b,wf,ttt)
war = interp1(ttt,real(wf),t);
wai = interp1(ttt,imag(wf),t);
ydot = zeros(2,1);
ydot(1)=-real(s1)*y(1)+imag(s1)*y(2)-real(b(1))*war+imag(b(1))*wai;
ydot(2)=-real(s1)*y(2)-imag(s1)*y(1)-real(b(1))*wai-imag(b(1))*war;
end

function  ydot = myode2(t,y,s2,b,wf,ttt)
war = interp1(ttt,real(wf),t);
wai = interp1(ttt,imag(wf),t);
ydot = zeros(2,1);
ydot(1)=-real(s2)*y(1)+imag(s2)*y(2)-real(b(2))*war+imag(b(2))*wai;
ydot(2)=-real(s2)*y(2)-imag(s2)*y(1)-real(b(2))*wai-imag(b(2))*war;
end

function  ydot = myode3(t,y,s3,b,wa,ttt)
war = interp1(ttt,real(wa),t);
wai = interp1(ttt,imag(wa),t);
ydot = zeros(2,1);
ydot(1)=real(s3)*y(1)-imag(s3)*y(2)+real(b(3))*war-imag(b(3))*wai;
ydot(2)=real(s3)*y(2)+imag(s3)*y(1)+real(b(3))*wai+imag(b(3))*war;
end

function  ydot = myode4(t,y,s4,b,wa,ttt)
war = interp1(ttt,real(wa),t);
wai = interp1(ttt,imag(wa),t);
ydot = zeros(2,1);
ydot(1)=real(s4)*y(1)-imag(s4)*y(2)+real(b(4))*war-imag(b(4))*wai;
ydot(2)=real(s4)*y(2)+imag(s4)*y(1)+real(b(4))*wai+imag(b(4))*war;
end
```

Appendix C: MATLAB code for time domain analysis of a SDOF structure equipped with TIhD and TMhDI

```
clear all
close all
clc

%% Parameters
% Structural mass
m=1;
% Properties of rubber bearing/hysteretic damper
wn=2*pi*0.05; % 0.05 is the first natural frequency (fn) in Hz unit
fn=wn/(2*pi); % Hz
k=wn^2*m;

% w=0:0.01:70;
% f=w/(2*pi);

%% Properties of the TID
% bd_TID=0.9;
% mu_TID=bd_TID/m;
% kd_TID=0.035;
% zeta=sqrt(3*mu_TID/(8*(1+mu_TID)));
% cd_TID=2*zeta*sqrt(kd_TID/bd_TID)*bd_TID;

b_TID=0.1;
mu_TID=b_TID/m;
La_TID=11.5474;
zeta_TID=0.0171;
kd_TID=k/La_TID;
cd_TID=zeta_TID*2*m*sqrt(k/m);
```

```
%% Properties of the TMDI
b_TMDI=b_TID;
mu_TMDI=b_TMDI/m;
La_TMDI=10.9;
kd_TMDI=k/La_TMDI;
cd_TMDI=cd_TID;

%% Properties of the TIhD
% b_TIhD=bd_TID;
% kd_TIhD=0.0325;
% eta_TIhD=cd_TID*wn/kd_TID;
% sh_TIhD=eta_TIhD*kd_TIhD;

b_TIhD=b_TID;
La_TIhD=11.5474;
kd_TIhD=k/La_TIhD;
eta_TIhD=0.3848;
sh_TIhD=eta_TIhD*kd_TIhD;

%% Properties of the TMhDI
b_TMhDI=b_TID;
La_TMhDI=10.9;
kd_TMhDI=k/La_TMhDI;
eta_TMhDI=eta_TIhD;
sh_TMhDI=eta_TMhDI*kd_TMhDI;

%% TMDI and TMhDI parameters
md=0.05*b_TID;

%% calculation for TIhD (book 6 page 70)
A_TIhD=[0 1 0 0;
    (-k/m) 0 (-kd_TIhD/m)*(1+i*eta_TIhD) 0;
    0 0 0 1;
    (-k/m) 0 ((-kd_TIhD/m)*(1+i*eta_TIhD)
    -(kd_TIhD/b_TIhD)*(1+i*eta_TIhD)) 0 ];

B_TIhD=[0;(k+kd_TIhD*(1+i*eta_TIhD))/m;
        0;((k+kd_TIhD*(1+i*eta_TIhD))/m)
        +((kd_TIhD*(1+i*eta_TIhD))/b_TIhD)];
        % base excitation (acceleration)

% eigenvectors
[V,D] = eig(A_TIhD);
%phi=V;
phi=[V(1,1)/V(1,1) V(1,2)/V(1,2) V(1,3)/V(1,3) V(1,4)/V(1,4);
     V(2,1)/V(1,1) V(2,2)/V(1,2) V(2,3)/V(1,3) V(2,4)/V(1,4);
     V(3,1)/V(1,1) V(3,2)/V(1,2) V(3,3)/V(1,3) V(3,4)/V(1,4);
     V(4,1)/V(1,1) V(4,2)/V(1,2) V(4,3)/V(1,3) V(4,4)/V(1,4)];
```

```
% teta^-1*A*teta
Q=inv(phi)*A_TIhD*phi;
% teta^-1*B
b=inv(phi)*B_TIhD;
% eigenvalues
s1=Q(1,1);
s2=Q(2,2);
s3=Q(3,3); % = -s1
s4=Q(4,4); % = -s2

%% calculation (book 5 page 52) for TMhDI
A_TMhDI=[0 1 0 0;
    (k*(md+b_TMhDI)/((b_TMhDI^2)-(m+b_TMhDI)*(md+b_TMhDI))) 0
    ((b_TMhDI*kd_TMhDI)+(i*sh_TMhDI*b_TMhDI))/((b_TMhDI^2)
    -(m+b_TMhDI)*(md+b_TMhDI)) 0;
    0 0 0 1;
    (-(k*b_TMhDI))/((m+b_TMhDI)*(md+b_TMhDI)-b_TMhDI^2) 0
    (-kd_TMhDI*(m+b_TMhDI)
    -(i*sh_TMhDI*(m+b_TMhDI)))/((m+b_TMhDI)*(md+b_TMhDI)
    -b_TMhDI^2) 0 ];

B_TMhDI=[0;((-k*(md+b_TMhDI))-(b_TMhDI*kd_TMhDI)
         -(i*sh_TMhDI*b_TMhDI))/((b_TMhDI^2)-(m+b_TMhDI)*(md+b_TMhDI));
         0;(k*b_TMhDI+kd_TMhDI*(m+b_TMhDI)
         +i*sh_TMhDI*(m+b_TMhDI))/((m+b_TMhDI)*(md+b_TMhDI)-b_TMhDI^2)];
     % base excitation (acceleration)

% eigenvectors
[V_TMhDI,D_TMhDI] = eig(A_TMhDI);
phi_TMhDI=[V_TMhDI(1,1)/V_TMhDI(1,1) V_TMhDI(1,2)/V_TMhDI(1,2)
           V_TMhDI(1,3)/V_TMhDI(1,3) V_TMhDI(1,4)/V_TMhDI(1,4);
           V_TMhDI(2,1)/V_TMhDI(1,1) V_TMhDI(2,2)/V_TMhDI(1,2)
           V_TMhDI(2,3)/V_TMhDI(1,3) V_TMhDI(2,4)/V_TMhDI(1,4);
           V_TMhDI(3,1)/V_TMhDI(1,1) V_TMhDI(3,2)/V_TMhDI(1,2)
           V_TMhDI(3,3)/V_TMhDI(1,3) V_TMhDI(3,4)/V_TMhDI(1,4);
           V_TMhDI(4,1)/V_TMhDI(1,1) V_TMhDI(4,2)/V_TMhDI(1,2)
           V_TMhDI(4,3)/V_TMhDI(1,3) V_TMhDI(4,4)/V_TMhDI(1,4)];

% teta^-1*A*teta
Q_md=inv(phi_TMhDI)*A_TMhDI*phi_TMhDI;
% teta^-1*B
b_md=inv(phi_TMhDI)*B_TMhDI;
% eigenvalues
s1_md=Q_md(1,1);
s2_md=Q_md(2,2);
s3_md=Q_md(3,3);
s4_md=Q_md(4,4);
```

```
%% Declare vectors to hold time series results

TT=500;      % total time in seconds
del=0.01;   % time interval and time vector
A0=1;        % amplitude of input signal
f=0.05;      % frequency of input signal in Hz
w=2*pi*f;        % frequency of input signal in rad/s

freq = w/(2*pi);
T = 1/freq;
cycle = ceil(TT/T); % round-up number of cycle
tendn = cycle*T;    % round-up end time

dt = ceil(T/del);
ht = T/dt;
tt = 0:ht:tendn;
n = numel(tt);

wr=A0*sin(w*tt);
rt=A0*sin(w*tt);
dot_rt=w*A0*cos(w*tt);

%% construct the hilbert function with zero padding at start and finish

% length=2048;
tm = -ht:-ht:-tendn;
tp = tendn+ht:ht:(2*tendn);
ttt = [fliplr(tm) tt tp];
Pmi=-A0*exp(eta_TIhD*wn*tm).*sin(w*tm);
% assumed force from t0 to -infinity
Ppi=A0*exp(-eta_TIhD*wn*(tp-tendn)).*sin(w*(tp-tendn));
% assumed force from tend to +infinity

% pp=zeros(1,length);
% temp=[pp wr pp];
temp = [fliplr(Pmi) wr Ppi];
temp1 = [fliplr(Pmi) dot_rt Ppi];
wt=hilbert(temp);
% now define the analytic forcing function
wa=wt; % wt(length+1:length+npts+1);

% figure(1)
% plot([ttt],[temp])

%% ODE45 integration TIhD

wf=flip(wa);
```

```
% ode45 integration backwards
y0 = [0;0];
tspan=[-tendn 2*tendn];
[T1,Q1] = ode45(@(t,y)myode(t,y,s1,b,wf,ttt),tspan,y0);
Qrev1 = interp1(T1,Q1,ttt,'spline');
qvals1 = flip(Qrev1);
figure(2)
plot(ttt,qvals1(:,1))
figure(3)
plot(ttt,qvals1(:,2))

% ode45 integration backwards
y0 = [0;0];
tspan=[-tendn 2*tendn];
[T2,Q2] = ode45(@(t,y)myode2(t,y,s2,b,wf,ttt),tspan,y0);
Qrev2 = interp1(T2,Q2,ttt,'spline');
qvals2 = flip(Qrev2);
figure(4)
plot(ttt,qvals2(:,1))
figure(5)
plot(ttt,qvals2(:,2))

% ode45 integration forwards
y0 = [0;0];
tspan=[-tendn 2*tendn];
[T3,Q3] = ode45(@(t,y)myode3(t,y,s3,b,wa,ttt),tspan,y0);
qvals3 = interp1(T3,Q3,ttt,'spline');
figure(6)
plot(ttt,qvals3(:,1))
figure(7)
plot(ttt,qvals3(:,2))

% ode45 integration forwards
y0 = [0;0];
tspan=[-tendn 2*tendn];
[T4,Q4] = ode45(@(t,y)myode4(t,y,s4,b,wa,ttt),tspan,y0);
qvals4 = interp1(T4,Q4,ttt,'spline');
figure(8)
plot(ttt,qvals4(:,1))
figure(9)
plot(ttt,qvals4(:,2))

x = phi*[(qvals1(:,1)+(1i*qvals1(:,2)))';
     (qvals2(:,1)+(1i*qvals2(:,2)))';
     (qvals3(:,1)+(1i*qvals3(:,2)))';
     (qvals4(:,1)+(1i*qvals4(:,2)))'];
```

```
%% ODE45 integration TMhDI
% ode45 integration backwards
y0 = [0;0];
tspan=[-tendn 2*tendn];
[T1_md,Q1_md] = ode45(@(t,y)myode_md(t,y,s1_md,b_md,wf,ttt),tspan,y0);
Qrev1_md = interp1(T1_md,Q1_md,ttt,'spline');
qvals1_md = flip(Qrev1_md);

% ode45 integration backwards
y0 = [0;0];
tspan=[-tendn 2*tendn];
[T2_md,Q2_md] = ode45(@(t,y)myode2_md(t,y,s2_md,b_md,wf,ttt),tspan,y0);
Qrev2_md = interp1(T2_md,Q2_md,ttt,'spline');
qvals2_md = flip(Qrev2_md);

% ode45 integration forwards
y0 = [0;0];
tspan=[-tendn 2*tendn];
[T3_md,Q3_md] = ode45(@(t,y)myode3_md(t,y,s3_md,b_md,wa,ttt),tspan,y0);
qvals3_md = interp1(T3_md,Q3_md,ttt,'spline');

% ode45 integration forwards
y0 = [0;0];
tspan=[-tendn 2*tendn];
[T4_md,Q4_md] = ode45(@(t,y)myode4_md(t,y,s4_md,b_md,wa,ttt),tspan,y0);
qvals4_md = interp1(T4_md,Q4_md,ttt,'spline');

x_md = phi_TMhDI*[(qvals1_md(:,1)+(1i*qvals1_md(:,2)))';
                  (qvals2_md(:,1)+(1i*qvals2_md(:,2)))';
                  (qvals3_md(:,1)+(1i*qvals3_md(:,2)))';
                  (qvals4_md(:,1)+(1i*qvals4_md(:,2)))'];

figure (10)
plot(tt,real(x(1,n:(2*n)-1)),':r','Linewidth',1.5)
hold on
plot(ttt,real(x_md(1,:)),'b','Linewidth',1.5)

%% TID
t  = ttt;
tdat = t;
y0 = [0;0;0;0];
tspan =[t(1):ht:t(end)];
[TR,ZR] = ode45(@(t,y)New_fun_SDOF_Ceq(t,y,wn,kd_TID,cd_TID,
               m,b_TID,tdat,temp,temp1),tspan,y0);

%% TMDI
y0 = [0;0;0;0];
tspan =[t(1):ht:t(end)];
```

```
[TR_md,ZR_md] = ode45(@(t,y)New_fun_SDOF_Ceq_md(t,y,kd_TMDI,cd_TMDI,
                    m,k,md,b_TMDI,tdat,temp,temp1),tspan,y0);

%% plot
figure(11)
plot(t,ZR(:,1),'--k','Linewidth',1.5)
hold on
plot(ttt,real(x(1,:)),':r','Linewidth',1.5)
hold on
plot(t,ZR_md(:,1),'g','Linewidth',1.5)
hold on
plot(ttt,real(x_md(1,:)),'b','Linewidth',1.5)
grid on
% yticks([-2e-3 -1e-3 0 1e-3 2e-3])
% axis([240 300 -2e-3 2e-3]);
yticks([-5 -4 -3 -2 -1 0 1 2 3 4 5])
axis([0 300 -5 5]);
i=legend('TID','TIhD','TMDI','TMhDI');
j=xlabel('time (s)');
ij=ylabel('displacement, X (cm)');

set(i,'Interpreter','Latex','FontSize',13);
set(j,'Interpreter','Latex','FontSize',17);
set(ij,'Interpreter','Latex','FontSize',17);

x01=10;
y01=10;
width=420;
height=220;
set(gcf,'position',[x01,y01,width,height]);

abc=ZR(:,1);
def=ZR_md(:,1);
ghi=real(x(1,:));
jkl=real(x_md(1,:));

axes('position',[0.585 0.25 0.3 0.2]);
box on
index= 200<TR & TR<300;
plot(TR(index),abc(index),'--k','Linewidth',1.5)
hold on
plot(TR(index),ghi(index),':r','Linewidth',1.5)
hold on
plot(TR(index),def(index),'g','Linewidth',1.5)
hold on
plot(TR(index),jkl(index),'b','Linewidth',1.5)
grid on
axis([227 231 3.8 4.2]);
```

```
%saveas(gcf,'SDOF_HIDs_005Hz','epsc');
%saveas(gcf,'SDOF_HIDs_30wn','epsc');

%% Functions
%% TIhD
function  ydot = myode(t,y,s1,b,wf,ttt)
war = interp1(ttt,real(wf),t);
wai = interp1(ttt,imag(wf),t);
ydot = zeros(2,1);
ydot(1)=-real(s1)*y(1)+imag(s1)*y(2)-real(b(1))*war+imag(b(1))*wai;
ydot(2)=-real(s1)*y(2)-imag(s1)*y(1)-real(b(1))*wai-imag(b(1))*war;
end

function  ydot = myode2(t,y,s2,b,wf,ttt)
war = interp1(ttt,real(wf),t);
wai = interp1(ttt,imag(wf),t);
ydot = zeros(2,1);
ydot(1)=-real(s2)*y(1)+imag(s2)*y(2)-real(b(2))*war+imag(b(2))*wai;
ydot(2)=-real(s2)*y(2)-imag(s2)*y(1)-real(b(2))*wai-imag(b(2))*war;
end

function  ydot = myode3(t,y,s3,b,wa,ttt)
war = interp1(ttt,real(wa),t);
wai = interp1(ttt,imag(wa),t);
ydot = zeros(2,1);
ydot(1)=real(s3)*y(1)-imag(s3)*y(2)+real(b(3))*war-imag(b(3))*wai;
ydot(2)=real(s3)*y(2)+imag(s3)*y(1)+real(b(3))*wai+imag(b(3))*war;
end

function  ydot = myode4(t,y,s4,b,wa,ttt)
war = interp1(ttt,real(wa),t);
wai = interp1(ttt,imag(wa),t);
ydot = zeros(2,1);
ydot(1)=real(s4)*y(1)-imag(s4)*y(2)+real(b(4))*war-imag(b(4))*wai;
ydot(2)=real(s4)*y(2)+imag(s4)*y(1)+real(b(4))*wai+imag(b(4))*war;
end

%% TMhDI
function  ydot = myode_md(t,y,s1_md,b_md,wf,ttt)
war = interp1(ttt,real(wf),t);
wai = interp1(ttt,imag(wf),t);
ydot = zeros(2,1);
ydot(1)=-real(s1_md)*y(1)+imag(s1_md)*y(2)
        -real(b_md(1))*war+imag(b_md(1))*wai;
ydot(2)=-real(s1_md)*y(2)-imag(s1_md)*y(1)
        -real(b_md(1))*wai-imag(b_md(1))*war;
end
```

```
function  ydot = myode2_md(t,y,s2_md,b_md,wf,ttt)
war = interp1(ttt,real(wf),t);
wai = interp1(ttt,imag(wf),t);
ydot = zeros(2,1);
ydot(1)=-real(s2_md)*y(1)+imag(s2_md)*y(2)
        -real(b_md(2))*war+imag(b_md(2))*wai;
ydot(2)=-real(s2_md)*y(2)-imag(s2_md)*y(1)
        -real(b_md(2))*wai-imag(b_md(2))*war;
end

function  ydot = myode3_md(t,y,s3_md,b_md,wa,ttt)
war = interp1(ttt,real(wa),t);
wai = interp1(ttt,imag(wa),t);
ydot = zeros(2,1);
ydot(1)=real(s3_md)*y(1)-imag(s3_md)*y(2)
        +real(b_md(3))*war-imag(b_md(3))*wai;
ydot(2)=real(s3_md)*y(2)+imag(s3_md)*y(1)
        +real(b_md(3))*wai+imag(b_md(3))*war;
end

function  ydot = myode4_md(t,y,s4_md,b_md,wa,ttt)
war = interp1(ttt,real(wa),t);
wai = interp1(ttt,imag(wa),t);
ydot = zeros(2,1);
ydot(1)=real(s4_md)*y(1)-imag(s4_md)*y(2)
        +real(b_md(4))*war-imag(b_md(4))*wai;
ydot(2)=real(s4_md)*y(2)+imag(s4_md)*y(1)
        +real(b_md(4))*wai+imag(b_md(4))*war;
end

%% TID
function  ydot = New_fun_SDOF_Ceq(t,y,wn,kd_TID,cd_TID,
                                  m,b_TID,tdat,temp,temp1)
temp  = interp1(tdat,temp,t);
temp1  = interp1(tdat,temp1,t);

ydot = zeros(4,1);
ydot(1)=y(2);
ydot(2)=-(wn)^2*(y(1)-temp)-(kd_TID/m)*(y(3)-temp)-(cd_TID/m)*(y(4)-temp1);
ydot(3)=y(4);
ydot(4)=-(wn)^2*(y(1)-temp)-(kd_TID/m)*(y(3)-temp)-(cd_TID/m)*(y(4)-temp1)-
        (kd_TID/b_TID)*(y(3)-temp)-(cd_TID/b_TID)*(y(4)-temp1);


end

%% TMDI
```

```
function  ydot = New_fun_SDOF_Ceq_md(t,y,kd_TMDI,cd_TMDI,
                                     m,k,md,b_TMDI,tdat,temp,temp1)
temp  = interp1(tdat,temp,t);
temp1  = interp1(tdat,temp1,t);

ydot = zeros(4,1);

% for base excitation (book 5 page 36)

ydot(1)=y(2); %dot x(t)
ydot(2)=((b_TMDI*cd_TMDI*(y(4)-temp1))+(b_TMDI*kd_TMDI*(y(3)-temp))+
        (k*(md+b_TMDI)*(y(1)-temp)))/(b_TMDI^2-(m+b_TMDI)*(md+b_TMDI));
        %ddot x(t)
ydot(3)=y(4); %dot d(t)
ydot(4)=(-(cd_TMDI*(m+b_TMDI)*(y(4)-temp1))-(kd_TMDI*(m+b_TMDI)*(y(3)
        -temp))-(k*b_TMDI*(y(1)-temp)))/((md+b_TMDI)*(m+b_TMDI)-b_TMDI^2);
        %ddot d(t)

end
```

Appendix D: MATLAB code for time domain analysis of a MDOF structure equipped with TIhD and TMhDI

```
clear all
close all
clc

%% Parameters
% Main structure parameters
m1=1; m2=1; m3=1; % ton = kNs^2/m
k1=1500; k2=1500; k3=1500; % kN/m
fn1=2.7; %Hz
wn1rad=2*pi*fn1; %rad/s
fn2=7.8; %Hz
fn3=11.1; %Hz

%% Properties of the TID
b_TID=0.48;
cd_TID=2.5;
kd_TID=138.6;

%% Properties of the TIhD
b_TIhD=b_TID;
kd_TIhD=138.6; % cd in kNs/m
kh=kd_TIhD;
eta_TIhD=cd_TID*(2*pi*fn1)/kd_TIhD;
sh_TIhD=eta_TIhD*kh;

%% calculation TIhD (book 4 page 154)
A= [0 1 0 0 0 0 0 0;
    (-k1-k2/m1) 0 (k2/m1) 0 0 0 -kd_TIhD/m1-(i*sh_TIhD/m1) 0;
    0 0 0 1 0 0 0 0;
```

```
    (k2/m2) 0 -k2/m2-k3/m2 0 k3/m2 0 0 0;
    0 0 0 0 0 1 0 0;
    0 0 k3/m3 0 -k3/m3 0 0 0;
    0 0 0 0 0 0 0 1;
    -k1/m1-k2/m1 0 k2/m1 0 0 0 (-kd_TIhD/m1-(i*sh_TIhD/m1)
    -kd_TIhD/b_TIhD-(i*sh_TIhD/b_TIhD)) 0];

B=[0;k1/m1+kd_TIhD/m1+(i*sh_TIhD/m1);
    0;0;0;0;0;
    (k1/m1+kd_TIhD/m1+(i*sh_TIhD/m1)+kd_TIhD/b_TIhD+(i*sh_TIhD/b_TIhD))];
    % base excitation (acceleration)

% eigenvectors
[V,D] = eig(A);
%phi=V;
phi=[V(1,1)/V(5,1) V(1,2)/V(5,2) V(1,3)/V(5,3) V(1,4)/V(5,4)
     V(1,5)/V(5,5) V(1,6)/V(5,6) V(1,7)/V(5,7) V(1,8)/V(5,8);
     V(2,1)/V(5,1) V(2,2)/V(5,2) V(2,3)/V(5,3) V(2,4)/V(5,4)
     V(2,5)/V(5,5) V(2,6)/V(5,6) V(2,7)/V(5,7) V(2,8)/V(5,8);
     V(3,1)/V(5,1) V(3,2)/V(5,2) V(3,3)/V(5,3) V(3,4)/V(5,4)
     V(3,5)/V(5,5) V(3,6)/V(5,6) V(3,7)/V(5,7) V(3,8)/V(5,8);
     V(4,1)/V(5,1) V(4,2)/V(5,2) V(4,3)/V(5,3) V(4,4)/V(5,4)
     V(4,5)/V(5,5) V(4,6)/V(5,6) V(4,7)/V(5,7) V(4,8)/V(5,8);
     V(5,1)/V(5,1) V(5,2)/V(5,2) V(5,3)/V(5,3) V(5,4)/V(5,4)
     V(5,5)/V(5,5) V(5,6)/V(5,6) V(5,7)/V(5,7) V(5,8)/V(5,8);
     V(6,1)/V(5,1) V(6,2)/V(5,2) V(6,3)/V(5,3) V(6,4)/V(5,4)
     V(6,5)/V(5,5) V(6,6)/V(5,6) V(6,7)/V(5,7) V(6,8)/V(5,8);
     V(7,1)/V(5,1) V(7,2)/V(5,2) V(7,3)/V(5,3) V(7,4)/V(5,4)
     V(7,5)/V(5,5) V(7,6)/V(5,6) V(7,7)/V(5,7) V(7,8)/V(5,8);
     V(8,1)/V(5,1) V(8,2)/V(5,2) V(8,3)/V(5,3) V(8,4)/V(5,4)
     V(8,5)/V(5,5) V(8,6)/V(5,6) V(8,7)/V(5,7) V(8,8)/V(5,8)];

% teta^-1*A*teta
Q=inv(phi)*A*phi;
% teta^-1*B
b=inv(phi)*B;
% eigenvalues
s1=Q(1,1);
s2=Q(2,2); % =-s1
s3=Q(3,3);
s4=Q(4,4); % =-s3
s5=Q(5,5);
s6=Q(6,6);
s7=Q(7,7); % =-s5
s8=Q(8,8); % =-s6

%% Declare vectors to hold time series results
```

```
TT=20;      % total time in seconds
del=0.001;   % time interval and time vector
A0=1;        % amplitude of input signal
f=fn2;
w=2*pi*f;        % frequency of input signal in rad/s

freq = w/(2*pi);
T = 1/freq;
cycle = ceil(TT/T); % round-up number of cycle
tendn = cycle*T;    % round-up end time

dt = ceil(T/del);
ht = T/dt;
tt = 0:ht:tendn;
n = numel(tt);

wr=A0*sin(w*tt);
dot_rt=w*A0*cos(w*tt);

%% construct the hilbert function with zero padding at start and finish

% length=2048;
tm = -ht:-ht:-tendn;
tp = tendn+ht:ht:(2*tendn);
ttt = [fliplr(tm) tt tp];
Pmi=-A0*exp(eta_TIhD*wn1rad*tm).*sin(w*tm);
% assumed force from t0 to -infinity
Ppi=A0*exp(-eta_TIhD*wn1rad*(tp-tendn)).*sin(w*(tp-tendn));
% assumed force from tend to +infinity

% pp=zeros(1,length);
% temp=[pp wr pp];
temp = [fliplr(Pmi) wr Ppi];
temp1 = [fliplr(Pmi) dot_rt Ppi];
wt=hilbert(temp);
% now define the analytic forcing function
wa=wt; % wt(length+1:length+npts+1);

% figure(1)
% plot([ttt],[temp])

%% ODE45 integration TIhD

wf=flip(wa);

% ode45 integration
y0 = [0;0];
tspan=[-tendn 2*tendn];
```

```
[T1,Q1] = ode45(@(t,y)myode1(t,y,s1,b,wf,ttt),tspan,y0);
Qrev1 = interp1(T1,Q1,ttt,'spline');
qvals1 = flip(Qrev1);

% ode45 integration
y0 = [0;0];
tspan=[-tendn 2*tendn];
[T2,Q2] = ode45(@(t,y)myode2(t,y,s2,b,wa,ttt),tspan,y0);
qvals2 = interp1(T2,Q2,ttt,'spline');

% ode45 integration
y0 = [0;0];
tspan=[-tendn 2*tendn];
[T3,Q3] = ode45(@(t,y)myode3(t,y,s3,b,wf,ttt),tspan,y0);
Qrev3 = interp1(T3,Q3,ttt,'spline');
qvals3 = flip(Qrev3);

% ode45 integration
y0 = [0;0];
tspan=[-tendn 2*tendn];
[T4,Q4] = ode45(@(t,y)myode4(t,y,s4,b,wa,ttt),tspan,y0);
qvals4 = interp1(T4,Q4,ttt,'spline');

% ode45 integration
y0 = [0;0];
tspan=[-tendn 2*tendn];
[T5,Q5] = ode45(@(t,y)myode5(t,y,s5,b,wf,ttt),tspan,y0);
Qrev5 = interp1(T5,Q5,ttt,'spline');
qvals5 = flip(Qrev5);

% ode45 integration
y0 = [0;0];
tspan=[-tendn 2*tendn];
[T6,Q6] = ode45(@(t,y)myode6(t,y,s6,b,wf,ttt),tspan,y0);
Qrev6 = interp1(T6,Q6,ttt,'spline');
qvals6 = flip(Qrev6);

% ode45 integration
y0 = [0;0];
tspan=[-tendn 2*tendn];
[T7,Q7] = ode45(@(t,y)myode7(t,y,s7,b,wa,ttt),tspan,y0);
qvals7 = interp1(T7,Q7,ttt,'spline');

% ode45 integration
y0 = [0;0];
tspan=[-tendn 2*tendn];
[T8,Q8] = ode45(@(t,y)myode8(t,y,s8,b,wa,ttt),tspan,y0);
qvals8 = interp1(T8,Q8,ttt,'spline');
```

```
x = phi*[(qvals1(:,1)+(1i*qvals1(:,2)))';
         (qvals2(:,1)+(1i*qvals2(:,2)))';
         (qvals3(:,1)+(1i*qvals3(:,2)))';
         (qvals4(:,1)+(1i*qvals4(:,2)))';
         (qvals5(:,1)+(1i*qvals5(:,2)))';
         (qvals6(:,1)+(1i*qvals6(:,2)))';
         (qvals7(:,1)+(1i*qvals7(:,2)))';
         (qvals8(:,1)+(1i*qvals8(:,2)))'];

%% ode45 TID
t  = ttt;
tdat = t;
y0 = [0;0;0;0;0;0;0;0];
tspan =[t(1):ht:t(end)];
[TR,ZR] = ode45(@(t,y)New_fun_MDOF_Ceq(t,y,m1,m2,m3,k1,k2,k3,
          kd_TID,cd_TID,b_TID,tdat,temp,temp1),tspan,y0);

%% plot

figure(18)
plot(ttt,real(x(5,:)),'-r','Linewidth',1.5)
hold on
plot(t,ZR(:,5),'-.b','Linewidth',1.5)
grid on
i=legend({'current method','equivalent viscous damping'},
          'Orientation','horizontal');
j=xlabel(['time (s)']);
ij=ylabel(['Top displacement, $x(t)$']);
set(i,'Interpreter','Latex','FontSize',9);
set(j,'Interpreter','Latex','FontSize',17);
set(ij,'Interpreter','Latex','FontSize',17);

%axis([0 20 -10 10]); % for f=fn1
axis([0 20 -30 30]); % for f=fn2

x01=10;
y01=10;
width=420;
height=220;
set(gcf,'position',[x01,y01,width,height]);

abc=real(x(5,:));
def=ZR(:,5);

axes('position',[0.585 0.25 0.3 0.2]);
box on
index= 0<ttt & ttt<20;
```

```
index1= 0<t & t<20;
plot(ttt(index),abc(index),'-r','Linewidth',1.5)
hold on
plot(ttt(index),def(index),'-.b','Linewidth',1.5)
grid on

%axis([7.54 7.63 6.0 7.2]); % for f=fn1
axis([16.85 17.2 -30 30]); % for f=fn2

saveas(gcf,'MDOF_TIDvsTIhD_fn2','epsc');

%% Functions TIhD

function  ydot = myode1(t,y,s1,b,wf,ttt)
war = interp1(ttt,real(wf),t);
wai = interp1(ttt,imag(wf),t);
ydot = zeros(2,1);
ydot(1)=-real(s1)*y(1)+imag(s1)*y(2)-real(b(1))*war+imag(b(1))*wai;
ydot(2)=-real(s1)*y(2)-imag(s1)*y(1)-real(b(1))*wai-imag(b(1))*war;
end

function  ydot = myode2(t,y,s2,b,wa,ttt)
war = interp1(ttt,real(wa),t);
wai = interp1(ttt,imag(wa),t);
ydot = zeros(2,1);
ydot(1)=real(s2)*y(1)-imag(s2)*y(2)+real(b(2))*war-imag(b(2))*wai;
ydot(2)=real(s2)*y(2)+imag(s2)*y(1)+real(b(2))*wai+imag(b(2))*war;
end

function  ydot = myode3(t,y,s3,b,wf,ttt)
war = interp1(ttt,real(wf),t);
wai = interp1(ttt,imag(wf),t);
ydot = zeros(2,1);
ydot(1)=-real(s3)*y(1)+imag(s3)*y(2)-real(b(3))*war+imag(b(3))*wai;
ydot(2)=-real(s3)*y(2)-imag(s3)*y(1)-real(b(3))*wai-imag(b(3))*war;
end

function  ydot = myode4(t,y,s4,b,wa,ttt)
war = interp1(ttt,real(wa),t);
wai = interp1(ttt,imag(wa),t);
ydot = zeros(2,1);
ydot(1)=real(s4)*y(1)-imag(s4)*y(2)+real(b(4))*war-imag(b(4))*wai;
ydot(2)=real(s4)*y(2)+imag(s4)*y(1)+real(b(4))*wai+imag(b(4))*war;
end

function  ydot = myode5(t,y,s5,b,wf,ttt)
war = interp1(ttt,real(wf),t);
wai = interp1(ttt,imag(wf),t);
```

```
ydot = zeros(2,1);
ydot(1)=-real(s5)*y(1)+imag(s5)*y(2)-real(b(5))*war+imag(b(5))*wai;
ydot(2)=-real(s5)*y(2)-imag(s5)*y(1)-real(b(5))*wai-imag(b(5))*war;
end

function  ydot = myode6(t,y,s6,b,wf,ttt)
war = interp1(ttt,real(wf),t);
wai = interp1(ttt,imag(wf),t);
ydot = zeros(2,1);
ydot(1)=-real(s6)*y(1)+imag(s6)*y(2)-real(b(6))*war+imag(b(6))*wai;
ydot(2)=-real(s6)*y(2)-imag(s6)*y(1)-real(b(6))*wai-imag(b(6))*war;
end

function  ydot = myode7(t,y,s7,b,wa,ttt)
war = interp1(ttt,real(wa),t);
wai = interp1(ttt,imag(wa),t);
ydot = zeros(2,1);
ydot(1)=real(s7)*y(1)-imag(s7)*y(2)+real(b(7))*war-imag(b(7))*wai;
ydot(2)=real(s7)*y(2)+imag(s7)*y(1)+real(b(7))*wai+imag(b(7))*war;
end

function  ydot = myode8(t,y,s8,b,wa,ttt)
war = interp1(ttt,real(wa),t);
wai = interp1(ttt,imag(wa),t);
ydot = zeros(2,1);
ydot(1)=real(s8)*y(1)-imag(s8)*y(2)+real(b(8))*war-imag(b(8))*wai;
ydot(2)=real(s8)*y(2)+imag(s8)*y(1)+real(b(8))*wai+imag(b(8))*war;
end



%% function TID
function  ydot = New_fun_MDOF_Ceq(t,y,m1,m2,m3,k1,k2,k3,kd_TID,
                                  cd_TID,b_TID,tdat,temp,temp1)
temp  = interp1(tdat,temp,t);
temp1  = interp1(tdat,temp1,t);
ydot = zeros(8,1);
% for base excitation (book 4 page 156)
ydot(1)=y(2);
ydot(2)=(-k1/m1)*(y(1)-temp)-(kd_TID/m1)*(y(7)-temp)
        -(cd_TID/m1)*(y(8)-temp1)+(k2/m1)*(y(3)-y(1));
ydot(3)=y(4);
ydot(4)=(-k2/m2)*(y(3)-y(1))+(k3/m2)*(y(5)-y(3));
ydot(5)=y(6);
ydot(6)=(-k3/m3)*(y(5)-y(3));
ydot(7)=y(8);
ydot(8)=(-k1/m1)*(y(1)-temp)-(kd_TID/m1)*(y(7)-temp)
        -(cd_TID/m1)*(y(8)-temp1)+(k2/m1)*(y(3)-y(1))
```

```
        -(kd_TID/b_TID)*(y(7)-temp)-(cd_TID/b_TID)*(y(8)-temp1);
end
```

Appendix E: MATLAB code for time domain analysis of a MDOF structure equipped with a TMhDI with a grounded inerter

```
clear all
close all
clc

%% Parameters
b=0.08; % width of columns (m)
h=0.01; % thickness of columns (m)
l=0.78; % storey height (m)
bolts_and_plates=12.4; %kg
storey=21.05; %kg
column=11.55; %kg

% Structural properties
m1=storey+(bolts_and_plates/4)+9; % 7kg is the mass of the two gel dampers
m2=storey+(bolts_and_plates/4);
m3=storey+(bolts_and_plates/4);
E=200e9;
I=4*(1/12)*(b)*(h)^3; %
k1=12.5*(E*I/l^3);
k2=15*(E*I/l^3);
k3=18.5*(E*I/l^3);

%% Properties of TMhDI
md=1+9;
b_TMhDI=16;
kh_TMhDI=29000;
eta_TMhDI=0.35;
sh_TMhDI=eta_TMhDI*kh_TMhDI;
```

```
wn1=5.5261;%35%2*pi*5.5261; % first natural freq in rad/s
w_input=30; %  % frequency of input signal in rad/s

%% calculation TMhDI - nongrounded (book 5 page 52)
% A_TMhDI= [0 1 0 0 0 0 0 0;
%     ((k1+k2)*(md+b_TMhDI)/((b_TMhDI^2)-(m1+b_TMhDI)*(md+b_TMhDI))) 0
%     (-k2*(md+b_TMhDI)/((b_TMhDI^2)-(m1+b_TMhDI)*(md+b_TMhDI)))
%     0 0 0 ((b_TMhDI*kh_TMhDI)+(i*sh_TMhDI*b_TMhDI))/((b_TMhDI^2)
%     -(m1+b_TMhDI)*(md+b_TMhDI)) 0;
%     0 0 0 1 0 0 0 0;
%     (k2/m2) 0 -k2/m2-k3/m2 0 k3/m2 0 0 0;
%     0 0 0 0 0 1 0 0;
%     0 0 k3/m3 0 -k3/m3 0 0 0;
%     0 0 0 0 0 0 0 1;
%     ((-k2*b_TMhDI)-(k1*b_TMhDI))/((m1+b_TMhDI)*(md+b_TMhDI)-b_TMhDI^2) 0
%     k2*b_TMhDI/((m1+b_TMhDI)*(md+b_TMhDI)-b_TMhDI^2)
%     0 0 0 (-kh_TMhDI*(m1+b_TMhDI)
%     -(i*sh_TMhDI*(m1+b_TMhDI)))/((m1+b_TMhDI)*(md+b_TMhDI)-b_TMhDI^2) 0];
%
% B_TMhDI=[0;((-k1*(md+b_TMhDI))-(b_TMhDI*kh_TMhDI)
%          -(i*sh_TMhDI*b_TMhDI))/((b_TMhDI^2)-(m1+b_TMhDI)*(md+b_TMhDI));
%          0;0;0;0;0;
%          (k1*b_TMhDI+kh_TMhDI*(m1+b_TMhDI)
%          +i*sh_TMhDI*(m1+b_TMhDI))/((m1+b_TMhDI)*(md+b_TMhDI)-b_TMhDI^2)];
          % base excitation (acceleration)


% %% calculation TMhDI - grounded (book 6 page 154)
A_TMhDI= [0 1 0 0 0 0 0 0;
    ((-k1-k2-kh_TMhDI-(i*sh_TMhDI))/m1) 0 (k2/m1)
    0 0 0 (kh_TMhDI+(i*sh_TMhDI))/m1 0;
    0 0 0 1 0 0 0 0;
    (k2/m2) 0 (-k2-k3)/m2 0 k3/m2 0 0 0;
    0 0 0 0 0 1 0 0;
    0 0 k3/m3 0 -k3/m3 0 0 0;
    0 0 0 0 0 0 0 1;
    (kh_TMhDI+(i*sh_TMhDI))/(md+b_TMhDI)
    0 0 0 0 0 (-kh_TMhDI-(i*sh_TMhDI))/(md+b_TMhDI) 0];

B_TMhDI=[0;(k1/m1);0;0;0;0;0;0]; % base excitation (displacement)
C_TMhDI=[0;0;0;0;0;0;0;(b_TMhDI/(md+b_TMhDI))];
% base excitation (acceleration)


%%
% eigenvectors
[V_TMhDI,D_TMhDI] = eig(A_TMhDI);
%phi=V;
```

```
phi_TMhDI=[V_TMhDI(1,1)/V_TMhDI(5,1) V_TMhDI(1,2)/V_TMhDI(5,2)
           V_TMhDI(1,3)/V_TMhDI(5,3) V_TMhDI(1,4)/V_TMhDI(5,4)
           V_TMhDI(1,5)/V_TMhDI(5,5) V_TMhDI(1,6)/V_TMhDI(5,6)
           V_TMhDI(1,7)/V_TMhDI(5,7) V_TMhDI(1,8)/V_TMhDI(5,8);
           V_TMhDI(2,1)/V_TMhDI(5,1) V_TMhDI(2,2)/V_TMhDI(5,2)
           V_TMhDI(2,3)/V_TMhDI(5,3) V_TMhDI(2,4)/V_TMhDI(5,4)
           V_TMhDI(2,5)/V_TMhDI(5,5) V_TMhDI(2,6)/V_TMhDI(5,6)
           V_TMhDI(2,7)/V_TMhDI(5,7) V_TMhDI(2,8)/V_TMhDI(5,8);
           V_TMhDI(3,1)/V_TMhDI(5,1) V_TMhDI(3,2)/V_TMhDI(5,2)
           V_TMhDI(3,3)/V_TMhDI(5,3) V_TMhDI(3,4)/V_TMhDI(5,4)
           V_TMhDI(3,5)/V_TMhDI(5,5) V_TMhDI(3,6)/V_TMhDI(5,6)
           V_TMhDI(3,7)/V_TMhDI(5,7) V_TMhDI(3,8)/V_TMhDI(5,8);
           V_TMhDI(4,1)/V_TMhDI(5,1) V_TMhDI(4,2)/V_TMhDI(5,2)
           V_TMhDI(4,3)/V_TMhDI(5,3) V_TMhDI(4,4)/V_TMhDI(5,4)
           V_TMhDI(4,5)/V_TMhDI(5,5) V_TMhDI(4,6)/V_TMhDI(5,6)
           V_TMhDI(4,7)/V_TMhDI(5,7) V_TMhDI(4,8)/V_TMhDI(5,8);
           V_TMhDI(5,1)/V_TMhDI(5,1) V_TMhDI(5,2)/V_TMhDI(5,2)
           V_TMhDI(5,3)/V_TMhDI(5,3) V_TMhDI(5,4)/V_TMhDI(5,4)
           V_TMhDI(5,5)/V_TMhDI(5,5) V_TMhDI(5,6)/V_TMhDI(5,6)
           V_TMhDI(5,7)/V_TMhDI(5,7) V_TMhDI(5,8)/V_TMhDI(5,8);
           V_TMhDI(6,1)/V_TMhDI(5,1) V_TMhDI(6,2)/V_TMhDI(5,2)
           V_TMhDI(6,3)/V_TMhDI(5,3) V_TMhDI(6,4)/V_TMhDI(5,4)
           V_TMhDI(6,5)/V_TMhDI(5,5) V_TMhDI(6,6)/V_TMhDI(5,6)
           V_TMhDI(6,7)/V_TMhDI(5,7) V_TMhDI(6,8)/V_TMhDI(5,8);
           V_TMhDI(7,1)/V_TMhDI(5,1) V_TMhDI(7,2)/V_TMhDI(5,2)
           V_TMhDI(7,3)/V_TMhDI(5,3) V_TMhDI(7,4)/V_TMhDI(5,4)
           V_TMhDI(7,5)/V_TMhDI(5,5) V_TMhDI(7,6)/V_TMhDI(5,6)
           V_TMhDI(7,7)/V_TMhDI(5,7) V_TMhDI(7,8)/V_TMhDI(5,8);
           V_TMhDI(8,1)/V_TMhDI(5,1) V_TMhDI(8,2)/V_TMhDI(5,2)
           V_TMhDI(8,3)/V_TMhDI(5,3) V_TMhDI(8,4)/V_TMhDI(5,4)
           V_TMhDI(8,5)/V_TMhDI(5,5) V_TMhDI(8,6)/V_TMhDI(5,6)
           V_TMhDI(8,7)/V_TMhDI(5,7) V_TMhDI(8,8)/V_TMhDI(5,8)];

% teta^-1*A*teta
Q_md=inv(phi_TMhDI)*A_TMhDI*phi_TMhDI;
% teta^-1*B
b_md=inv(phi_TMhDI)*B_TMhDI;
c_md=inv(phi_TMhDI)*C_TMhDI;

% eigenvalues
s1_md=Q_md(1,1);
s2_md=Q_md(2,2); % =-s1
s3_md=Q_md(3,3);
s4_md=Q_md(4,4); % =-s3
s5_md=Q_md(5,5);
s6_md=Q_md(6,6);
s7_md=Q_md(7,7); % =-s5
s8_md=Q_md(8,8); % =-s6
```

```
%% Declare vectors to hold time series results

TT=30;      % total time in seconds
del=0.001;   % time interval and time vector
w=w_input;        % frequency of input signal in rad/s
A0=1;        % amplitude of input signal

freq = w/(2*pi);
T = 1/freq;
cycle = ceil(TT/T); % round-up number of cycle
tendn = cycle*T;    % round-up end time

dt = ceil(T/del);
ht = T/dt;
tt = 0:ht:tendn;
n = numel(tt);

wr=A0*sin(w*tt);
wr_ddot=(w_input^2)*A0*-sin(w*tt);

%% construct the hilbert function with zero padding at start and finish

% length=2048;
tm = -ht:-ht:-tendn;
tp = tendn+ht:ht:(2*tendn);
ttt = [fliplr(tm) tt tp];
Pmi=-A0*exp(eta_TMhDI*wn1*tm).*sin(w*tm);
% assumed force from t0 to -infinity
Ppi=A0*exp(-eta_TMhDI*wn1*(tp-tendn)).*sin(w*(tp-tendn));
% assumed force from tend to +infinity
Pmi_ddot=-A0*exp(eta_TMhDI*wn1*tm).*-w^2.*sin(w*tm);
% assumed force from t0 to -infinity
Ppi_ddot=A0*exp(-eta_TMhDI*wn1*(tp-tendn)).*-w^2.*sin(w*(tp-tendn));
% assumed force from tend to +infinity

% pp=zeros(1,length);
% temp=[pp wr pp];
temp = [fliplr(Pmi) wr Ppi];
temp1= [fliplr(Pmi_ddot) wr_ddot Ppi_ddot];
wt=hilbert(temp);
wt_ddot=hilbert(temp1);
% now define the analytic forcing function
wa=wt; % wt(length+1:length+npts+1);
wa_ddot=wt_ddot;

figure(1)
plot([ttt],[imag(wa_ddot)],'b')
```

```
hold on
plot([ttt],[real(wa_ddot)],'r')

%% ODE45 integration TMhDI
wf=flip(wa);
wf_ddot=flip(wa_ddot);
% ode45 integration
y0 = [0;0];
tspan=[-tendn 2*tendn];
[T1_md,Q1_md] = ode45(@(t,y)myode1_md(t,y,s1_md,b_md,
                                      c_md,wf,wf_ddot,ttt),tspan,y0);
Qrev1_md = interp1(T1_md,Q1_md,ttt,'spline');
qvals1_md = flip(Qrev1_md);
figure(2)
plot(ttt,qvals1_md(:,1))
figure(3)
plot(ttt,qvals1_md(:,2))

% ode45 integration
y0 = [0;0];
tspan=[-tendn 2*tendn];
[T2_md,Q2_md] = ode45(@(t,y)myode2_md(t,y,s2_md,b_md,
                                      c_md,wa,wa_ddot,ttt),tspan,y0);
qvals2_md = interp1(T2_md,Q2_md,ttt,'spline');
figure(4)
plot(ttt,qvals2_md(:,1))
figure(5)
plot(ttt,qvals2_md(:,2))

% ode45 integration
y0 = [0;0];
tspan=[-tendn 2*tendn];
[T3_md,Q3_md] = ode45(@(t,y)myode3_md(t,y,s3_md,b_md,
                                      c_md,wf,wf_ddot,ttt),tspan,y0);
Qrev3_md = interp1(T3_md,Q3_md,ttt,'spline');
qvals3_md = flip(Qrev3_md);
figure(6)
plot(ttt,qvals3_md(:,1))
figure(7)
plot(ttt,qvals3_md(:,2))

% ode45 integration
y0 = [0;0];
tspan=[-tendn 2*tendn];
[T4_md,Q4_md] = ode45(@(t,y)myode4_md(t,y,s4_md,b_md,
                                      c_md,wa,wa_ddot,ttt),tspan,y0);
qvals4_md = interp1(T4_md,Q4_md,ttt,'spline');
figure(8)
```

```
plot(ttt,qvals4_md(:,1))
figure(9)
plot(ttt,qvals4_md(:,2))

% ode45 integration
y0 = [0;0];
tspan=[-tendn 2*tendn];
[T5_md,Q5_md] = ode45(@(t,y)myode5_md(t,y,s5_md,b_md,
                                      c_md,wf,wf_ddot,ttt),tspan,y0);
Qrev5_md = interp1(T5_md,Q5_md,ttt,'spline');
qvals5_md = flip(Qrev5_md);
figure(10)
plot(ttt,qvals5_md(:,1))
figure(11)
plot(ttt,qvals5_md(:,2))

% ode45 integration
y0 = [0;0];
tspan=[-tendn 2*tendn];
[T6_md,Q6_md] = ode45(@(t,y)myode6_md(t,y,s6_md,b_md,
                                      c_md,wf,wf_ddot,ttt),tspan,y0);
Qrev6_md = interp1(T6_md,Q6_md,ttt,'spline');
qvals6_md = flip(Qrev6_md);
figure(12)
plot(ttt,qvals6_md(:,1))
figure(13)
plot(ttt,qvals6_md(:,2))

% ode45 integration
y0 = [0;0];
tspan=[-tendn 2*tendn];
[T7_md,Q7_md] = ode45(@(t,y)myode7_md(t,y,s7_md,b_md,
                                      c_md,wa,wa_ddot,ttt),tspan,y0);
qvals7_md = interp1(T7_md,Q7_md,ttt,'spline');
figure(14)
plot(ttt,qvals7_md(:,1))
figure(15)
plot(ttt,qvals7_md(:,2))

% ode45 integration
y0 = [0;0];
tspan=[-tendn 2*tendn];
[T8_md,Q8_md] = ode45(@(t,y)myode8_md(t,y,s8_md,b_md,
                                      c_md,wa,wa_ddot,ttt),tspan,y0);
qvals8_md = interp1(T8_md,Q8_md,ttt,'spline');
figure(16)
plot(ttt,qvals8_md(:,1))
figure(17)
```

```
plot(ttt,qvals8_md(:,2))

x_md = phi_TMhDI*[(qvals1_md(:,1)+(1i*qvals1_md(:,2)))';
          (qvals2_md(:,1)+(1i*qvals2_md(:,2)))';
          (qvals3_md(:,1)+(1i*qvals3_md(:,2)))';
          (qvals4_md(:,1)+(1i*qvals4_md(:,2)))';
          (qvals5_md(:,1)+(1i*qvals5_md(:,2)))';
          (qvals6_md(:,1)+(1i*qvals6_md(:,2)))';
          (qvals7_md(:,1)+(1i*qvals7_md(:,2)))';
          (qvals8_md(:,1)+(1i*qvals8_md(:,2)))'];

%% plot

figure(18)
plot(ttt,real(x_md(5,:)),'b','Linewidth',1.5)
grid on
i=legend('TMhDI');
j=xlabel('time (s)');
ij=ylabel('displacement, $X_3$ (cm)');

set(i,'Interpreter','Latex','FontSize',13);
set(j,'Interpreter','Latex','FontSize',17);
set(ij,'Interpreter','Latex','FontSize',17);

x01=10;
y01=10;
width=420;
height=220;
set(gcf,'position',[x01,y01,width,height]);

%% Functions TMhDI

function  ydot = myode1_md(t,y,s1_md,b_md,c_md,wf,wf_ddot,ttt)
war = interp1(ttt,real(wf),t);
wai = interp1(ttt,imag(wf),t);
war_ddot = interp1(ttt,real(wf_ddot),t);
wai_ddot = interp1(ttt,imag(wf_ddot),t);
ydot = zeros(2,1);
ydot(1)=-real(s1_md)*y(1)+imag(s1_md)*y(2)-real(b_md(1))*war
        +imag(b_md(1))*wai-real(c_md(1))*war_ddot+imag(c_md(1))*wai_ddot;
ydot(2)=-real(s1_md)*y(2)-imag(s1_md)*y(1)
        -real(b_md(1))*wai-imag(b_md(1))*war
        -real(c_md(1))*wai_ddot-imag(c_md(1))*war_ddot;
end

function  ydot = myode2_md(t,y,s2_md,b_md,c_md,wa,wa_ddot,ttt)
war = interp1(ttt,real(wa),t);
wai = interp1(ttt,imag(wa),t);
```

```
war_ddot = interp1(ttt,real(wa_ddot),t);
wai_ddot = interp1(ttt,imag(wa_ddot),t);
ydot = zeros(2,1);
ydot(1)=real(s2_md)*y(1)-imag(s2_md)*y(2)+real(b_md(2))*war
        -imag(b_md(2))*wai+real(c_md(2))*war_ddot-imag(c_md(2))*wai_ddot;
ydot(2)=real(s2_md)*y(2)+imag(s2_md)*y(1)
        +real(b_md(2))*wai+imag(b_md(2))*war
        +real(c_md(2))*wai_ddot+imag(c_md(2))*war_ddot;
end

function  ydot = myode3_md(t,y,s3_md,b_md,c_md,wf,wf_ddot,ttt)
war = interp1(ttt,real(wf),t);
wai = interp1(ttt,imag(wf),t);
war_ddot = interp1(ttt,real(wf_ddot),t);
wai_ddot = interp1(ttt,imag(wf_ddot),t);
ydot = zeros(2,1);
ydot(1)=-real(s3_md)*y(1)+imag(s3_md)*y(2)-real(b_md(3))*war
        +imag(b_md(3))*wai-real(c_md(3))*war_ddot+imag(c_md(3))*wai_ddot;
ydot(2)=-real(s3_md)*y(2)-imag(s3_md)*y(1)
        -real(b_md(3))*wai-imag(b_md(3))*war
        -real(c_md(3))*wai_ddot-imag(c_md(3))*war_ddot;
end

function  ydot = myode4_md(t,y,s4_md,b_md,c_md,wa,wa_ddot,ttt)
war = interp1(ttt,real(wa),t);
wai = interp1(ttt,imag(wa),t);
war_ddot = interp1(ttt,real(wa_ddot),t);
wai_ddot = interp1(ttt,imag(wa_ddot),t);
ydot = zeros(2,1);
ydot(1)=real(s4_md)*y(1)-imag(s4_md)*y(2)+real(b_md(4))*war
        -imag(b_md(4))*wai+real(c_md(4))*war_ddot-imag(c_md(4))*wai_ddot;
ydot(2)=real(s4_md)*y(2)+imag(s4_md)*y(1)
        +real(b_md(4))*wai+imag(b_md(4))*war
        +real(c_md(4))*wai_ddot+imag(c_md(4))*war_ddot;
end

function  ydot = myode5_md(t,y,s5_md,b_md,c_md,wf,wf_ddot,ttt)
war = interp1(ttt,real(wf),t);
wai = interp1(ttt,imag(wf),t);
war_ddot = interp1(ttt,real(wf_ddot),t);
wai_ddot = interp1(ttt,imag(wf_ddot),t);
ydot = zeros(2,1);
ydot(1)=-real(s5_md)*y(1)+imag(s5_md)*y(2)-real(b_md(5))*war
        +imag(b_md(5))*wai-real(c_md(5))*war_ddot+imag(c_md(5))*wai_ddot;
ydot(2)=-real(s5_md)*y(2)-imag(s5_md)*y(1)
        -real(b_md(5))*wai-imag(b_md(5))*war
        -real(c_md(5))*wai_ddot-imag(c_md(5))*war_ddot;
end
```

```
function  ydot = myode6_md(t,y,s6_md,b_md,c_md,wf,wf_ddot,ttt)
war = interp1(ttt,real(wf),t);
wai = interp1(ttt,imag(wf),t);
war_ddot = interp1(ttt,real(wf_ddot),t);
wai_ddot = interp1(ttt,imag(wf_ddot),t);
ydot = zeros(2,1);
ydot(1)=-real(s6_md)*y(1)+imag(s6_md)*y(2)-real(b_md(6))*war
        +imag(b_md(6))*wai-real(c_md(6))*war_ddot+imag(c_md(6))*wai_ddot;
ydot(2)=-real(s6_md)*y(2)-imag(s6_md)*y(1)
        -real(b_md(6))*wai-imag(b_md(6))*war
        -real(c_md(6))*wai_ddot-imag(c_md(6))*war_ddot;
end

function  ydot = myode7_md(t,y,s7_md,b_md,c_md,wa,wa_ddot,ttt)
war = interp1(ttt,real(wa),t);
wai = interp1(ttt,imag(wa),t);
war_ddot = interp1(ttt,real(wa_ddot),t);
wai_ddot = interp1(ttt,imag(wa_ddot),t);
ydot = zeros(2,1);
ydot(1)=real(s7_md)*y(1)-imag(s7_md)*y(2)+real(b_md(7))*war
        -imag(b_md(7))*wai+real(c_md(7))*war_ddot-imag(c_md(7))*wai_ddot;
ydot(2)=real(s7_md)*y(2)+imag(s7_md)*y(1)
        +real(b_md(7))*wai+imag(b_md(7))*war
        +real(c_md(7))*wai_ddot+imag(c_md(7))*war_ddot;
end

function  ydot = myode8_md(t,y,s8_md,b_md,c_md,wa,wa_ddot,ttt)
war = interp1(ttt,real(wa),t);
wai = interp1(ttt,imag(wa),t);
war_ddot = interp1(ttt,real(wa_ddot),t);
wai_ddot = interp1(ttt,imag(wa_ddot),t);
ydot = zeros(2,1);
ydot(1)=real(s8_md)*y(1)-imag(s8_md)*y(2)+real(b_md(8))*war
        -imag(b_md(8))*wai+real(c_md(8))*war_ddot-imag(c_md(8))*wai_ddot;
ydot(2)=real(s8_md)*y(2)+imag(s8_md)*y(1)
        +real(b_md(8))*wai+imag(b_md(8))*war
        +real(c_md(8))*wai_ddot+imag(c_md(8))*war_ddot;
end
```

Appendix F: MATLAB code for time domain analysis of a MDOF structure equipped with a TVIhD

```
clear all
close all
clc

%% Host structure parameters
b=0.08; % width of columns (m)
h=0.01; % thickness of columns (m)
l=0.78; % storey height (m)
bolts_and_plates=12.4; %kg
storey=21.05; %kg
column=11.55; %kg

% Structural properties
m1=storey+(bolts_and_plates/4)+9; % 9kg is the mass of the two gel dampers
m2=storey+(bolts_and_plates/4);
m3=storey+(bolts_and_plates/4);
E=200e9;
I=4*(1/12)*(b)*(h)^3; %
k1=12.5*(E*I/l^3);
k2=15*(E*I/l^3);
k3=18.5*(E*I/l^3);

%% Properties of IVED
bd=33.6000;
cd=353.4755;
kd=35200;
eta=0.5300;
sh=eta*kd;

wn1=5.5261;
w_input=152.82; %  % frequency of input signal in rad/s
```

```
%% calculation IVED - grounded (book 7 page 11)
A_IVED= [0 1 0 0 0 0 0 0;
         (-k1-k2)/m1 0 (k2/m1) 0 0 0 (-kd/m1)*(1+i*eta) 0;
         0 0 0 1 0 0 0 0;
         (k2/m2) 0 (-k2-k3)/m2 0 k3/m2 0 0 0;
         0 0 0 0 0 1 0 0;
         0 0 k3/m3 0 -k3/m3 0 0 0;
         0 0 0 0 0 0 0 1;
         (-k1-k2)/m1 (cd/bd) (k2/m1) 0 0 0 (((-kd/m1)*(1+i*eta))
         -((kd/bd)*(1+i*eta))) -cd/bd];

B_IVED=[0;(k1/m1)+((kd/m1)*(1+i*eta));0;0;0;0;0;
       (k1/m1)+(((kd/m1)+(kd/bd))*(1+i*eta))];
       % base excitation (displacement)


%%
% eigenvectors
[V_IVED,D_IVED] = eig(A_IVED);
%phi=V;
phi_IVED=[V_IVED(1,1)/V_IVED(5,1) V_IVED(1,2)/V_IVED(5,2)
          V_IVED(1,3)/V_IVED(5,3) V_IVED(1,4)/V_IVED(5,4)
          V_IVED(1,5)/V_IVED(5,5) V_IVED(1,6)/V_IVED(5,6)
          V_IVED(1,7)/V_IVED(5,7) V_IVED(1,8)/V_IVED(5,8);
          V_IVED(2,1)/V_IVED(5,1) V_IVED(2,2)/V_IVED(5,2)
          V_IVED(2,3)/V_IVED(5,3) V_IVED(2,4)/V_IVED(5,4)
          V_IVED(2,5)/V_IVED(5,5) V_IVED(2,6)/V_IVED(5,6)
          V_IVED(2,7)/V_IVED(5,7) V_IVED(2,8)/V_IVED(5,8);
          V_IVED(3,1)/V_IVED(5,1) V_IVED(3,2)/V_IVED(5,2)
          V_IVED(3,3)/V_IVED(5,3) V_IVED(3,4)/V_IVED(5,4)
          V_IVED(3,5)/V_IVED(5,5) V_IVED(3,6)/V_IVED(5,6)
          V_IVED(3,7)/V_IVED(5,7) V_IVED(3,8)/V_IVED(5,8);
          V_IVED(4,1)/V_IVED(5,1) V_IVED(4,2)/V_IVED(5,2)
          V_IVED(4,3)/V_IVED(5,3) V_IVED(4,4)/V_IVED(5,4)
          V_IVED(4,5)/V_IVED(5,5) V_IVED(4,6)/V_IVED(5,6)
          V_IVED(4,7)/V_IVED(5,7) V_IVED(4,8)/V_IVED(5,8);
          V_IVED(5,1)/V_IVED(5,1) V_IVED(5,2)/V_IVED(5,2)
          V_IVED(5,3)/V_IVED(5,3) V_IVED(5,4)/V_IVED(5,4)
          V_IVED(5,5)/V_IVED(5,5) V_IVED(5,6)/V_IVED(5,6)
          V_IVED(5,7)/V_IVED(5,7) V_IVED(5,8)/V_IVED(5,8);
          V_IVED(6,1)/V_IVED(5,1) V_IVED(6,2)/V_IVED(5,2)
          V_IVED(6,3)/V_IVED(5,3) V_IVED(6,4)/V_IVED(5,4)
          V_IVED(6,5)/V_IVED(5,5) V_IVED(6,6)/V_IVED(5,6)
          V_IVED(6,7)/V_IVED(5,7) V_IVED(6,8)/V_IVED(5,8);
          V_IVED(7,1)/V_IVED(5,1) V_IVED(7,2)/V_IVED(5,2)
          V_IVED(7,3)/V_IVED(5,3) V_IVED(7,4)/V_IVED(5,4)
          V_IVED(7,5)/V_IVED(5,5) V_IVED(7,6)/V_IVED(5,6)
```

```
          V_IVED(7,7)/V_IVED(5,7) V_IVED(7,8)/V_IVED(5,8);
          V_IVED(8,1)/V_IVED(5,1) V_IVED(8,2)/V_IVED(5,2)
          V_IVED(8,3)/V_IVED(5,3) V_IVED(8,4)/V_IVED(5,4)
          V_IVED(8,5)/V_IVED(5,5) V_IVED(8,6)/V_IVED(5,6)
          V_IVED(8,7)/V_IVED(5,7) V_IVED(8,8)/V_IVED(5,8)];

% teta^-1*A*teta
Q_md=inv(phi_IVED)*A_IVED*phi_IVED;
% teta^-1*B
b_md=inv(phi_IVED)*B_IVED;

% eigenvalues
s1_md=Q_md(1,1);
s2_md=Q_md(2,2); % =-s1
s3_md=Q_md(3,3);
s4_md=Q_md(4,4); % =-s3
s5_md=Q_md(5,5);
s6_md=Q_md(6,6);
s7_md=Q_md(7,7); % =-s5
s8_md=Q_md(8,8); % =-s6

%% Declare vectors to hold time series results

TT=30;      % total time in seconds
del=0.0001;   % time interval and time vector
w=w_input;        % frequency of input signal in rad/s
A0=1;        % amplitude of input signal

freq = w/(2*pi);
T = 1/freq;
cycle = ceil(TT/T); % round-up number of cycle
tendn = cycle*T;    % round-up end time

dt = ceil(T/del);
ht = T/dt;
tt = 0:ht:tendn;
n = numel(tt);

wr=A0*sin(w*tt);

%% construct the hilbert function with zero padding at start and finish

% length=2048;
tm = -ht:-ht:-tendn;
tp = tendn+ht:ht:(2*tendn);
ttt = [fliplr(tm) tt tp];
Pmi=-A0*exp(eta*wn1*tm).*sin(w*tm);
% assumed force from t0 to -infinity
```

```
Ppi=A0*exp(-eta*wn1*(tp-tendn)).*sin(w*(tp-tendn));
% assumed force from tend to +infinity

% pp=zeros(1,length);
% temp=[pp wr pp];
temp = [fliplr(Pmi) wr Ppi];
wt=hilbert(temp);
% now define the analytic forcing function
wa=wt; % wt(length+1:length+npts+1);

%% ODE45 integration IVED
wf=flip(wa);
% ode45 integration
y0 = [0;0];
tspan=[-tendn 2*tendn];
[T1_md,Q1_md] = ode45(@(t,y)myode1_md(t,y,s1_md,b_md,wa,ttt),tspan,y0);
qvals1_md = interp1(T1_md,Q1_md,ttt,'spline');
figure(2)
plot(ttt,qvals1_md(:,1))
figure(3)
plot(ttt,qvals1_md(:,2))

% ode45 integration
y0 = [0;0];
tspan=[-tendn 2*tendn];
[T2_md,Q2_md] = ode45(@(t,y)myode2_md(t,y,s2_md,b_md,wf,ttt),tspan,y0);
Qrev2_md = interp1(T2_md,Q2_md,ttt,'spline');
qvals2_md = flip(Qrev2_md);
figure(4)
plot(ttt,qvals2_md(:,1))
figure(5)
plot(ttt,qvals2_md(:,2))

% ode45 integration
y0 = [0;0];
tspan=[-tendn 2*tendn];
[T3_md,Q3_md] = ode45(@(t,y)myode3_md(t,y,s3_md,b_md,wa,ttt),tspan,y0);
qvals3_md = interp1(T3_md,Q3_md,ttt,'spline');
figure(6)
plot(ttt,qvals3_md(:,1))
figure(7)
plot(ttt,qvals3_md(:,2))

% ode45 integration
y0 = [0;0];
tspan=[-tendn 2*tendn];
[T4_md,Q4_md] = ode45(@(t,y)myode4_md(t,y,s4_md,b_md,wf,ttt),tspan,y0);
Qrev4_md = interp1(T4_md,Q4_md,ttt,'spline');
```

```
qvals4_md = flip(Qrev4_md);
figure(8)
plot(ttt,qvals4_md(:,1))
figure(9)
plot(ttt,qvals4_md(:,2))

% ode45 integration
y0 = [0;0];
tspan=[-tendn 2*tendn];
[T5_md,Q5_md] = ode45(@(t,y)myode5_md(t,y,s5_md,b_md,wa,ttt),tspan,y0);
qvals5_md = interp1(T5_md,Q5_md,ttt,'spline');
figure(10)
plot(ttt,qvals5_md(:,1))
figure(11)
plot(ttt,qvals5_md(:,2))

% ode45 integration
y0 = [0;0];
tspan=[-tendn 2*tendn];
[T6_md,Q6_md] = ode45(@(t,y)myode6_md(t,y,s6_md,b_md,wa,ttt),tspan,y0);
qvals6_md = interp1(T6_md,Q6_md,ttt,'spline');
figure(12)
plot(ttt,qvals6_md(:,1))
figure(13)
plot(ttt,qvals6_md(:,2))

% ode45 integration
y0 = [0;0];
tspan=[-tendn 2*tendn];
[T7_md,Q7_md] = ode45(@(t,y)myode7_md(t,y,s7_md,b_md,wf,ttt),tspan,y0);
Qrev7_md = interp1(T7_md,Q7_md,ttt,'spline');
qvals7_md = flip(Qrev7_md);
figure(14)
plot(ttt,qvals7_md(:,1))
figure(15)
plot(ttt,qvals7_md(:,2))

% ode45 integration
y0 = [0;0];
tspan=[-tendn 2*tendn];
[T8_md,Q8_md] = ode45(@(t,y)myode8_md(t,y,s8_md,b_md,wa,ttt),tspan,y0);
qvals8_md = interp1(T8_md,Q8_md,ttt,'spline');
figure(16)
plot(ttt,qvals8_md(:,1))
figure(17)
plot(ttt,qvals8_md(:,2))

x_md = phi_IVED*[(qvals1_md(:,1)+(1i*qvals1_md(:,2)))';
```

```
          (qvals2_md(:,1)+(1i*qvals2_md(:,2)))';
          (qvals3_md(:,1)+(1i*qvals3_md(:,2)))';
          (qvals4_md(:,1)+(1i*qvals4_md(:,2)))';
          (qvals5_md(:,1)+(1i*qvals5_md(:,2)))';
          (qvals6_md(:,1)+(1i*qvals6_md(:,2)))';
          (qvals7_md(:,1)+(1i*qvals7_md(:,2)))';
          (qvals8_md(:,1)+(1i*qvals8_md(:,2)))'];

%% plot

figure(18)
plot(ttt,real(x_md(5,:)),'b','Linewidth',1.5)
grid on
i=legend('IVED');
j=xlabel('time (s)');
ij=ylabel('displacement, $X_3$ (cm)');

set(i,'Interpreter','Latex','FontSize',13);
set(j,'Interpreter','Latex','FontSize',17);
set(ij,'Interpreter','Latex','FontSize',17);

x01=10;
y01=10;
width=420;
height=220;
set(gcf,'position',[x01,y01,width,height]);
%savefig('w30_2.fig')

%% Functions TMhDI

function  ydot = myode1_md(t,y,s1_md,b_md,wa,ttt)
war = interp1(ttt,real(wa),t);
wai = interp1(ttt,imag(wa),t);
ydot = zeros(2,1);
ydot(1)=real(s1_md)*y(1)-imag(s1_md)*y(2)
        +real(b_md(1))*war-imag(b_md(1))*wai;
ydot(2)=real(s1_md)*y(2)+imag(s1_md)*y(1)
        +real(b_md(1))*wai+imag(b_md(1))*war;
end

function  ydot = myode2_md(t,y,s2_md,b_md,wf,ttt)
war = interp1(ttt,real(wf),t);
wai = interp1(ttt,imag(wf),t);
ydot = zeros(2,1);
ydot(1)=-real(s2_md)*y(1)+imag(s2_md)*y(2)
        -real(b_md(2))*war+imag(b_md(2))*wai;
ydot(2)=-real(s2_md)*y(2)-imag(s2_md)*y(1)
        -real(b_md(2))*wai-imag(b_md(2))*war;
```

```
end

function  ydot = myode3_md(t,y,s3_md,b_md,wa,ttt)
war = interp1(ttt,real(wa),t);
wai = interp1(ttt,imag(wa),t);
ydot = zeros(2,1);
ydot(1)=real(s3_md)*y(1)-imag(s3_md)*y(2)
        +real(b_md(3))*war-imag(b_md(3))*wai;
ydot(2)=real(s3_md)*y(2)+imag(s3_md)*y(1)
        +real(b_md(3))*wai+imag(b_md(3))*war;
end

function  ydot = myode4_md(t,y,s4_md,b_md,wf,ttt)
war = interp1(ttt,real(wf),t);
wai = interp1(ttt,imag(wf),t);
ydot = zeros(2,1);
ydot(1)=-real(s4_md)*y(1)+imag(s4_md)*y(2)
        -real(b_md(4))*war+imag(b_md(4))*wai;
ydot(2)=-real(s4_md)*y(2)-imag(s4_md)*y(1)
        -real(b_md(4))*wai-imag(b_md(4))*war;
end

function  ydot = myode5_md(t,y,s5_md,b_md,wa,ttt)
war = interp1(ttt,real(wa),t);
wai = interp1(ttt,imag(wa),t);
ydot = zeros(2,1);
ydot(1)=real(s5_md)*y(1)-imag(s5_md)*y(2)
        +real(b_md(5))*war-imag(b_md(5))*wai;
ydot(2)=real(s5_md)*y(2)+imag(s5_md)*y(1)
        +real(b_md(5))*wai+imag(b_md(5))*war;
end

function  ydot = myode6_md(t,y,s6_md,b_md,wa,ttt)
war = interp1(ttt,real(wa),t);
wai = interp1(ttt,imag(wa),t);
ydot = zeros(2,1);
ydot(1)=real(s6_md)*y(1)-imag(s6_md)*y(2)
        +real(b_md(6))*war-imag(b_md(6))*wai;
ydot(2)=real(s6_md)*y(2)+imag(s6_md)*y(1)
        +real(b_md(6))*wai+imag(b_md(6))*war;
end

function  ydot = myode7_md(t,y,s7_md,b_md,wf,ttt)
war = interp1(ttt,real(wf),t);
wai = interp1(ttt,imag(wf),t);
ydot = zeros(2,1);
ydot(1)=-real(s7_md)*y(1)+imag(s7_md)*y(2)
        -real(b_md(7))*war+imag(b_md(7))*wai;
```

```
ydot(2)=-real(s7_md)*y(2)-imag(s7_md)*y(1)
        -real(b_md(7))*wai-imag(b_md(7))*war;
end

function  ydot = myode8_md(t,y,s8_md,b_md,wa,ttt)
war = interp1(ttt,real(wa),t);
wai = interp1(ttt,imag(wa),t);
ydot = zeros(2,1);
ydot(1)=real(s8_md)*y(1)-imag(s8_md)*y(2)
        +real(b_md(8))*war-imag(b_md(8))*wai;
ydot(2)=real(s8_md)*y(2)+imag(s8_md)*y(1)
        +real(b_md(8))*wai+imag(b_md(8))*war;
end
```